Conduction phenomena through gas and insulating solids in HVDC gas insulated substations, and consequences on electric field distribution

Laëtitia Zavattoni

UNIVERSITÉ DE GRENOBLE

THÈSE

Pour obtenir le grade de

DOCTEUR DE L'UNIVERSITÉ DE GRENOBLE

Spécialité : **Génie Éléctrique**

Arrêté ministériel : 7 Août 2006

Présentée par

Laëtitia ZAVATTONI

Thèse dirigée par **Pr. Olivier LESAINT**
et codirigée par **Dr. Olivier GALLOT-LAVALLÉE**

préparée au sein du **G2Elab**
et de **École Doctorale EEATS**

Conduction phenomena through gas and insulating solids in HVDC Gas Insulated Substations, and consequences on electric field distribution

Thèse soutenue publiquement le **07/10/2014**,
devant le jury composé de :

Prof. François BURET
Professeur à l'école Centrale de Lyon, Rapporteur

Prof. Emmanuel ODIC
Professeur à SUPELEC, Paris, Rapporteur

Prof. David MALEC
Professeur à l'Université Paul Sabatier, Toulouse, Examinateur

Dr. Karim BOUSOLTANE
Chef de Projet à Siemens T&D, Grenoble, Examinateur

Prof. Olivier LESAINT
Directeur de recherche au CNRS-G2Elab, Directeur de thèse

Dr. Olivier Gallot-Lavallée
Maître de conférences à l'Université Joseph Fourier, Grenoble, Co-Encadrant de thèse

A la mémoire de mon grand-père...

«*Aie le courage de te servir de ton propre entendement.*»

Les philosophes des Lumières

«*I am somebody. I was somebody before I came,*
and I will be a better somebody when I'll leave.»

Rita Pearson

Remerciements

Un grand merci à toutes et à tous ceux qui m'ont accompagné au cours de ces trois années...

Je ne sais pas vraiment par qui ni par où commencer et j'espère surtout que je ne vais oublier personne. Allez je me lance!

Aussi ironique que cela puisse paraître je tiens tout d'abord à remercier Georges Gaudart, qui avant de quitter Siemens, a eu la bonne idée de me recruter pour cette thèse. Merci à toi Georges, mais aussi un grand merci à Sylvain Verger. Vous avez tous les deux su me motiver au début de mon travail et me transmettre votre passion pour ce projet.

Je tiens également à remercier Christophe Descottes pour m'avoir permis d'intégrer la structure Siemens et l'équipe R& D de Grenoble. Merci à Aurélie Morin, qui a encadré mes travaux de recherche côté entreprise et qui m'a beaucoup appris en méthode d'organisation. Tu as été une chef géniale, toujours à l'écoute des membres de l'équipe et très disponible. Merci également à Karim Bousoltane.

Je voudrais aussi remercier mes encadrants du G2ELab. Merci à Olivier Gallot-Lavallée qui a co-encadré mes travaux de recherche au cours de ces trois ans. Merci aussi à Jean-Luc Reboud pour son aide précieuse en simulation numérique (mais surtout pour LA course à pied!). Je remercie tout particulièrement Olivier Lesaint, mon directeur de thèse, qui m'a accompagnée, soutenue, guidée et conseillée tout au long de ma thèse. Tu as été un vrai soutien au cours des expériences (on a eu de grosses frayeurs et on a aussi bien rigolé), ainsi que pendant la période de rédaction.

Un grand merci à tous ceux qui m'ont soutenue et aidée dans la réalisation de mes bancs expérimentaux. Je pense ici bien sûr à Alain Tisserand qui nous a quitté l'an dernier... Et qui a beaucoup contribué à la fabrication des différentes pièces. Je pense également à Néné, Paul, Angelo, Gégé, Gilou, Philippe, Alain, Jean-Luc, Christophe, Jean-Paul, Grégor, Patrick, Pierrot et messire Daniel avec qui j'ai travaillé et aussi partagé de bon fous rires pendant les essais/pauses cafés. Une pensée également à Serge, Alain et Jean-Luc. Je remercie également mes collègues de bureau: Vincent, Marc, James, Frank, Thierry, Fabrice, Niston, Rosette et Stéphan.

Je voudrai également remercier mes amis qui m'ont soutenue tout au long de cette thèse. Je remercie Sören, qui m'a supporté comme chef au cours de son stage et avec qui j'ai bien rigolé, on a fait pas mal de poiiint et on a bien avancé. Je remercie également Eric Durhone pour m'avoir conseillé et travaillé avec moi sur mon projet de thèse. Les multiples réunions et collaborations avec les allemands ne nous ont pas empêché de faire du beau travail! Je remercie aussi Pierre d'avoir partagé son bureau avec moi au labo et d'avoir inventé le super ventilateur en été! Sans cela on serait certainement mort de chaud la première année!

Je tiens également à remercier une amie qui m'est très chère et qui a su me soutenir, me faire rire et m'encourager tout au long de cette dernière année: Choukran Rrrrachelle! Ça a été un vrai plaisir de squatter ton bureau et tes fous rires. Tu es une amie géniale et tu vas bien me manquer!

Je veux ici remercier tout particulièrement un homme qui a changé ma vie et qui est très important à mes yeux. Je te remercie profondément Pablo Acosta, pour m'avoir accompagné pendant les durs moments de la rédaction, de m'avoir supporté, encouragé, conseillé, écouté et aussi pour tes innombrables relectures. Je te remercie également pour tous ces moments, ces fous rires, ces folies et aventures que nous avons partagées. Je pourrai en écrire bien davantage mais je vais en garder pour la suite ;) .

Je remercie enfin tous les membres de ma famille: Papa, Maman, Robert et Thomas. Sans votre appui et votre soutien je n'en serai sans doute pas là aujourd'hui. Notre famille a toujours été une force et m'a toujours permis d'avancer sans me retourner puisque je savais que vous veilliez sur mes arrières. Vous avez toujours été là pour moi et je vous aime tous très fort. Je vous dis encore une fois MERCI.

Merci aussi à Pablo d'être entré ainsi dans ma vie et m'avoir apporté joie et bonheur. Je te remercie aussi car grâce à toi la famille s'est bien agrandie.. Par là je voudrais également remercier Ivonne, Joachim, Elizabeth y Diego. Gracias por dejarme entrar en su vida y gracias por compartir estos momentos importantes de mi vida. La preparación de la defensa fue un hermoso momento gracias a esta gran familia, fue una emoción grandísima, otra vez muchas gracias por to'o.

Je termine ces remerciements en remerciant une fois encore toute ma famille et en émettant une pensée toute particulière à mon grand-père.

Contents

Introduction

The demand for reliable, economic and environment-friendly energy resources is increasing, especially for long distance transmission. During the last ten years, the energy production from wind turbines has strongly increased. The development of offshore wind farms brings considerable economic opportunities. Indeed, it will represent 14% of Europe electricity demand by 2030. These new energy sources are often located far from the consumption areas, thus, new technologies are required to interconnect those power grids over long distances.

Nowadays, the development of High Voltage Direct Current (HVDC) transmission lines is very promising for next networks generations, which will overcome High Voltage Alternative Current (HVAC) limitations. *Gas Insulated Substations* (GIS) constitute an important element of power grids. Under HVAC, it has been thoroughly developed and optimized. However, it remains really difficult to develop and optimize a reliable system under HVDC. The knowledge about the DC behaviour of both insulating solid materials and gases is essential for an optimized design and for the reliability of HVDC equipment.

The main purpose of this thesis is first to experimentally investigate conduction phenomena in both solid and gaseous insulators, in HVDC GIS functional conditions of use. Based on these data, the objective is to develop a numerical model to evaluate the influence of various parameters and estimate their impact on conduction phenomena in solid insulator, and hence on the electric field distribution which constitutes the basic data for design and optimization.

In chapter 1, we review the existing challenges concerning energy transmission and distribution across long distances. A comparison between Alternative Currents (AC) and Direct Currents (DC) is first presented allowing to assess the main differences between both techniques. Then, we describe the investigations performed so far in Gas Insulated Substations under HVDC. Based on the existing work, we are able to define the key parameters to investigate, in order to better understand and improve HVDC insulation technology, and propose innovative solutions.

In chapter 2, we review the state of the art of current measured through pressurized gas and vacuum, at low and high electric field. Then, we proceed with experimental measurements on current through pressurized gases in two electric field geometries, and analyze the results obtained to discuss the origins of these currents.

In chapter 3, the experimental devices used for the characterization of conduction phenomena through the solid insulator are presented. We investigate the influence of temperature, electric field and relative humidity on the conduction through the insulator volume and on its surface.

Finally, in chapter 4 we present several numerical calculations accounting for the influence of parameter investigated in a real GIS insulator geometry. The contribution of such parameters can be estimated and their impact on the conduction current and electric field distribution through the solid insulator is evaluated.

1 | State of the art on electrical insulation for HVDC GIS

Contents

In this chapter we will first present the evolution of energy distribution networks from High Voltage Alternating Current (*HVAC*) transmission to High Voltage Direct Current (*HVDC*). A brief description of advantages and drawbacks of these techniques is presented. The structure and operating conditions of Gas Insulated Substations (GIS) are then introduced. Some existing HVDC technologies are detailed, highlighting the main parameters to take into account to design and optimize HVDC GIS. Then, we will present the current understanding of charge accumulation and relaxation on solid insulators, which are of major importance for the reliability and optimization of HVDC technology. Finally, the main objectives and topics addressed in this work are presented.

1.1 | General considerations on electrical transport and distribution

High power production facilities, such as nuclear, hydraulic, photo-voltaic, and wind farms power plants, are often located far away from consumers. To transport electrical energy from the source toward consumers, the entire electrical network, basically composed of

transmission networks and distribution lines, is used. Figure 1.1 shows an illustration of grid structure, with the combination of networks and substation transformers. The substation transformers are placed at each node of the network and permit converting high voltage to low voltage and vice versa. Two different types of substations can be used, Air-Insulated-Substation (AIS) and Gas-Insulated-Substation (GIS).

The transport of electrical energy presents some losses (due to Joule effects and other phenomena), notably concerning the transport over long distances. Indeed, when electricity passes through electrical cables, a certain quantity of this energy is transformed into heat due to the Joule effect. This energy loss can be reduced by increasing the voltage and decreasing the current for long distance transmission. That is why high voltage is usually employed for long distances transmission ($> 100\,km$) while low and medium voltages are used for distribution networks ($< 100\,km$). These three voltage levels are represented in figure 1.1.

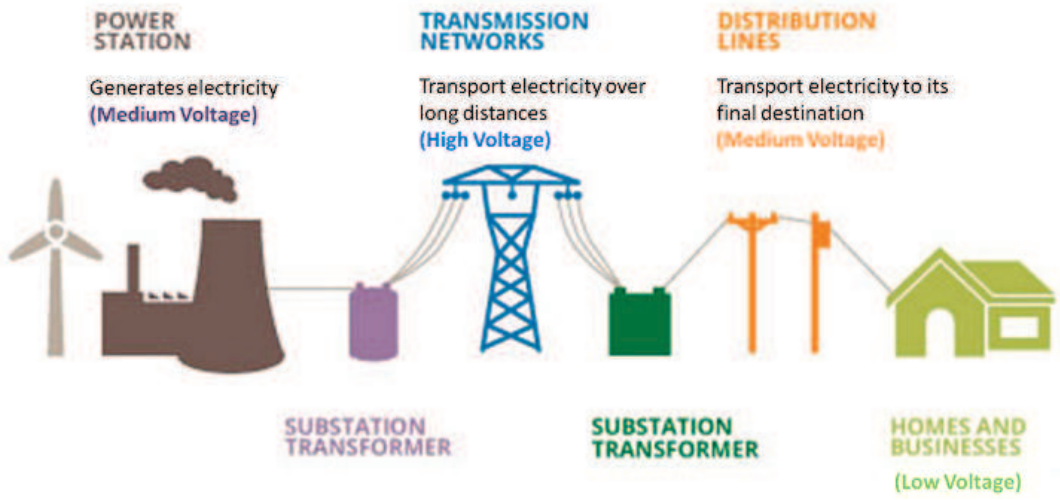

Fig. 1.1: Schematic illustration describing the global network used to the transport of electrical energy. Transmission networks and distribution lines are interconnected through substations transformers.

Additionally to the transport of electricity, this structure permits to isolate dysfunctions on a specific section of the network without cutting-off electricity over the entire network.

1.2 | From Alternating Current to Direct Current

Two types of currents are used for energy transport: Alternating Current (AC) and Direct Current (DC). Both started many years ago, in $1880's$, with the War of Currents between Thomas Edison (who was pushing for the development of DC power networks), and Georges Westinghouse, (who believed in AC power networks). At that time, DC networks were suitable and well-adapted to the consumers. However, some improvements on the AC systems

(creation of a transformer stage between the transmission network and consumer materials), allowed higher power and insulation levels within one unit. This system was simple and only required little maintenance. For these reasons, AC technology was introduced at a very early stage in the development of electrical power systems. Nevertheless, *HVAC* transmission technology presents some drawbacks which compelled a change to DC technology. The transmission capacity and distance of AC links are limited by inductive and capacitive phenomena occurring within overhead lines and cables. These issues are of major importance for cables longer than about 100 km since the achievable transmission will be limited by the charging current. Besides, it is not possible to directly connect two AC systems working at different frequencies.

With the development of high voltage valves, it becomes possible to transmit power at high voltages over long distances, giving rise to *HVDC* transmission systems. Such technology has several advantages compared to the AC transmission which make it especially attractive in certain transmission applications. *HVDC* systems are getting increasingly important in the global development of energy sources and networks for technical, economical and environmental reasons.

1.2.1 | Technical merits of *HVDC*

With an increased demand for energy and construction of new generation plants at remote locations (*e.g* off-shore wind farms), the complexity of power system has grown and higher voltages are needed to transmit energy across very long distances, with as low losses as possible. As inductive and capacitive parameters do not limit the transmission capacity or the maximum length of a DC cable, *HVDC* offers a suitable solution compared to *HVAC* for such power systems.

A simplified representation of a *HVDC* interconnection is shown in figure 1.2. A converter, operating as a rectifier will transform AC power to DC power. The latter is then transmitted and applied to the DC terminals of a second converter, which allows the DC power to flow into the receiving AC network. The composition of a *HVDC* system varies with the technology used in converters. However, a common structure formed by AC filters, transformers, converters, DC capacitors or reactors and DC cables, can be established. Further detailed description of *HVDC* systems are made in a technological paper published by Rudervall *et al.* [1].

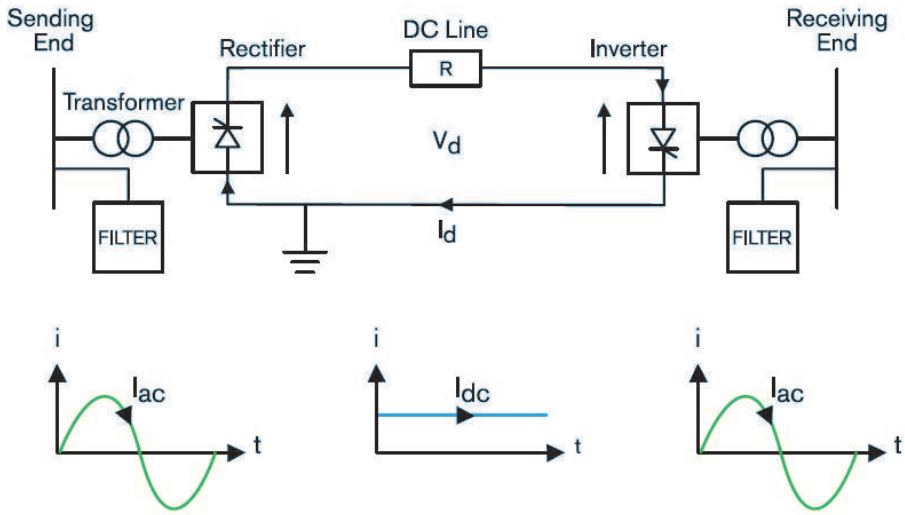

Fig. 1.2: Simplified representation of HVDC interconnection between two AC networks.

1.2.2 | Economic and environmental considerations

Depending on the transmission task, feasibility studies are performed to estimate the cost of AC/DC lines according to losses and distances. Figure 1.3 shows (b) losses comparison and (a) typical cost comparison curve between AC and DC transmission, accounting for the terminal cost, line cost as well as the value of losses for each AC and DC technology. It can be observed that on the one hand, the investment costs for *HVDC* stations are higher than for *HVAC*. On the other hand, the costs of transmission medium and line per kilometer are considerably lower for DC. The distance for which total AC and DC costs are equals is named the *break-even* distance. It is usually in the range of 500 to 800 km, and depends on project financing, loss evaluation, cost of right of way, etc. It can be observed that for distance superior than the *break-even* distance, the total AC costs are higher than total DC costs considering similar transmission distances.

The desire to limit environmental impact also conducts to a *HVDC* transmission system. Indeed, *HVDC* network can transmit more power over fewer lines and hence reduce the visual impact and save land compensation for other projects. Moreover, there is no induction of alternating electro-magnetic fields from *HVDC* transmission, and lower underground cable losses improves efficiency.

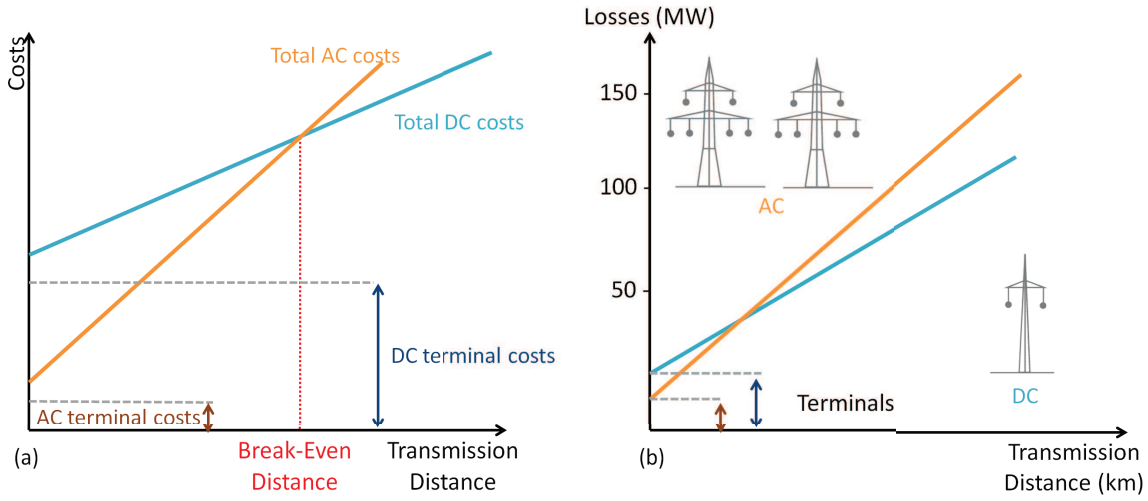

Fig. 1.3: (a) Comparison of costs between AC and DC technologies according to transmission distances, and accounting for the terminal costs, line costs and values of losses. (b) Comparison of losses between AC and DC technologies according to transmission distances.

1.3 | Gas-Insulated-Substations (GIS)

With the evolution of high voltage and very high voltage electrical networks, the realization of substations had significantly evolved. The consumption of electrical energy is located closer to industrial or urban areas, which implied to distribute high power in regions where the space is restricted and rare. The dimensions of Air Insulated Substations (AIS) are imposed by the insulation distances in air, so the solution to make them more compact is to use a better insulating gas within an enclosure under pressure (GIS). Figure 1.4 shows an illustration of an AIS (a) and a GIS (b). AIS technology requires an important area (0.5 to 2 $hectares$), while GIS allows reducing this area by a factor 3 or 4. With this technology, it is thus possible to transmit higher voltages close to urban sites in a compact, reliable and robust enclosure.

An illustration of GIS compartments is presented in figure 1.5. They are composed of a metallic enclosure linked to the ground (grounded vessel), a central conductor, insulating solids and gas. The conductor is isolated from the grounded enclosure using pressurized sulfur hexafluoride (SF_6) and epoxy resin insulator, which has a double functionality. The solid insulator is used to carry the conductor, and can also be used as a tight spacer which enables the separation between two compartments.

This structure, already used for HVAC systems, is of major interest for HVDC technology. Our study is based on this GIS model, and the different elements composing the GIS are detailed hereafter.

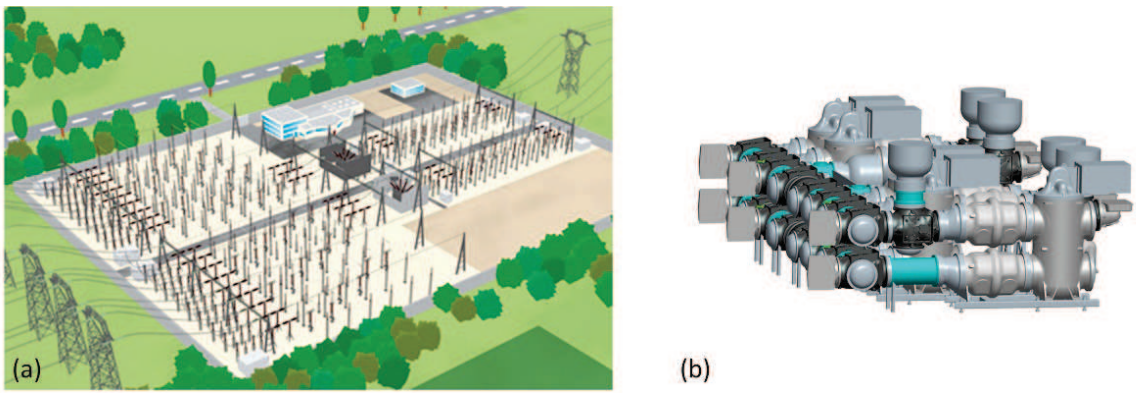

Fig. 1.4: Illustration of (a) an AIS, and (b) a GIS.

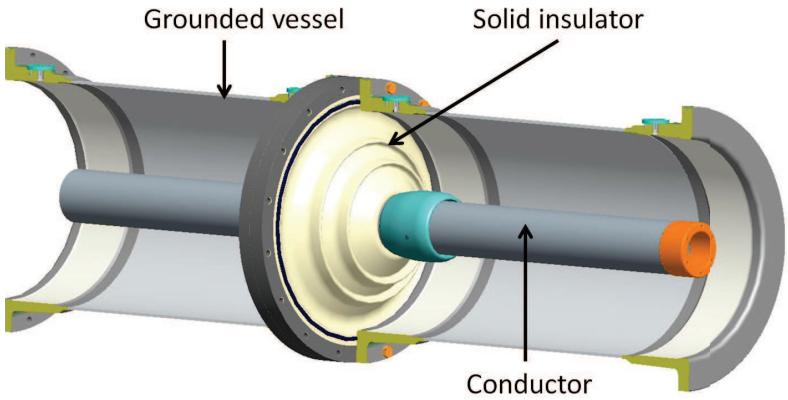

Fig. 1.5: Illustration of a junction between two compartments in a GIS.

1.3.1 | Solid dielectrics

In a GIS, solid insulators mainly constitute a mechanic support for conductors, and must also be able to transmit the heat flow between the different parts of the device.

The insulator design takes into account the applied electric field, and various constraints such as: chemical interactions with gas, mechanical and thermal constraints. Depending on the insulation requirements, various categories are existing. High voltage insulators have been first developed with ceramic and porcelain [2], and then were later changed by modern polymeric insulators [3]. First introduced in 1959, they were made of SiO_2 or Al_2O_3 filled epoxy resin [4]. Their design flexibility, light weight, withstands performance to pressure and their ease of handling for manufacturing, make them preferable compared to ceramics. Moreover these composite materials are safer than porcelain since they are not brittle so the risk of explosion is largely reduced.

Up to now, those materials are adapted and withstand AC voltages but are not suitable for DC technology. The challenge consisting in finding a suitable design which withstand HVDC, constitutes the basis of our study. We focused on organic synthetic insulators

(polymer composite) currently used for AC technology. The behavior of these materials under DC is totally different since electric field distribution depends on conductivities, charge accumulation, and not on permittivities anymore.

1.3.2 | SF_6 gas

Sulfur hexafluoride was discovered by Moissan and Lebeau [5, 6] in 1900. It is synthesized directly from sulfur and fluorine elements, with a strong exothermic reaction (262 $Kcal$ per mole) written as, [7]:

$$S + 3F_2 \rightarrow SF_6 + 262\,kcal \tag{1.1}$$

Since its first industrial application in 1940 (patent from Thomson-Houston in 1939), the SF_6 was widely used in the field of industrial insulation due to its high dielectric strength, and very good behaviour in circuit breakers.

SF_6 is one of the heaviest known gases. With a density of 6.139 kg/m^3 (at 20 °C and 0.1 MPa), it is almost five times heavier than air (146 g/mol for the SF_6 and 28 g/mol for air). As shown in figure 1.6, SF_6 molecule is perfectly symmetric. It is a stable and inert molecule.

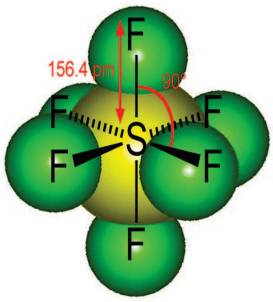

Fig. 1.6: Illustration of a molecule of SF_6.

It is an electronegative gas due to its Fluorine (F) atom, which means that it is able to capture free electrons, forming heavy ions with low mobility, and thus making the development of electron avalanches very difficult [8]. Besides, due to its high dissociation temperature (500 °C) and high dissociation energy, SF_6 has excellent arc-interruption properties.

However, the SF_6 also has drawbacks, mostly concerning environment. When SF_6 is in decomposition (during strong electrical discharge), toxic and corrosive by-products such as Hydrogen Fluoride (HF) can be created. Moreover, as this gas is very stable and chemically inert, its global warming potential is approximately 24000 times higher than that of CO_2.

Thus, severe conditions of use had been established in order to control the loss quantities of this gas and re-use it when no decomposition occurred.

Investigations on various alternative gases (N_2, CO_2, ...) are currently in progress to replace SF_6 in some parts of the GIS, or also to mix it with other gases [9–11]. Nevertheless, up to now no other gases or techniques were found to fully replace advantages presented by SF_6.

1.4 | Development and optimization of HVDC GIS

The «Kii-channel» HVDC system ($\pm 250\,kV$, $2800\,A$) was the first and largest bulk HVDC transmission system, built in Japan. It was put in commercial use in June 2000 [12]. Further investigations were conducted in order to upgrade this existing system to a capacity up to $2800\,MW$ ($\pm 500\,kV$, $2800\,A$) [13]. In same years, ABB corporation performed a feasibility study of SF_6 GIS for HVDC at $500\,kV$ and $600\,kV$ based on existing AC materials (insulating parts). Finally, their long term performance required special spacers modified for DC technology [14]. Criteria for design and optimization of HVDC GIS are not well understood up to now. Thus, existing devices were over-sized to ensure a safe operation.

Several research works have been reported concerning the insulator behaviour under HVDC. These researches take into account the insulator geometry [15–17], which is shown to have a great influence on breakdown voltage level. Some studies [18, 19] also underlined the predominant influence of the surface charge accumulation phenomena, which is one of the major issue in HVDC. Other experiments have also been able to evaluate the influence of the insulator's roughness, and of the nature of the high voltage electrode used for the experiments [17]. The presence of metallic particles in a GIS has also been investigated [15]. In addition, some simulation methods have been developed [20–23]. The relevant literature concerning these issues is reviewed in the following.

1.4.1 | Charge accumulation

Under impulses and AC voltages, the voltage distribution along the insulator surface and within its volume is dependent on the dielectric constant (ε) of the insulator. In contrast, for DC voltages the situation is much more complex. The initial distribution under DC is determined by the capacitive grading. Then, over prolonged application time, the stress distribution is determined by the resistivity of the insulator. In HVDC GIS, charges can also accumulate on the insulator surface and they will introduce additional changes in the voltage distribution and lead to field distortions, that may result in the reduction of the insulator flashover voltage. Figure 1.7 shows measurements of the flashover voltage versus surface charge density. It was obtained with switching impulses applied after application of a $200\,kV$ pre-stress, with various polarity combinations. The flashover voltage significantly

decreases with σ, especially when pre-stress and switching impulses are of opposite polarities. This confirms the major impact of charge accumulation on the insulator dielectric strength.

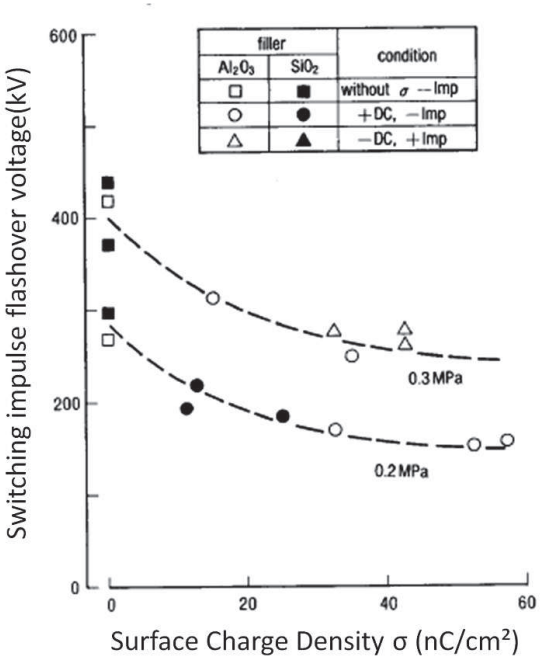

Fig. 1.7: Relation between charge density (measured by a non-contacting probe) and flashover voltage [22].

Both volume and surface resistivities of the material influence charge accumulation and relaxation. The actual origin of surface charges is not clearly established. The relevant literature will be analyzed in chapter 2.

In the following, we review the main parameters involved in the complex equilibrium between charge accumulation and relaxation.

1.4.1.1 Field calculations

In HVDC, a small quantity of free charges are generated in the gas (see section 2.1 in chapter 2). These charges move along the electric flux lines toward the insulator surface. If the surface resistivity is high, charge accumulation over long periods of time can occur on the insulator surface. Numerical simulations of surface charge accumulation on GIS insulator were reported by Messerer *et al.* [24–27]. In their work [27], they studied the phenomenon of charge accumulation on a spacer surface, using artificial charge generation with points (corona effect). These points create charges which are transported onto the insulator surface following electric field lines. Figure 1.8 shows the results of the charging process at three different time, obtained by simulation.

In their simulation, they consider that the saturated charge density is given by boundary conditions following equation 1.2, where ε_1 is the dielectric constant of the gas ($= 1$) and ε_2

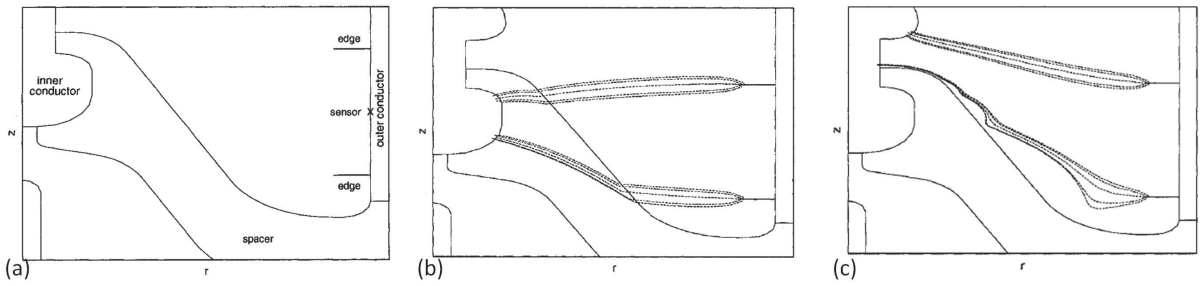

Fig. 1.8: Movement of charges for various charging time, (a) $0\,h$, (b) $53\,h$, and (c) $838\,h$ [27].

the dielectric constant of the material considered.

$$\varepsilon_1 E_{1n} - \varepsilon_2 E_{2n} = \sigma_{sat} \tag{1.2}$$

The electric field is composed of a normal (E_n) and a tangential (E_t) components. It is considered that charge accumulation is enhanced by normal electric field on the spacer surface whereas the tangential component helps charge relaxation and is responsible for breakdowns. The charge accumulation reduces E_{1n} at gas side, while it enhances gradually E_{2n} on the insulator surface side, until a steady state is reached when the normal electric field at the gas side equals to zero [28]. This means that the insulator is fully charged (σ_{sat}).

A similar calculation method is found in Fujinami *et al.* work [22]. Four types of insulators were used with various electrode diameters and metal inserts. The objective was to study the normal and tangential fields for each configuration and compare the calculated charge accumulation to experimental data after several voltage application periods. In practical cases, the electric field for a spacer in SF_6 gas would change from a capacitive distribution to a resistive one at very long times.

It is reported that for short application time ($5\,h$), the calculated values of surface charge densities are superior to the experimental measured values (obtained using a multi-point measurement method via electrostatic probes). Results obtained after $139\,h$ of applied voltage are shown in figure 1.9, for one type of insulator (type C).

Both calculations and measurements are in agreement when the application of voltage lasts very long time.

Charge accumulation on insulator surface is a mechanism mainly controlled by electrical field components (normal and tangential), which has a strong effect on insulator flashover and dielectric strength. To reduce the charge accumulation, the insulator shape must be optimized. The ideal geometry to avoid charge accumulation would be a geometry with only tangential electric field on insulator surface (as suggested by Fujinami [22]).

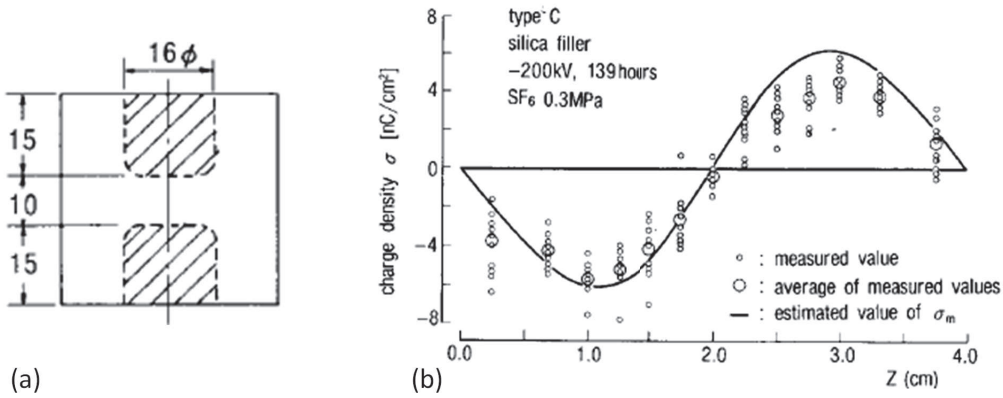

Fig. 1.9: (a) Sectional view of type C insulator, (b) charge distribution after $139\,h$ application of DC voltage [22].

1.4.2 | Influencing parameters

1.4.2.1 Insulator shape

Several authors [15, 16, 22, 29–31] have made researches concerning the influence of insulator shape onto the breakdown field strength under DC voltages.

An investigation led by Hasegawa *et.al* [32] points out the influence of the insulator shape on its dielectric strength under HVDC. Figure 1.10 presents the electric field evolution according to three different insulators shapes. It was observed that high tangential field are obtained for a disk spacer (a) while low tangential field and high normal field are obtained for a conical spacer. The semi-conical spacer (c) presented the best solution since it satisfied the requirements of low tangential and normal field. The optimized insulator, tested under AC and DC voltages, with lightning and switching impulse and polarity reversal, satisfied the insulation with sufficient margins.

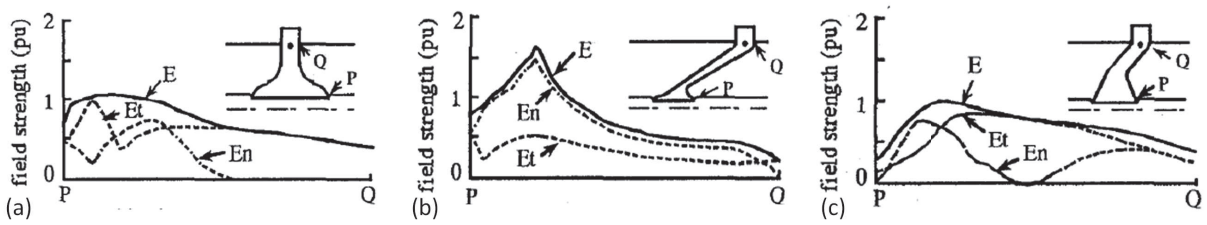

Fig. 1.10: DC electric field distributions on spacer surface on the concave side of (a) a disk spacer, (b) a conical spacer and (c) a semiconical spacer [32].

Another investigation done by Volpov *et al.* [30] shows the influence of the insulator shape on the charge accumulated onto the insulator surface. Their experiments, initially performed using a $1150\,kV$ HVAC GIS insulator, failed under long term HVDC. The authors postulate that to optimize the insulator, a maximum value of charge accumulation can be tolerated. They recommend to not exceed a normal electric field of $1\,MV/m$ and a

tangential electric field of $3.5\,MV/m$. These constrains would allow to control the R-C field transition so that maximum accumulated surface charge density does not exceed $10-20\,\mu C/m^2$, and causes no appreciable distortion in the spacer field. Figure 1.11 shows the investigated shapes with corresponding normal and tangential electric field respectively for (a) existing AC insulator and (b) optimized DC insulator. It has been observed that optimizing the insulator shape results in significantly lowering the normal component of the electric field and thus the surface charge density along the insulator surface.

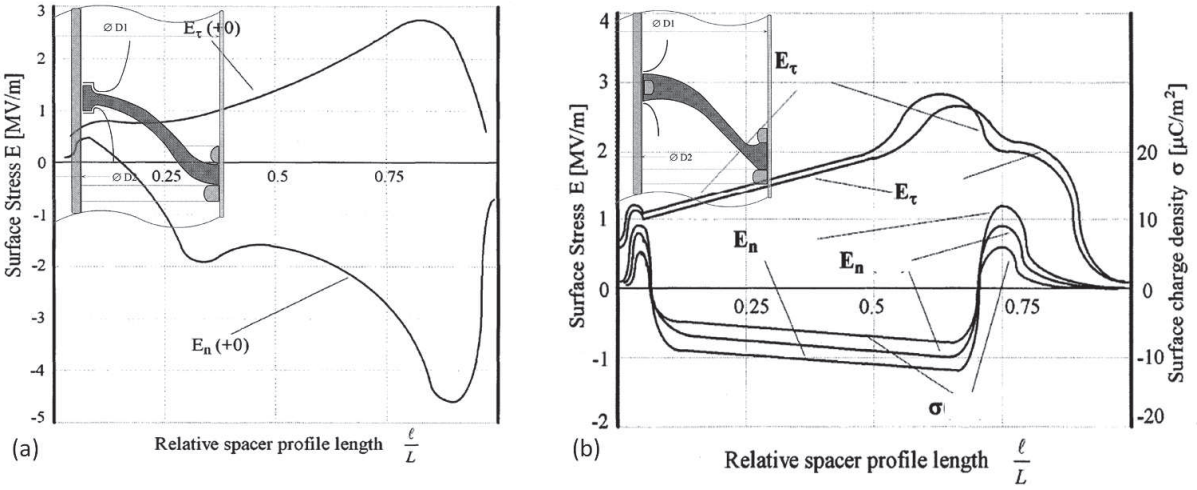

Fig. 1.11: Design shape of insulator used for (a) HVAC GIS and (b) optimized shape withstanding $750\,kV$ HVDC, and corresponding electric stress on the insulator surface [30].

According to their field requirements, they obtained a surface charge density $\leq 10\,\mu C/m^2$, which led to only a slight difference between the initial and DC stabilized field distribution along the spacer surface. No abnormal reductions in the insulator electric field strength were registered at long term DC voltage application.

The study of Lorenzi *et al.* [31] agreed with the previous work concerning the large influence of the normal electric field component on both charge accumulation and dielectric strength variations. The main difference pointed out is the consideration of surface and volume resistivity impact on the charge accumulation. Indeed, modifying the shape of insulators allows reducing the normal component, but only for the cases in which the volume resistivity is the dominant mechanism leading to charge relaxation, compared to the surface and SF_6 resistivities. In other cases, the optimization of the insulator profile may not induce a reduction of the surface charge. In their simulation, best results were obtained with low volume resistivity in presence of a non-linear surface resistivity.

1.4.2.2 Insulation properties and charging time estimation

Charge accumulation results from an equilibrium between charges flowing onto the insulator surface (surface resistivity), through its volume (volume resistivity) and charges coming from the gas. Depending on these dynamics, different charge accumulations can be reported.

Examples of volume and surface resistivity measurements according to both electric field and temperature are shown in figure 1.12 [21]. Measurements were performed on alumina-filled epoxy resin, in SF_6 with a pressure varying between $0.25\,MPa$ to $0.35\,MPa$. It was observed that both surface and volume resistivities depend on electric field and temperature. However, it seemed that the volume resistivity mainly depends on temperature, whereas surface resistivity shows a large variation versus electric field.

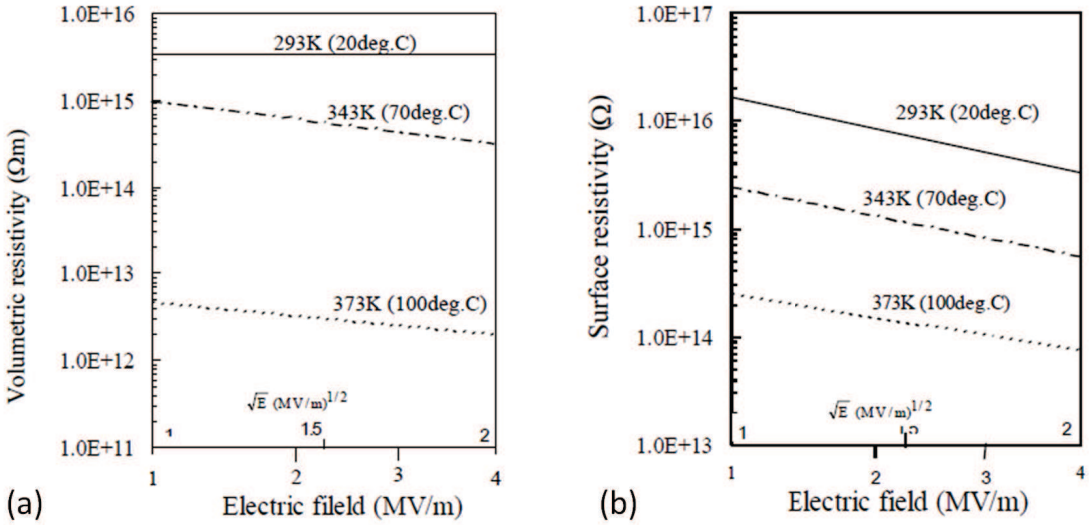

Fig. 1.12: (a) Volume and (b) surface resistivities according to electric field and temperature variations [21].

To explain the basic mechanism of charging insulator surfaces, the properties of the insulating gas must be also considered. However, it is very difficult to estimate the influence of the gas since charge generation processes are not clearly identified. Charges can presumably be due to natural ionization, field emission from electrode surfaces, charged particles within gas, and partial discharges (corona discharges). In their work, Kumada *et al.* [33] calculated a virtual «volume resistivity» of air only considering the charge carriers generated by natural ionization. Then, considering that the number of charge carriers in air can also be influenced by micro-discharges or field emission from the conductors, they considered a volume resistivity ratio of the gas ρ_g to the insulator ρ_s in order to estimate the charge density accumulated on the insulator, as well as its charging time. Those calculations are presented in figure 1.13.

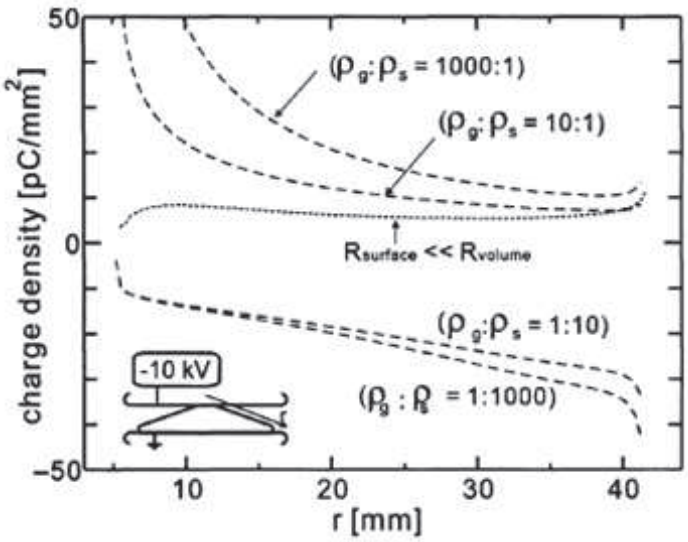

Fig. 1.13: Numerical calculation of charge density distribution along a conical slope spacer [33].

1.4.2.3 Influence of insulator surface roughness

Some works have reported the influence of insulator surface roughness on charge accumulation [16, 21, 22]. The roughness may slow down or enhance the surface charge decay, and thus modify the dielectric properties of insulators.

Fujinami *et al.* showed in their work [22] that charge density is higher when surface roughness is larger. This result was also verified by Iwabuchi *et al.* [34] on an epoxy disk spacer presenting a flat and an inclined surface. Figure 1.14 shows a schematic view of the insulator partly roughened by sand blasting (a) and a charge distribution measured on the flat surface of this insulator (b).

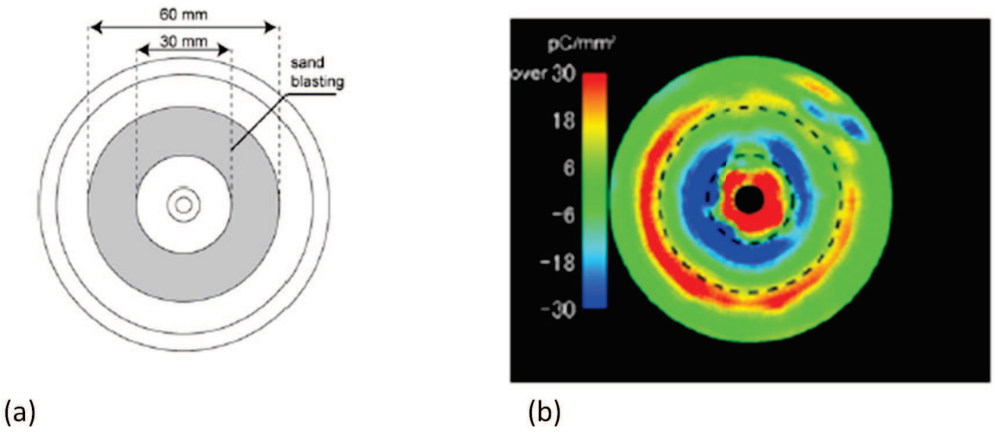

Fig. 1.14: (a) Schematic view of the insulator with an area roughened by sand blasting, and (b) charge distribution measured on the flat surface of the corresponding insulator after $240\,h$ of voltage application ($30\,kV$ on the central conductor) [34].

In their experiment, HVDC was applied for a long time on this sand blasted insulator ($240\,h$). It can be observed that the higher surface charge concentration is localized on the boundary of the roughened region (figure 1.14 (b)). Authors assume that the roughness has an indirect impact on charge accumulation. After sand blasting, fillers of the insulator appeared on the insulator surface, resulting in a non-uniformity of surface resistivity along the insulator. This non-uniformity of surface resistivity is assumed to provoke charge accumulation.

1.4.2.4 Influence of electrode surface coating

Charges in the gas can be presumably created due to micro-protrusion on the grounded vessel or on electrode surfaces. Some studies were performed by Endo *et al.* [35], Menju *et al.* [17] and Okabe *et al.* [21] concerning the possible effect of a coating on electrodes, in order to reduce the charge emission.

Coated electrodes have been tested, assuming that an insulating polymer coating may reduce the effect of micro-protrusions, and then increase the breakdown field strength (E_{BD}). Work of Yoshida *et al.*, reported in [21] is presented in table 1.1 and figure 1.15.

$N°$	*Electrode Coating*	*Insulator Coating*	*Insulator Surface Resistivity* [Ω]
(1)	None	None	$10^{16} - 10^{17}$
(2)	None	Epoxy ($300 - 800\,\mu m$)	$10^{14} - 10^{15}$
(3)	Epoxy	None	$10^{16} - 10^{17}$

Tab. 1.1: Summary of the experimental conditions, describing electrode and epoxy insulator surface condition presented in figure 1.15.

It is observed that with a dielectric coating on the electrode, the surface charge density measured is significantly lowered (close to $1\,nC/cm^2$). Thus, the charge density measured in case of $N°1$ and $N°2$ was assumed to be due to field emission. In their experiment, the surprising higher charge density obtained in case $N°2$ compared to $N°1$ is not explained. Indeed, it is well known that the lower the surface resistivity, the lower the charge density.

A complementary investigation [17] showing the evolution of the breakdown field strength in a coaxial geometry with coated and un-coated anode and cathode electrodes is presented in figure 1.16. It is observed that for un-coated electrodes, positive E_{BD} is close to theoretical values while the negative value is lower. Then, coating the cathode electrode in negative polarity results in an increase of E_{BD}. Besides, in positive polarity, no influence of the electrode coating is observed. This strongly suggests that the decrease of E_{BD} observed without coating was due to field emission from micro-protrusion on the cathode.

To avoid field emission from tips present onto electrodes, a dielectric coating is recommended onto the negative electrode, or a good polishing is recommended. However, Hairour

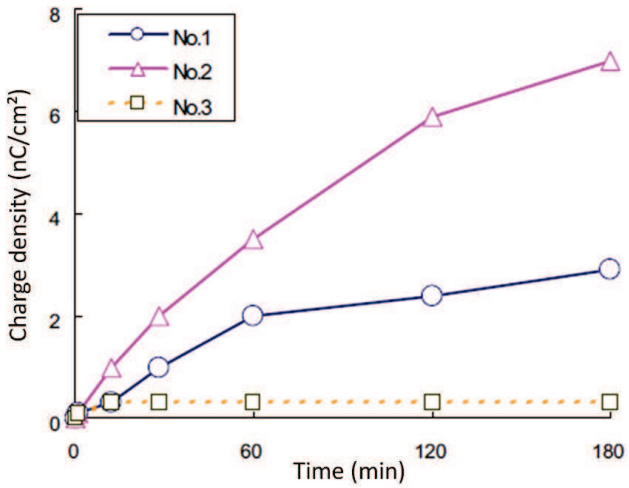

Fig. 1.15: Measurements of charge density over time for three different spacer surface and electrode conditions presented in table 1.1 [21].

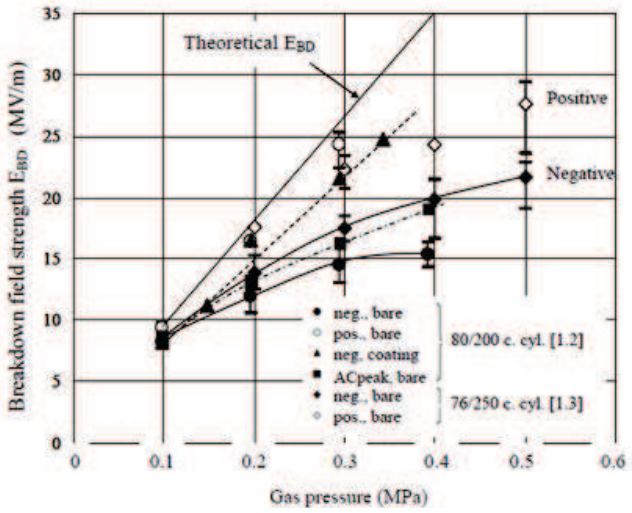

Fig. 1.16: Effect of electrode coating on DC breakdown voltages in SF_6, for a coaxial geometry [17].

et al. [36] also investigated the influence of the breakdown field strength in presence of a coating onto the conductor. They evidenced that a dielectric coating results in a lower average of the breakdown field strength in both polarities. Thus, further work should be performed in order to reduce the charge injected from the conductor, without reducing the breakdown field strength.

1.4.2.5 Metallic particles

Dust and conducting particles may be present within GIS, and might deteriorate the dielectric performance of the system. Several investigations were performed [32, 33, 37–40] to determine the impacts of those particles on the electric breakdown voltage, and on the

charge accumulation. It is known that in GIS, both free and attached particles can trigger breakdown. The influence of particles will vary with their nature (dielectric or conductive), shape and dimensions, location and orientation within the system. Those influences were detailed by Cookson *et al.* [37, 39].

It is reported that for a DC field, a particle (in the absence of corona) is driven across the gap electrodes until it strikes the opposite electrode, where it is oppositely charged, and driven back to repeat the motion and oscillate between the electrodes. In the case of negative polarity, particles float around the high voltage conductor, which is called «firefly» phenomenon. During their random movement, particles may attach themselves to the insulator, and greatly decrease its insulation strength. To increase insulation reliability of DC GIS, a system allowing to remove particles should be developed.

Hasegawa *et al.* [32] proposed a new GIS design including a particle trap, and a particle driver presented in figure 1.17 (a).

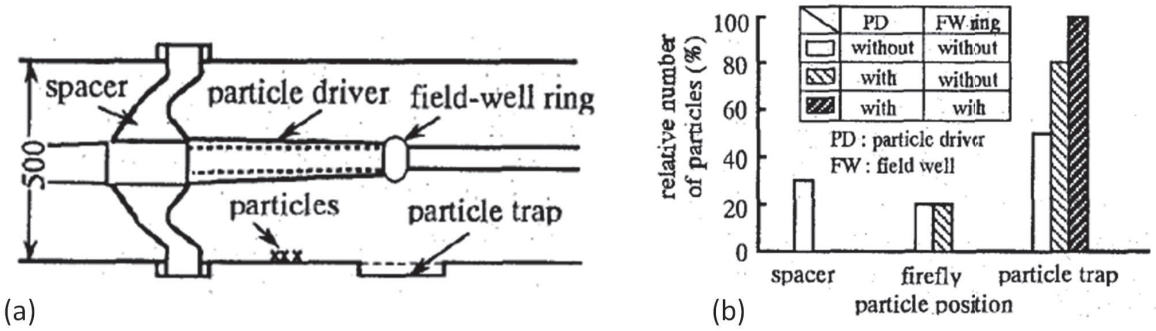

Fig. 1.17: Illustration of a basic insulation structure of a GIS including a particle trap system (a), and experimental results showing the efficiency of a particle driver at DC $-250\,kV$, and with $3\,mm$ long aluminum particles (b). [32].

In their device, a particle driver is placed on both high-voltage conductor side, and onto the vessel allowing to drive the particles into the trap. Moreover, an additional shielded ring named «field-well» ring was positioned at the end of the particle drivers to get rid of fireflies phenomena for electric field lower than $2\,MV/m$. Figure 1.17 (b) shows the relative number of particles attached on the insulator, fire-flying within the gas and trapped. It was observed that if neither the particle driver nor the field-well ring were present, 50 % of particles were trapped, while with both systems all particles were successfully trapped.

1.4.3 | Charge decay

The charge accumulated on the insulator surface can decay following three mechanisms: electric conduction along the insulator surface, through its volume, and charge neutralization by gas ions. This phenomenon had been widely investigated [18, 19, 41–44] on various materials and for different conditions, using Surface Potential Decay (SPD) measurements.

SPD (detailed in [18]) consists in a deposition of charges created by corona discharge, on a localized area of the insulator surface. Once charges are deposed, the potential on this charged area is measured versus time. This technique allows investigating the dynamics of charge versus various parameters (RH, time, charge deposited). Hereafter, only the influence of relative humidity and surrounding gas are presented to point out the possible influence of such parameters in the real application. However, it is worth noting that the correlation between potential decay measurements and real case in GIS is questionable since rather different conditions and geometries are used.

1.4.3.1 Influence of relative humidity

The effect of gas Relative Humidity (RH) and water absorption by the solid on surface charge decay and volume resistivity had been studied by few authors [18, 45–48].

It has been demonstrated on different materials (epoxy resin, quartz and PTFE) that the electrical properties of the insulator surface depended on the amount of adsorbed water vapor. Figure 1.18 shows the surface resistivity variations obtained at different RH in case of epoxy resin by Crisci and Lutz [18, 47]. Those results evidence that with increasing RH, up to 80%, surface resistivity dramatically decreases.

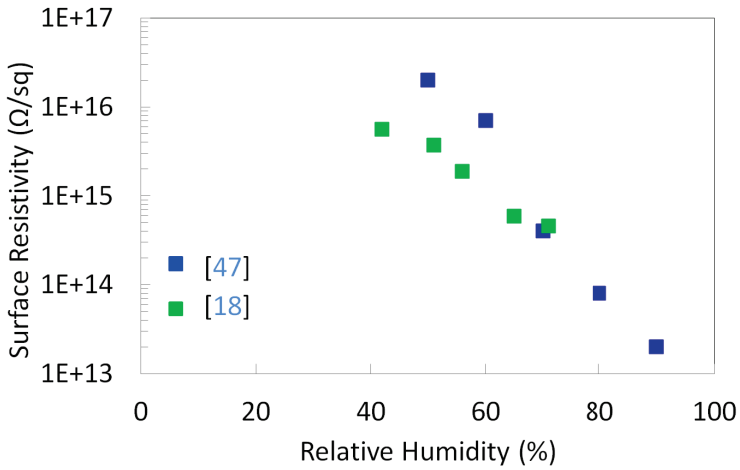

Fig. 1.18: Surface resistivity variations of an epoxy resin with relative humidity [18, 47].

In both studies, by increasing RH from 55% to 65%, the surface resistivity decreases by one order of magnitude. It is then deduced that the humidity can play an important role on the surface potential decay at rather high values of RH. It is worth noting that no investigations have been performed with low RH ($\leq 30\%$) so far. According to Awakuni *et al.* [46], water molecules adsorbed on the insulator surface contribute to the surface conduction. In their work, it is reported that the surface resistivity exponentially decreases with the number of water molecules layers.

In addition, volume resistivity measurements have also been performed [45, 48]. The results show that with increasing water concentration within the solid, its volume resistivity significantly decreases.

1.4.3.2 Influence of surrounding gas

An investigation led by Kindersberger *et al.* [20,49] evidences the influence of the surrounding gas on potential decay experiments. It has been shown that the charge can be neutralized by the gas ions. These ions are generated by natural radiation. Only ions, generated within a certain volume around the charged area (where the electric field strength is high enough to prevent recombination), can contribute to charge neutralization. Figure 1.19 shows the surface potential distribution directly after charge deposition (a) and after 660 min (b).

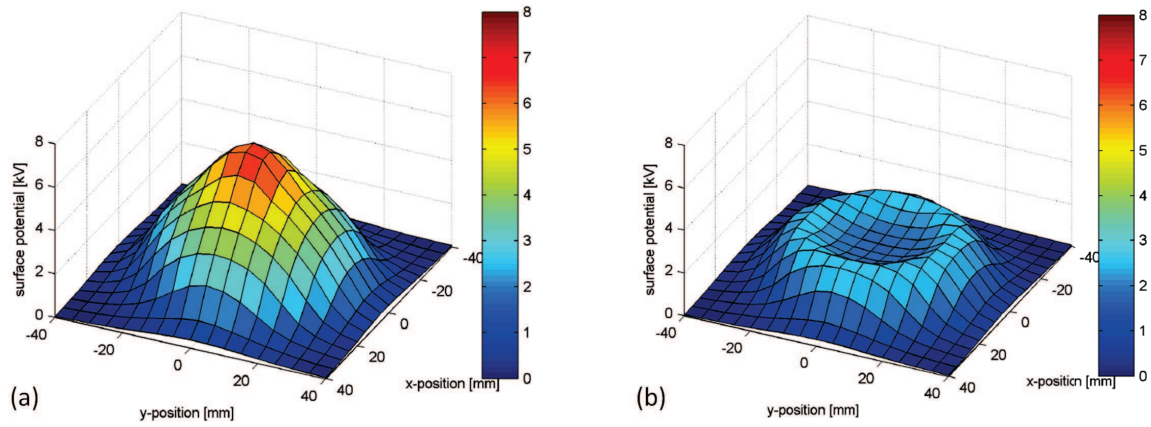

Fig. 1.19: Surface potential distribution on epoxy resin (a) immediately after charge deposition, (b) after 660 min [49].

Depending on the surface potential distribution shape, the mechanism responsible for the decay can be identified. If the «bell» shape obtained just after charge deposition remains during decay, no influence of gas neutralization is observed, whereas when a crater-like shape is observed, this strongly suggests the charge neutralization by gas ions. Comparing their results with a simulation model which accounts for charge neutralization by gas ions, they were able to confirm this assumption. Thus, depending on the solid insulator material, the conditions and properties of the surrounding gas near the charged area, and the electric field applied in such device, the charge decay may be significantly influenced by the surrounding gas. However, this neutralization mechanism cannot be directly extrapolated to the real application. Indeed, in such experiments, a charge is deposed onto the insulator surface by a corona discharge. Then, immediately after charge deposition, the surface potential is measured. In this case, charges on the insulator surface create the electric field distribution and neutralization by gas is possible. This is not the case in the real application, where the applied electric field brings charges of the same polarity than those present on the insulator

surface. In such conditions, the neutralization by the surrounding gas cannot occur.

1.4.4 | Simulation models

Various simulation models have been developed around phenomena involved in the charge accumulation.

Some models [21, 33] developed a simulation tool which enables to estimate the charge on the insulator based on potential measurements along the insulator surface.

In [22–24, 30, 50], models taking into account the variations of volume and surface resistivities with electric field were developed, considering solid and gaseous dielectrics to be linear media. Such models allow describing the evolution of the electric field for various types of insulators and estimate the charge accumulation along the insulator surface. Based on those calculations, critical values for the maximum charge accumulated on the surface, and also for the normal and tangential components of the applied electric field have been determined ($10 - 20\,\mu C/m^2$) [30].

However, in the above quoted models, the phenomena of charge transport through gas were not considered. Volpov *et al.* recommend accounting for the processes of ion generation, recombination and ion drift in compressed gases to establish a correct model. Another simulation work reported by Kindersberger *et al.* [20] presents a simulation tool describing the charge decay on a solid dielectric accounting for electric conduction of both surface and volume, and also charge neutralization by gas ions. In their work, the influence of gas was implemented in the model by calculating the ion pair generation by natural ionization in their experimental devices. Then, based on this ion pair generation rate, the resulting current density in electric field was estimated.

The existing models permit evidencing the influence of the insulator shape, electric field orientation and solid and gaseous dielectric properties on the mechanism of charge accumulation. However, up to now, no model describes those phenomena altogether. Furthermore, additional mechanisms such as charge injected from the electrode surface may also be considered in the simulation of charge accumulation.

1.5 | Conclusions

In this chapter, we have reviewed nowadays challenges which make HVDC GIS an attractive technology for long distance transmission compared to AC technologies. Concerning HVDC GIS insulation optimization, the charge accumulation mechanism occurring on the surface of the dielectric solid has been mainly considered. The principal phenomena involved in charge accumulation and relaxation have been detailed. It has been shown that charge accumulation is strongly dependent on the electric field component orientation (normal

and tangential field). Based on numerical calculations considering the components of the electric field, the insulator shape can be modified in such a way that charge accumulation could be reduced.

In addition, the electric field distribution (and hence the charge accumulation) also depends on the solid dielectric properties (surface and volume resistivities). Those properties vary with the temperature, electric field, presence of water, but rather few works were devoted to study the influence of these parameters.

Hence, the charge accumulation results in a complex equilibrium between electrical conduction through the volume and on the surface of the dielectric solid, as well as charge generation and transport through the dielectric gas. To reduce this charge accumulation, it has been suggested to:

$\longrightarrow$ Add a dielectric coating on the high voltage electrode surface to reduce the charge injection,

$\longrightarrow$ Implement a semi-conductive layer on the insulator surface to adjust its resistivity,

$\longrightarrow$ Optimize the insulator shape,

$\longrightarrow$ Reduce particle contamination within the device by the implementation of particles traps.

However, those recommendations are not sufficient to allow the development and optimization of a reliable HVDC GIS. It is then reasonable to suppose that other phenomena and parameters, not yet investigated, may have an important contribution to the charge accumulation. Hence, the purpose of this thesis is twofold. On the one hand we will investigate the charge generation process within the insulating gas, and on the other hand we will develop a numerical model allowing to estimate the electric field distribution and calculate the leakage current through the solid insulator.

In chapter 2, we will first review the state of the art of charge generation processes in gas and vacuum. Then, we will focus on two main questions:

1) The possible origins of those charges,

2) The parameters influencing those charges.

Thus, we will develop experimental test setup allowing to precisely measure low currents under HVDC (up to $250\,kV$) and characterize these currents according to different parameters.

Afterwards, a numerical model will be developed (chapter 4) in order to evaluate the modification of electric field distribution and leakage current in presence of different parameters. In a GIS, the conductor is often at higher temperature than the vessel, resulting in a temperature gradient along the solid insulator. The influence of this temperature

gradient on the field distribution was not reported up to now. In addition, the presence of water within solid insulator will be evidenced in chapter 3. The latter will also be implemented within the model.

The model is based on characterization of solid insulators physical properties, using typical conditions of GIS (SF_6 environment, and electric field up to $5\,kV/mm$). Experimental test setups able to measure low-noise currents under high voltages and different temperatures will be developed and presented. Hence, solid dielectric will be characterized in conditions relevant of GIS (in pressurized SF_6 at high electric field), with a good control of sample processing (drying) and following an optimized protocol.

Bibliography

[1] R. Rudervall, J. Charpentier, and R. Sharma, "High voltage direct current (hvdc) transmission systems technology review paper," *Energy week*, vol. 2000, 2000. (cited in page 5)

[2] J. Holtzhausen, "High voltage insulators," in *Electrical IDC technologies*. (cited in page 8)

[3] T. Sorquist and A. Vlastos, "Outdoor polymeric insulators long-term exposed to hvdc," in *Transmission and Distribution Conference, 1996. Proceedings., 1996 IEEE*, pp. 135–142, IEEE, 1996. (cited in page 8)

[4] J. Kuffel, E. Kuffel, and W. S. Zaengl, *High voltage engineering fundamentals*. Newnes, 2000. (cited in page 8)

[5] M. H, "Action d'un courant électrique sur l'acide fluorhydrique anhydre," pp. 102–1544, 1886. (cited in page 9)

[6] M. H, "Sur la décomposition de l'acide fluorhydrique par un courant électrique," pp. 103–202, 1886. (cited in page 9)

[7] W. C. Schumb and E. L. Gamble, "The preparation of sulfur hexafluoride and some of its physical properties," *Journal of the American Chemical Society*, vol. 52, no. 11, pp. 4302–4308, 1930. (cited in page 9)

[8] L. G. Christophorou, J. K. Olthoff, and R. J. Van Brunt, "Sulfur hexafluoride and the electric power industry," *Electrical Insulation Magazine, IEEE*, vol. 13, no. 5, pp. 20–24, 1997. (cited in page 9)

[9] A. Winter, J. Kindersberger, M. Tenzer, V. Hinrichsen, L. Zavattoni, O. Lesaint, R. Muhr, and D. Imamovic, "Solid/gaseous insulation systems for compact hvdc solutions," *CIGRE*, pp. 8–9, 2014. (cited in page 10)

[10] H. Looe, J. Yan, and J. Spencer, "Development of a non-sf 6 self-blast type interrupter unit," in *Gas Discharges and Their Applications, 2008. GD 2008. 17th International Conference on*, pp. 117–120, IEEE, 2008. (cited in page 10)

[11] K. Bousoltane, *Alternatives au SF6 dans le disjoncteur haute tension*. PhD thesis, Thèse de doctorat de l'université de Provence–Aix–Marseille 1, 2008. (cited in page 10)

[12] T. Shimato and al., "The kii channel hvdc link in japan," CIGRE 14-106, 2002. (cited in page 10)

[13] M. Shikata, K. Yamaji, M. Hatano, E. Tsuchie, H. Takeuchi, and K. Inami, "Development and design of dc-gis," *Electrical Engineering in Japan*, vol. 129, no. 2, pp. 51–61, 1999. (cited in page 10)

[14] M. Mendik, S. Lowder, and F. Elliott, "Long term performance verification of high voltage dc gis," in *Transmission and Distribution Conference, 1999 IEEE*, vol. 2, pp. 484–488, IEEE, 1999. (cited in page 10)

[15] T. Hasegawa, K. Yamaji, M. Hatano, H. Aoyagi, Y. Taniguchi, and A. Kobayashi, "Dc dielectric characteristics and conception of insulation design for dc gis," *Power Delivery, IEEE Transactions on*, vol. 11, no. 4, pp. 1776–1782, 1996. (cited in pages 10 and 13)

[16] Z. Jia, B. Zhang, X. Tan, and Q. Zhang, "Flashover characteristics along the insulator in sf6 gas under dc voltage," in *Power and Energy Engineering Conference, 2009. APPEEC 2009. Asia-Pacific*, pp. 1–4, IEEE, 2009. (cited in pages 10, 13 and 16)

[17] H. Hama, F. Endo, S. Okabe, J. Kindersberger, K. Juhre, S. Meijer, and U. Schichler, "Gas insulated systems for hvdc: Dc stress at dc and ac systems," CIGRE Task force D1.03.11105, 2011. (cited in pages 10, 17 and 18)

[18] A. Crisci, B. Gosse, J. Gosse, and V. Ollier-Duréault, "Surface-potential decay due to surface conduction," *EPJ Applied physics*, vol. 4, pp. 107–1116, 1998. (cited in pages 10, 19, 20 and 129)

[19] P. Molinié, "Measuring and modeling transient insulator response to charging: the contribution of surface potential studies," *Dielectrics and Electrical Insulation, IEEE Transactions on*, vol. 12, no. 5, pp. 939–950, 2005. (cited in pages 10 and 19)

[20] J. Kindersberger and C. Lederle, "Surface charge decay on insulators in air and sulfurhexafluorid-part i: Simulation," *Dielectrics and Electrical Insulation, IEEE Transactions on*, vol. 15, no. 4, pp. 941–948, 2008. (cited in pages 10, 21 and 22)

[21] S. Okabe, "Phenomena and mechanism of electric charges on spacers in gas insulated switchgears," *Dielectrics and Electrical Insulation, IEEE Transactions on*, vol. 14, no. 1, pp. 46–52, 2007. (cited in pages 10, 15, 16, 17, 18, 22, 41, 114 and 124)

[22] H. Fujinami, T. Takuma, M. Yashima, and T. Kawamoto, "Mechanism and effect of dc charge accumulation on sf 6 gas insulated spacers," *Power Delivery, IEEE Transactions on*, vol. 4, no. 3, pp. 1765–1772, 1989. (cited in pages 10, 11, 12, 13, 16 and 22)

[23] E. Volpov, "Electric field modeling and field formation mechanism in hvdc sf 6 gas insulated systems," *Dielectrics and Electrical Insulation, IEEE Transactions on*, vol. 10, no. 2, pp. 204–215, 2003. (cited in pages 10, 22, 30 and 31)

[24] F. Messerer and W. Boeck, "Field optimization of an hvdc-gis-spacer," in *Electrical Insulation and Dielectric Phenomena, 1998. Annual Report. Conference on*, vol. 1, pp. 15–18, IEEE, 1998. (cited in pages 11 and 22)

[25] F. Messerer and W. Boeck, "Gas insulated substation (gis) for hvdc," in *Electrical Insulation and Dielectric Phenomena, 2000 Annual Report Conference on*, vol. 2, pp. 698–702, IEEE, 2000. (cited in page 11)

[26] F. Messerer, W. Boeck, H. Steinbigler, and S. Chakravorti, "Enhanced field calculation for hvdc gis," in *Gaseous Dielectrics IX*, pp. 473–483, Springer, 2001. (cited in page 11)

[27] F. Messerer, M. Finkel, and W. Boeck, "Surface charge accumulation on hvdc-gis-spacer," in *Electrical Insulation, 2002. Conference Record of the 2002 IEEE International Symposium on*, pp. 421–425, IEEE, 2002. (cited in pages 11 and 12)

[28] S. Sato, W. Zaengl, and A. Knecht, "A numerical analysis of accumulated surface charge on dc epoxy rrsin spaces," *Electrical Insulation, IEEE Transactions on*, no. 3, pp. 333–340, 1987. (cited in page 12)

[29] T. Nitta and K. Nakanishi, "Charge accumulation on insulating spacers for hvdc gis," *Electrical Insulation, IEEE Transactions on*, vol. 26, no. 3, pp. 418–427, 1991. (cited in page 13)

[30] E. Volpov, "Dielectric strength coordination and generalized spacer design rules for hvac/dc sf 6 gas insulated systems," *Dielectrics and Electrical Insulation, IEEE Transactions on*, vol. 11, no. 6, pp. 949–963, 2004. (cited in pages 13, 14, 22 and 130)

[31] A. De Lorenzi, L. Grando, R. Gobbo, G. Pesavento, P. Bettini, R. Specogna, and F. Trevisan, "The insulation structure of the 1mv transmission line for the iter neutral beam injector," *Fusion Engineering and Design*, vol. 82, no. 5, pp. 836–844, 2007. (cited in pages 13 and 14)

[32] T. Hasegawa, K. Yamaji, M. Hatano, F. Endo, T. Rokunohe, and T. Yamagiwa, "Development of insulation structure and enhancement of insulation reliability of 500 kv dc gis," *Power Delivery, IEEE Transactions on*, vol. 12, no. 1, pp. 194–202, 1997. (cited in pages 13, 18 and 19)

[33] A. Kumada and S. Okabe, "Charge distribution measurement on a truncated cone spacer under dc voltage," *Dielectrics and Electrical Insulation, IEEE Transactions on*, vol. 11, no. 6, pp. 929–938, 2004. (cited in pages 15, 16, 18 and 22)

[34] H. Iwabuchi, T. Donen, S. Matsuoka, A. Kumada, K. Hidaka, M. Takei, and Y. Hoshina, "Influence of surface-conductivity distribution on charge accumulation of gis insulator under dc field," *Int'l. Sympos. High Voltage Engineering ISH, Hannover, Germany, Paper D-031*, 2011. (cited in page 16)

[35] F. Endo, T. Kichikawa, R. Ishikawa, and J. Ozawa, "Dielectric characteristics of sf6 gas for application to hvdc systems," *Power Apparatus and Systems, IEEE Transactions on*, no. 3, pp. 847–855, 1980. (cited in pages 17, 36, 37, 38, 40 and 41)

[36] M. Hairour, *Etude diélectrique d'une isolation hybride gaz-solide pour appareillage haute tension*. PhD thesis, Université Montpellier II-Sciences et Techniques du Languedoc, 2007. (cited in page 18)

[37] A. H. Cookson, "Electrical breakdown for uniform fields in compressed gases," in *Proceedings of the Institution of Electrical Engineers*, vol. 117, pp. 269–280, IET, 1970. (cited in pages 18 and 19)

[38] A. Moukengue Imano, R. Schurer, and K. Feser, "The influence of a conducting particle on a spacer on the insulation properties in sf6/n2 mixtures," in *IEE conference publication*, pp. 3–232, Institution of Electrical Engineers, 1999. (cited in page 18)

[39] C. M. Cooke, R. E. Wootton, and A. H. Cookson, "Influence of particles on ac and dc electrical performance of gas insulated systems at extra-high-voltage," *Power Apparatus and Systems, IEEE Transactions on*, vol. 96, no. 3, pp. 768–777, 1977. (cited in pages 18 and 19)

[40] H. Anis and K. Srivastava, "Free conducting particles in compressed gas insulation," *Electrical Insulation, IEEE Transactions on*, no. 4, pp. 327–338, 1981. (cited in page 18)

[41] M. Pepin and H. Wintle, "Charge injection and conduction on the surface of insulators," *Journal of applied physics*, vol. 83, no. 11, pp. 5870–5879, 1998. (cited in page 19)

[42] P. Llovera and P. Molinié, "New methodology for surface potential decay measurements: application to study charge injection dynamics on polypropylene films," *Dielectrics and Electrical Insulation, IEEE Transactions on*, vol. 11, no. 6, pp. 1049–1056, 2004. (cited in page 19)

[43] T. Sonnonstine and M. Perlman, "Surface-potential decay in insulators with field-dependent mobility and injection efficiency," *Journal of Applied Physics*, vol. 46, no. 9, pp. 3975–3981, 2008. (cited in page 19)

[44] H. Wintle, "Surface-charge decay in insulators with nonconstant mobility and with deep trapping," *Journal of Applied Physics*, vol. 43, no. 7, pp. 2927–2930, 2003. (cited in page 19)

[45] B. Lutz and J. Kindersberger, "Influence of absorbed water on volume resistivity of epoxy resin insulators," in *Solid Dielectrics (ICSD), 2010 10th IEEE International Conference on*, pp. 1–4, IEEE, 2010. (cited in pages 20, 21 and 117)

[46] Y. Awakuni and J. Calderwood, "Water vapour adsorption and surface conductivity in solids," *Journal of Physics D: Applied Physics*, vol. 5, no. 5, p. 1038, 1972. (cited in page 20)

[47] B. Lutz and J. Kindersberger, "Influence of relative humidity on surface charge decay on epoxy resin insulators," in *Properties and Applications of Dielectric Materials, 2009. ICPADM 2009. IEEE 9th International Conference on the*, pp. 883–886, IEEE, 2009. (cited in pages 20 and 129)

[48] D. K. Das-Gupta, "Electrical properties of surfaces of polymeric insulators," *Electrical Insulation, IEEE Transactions on*, vol. 27, no. 5, pp. 909–923, 1992. (cited in pages 20 and 21)

[49] J. Kindersberger and C. Lederle, "Surface charge decay on insulators in air and sulfurhexafluorid-part ii: measurements," *Dielectrics and Electrical Insulation, IEEE Transactions on*, vol. 15, no. 4, pp. 949–957, 2008. (cited in page 21)

[50] E. Volpov, "Hvdc gas insulated apparatus: electric field specificity and insulation design concept," *Electrical Insulation Magazine, IEEE*, vol. 18, no. 2, pp. 7–36, 2002. (cited in page 22)

2 | Charge generation in SF_6 at high electric field

Contents

As explained in Chapter 1, in the case of *HVDC GIS* technology, the charge generation, accumulation and relaxation on solid insulators are important mechanisms influencing the dielectric strength of the system. It has also been mentioned that the origin of charges coming from the gas is not well known, as well as the parameters influencing the charge generation. The objective of this chapter is to get a better knowledge on these processes, by trying to experimentally measure the currents flowing through the gas at high electric field.

We will first review the state of the art about currents measured through pressurized gases and vacuum for high applied electric fields. The current measured may have different

origins. It could be due to corona discharges, presence of particles within the system, or to *«dark currents»* of unknown origin. Then, we will present the experimental devices especially developed for the measurement of very low currents in gases (down to $10^{-13}\,A$) at high voltages (up to $250\,kV$). Finally, the main parameters influencing the measured current will be presented and its origin will be discussed.

2.1 | Review of charge generation in pressurized gases and vacuum

Depending on the electric field range applied to the gas, different mechanisms can take place. At low electric field (below $1\,kV/mm$), the generated charges within the gas are generally attributed to the natural ionization. At high electric field, emission mechanisms from the electrodes must be taken into account. These mechanisms are detailed hereafter.

2.1.1 | Natural ionization in gases at low electric field

In several investigations [1–4] concerning the *HVDC GIS*, the origin of the current passing through gas was explained by natural ionization processes. In absence of electric field, at room temperature and pressure, the creation of electron/ion pairs results from cosmic radiations and natural radioactivity, present in earth and in the atmosphere. In such conditions, an average value of $10\,ion\,pairs\,IP/\,(\,cm^3.s.bar)$ can be assumed [5]. The phenomenon of natural ionization has been used to estimate the amount of charge accumulation on solid insulators due to the gas [3, 6]. It has also been used to predict the breakdown probability in SF_6 [7]. The variation of the gas current measured between two parallel plate electrodes was first studied by Townsend [8] as a function of the applied voltage (figure 2.1).

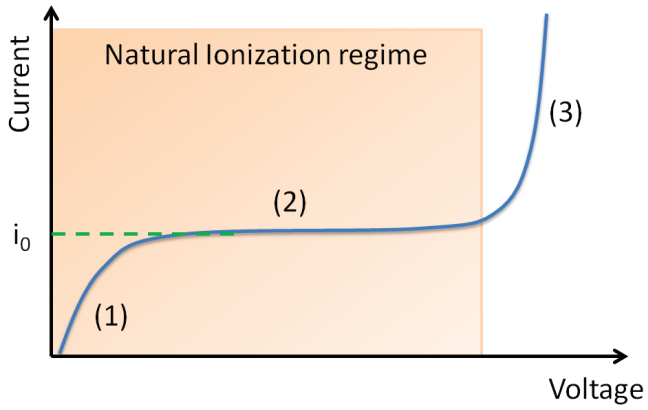

Fig. 2.1: Typical current voltage characteristic for a plane to plane gap in air, (1) and (2) natural ionization regime, (3) corona regime (adapted from [9]).

The natural ionization causes the dissociation of neutral molecules into electrons and ions. When an electric field is applied between the electrodes three regimes of current are obtained. In the first regime (1), the current increases proportionally to the applied voltage. This current results from the equilibrium between molecules dissociation and recombination kinetics. Then, over the second regime (2), the current remains constant at a value i_0 which corresponds to the saturation current. This saturation is observed when all charges due to ionization are collected by electrodes (no more recombination occurs). In air, the saturation current is reached for low electric field values, estimated to be approximately $10\,V/m$ [2]. For example, if an average of $10\,ion\,pairs\,IP/\left(cm^3.s.bar\right)$ is considered within a volume of $1\,cm^3$ of gas, a very low saturation current density of $1.6.10^{-18}\,A/cm^2$ is obtained.

In regime 3, when the applied voltage is higher than the ionization threshold voltage, the current increases beyond i_0 following an exponential law. According to Townsend [8], this is due to the ionization of the gas by electron collisions. When the energy of accelerated electrons is high enough, their collisions with gas molecules or atoms can cause their ionization.

For the application to GIS, most of authors [3–5,7] only considered the natural ionization regime (represented in Figure 2.2) in their simulation tool.

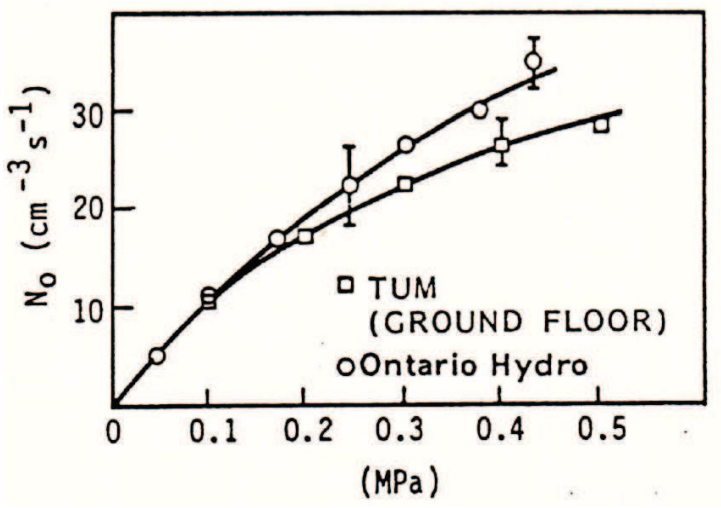

Fig. 2.2: Natural ionization production rates obtained by Munich Technical University and Ontario Hydro, in cylindrical test vessels of differing outer diameters (respectively $52\,cm$ and $27.8\,cm$ diameters) [7].

Kindersberger *et al.* [7] demonstrated the influence of pressure and electric field on ion generation, in the case of the in-homogeneous field breakdown in GIS. It has been observed that for pressure above $0.1\,MPa$ (figure 2.2), the ionization rate of SF_6 increases slower than linearly with pressure.

It is worth noting that the ionization rate is not field-dependent. Only the ion drift is accelerated under electric field, leading to variations of equilibrium and steady-state current

at very low electric fields (a few V/m). In case of *HVDC GIS*, electric fields much higher than that used to investigate the natural ionization processes can be reached in functional conditions (up to $5\,kV/mm$). In these conditions, only a saturated current should result from the gas natural ionization.

2.1.2 | Charge emission mechanisms in vacuum at high electric field

Dark currents are currents which are not correlated to any light emission. In high vacuum, these currents can be composed of currents due to primary and/or secondary emission [10].

2.1.2.1 Primary emission

To extract an electron from a metal, it must overtake a potential barrier with a height corresponding to the work-function (φ), at absolute zero. In a metal, at absolute zero, electrons are on energy levels up to a maximal energy level named *Fermi level* (E_f) (figure 2.3). Hence the work-function corresponds to the difference between *Fermi level* and vacuum. In normal conditions, electrons do not have sufficient energy to be spontaneously extracted from the metal surface. If we consider that the metal is thermally excited, electrons get sufficiently high energy to occupy higher energy levels, due to thermal vibrations. If this energy is superior to the metal work-function, electrons can be emitted from the metal even without external electric field; this corresponds to the thermionic emission (known as *Schottky* effect, studied in particular by *Owen Richardson* in 1928).

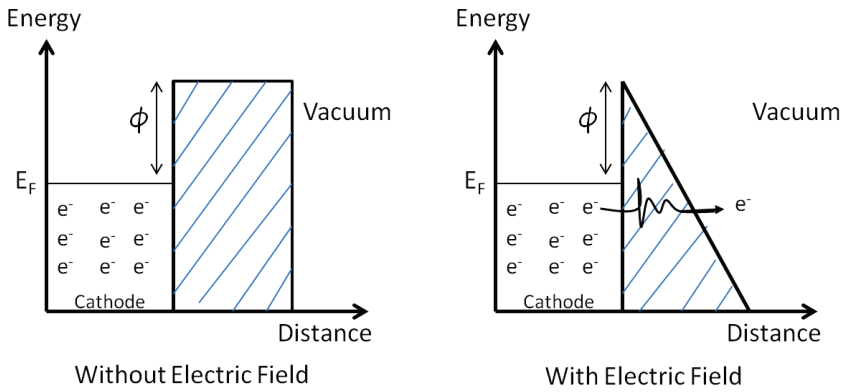

Fig. 2.3: Lowering the potential barrier applying an electric field.

If a high electric field is applied to the metal (several gigavolts per meter), the potential barrier can be significantly reduced. Hence electrons can directly pass from the metal toward gas even for low temperatures (figure 2.3). In this case, the emission is realized by tunnel effect. The higher the electric field, the lower the potential barrier, increasing the probability of an electron to cross this barrier.

2.1.2.2 Secondary emission

The mechanism of secondary emission is illustrated in Figure 2.4. Electrons generated by primary emission (a) are accelerated under the effect of the electric field toward the anode. If they do not collide during their movement, their energy increases proportionally with the applied voltage. This bombardment of the anode (b) could contribute to the local heating, the surface deformation and ionization. Hence, positive ions and/or neutral molecules (c), which are liberated from the anode by this electron bombardment, or by electron impact, will create ions. These ions will be accelerated back to the cathode (d) where they create secondary electrons and ions (e), inducing secondary field emissions from the cathode. These secondary electrons are accelerated toward the anode.

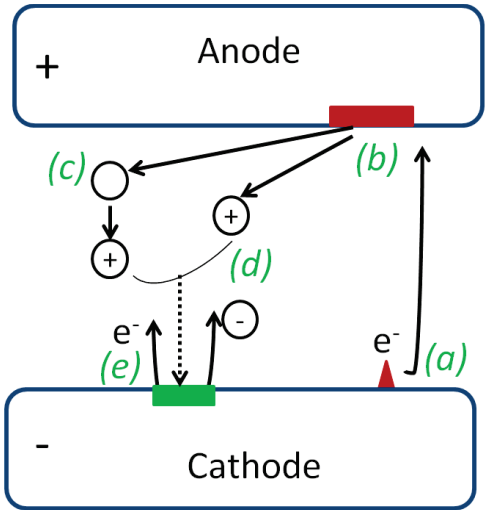

Fig. 2.4: Schematic presentation of primary and secondary emission by bombardment [10].

These processes will depend on the kinetic energy of the electrons arriving onto the anode, on the energy of accelerated positive ions and on the material of electrode. It is worth noting that if the measured current between electrodes at constant field varies with gap distance, a secondary emission is to be considered, if not, primary emission solely occurs.

2.1.2.3 Theory of field emission

As presented previously, an electron can leave the metal if its energy is superior or equal to the work-function. Two main mechanisms are reported: the thermionic emission, for which the temperature will bring energy to the electron, allowing it to cross the potential barrier, and the field emission, which is driven by the electric field. Figure 2.5 represents a schematic view of the band diagram at the metal-dielectric interface. Three paths are

represented, one for the electron displacement in the case of a *Schottky* effect (1), the others in the case of a tunnel effect (2) and (3). These two mechanisms are detailed below.

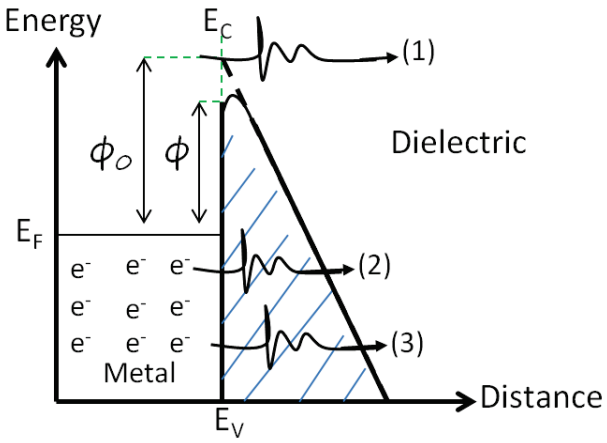

Fig. 2.5: Band diagram at the metal-dielectric interface. (1) *Schottky* emission, (2) Tunnel effect after a gain in energy, (3) Tunnel effect for a constant energy. E_v and E_c representing respectively the energy corresponding to the higher level of the valence band, and the lower level of the conduction band.

2.1.2.4 Thermionic emission (*Schottky* effect)

The *Schottky* effect corresponds to the charge injection in a dielectric, overcoming the potential barrier, represented by the interface (figure 2.5 (1)). When applying an electric field, the potential barrier is lowered, which enhances the charge injection by this mechanism. The height of the potential barrier is written as follows [11],

$$\varphi = \varphi_0 - \beta_S \sqrt{E} \tag{2.1}$$

where E is the electric field, φ_0 is the potential barrier of the dielectric.

β_S is the *Schottky* constant. Its value depends on the considered dielectric and is calculated following (2.2)

$$\beta_S = \sqrt{\frac{e^3}{4\pi\varepsilon_r\varepsilon_0}} \tag{2.2}$$

where e is the elementary charge ($1.602 \times 10^{-19}\,C$), ε_r is the relative permittivity of the dielectric and ε_0 the permittivity of the vacuum [11]. Current density emitted by such mechanism is given by equation (2.3). In this equation, A the *Richardson-Schottky* constant, equals to $120\,A.cm^2$.

$$J = AT^2 exp[-\frac{(\varphi_0 - \beta_S\sqrt{E})}{kT}] \tag{2.3}$$

This mechanism can be represented as a straight line on a graph $lnJ = f(\sqrt{E})$ as plotted in figure 2.6. The value of the slope is $\frac{\beta_S}{kT}$, with β_S depending on the dielectric permittivity. On this plot, the extrapolation to zero field, gives the height of the potential barrier at the metal-dielectric interface φ_0.

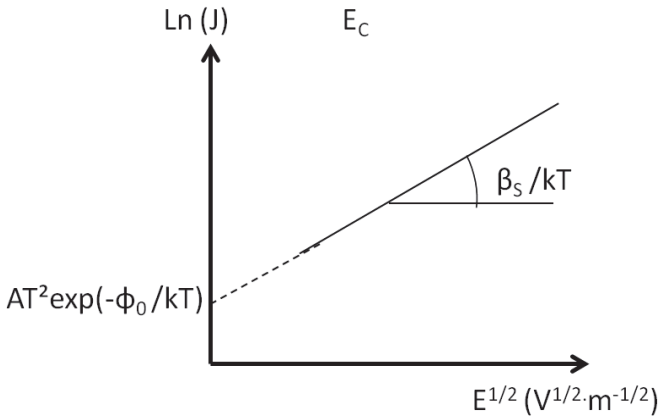

Fig. 2.6: Current density variations versus electric field, for a *Schottky* injection mechanism.

2.1.2.5 *Fowler-Nordheim (FN)* effect

This effect, represented by mechanism (2) and (3) in figure 2.5, corresponds to the injection due to the electric field [12], linked with the quantum theory and also known as *tunnel effect*. Electrons may be extracted from a metal surface by high electrostatic fields of the order of $10^7 - 10^8\, V/cm$. This emission current has been widely studied by *Fowler-Nordheim* [13], they have shown that few electrons in a metal will have an energy slightly above the *Fermi level* and thus will have a greater probability to penetrate the potential barrier. This mechanism is due to the wave nature of electrons. When the potential barrier is thin enough, the probability that electrons can be on the other side of the barrier is different to zero. The current density related to a *Fowler-Nordheim* emission is written as follows:

$$J = AE^2 exp[-\frac{B \times v(y) \times \varphi^{3/2}}{E}] \tag{2.4}$$

With $A = (1.54 \times 10^6)/(\varphi \times t^2(y))$, ϕ the work-function of the metal and $B = 6.83 \times 10^9$, and $t(y)$ and $v(y)$ functions varying with y, and $y = 3.795 \times 10^{-5} \times E^{0.5} \times \varphi^{-1}$.

According to Zeitoun [14] approximations:

$$t(y) \sim 1 \; and \; v(y) \sim 0.956 - 1.062 \times y^2 \tag{2.5}$$

In case of a *Fowler-Nordheim* emission, the plot of $ln(i/E^2)$ versus $1/E$ gives an affine straight line. It is worth noting that FN effect does not depend on temperature.

In a general way, it has been demonstrated that in most cases, the electric field is not uniform on the surface and that micro protrusions play an important role on the electric field reinforcement. In the literature the amplification factor linked to micro protrusions could vary between 1 to 1000 [15]. Hence, it is important to deal with local electric field related to micro protrusions rather than average electric field related to a potential difference between two surfaces. The main issue is to estimate the value of this coefficient linked to the shape of the micro protrusion. Thus, previous formulas can be used replacing E by $\beta \times E$. Then, using the curves plotted in *Fowler-Nordheim* coordinates, it is possible to determine the values of β and the surface (S) related to the characterized emission.

$$\beta = -\frac{6.53 \times 10^9 \times \varphi^{3/2}}{slope} \; and \; S = \frac{exp(Y_0 - \frac{10.45}{\varphi^{1/2}})}{A \times \beta^2} \tag{2.6}$$

With Y_0 the $Y-$intercept.

It is worth noting that the FN law allows calculating an emitting surface considering only one site and surface of emission. However, many micro protrusions usually contribute to the measured current. Thus, a superposition of emitting sites should be considered. That is why the interpretation of the measured current, based on the FN law, often lead to aberrant values of surface emission. We recommend referring to the Ph.D. thesis by Almaksour [16] for further detailed analysis of *Fowler-Nordheim* plots.

2.1.3 | *Dark currents* through pressurized gases (Air and SF_6) at high electric field

Many authors have reported studies concerning «*dark current*» in vacuum under high electric field [10, 15, 17–19]. Up to now, only few investigations have been done in SF_6 [17, 20–22]. Although physical phenomena occurring in vacuum or in SF_6 are not comparable, it is interesting to compare the impact of various parameters in both cases.

Shibuya *et al.* [23] investigated *«dark currents»* in pressurized SF_6, and compared these results with *dark current* obtained with same electrodes in vacuum and air [24]. Their results, presented in figure 2.7 (a) and (b), show two main interesting points. First, it evidences that current measured through pressurized gases (air and SF_6 at $14kV/mm$ respectively for $5\,mm$ and $2\,mm$ gap) are much lower than that obtained under vacuum conditions at $10^{-6}\,Torr$ ($29\,nA$ and $920\,nA$ at $14kV/mm$, respectively for $1.2\,mm$ and $2\,mm$ gap). It points out that current emission phenomena are different in vacuum and gases. Indeed, plotting the measured current in a FN representation (figure 2.7 (a)), we clearly observe that a linear relation is obtained in case of vacuum, but not in case of pressurized gases. In addition, when those currents are simply represented as a function of the electric field, they depend on the distance between electrodes, evidencing that there is

no simple relation between the current and the electric field in gases.

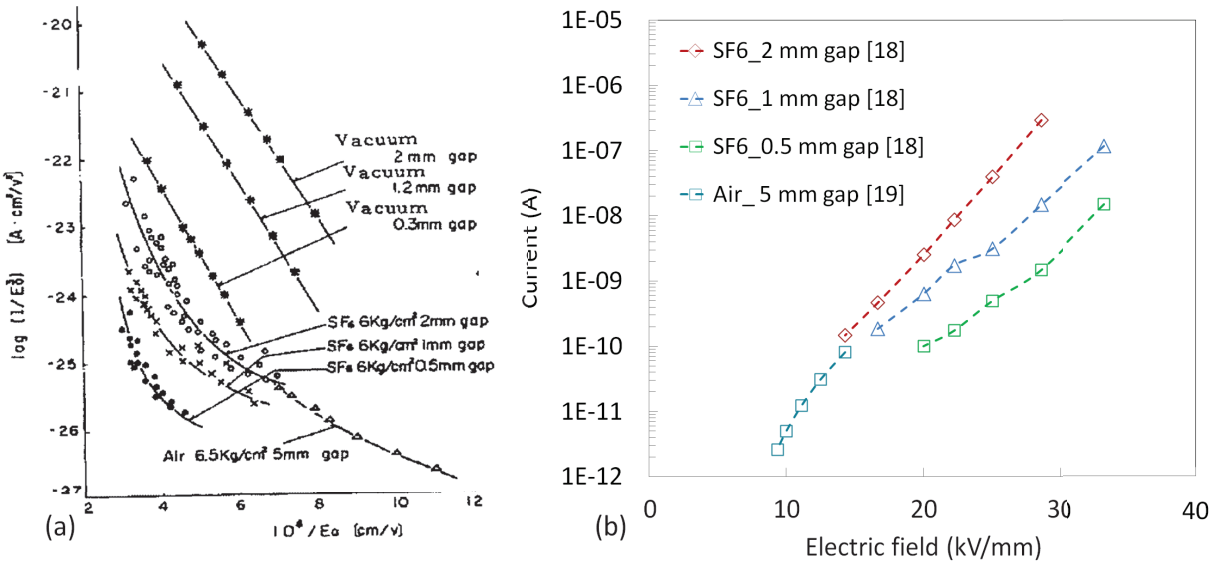

Fig. 2.7: Characteristic of dark current for various gap conditions and nature of gas, with identical electrodes with an area of about $1\,cm^2$. (a), FN curves, (b), corresponding current versus electric field strength (calculated from (a)) [23].

To explain their observations, Shibuya *et al.* propose a model in which the *dark current* in high pressure gases has the same field dependence as in vacuum. However, they postulate that the electric field (E) at the cathode is reduced due to the influence of space charges. These charges are assumed to be due to emitted electrons attached to gas molecules, forming a space charge layer around the emission site. This results in small *dark currents* in gases.

In addition, Shibuya *et al.* also observed that depending on the surface roughness of electrodes used, the onset of *dark currents* in SF_6 is different. For polished electrodes, *dark currents* appear for electric field higher than $43\,kV/mm$ whereas for rough electrodes such currents appear for electric fields around $10\,kV/mm$. These results are in agreement with the work of *Endo et al.* [20], which presents large variations on the measured current depending on the roughness of the cathode/anode system. It is stressed out that if the anode and the cathode are both rough, the electric field for which *dark currents* are measured is $15\,kV/mm$, whereas this field is about $25\,kV/mm$ for both polished electrodes. They also reported that when the anode is rough and the cathode is polished, a *dark current* can be measured at low electric field strength ($\sim 8\,kV/mm$). On the corresponding FN plots (see figure 2.8), there are two different slopes, one corresponding to a rough cathode and the other corresponding to a rough anode.

Another study was done by MacAlpine *et al.* [21] on *dark current* emission in a point/plane electrode system, depending on pressure and surface roughness of electrodes. Figure 2.9 shows that for low pressures (0.1 and $0.3\,MPa$) two different current regimes

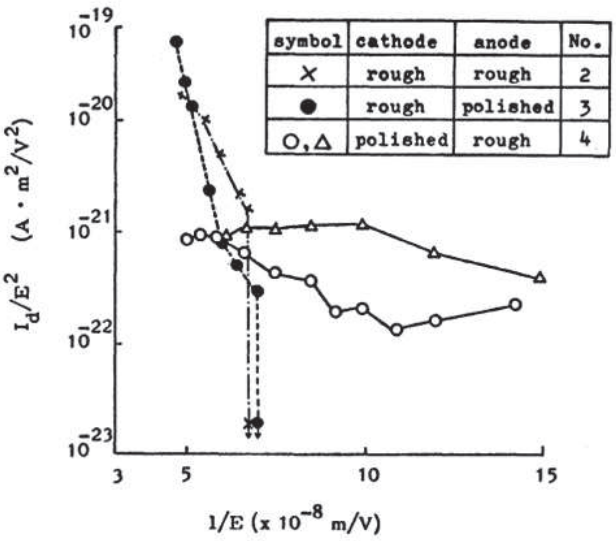

Fig. 2.8: Fowler-Nordheim plots of *dark currents* obtained in $0.4\,MPa$ of SF_6 [20].

are observed, while only one regime is present at $0.6\,MPa$. According to the authors, this current is composed of one component due to natural ionization and another resulting from cathode emission. For all pressures, currents are higher for rougher electrodes. In those experiments, currents measured were tentatively fitted by a *Schottky-emission* process, assuming that the under-evaluation of measured current compared to *Schottky*'s law is due to a reduction of the electric field strength, caused by electron space charges. They also supposed that these charges originates from areas of low work-function due to impurities adsorbed on the cathode surface.

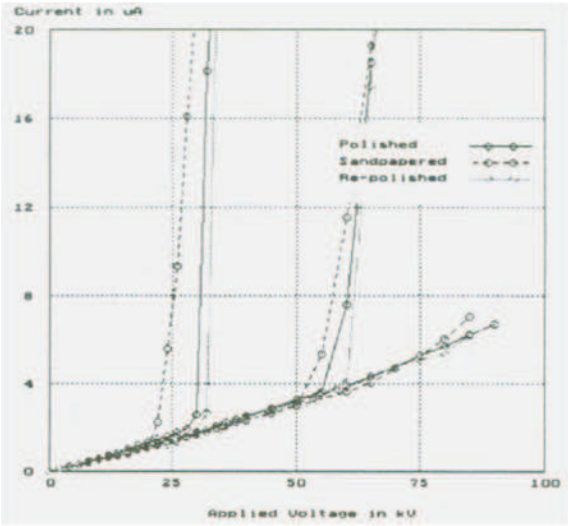

Fig. 2.9: Current measurements depending on electric field strength for a point/plane electrode system at 0.1, 0.3 and $0.6\,MPa$ of SF_6 [21].

Studies performed in compressed air [24–28] investigated the effect of the nature of

electrodes and their surface roughness on *dark currents*. They evidence that there is a large variation of the current depending on the electrode material. Additionally, for a given metal, the current strongly depended on the surface finishing. Contrary to Shibuya's experiments in SF_6, *dark currents* measurements in air can perfectly be fitted by the *Fowler-Nordheim's* law, suggesting a mechanism of electron field emission (figure 2.10).

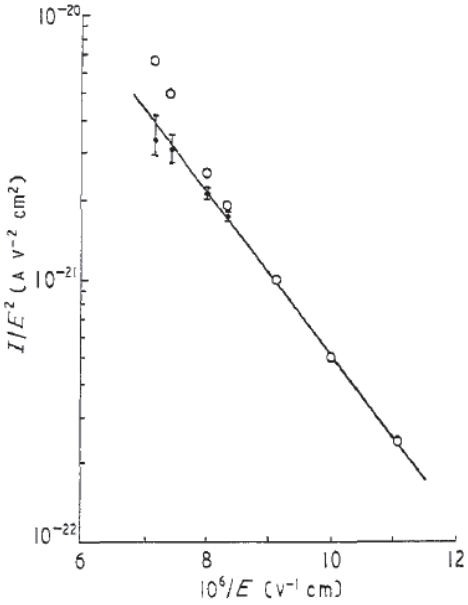

Fig. 2.10: FN for current measured in air depending on electric field strength for a plane to plane electrode system [24].

However, based on these measurements, the calculation of the experimental work-function of the electrode's metal leads to values much lower than theoretically values.

Jones *et al.* [25], found an experimental work-function of $0.5\,eV$ whereas the theoretical one was of $4.5\,eV$. Based on the work of Stern *et al.* [26], they postulate that a $10^{-7}\,cm$-thick insulating oxide layer, present on the surface of the metal was responsible for the decrease of the work-function. This thin insulating film also led to an intense electric field, set up by positive ions within the layer. Further investigations showed that removing this thin oxide layer lowered the emitted current.

2.1.4 | Influence of several parameters on current measured in vacuum at high electric field

In order to better understand mechanisms occurring in SF_6, we will review results reported in the literature in the case of vacuum. Compared to SF_6, much more research has been done concerning current measurements in vacuum [10, 15, 17–19]. We will present the main influencing parameters which allow determining the origin of the measured current.

2.1.4.1 Influence of electrode polishing and cleaning

In order to control surface properties of an electrode, the latter must be processed using various polishing and cleaning techniques. The main technique used for surface polishing is the mechanical polishing [10, 15, 19, 20, 29]. Other techniques such as electro-polishing (EP) [18], and chemical polishing [19] were also used. It has been observed that the processing technique can have a large impact on the surface roughness and thus on the measured *dark current*. Pupeter *et al.* [19] evidenced that depending on the treatment applied (mechanical or chemical polishing) various types of local charge emitters appear, such as surface defects, foreign-element inclusions, and damages on the surface morphology. In their experiment, Nobium (Nb) samples were mechanically polished with diamond tools, resulting in an average roughness of about $10\,\mu m$, while others were treated by buffered chemical polishing (BCP). After these treatments, all samples were rinsed with ultra-pure water and dried in nitrogen gas flow. They evidenced two types of defects on Nobium cathodes, depending on the polishing treatment (figure 2.11). For a mechanically polished Nb cathode, emitters were associated to surface defects caused by the diamond tool, whereas for the chemically polished Nb cathode, emitters were identified as sticking particles.

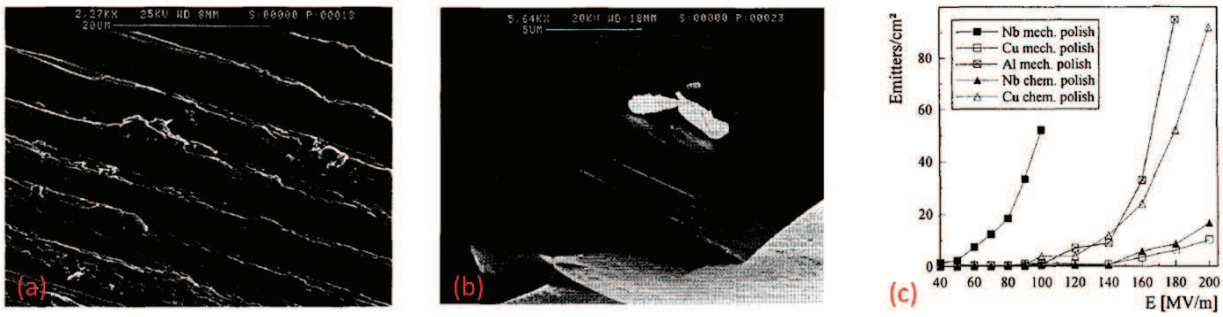

Fig. 2.11: Scanning Electron Microscope images of (a) surface defect on mechanically polished Nobium surface ($E_{on} = 45\,MV/m$); (b) Nobium particle on chemically polished Nb ($E_{on} = 59\,MV/m$); (c) Average emitter densities per cm^2 on Nb, Cu and Al cathodes after chemical or mechanical polishing depending on scanning field strength [19].

This results in a larger number of emitters for the mechanically polished Nb ($52\,emitters/cm^2$ at $110\,MV/m$) than for the chemically polished ($15\,emitters/cm^2$ at $200\,MV/m$). Other investigations also used thermal treatment and ultra pure water rinsing [10, 18] in order to remove residual water adsorbed on the electrode and to get rid of contaminant or remaining particles. The rinsing using ultrasonic bath was also used in several work [15, 20, 30].

2.1.4.2 Influence of electrode nature

The influence of electrode nature on *dark current* was investigated by several authors [10, 19, 30]. Their aim was to reduce the *dark current* in order to apply higher electric field while avoiding breakdowns. The investigation led by Furuta *et al.* [10] suggests a solution

to avoid those currents for field lower than $100\,MV/m$. They measured *dark currents* in vacuum for four electrode materials: Molybdenum (Mo), Titanium (Ti), Copper (Cu) and stainless steel (SUS) (figure 2.12). The results present the *dark current* measured for a cathode and an anode of the same nature, with a gap distance of $0.5\,mm$.

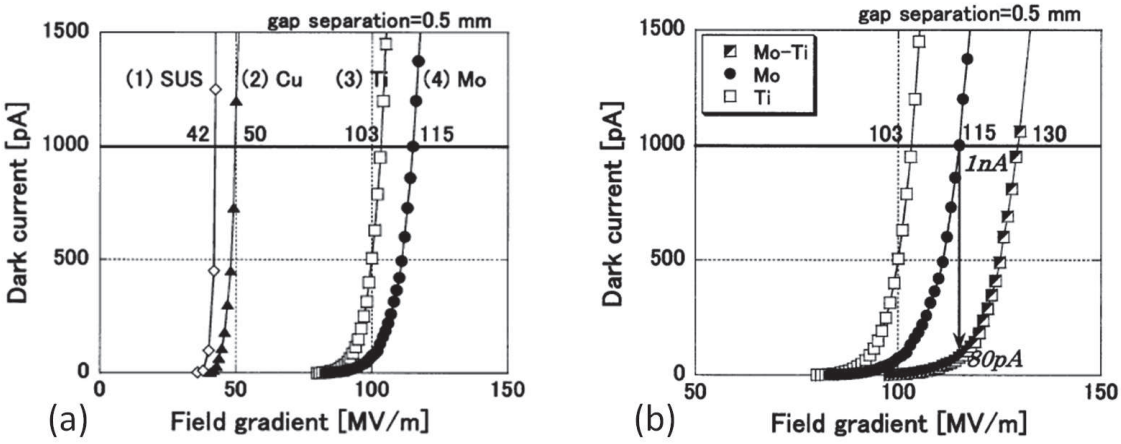

Fig. 2.12: *Dark currents* depending on electric field for (a) four different electrodes: Stainless steel, Copper, Titanium and Molybdenum, for $0.5\,mm$ gap distance; and (b) for three electrodes configurations: Mo cathode and Ti anode, Mo cathode and anode, Ti anode and cathode [10].

Best results were obtained for Ti and Mo electrodes, where *dark currents* of $1\,nA$ were measurable for electric fields higher than $80\,MV/m$. They showed that current emitted was lower in the case of Mo electrodes than with Ti (figure 2.12 (a) and (b)), which agrees with the electron work-function of these metals ($\varphi_{molybdenum} = 4.6\,eV$ and $\varphi_{titanium} = 4.3\,eV$). Using the same electrodes, they also performed *dark current* measurements as a function of the gap distance between electrodes. A low dependence of this parameter had been observed in case of titanium, meaning that in this case, secondary emission is lower than for molybdenum. Hence, a combination of a titanium anode and a molybdenum cathode presents even lower emitted current (figure 2.12 (b)).

2.1.4.3 Influence of surface roughness

In addition to these parameters, the surface roughness of electrodes was also investigated. The surface roughness is responsible of the local electric field reinforcement on the cathode, which favors the primary emission. Several authors [15, 20, 31] reported the influence of this parameters. Almaksour *et al.* show the impact of the surface roughness for $316\,L$ stainless steel electrodes, under vacuum conditions, with a fixed inter-electrode distance of $1000\,\mu m$ (figure 2.13). Electrodes used were previously mechanically polished using SiC paper with different grain-size in order to reduce the roughness. Figure 2.13 evidences that for increasing values of cathode roughness, the measured current is higher. For example, a

current of $20\,pA$ is obtained for an applied field of $18\,MV/m$ for $Ra = 118\,nm$, $22\,MV/m$ for $Ra = 95\,nm$, and $25\,MV/m$ for $Ra = 13\,nm$.

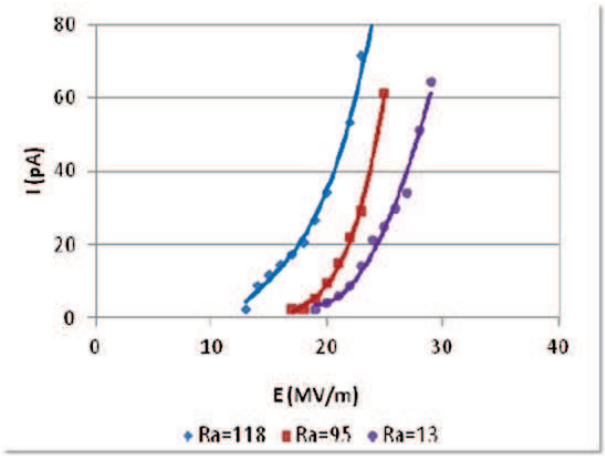

Fig. 2.13: *Dark currents* as a function of field gradient at the cathode surface for a gap distance of $1\,mm$. Ra unit is in nm [15].

The control of the cathode surface roughness is essential to reduce the current due to primary emission. Besides, the control of the anode roughness is also of importance in order to limit positive ions emissions from the anode and so reduce secondary emission mechanisms. Suzuki *et al.* [18] have shown that depending on the treatment applied on the anode, it may easily release positive ions under electronic bombardment. They investigated various treatments, such as electro-polishing, which allow controlling the surface roughness. It has been shown that even if the treatment allowed obtaining good surface roughness, it frequently induces higher *dark currents* than without treatment.

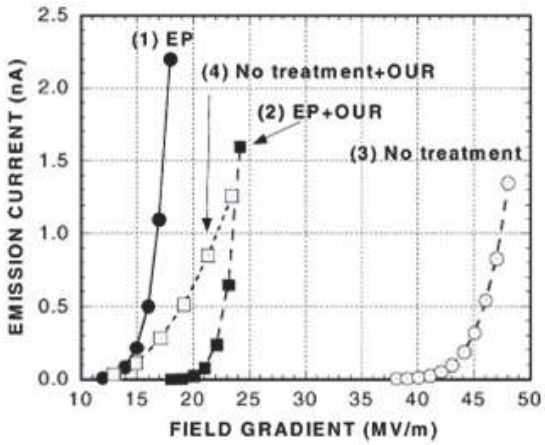

Fig. 2.14: *Dark currents* versus electrical field for a gap distance of $1\,mm$, diamond polished electrodes (copper) with various treatments: (1)EP, (2) $EP + OUR$, (3) no treatment, (4) no treatment $+OUR$. EP: electro-polishing, OUR: Ozonized Ultra-pure Water Rinsing [18].

The lowering of the electric field observed in figure 2.14 was attributed by Suzuki *et al.* to the presence of an oxide layer on the electrode surface which favors the emission of positive ions under electronic bombardment (secondary emission). This explanation agrees with the observation that the pressure increases (from $10^{-12}\,Torr$ to $10^{-10}\,Torr$), correlated with the *dark currents* in the case of electro-polished electrode (due to oxide degassing). This theory also justifies the result presented in figure 2.15.

2.1.4.4 Influence of gap distance

Figure 2.15 presents *dark currents* measurements for copper electrodes with and without EP treatment, for three different gap distances. Without treatment, the same current is measured for both 0.5 and $1\,mm$ gap distances. It is explained by the fact that *dark current* without electro-polishing is mainly due to electron primary emission. On the contrary, with electrodes treated with electro-polishing, a strong dependence with gap distance is observed. This means that the predominant mechanism occurring is secondary emission, enhanced by the oxide layer on the anode.

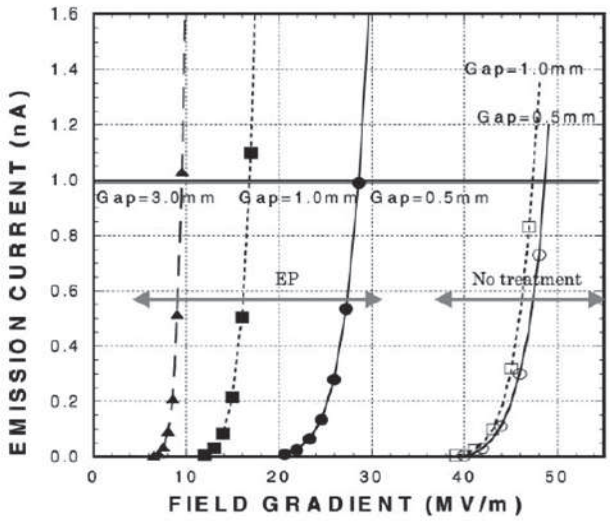

Fig. 2.15: *Dark currents* with electrodes with no surface treatment, and treated by EP for different gap distances, in vacuum [18].

The distance between electrodes can influence the charge emission process under vacuum. If some secondary emission mechanisms are present, the current at constant average electric field will vary with the gap. Furuta *et al.* investigated this parameter (figure 2.16) for the electrode's nature presented above. It is shown that in case of copper (2) and stainless steel (1), the variation of electric field corresponding to a *dark current* of $1\,nA$, is not significant ($\Delta E \sim 2.5$ and $6.5\,MV/m$ respectively). This difference is higher for Ti and Mo electrodes, which shows a large impact of secondary emission with these metals.

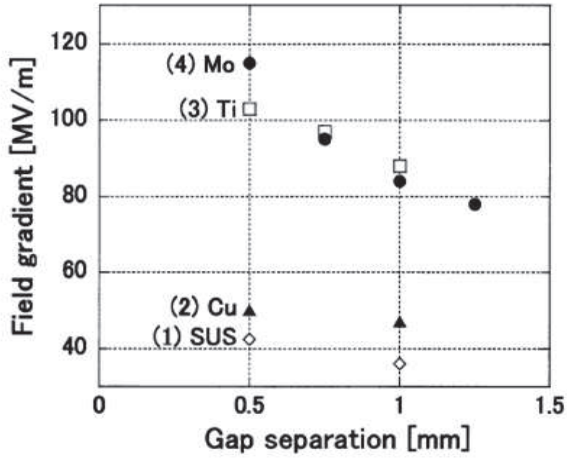

Fig. 2.16: Gap separation dependence of the field, corresponding to a *dark current* of $1\,nA$ for four electrodes: Stainless steel, Titanium, Copper and Molybdenum [10].

2.1.5 | Influence of the introduction of low pressure gases in vacuum experiments

Besides the effects of electrode processing, nature, and distance, the influence of small amounts of gas on field emission through vacuum has also been investigated. These results may provide indications on the phenomena involved in higher pressure gases. The aim of introducing some small gas pressure was to reduce as much as possible the emission current, in order to increase the breakdown field strength. Such experiments are limited to low values of pressure ($\leq 0.01\,MPa$) to avoid a large current increase due to the Townsend mechanism (ionization of the gas by collision). In some cases, it has been observed that current is enhanced when pressure increases within the device [32], but in most cases, the decrease of *dark current* was observed [16,33–35]. Simonin *et al.* [35] shows that an increase of the hydrogen pressure induces a reduced current (with a cathode surface of about $50\,m^2$). Figure 2.17 shows the *dark current* measured versus voltage (electric field between 2 and $6\,kV/mm$). At $500\,kV$ an increase of $2.1.10^{-3}\,Pa$ (between P_1 and P_4) led to a reduction of $45\,mA$ on the measured current. This phenomenon is enhanced at higher voltages: for $V = 700\,kV$, a pressure increase of $8.4.10^{-3}\,Pa$ induces a current reduction of about $50\,mA$. These results also underline that this effect is further enhanced in the case of Helium. This was attributed to the fact that the work-function depends of the metal and gas types.

The same phenomenon is described in the work of Hajra *et al* [34]. They observed the same behaviour: when N_2 or Ar gas pressure increases, the measured current decreases. These observations are explained by the formation of micro-plasma in front of the emitting tips, which then results in the surface bombardment by Ar or N atoms. This bombardment leads to hydrogen species desorption, resulting in an electron emission reduction.

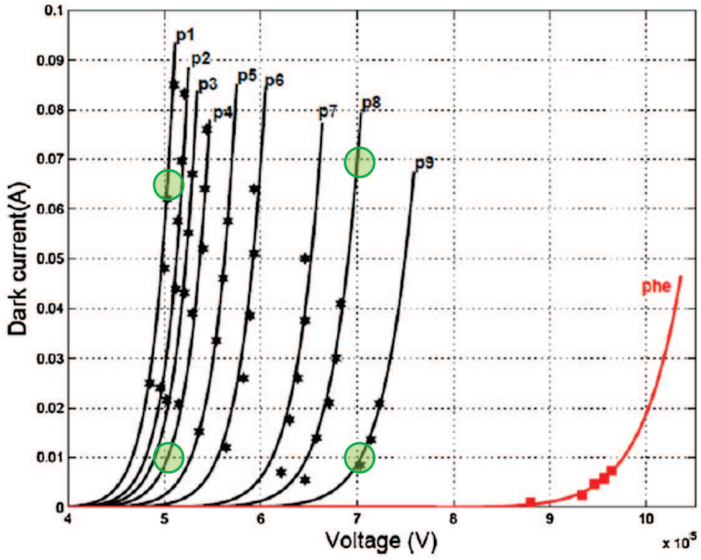

Fig. 2.17: Dependence of the *dark current* as function of the high voltage and pressure (from $P_1 = 1.7.10^{-3}\,Pa$ to $P_9 = 28.2.10^{-3}\,Pa$) in the enclosure. Black lines: Hydrogen gas, red line: Helium gas. [35].

The decrease of *dark currents* when gas is introduced was related to a selective sputtering of the emitting micro-tips, induced by electron bombardment of the gas molecules. According to [33], ions created by impinging electrons, have a strong probability of striking the emission sites and change their shape, which results in a lower field reinforcement and thus lower current. The current reduction was also explained by an increase of the work-function of the metal's electrode due to gas adsorption on its surface, via Van der Waals interactions [35]. These observations are in qualitative agreement with the observation of Shibuya (*i.e.,* large reduction of the current when high pressure SF_6 replaces vacuum).

2.1.6 | Discussion and objectives of the study

In this section, phenomena responsible for the presence of charges in gases at zero field (natural ionization), and charge injection in vacuum and pressurized gases at high field, have been presented. Measured *dark currents* in pressurized gases do not only originates from natural ionization since current densities reported in the literature are much higher than $10^{-18}\,A/cm^2$, and thus additional mechanisms must be considered. *Dark currents* through gas are well inferior than those obtained in vacuum with the same electrodes [23]. This observation is in qualitative agreement with the decrease of current in vacuum when the gas partial pressure is increased.

Concerning charge emission mechanisms in vacuum, *Fowler-Nordheim* emission is usually taken into account. In pressurized gases the few studies available do not provide clear answers on this subject. Shibuya *et al.* evidence that measurements in SF_6 do not fit with FN law, whereas in vacuum a good fit was obtained with the same electrodes. The authors

suppose that a space charge layer close to the electrode surface, leads to a modified emission law. Another proposition, by MacAlpine *et al.* consists in applying a *Schottky* fit, and also considering the presence of space charges. The last one, developed by Stern *et al.*, and re-used by Jones *et al.* in air, states that the *dark current* follows a FN injection process, considering a thin insulating layer (of unknown nature) on the cathode surface. The latter gets a large surface charge of positive ions, leads to lower «apparent» metal work-function, and thus to a better FN fit of data.

As in vacuum, the influence of electrode surface roughness was observed in pressurized air and SF_6 (*i.e.,* the current increases with the electrode roughness).

To get a better understanding of mechanisms occurring in SF_6 in conditions relevant to HVDC GIS, many additional investigations should be performed, concerning the influence of several parameters:

- The gas pressure: this parameter has not been investigated in pressurized gases yet.

- The gap distance and applied electric field: the results of Shibuya *et al.* (figure 2.7) show a large increase of current at constant electric field when the gap is increased (more than one decade between 0.5 and $2\,mm$). Experiments must be carried out in conditions relevant of HVDC GIS, *i.e.,* at much larger distances (several centimeters) and lower electric fields (a few kV/mm).

- The polarity: experiments presented so far were only performed in negative polarity. Measurements should be realized in positive polarity.

- The temperature: this parameter was not investigated, neither in vacuum nor in gases.

- The electrode roughness: typical surface roughness in real GIS applications are in the range of $R_a = 3\,\mu m$.

- The gas purity: industrial gases are not of very high purity, and may contain other gases (up to about 2%), and some water (a dew point of approximately $-27\,°C$ corresponding to 3% relative humidity RH at atmospheric pressure is acceptable).

To perform measurements, we have developed two specific devices which allow measuring currents with low noise level at high voltages, in two different electrodes configurations.

2.2 | Experimental systems

Two experimental devices have been built to perform *dark current* measurements in two different electric field configurations: a small scale coaxial geometry, and a larger scale parallel-plate electrodes system, with dimensions close to those of the real application. Measurement of very low currents (down to $0.1\,pA$) at high voltage (up to $250\,kV$) was especially challenging, and required great care to reduce measurement noise, and protect electrometers against breakdown.

2.2.1 | Small scale coaxial electrode system

To measure currents flowing through gases, a coaxial electrode system with a guard electrode was first used (figure 2.18). Thanks to the guard electrode, only currents passing through the gas are measured. The gap distance is fixed to $d = 5.5\,mm$. The radius R_{HV} of the High Voltage (HV) electrode is $2.5\,mm$, and the inner radius of the measurement electrode $R_{mes} = 8\,mm$. The electrode system is placed in a high-pressure vessel ($1.1\,MPa$ maximum) equipped with a high-voltage bushing. The coaxial electrodes system is positioned vertically. If solid particles are present, they can fall down in a region where they have no influence on measured currents. In the following text, quoted values for the electric field E_{HV} correspond to the maximum electric field at the HV electrode:

$$E_{HV} = \frac{V}{R_{HV} \times ln\dfrac{R_{mes}}{R_{HV}}} \tag{2.7}$$

At $V = 100\,kV$, the electric field E_{HV} reaches $34\,kV/mm$. The electrodes are composed of brass material. Only the surface roughness of the HV electrode can be changed, using mechanical sandpaper polishing. The roughness of the outer electrode does not change during experiments.

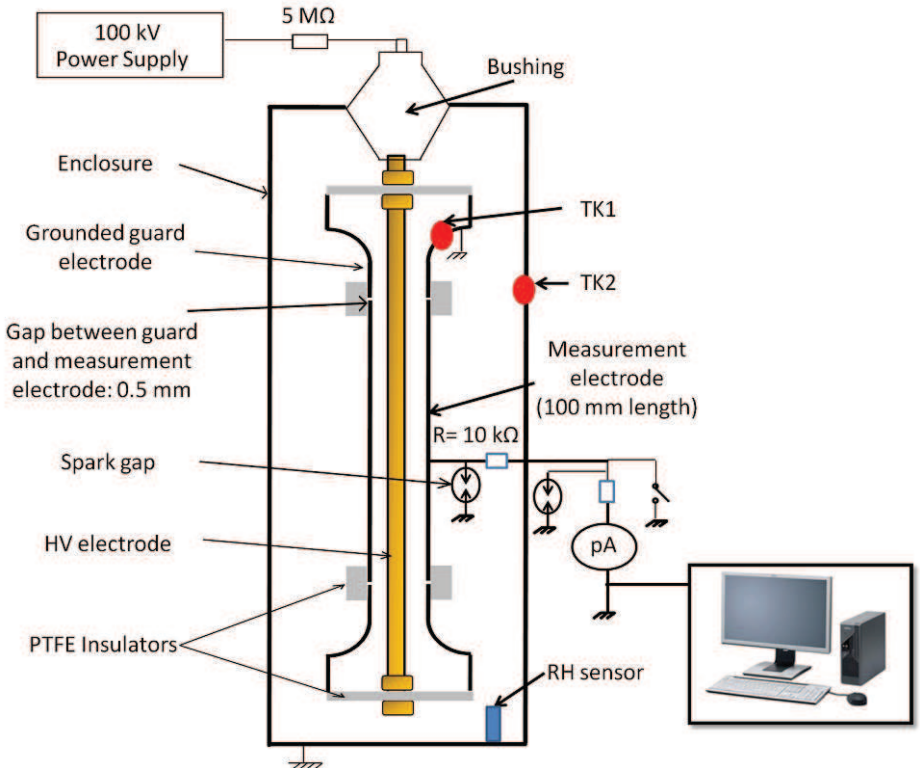

Fig. 2.18: Schema of the coaxial electrodes system developed for current measurements. (Maximum voltage: $100\,kV$)

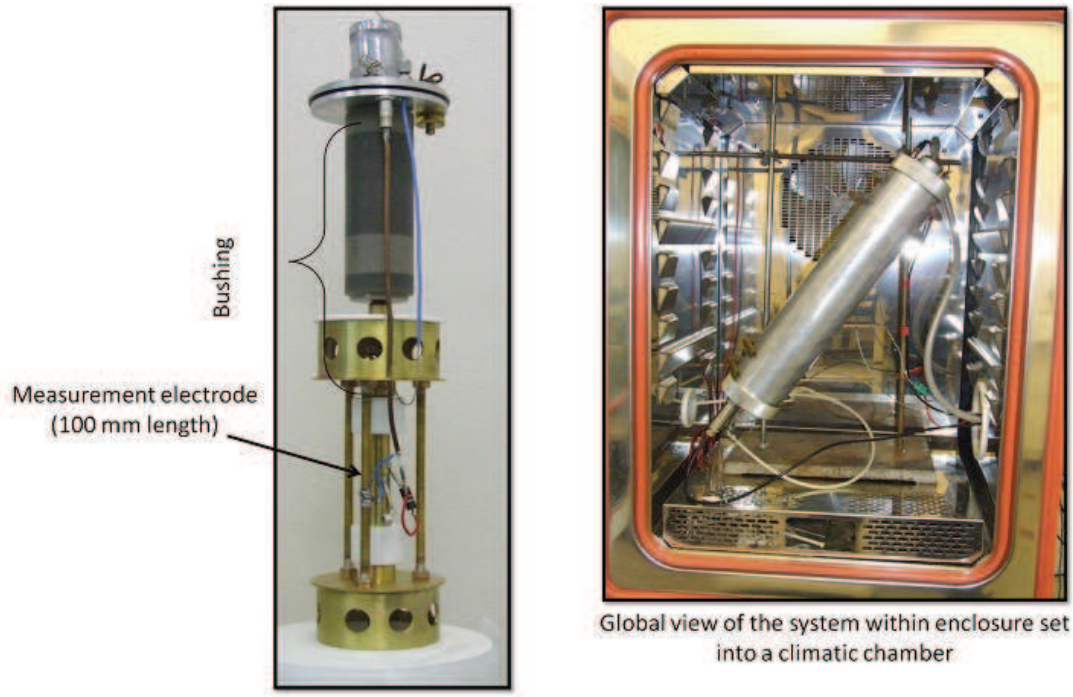

Fig. 2.19: Photographs of the coaxial electrodes system developed for current measurements, represented in figure 2.18.

Currents are measured with an electrometer (Keithley ® model 6517B) connected to a numerical recording system. A protection system composed of spark gaps, and of resistances in series with the test cell (both at the high voltage connection and at the ground side), avoid applying large over-voltage to the electrometer in case of breakdown. Moreover, a switch is set to short-circuit the electrometer input during application or removal of the applied voltage. The high voltage up to $\pm 100\,kV$ is provided by a Spellman $RHR100$ power supply with 10^{-5} ripple. The noise of current measurements was typically $\pm 0.5\,pA$. Quoted values for the current correspond to the numerical averaging of 20 consecutive samples (*i.e.,* corresponding to a $200\,s$ measurement period).

In addition to this initial setup used for the first series of measurements, a RH sensor was installed in the enclosure, with an absolute precision of $\pm 0.8\%$. Two thermocouples provide precise measurements of the temperature of the test cell (*TK1*) and of the enclosure (*TK2*). The entire system is placed into a climatic chamber, allowing the control of the temperature between 10 °C and 80 °C. *Dark currents* measurements were performed using different gases (N_2, synthetic dry air, and SF_6). The water content of N_2 and dry air was below $3\,ppm$, and the dew point of SF_6 was -27.7 °C at atmospheric pressure and 20 °C. Moreover, mixtures of dry and ambient humid air were used to obtain different water concentrations within the system.

Using this experimental device, *dark currents* can be characterized depending on the applied electric field, polarity, gas nature and pressure, HV electrode roughness, temperature,

and Relative Humidity (RH) within the gas. However, in this device, it was not possible to modify the gap distance, and use machined electrodes with a surface roughness relevant of GIS.

2.2.2 | Large scale plane-to-plane electrode system

This geometry allows obtaining an uniform electric field between electrodes. The experimental device is presented in figure 2.20 and figure 2.21.

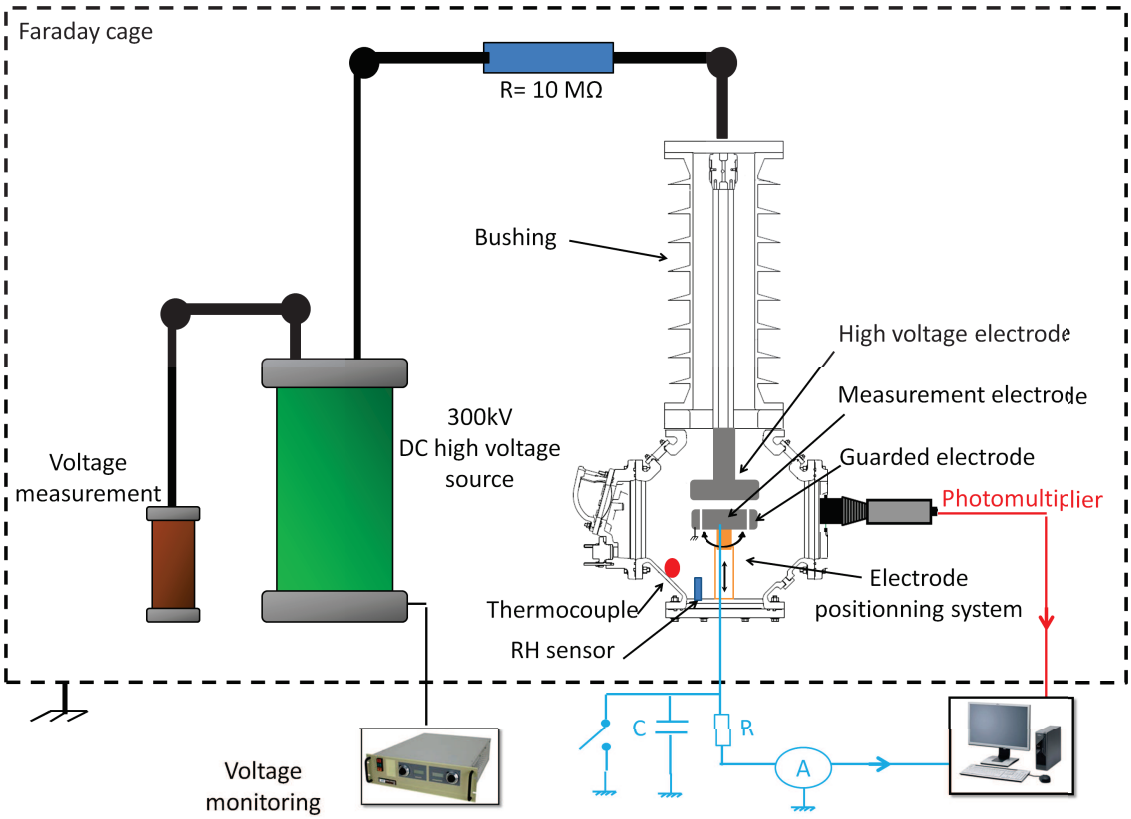

Fig. 2.20: Schema of the experimental test setup built for current measurement through gases under uniform electric field. Maximum voltage: $250\,kV$.

As for GIS, the setup is composed of an epoxy bushing and a metallic pressure-tight vessel. The vessel used for these experiments includes two specific covers, one containing a safety valve in case of burst, and the other includes a quartz window. The high voltage is applied through a conductor across the bushing, on which the HV aluminum electrode is fixed. The measurement electrode is composed of two concentric electrodes (figure 2.22). The inner electrode, with a diameter of $100\,mm$, allows measuring the current, while the outer guard electrode is linked to the ground. The distance between these electrodes is $0.2\,mm$. On the measurement electrode, a heating system realized using resistances (figure 2.22 (a) and (b)) allows controlling the temperature of the measurement electrode from $20\,°C$ up to $100\,°C$. The measurement electrode is insulated from the ground using

Fig. 2.21: Photograph of the experimental test setup corresponding to figure 2.20.

epoxy spacers. The temperature can be controlled from outside the Faraday cage, and is recorded using a thermocouple. A relative humidity sensor with an absolute precision of $\pm 0.8\%$ is placed within the vessel. The device can be filled with pressurized gases (up to $1\,MPa$). The setup withstands DC voltages up to $250\,kV$, generated by a Spellman $SLS360$ power supply which can deliver up to $\pm 360\,kV$ DC. A $10\,M\Omega$ resistance is set between the power supply and the test setup in order to limit the current in case of electrical breakdown and to reduce the high frequency noise of the supply. To adjust the parallelism of electrodes, we used a ball joint presented in figure 2.22 (c). As distance between electrodes can be controlled thanks to a manual positioning system, both HV and measuring electrodes are first set in contact to adjust parallelism.

This electrode system allows measuring *dark currents* with an uniform electric field $E = V/d$ (with V the applied voltage and d the gap distance). This current can be characterized depending on electric field, distance, and gas pressure. The quartz window present on one cover of the vessel allows to perform light emission measurements from electrodes using a photo-multiplier (figure 2.20).

The main advantages of this test setup are that the gap distance can be changed, the

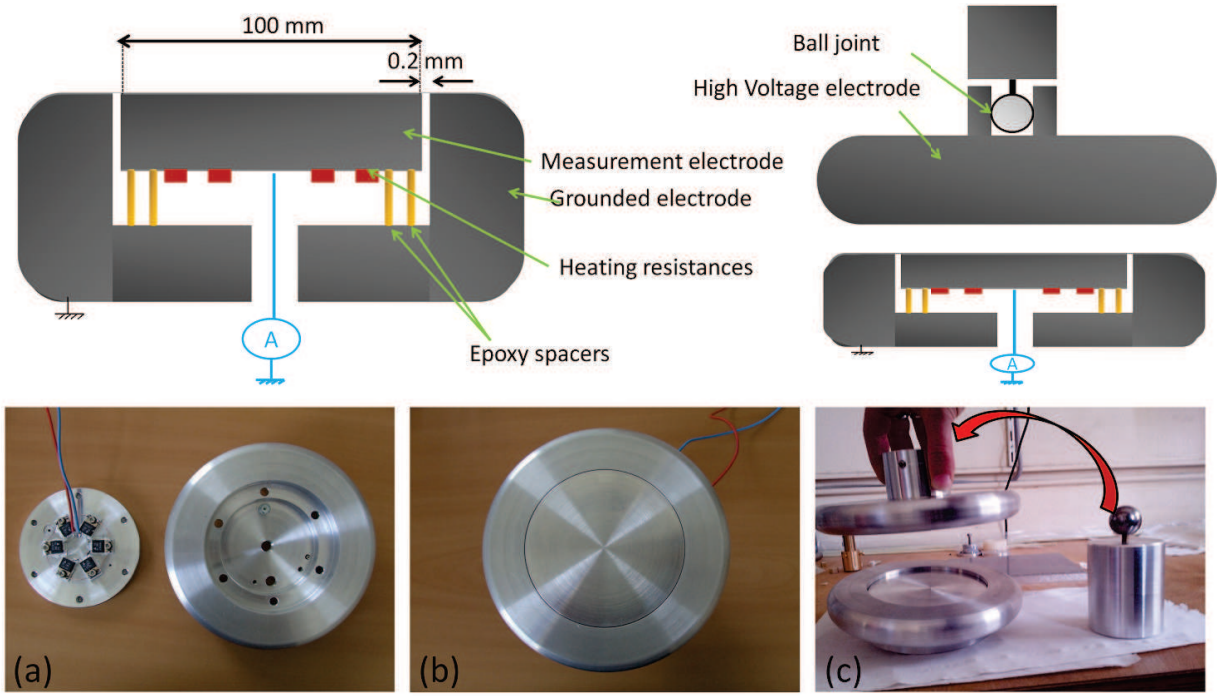

Fig. 2.22: Photographs of the electrodes system. (a) back-side and (b) front-side of the measurement electrode, (c) high voltage electrode system with the ball joint allowing a good parallelism.

electrode roughness can be adjusted using mechanical machining, electric fields similar or well superior to those present in GIS can be reached (between $1\,kV/mm$ and $25\,kV/mm$), and the temperature of one electrode can be controlled, reproducing the thermal gradient often present in *GIS* (high voltage electrode heated by the current while the grounded vessel is at ambient temperature). However, it was not possible to change the whole system temperature.

Using this experimental setup, we can investigate the influence of several experimental parameters on *dark currents*. We studied the influence of gas nature, pressure, applied voltage and polarity, surface roughness of electrodes, electrode temperature, and water content of the gas. Experimental protocols allowing to perform this study, are detailed in the next section.

2.2.3 | Experimental protocols

In this section, the electrode preparation and the test-cell conditioning are presented. In addition, external parameters investigated are defined.

2.2.3.1 Electrodes

Depending on the electrode system used (coaxial or plane to plane), the electrodes nature and processing were different. In the case of the coaxial system, the high voltage electrodes were made of aluminum alloy or brass with three different surface roughnesses. The first electrode (A) is not polished and remains at its «initial» surface state, the second (B) is polished in an acid bath, while the third electrode (C) is mechanically scratched using SiC sandpaper with grain size of $180\,\mu m$. The corresponding average roughness (Ra) is measured using a portable surface roughness tester *SURFTERT SJ-201M* (Mitutoyo American corporation). Table 2.1 summarizes the electrode's parameters.

High Voltage electrode	*Material*	*Polishing*	*Ra* [μm]
(A)	Brass – Aluminum	Initial	0.57
(B)	Brass – Aluminum	Chemical	1.2
(C)	Brass – Aluminum	Mechanical	2.2

Tab. 2.1: Parameters of high voltage electrodes used with the coaxial system.

After polishing, the electrodes were cleaned with ethanol and acetone before putting them in an ultrasonic bath of distilled water, to ensure that any traces of polishing material were removed from the surface. It shall be noted that this treatment did not follow a sophisticated cleaning procedure as recommended in the literature [10, 18], in order to reproduce similar conditioning as that used for *GIS*.

In the case of plane-to-plane system, electrodes used for measurements were made in aluminum alloy with an average roughness fixed to $Ra = 3\,\mu m$, in order to have comparable electrode surface than in the industrial application. Electrodes have been fabricated using dry machining (without oil) and were cleaned by ethanol, acetone and distilled water.

In both systems, following the electrodes preparation, the device mounting was performed to present as least particles as possible.

2.2.3.2 Test cell conditioning

Two different «conditioning» procedures of the test cell were used prior to filling with gases:

- A «standard procedure (C_1)» : the test cell, initially exposed to ambient air, is evacuated down to $10\,Pa$ for 15 min at room temperature;

- An «enhanced drying procedure (C_2)» : the test cell is evacuated down to $10\,Pa$ at $80\,°C$ for 30 min, then filled with dry air ($3\,ppm$ at atmospheric pressure), and evacuated again. This whole sequence was repeated 3 times until low RH were reached (between 1% to 5%).

Moreover, in the case of coaxial electrode system, before measurement, high negative voltage ($\sim -80\,kV$) was applied for about 30 min to make an «electrical conditioning» of the HV electrode, and obtain more stable currents. No electric field conditioning was performed in the plane-to-plane geometry in order to avoid any electrode evolution. For both systems, measurement versus electric field were performed by slowly increasing the voltage by steps. The maximum voltage value reached corresponds to 60 % of the Paschen's breakdown voltage for the considered gas and pressure, in order to avoid breakdown. For each step, the voltage remains constant until the measured current stabilizes. Depending on the experiments, the stabilization time varied from several minutes to more than one day. In the case of filling with SF_6, after each measurement, the gas was recovered in its initial bottle using a pre-compressor system.

Some experiments were done in dry gases (synthetic dry air and SF_6). However, commercial SF_6 available had in the best case, a dew point of $-40\,°C$ at atmospheric pressure (*i.e.*, $RH = 0.8\%$), which is higher than the water concentration of available synthetic dry air ($RH = 0.02\%$ at atmospheric pressure). To further dry SF_6, a drying system composed of a silica gel cartridge was placed between the gas bottle and the test cell. Thanks to this technique, SF_6 with RH down to 0.25% at ambient conditions was obtained (this corresponds to a dew point of $-50\,°C$ in ambient conditions).

For both electrode systems, the parameters investigated are listed in table 2.2.

	Coaxial Electrode System	*Plane to plane Electrode System*
Material	Brass – Aluminum	Aluminum
Electrode roughness	0.6 to $2.2\,\mu m$	$3\,\mu m$
Gas	SF_6 – Air	SF_6 – Air
Electric field	1 to $30\,kV/mm$	1 to $25\,kV/mm$
Gap distance	$5.5\,mm$	1 to $20\,mm$
Pressure	up to $1\,MPa$	up to $1\,MPa$
Temperature	Uniform (20 to 60 °C)	One electrode heated
Relative Humidity	×	×

Tab. 2.2: Summary of the experimental parameters investigated in both systems.

2.3 | Experimental results

2.3.1 | Preliminary experiments: coaxial system

This first series of experiments have been performed without relative humidity measurements. In this section, the current evolution is investigated for both polarities depending on electrode surface roughness and material nature, as well as nature and pressure of gases.

2.3.1.1 Measurements in SF_6

Influence of high voltage electrode roughness in negative and positive polarities

Using electrodes (A), (B) and (C), and standard conditioning procedure, current has been first measured depending on the electric field applied. Figure 2.23 shows a typical current recording versus time, for electrode (B) in SF_6. The pressure is fixed at $0.6\,MPa$ and the temperature is of $20\,°C$ during the whole experiment. For voltages below $20\,kV$ (*i.e.*, $E \leq 6\,kV/mm$) the measured currents are very low ($< 1\,pA$) and close to the noise level. For higher voltages, it is observed that the current strongly increases with voltage. After voltage application, currents tend to decrease until a stabilization value is reached. It is shown that the higher the voltage, the longer the stabilization time. At $40\,kV$ a stabilization time of $500\,s$ was sufficient to reach a stable value, while at $70\,kV$, the stabilized current is still not reached after $2000\,s$. The quoted current values in plots correspond to the average of 20 consecutive samples (corresponding to an effective time of $200\,s$), taken when the current has reached the stabilization.

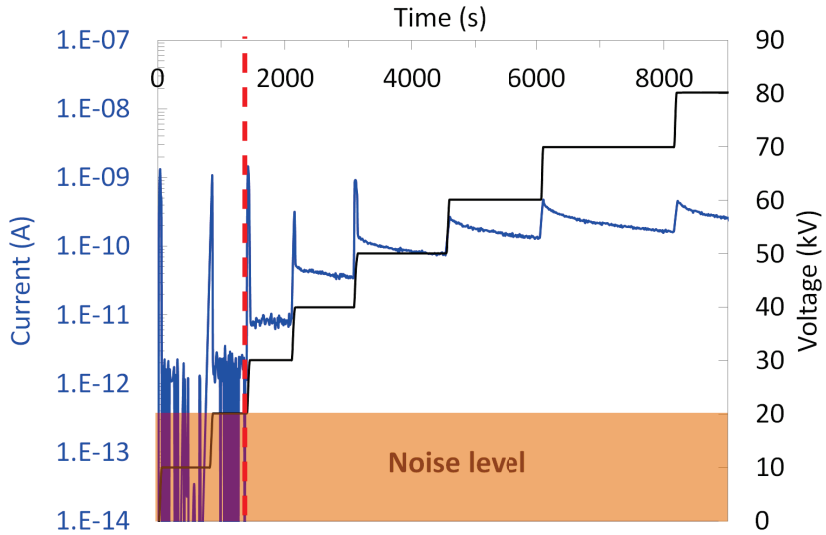

Fig. 2.23: Typical recording of currents versus time and electric field (positive polarity) with brass electrode (B) in SF_6 ($0.6\,MPa$, $20\,°C$).

Figure 2.24 shows stabilized currents for electric field from 2 to 30 kV/mm under 0.6 MPa of SF_6. Currents between 0.5 pA and 10 nA, are recorded in positive polarity. Those currents are strongly influenced by the surface roughness, with a two-decades difference between electrodes (A) and (C).

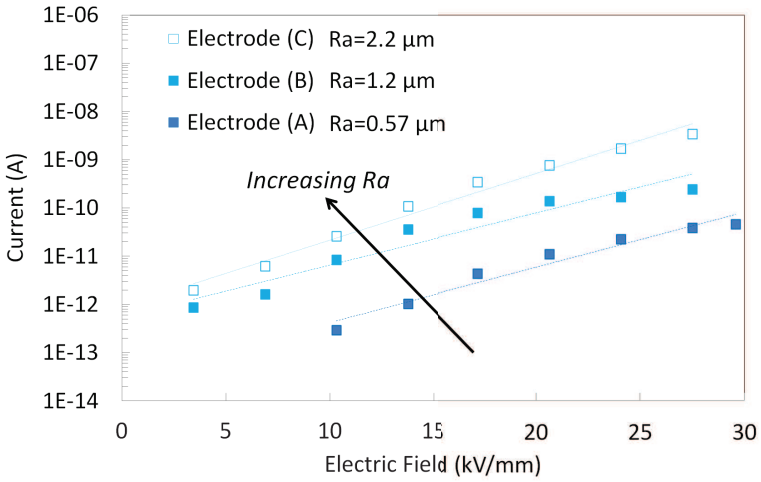

Fig. 2.24: Current measured in SF_6, versus electric field for three different electrode roughnesses (A), (B) and (C) in positive polarity, ($0.6\,MPa$, 20 °C, calculated $RH = 12\%$).

It is observed that for electrode (B), measured roughness is higher than for an «initial» electrode (A), and that the measured current is also well-superior (more than a decade). These measurements show an exponential increase of the current depending on the electric field.

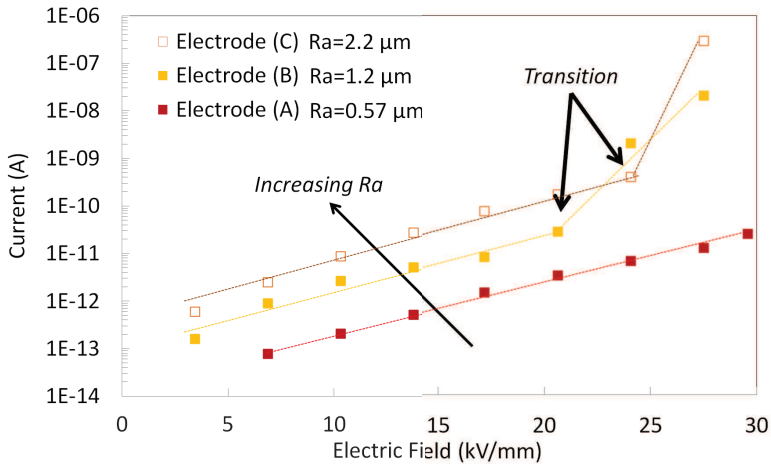

Fig. 2.25: Current measured in SF_6, versus electric field for three different electrode roughnesses (A), (B) and (C) in negative polarity, ($0.6\,MPa$, 20 °C, calculated $RH = 12\%$).

Using same electrodes and conditions, the current has also been measured in negative polarity (figure 2.25). It is observed that for electrodes (B) and (C) the current dramatically increases above $20\,kV/mm$. This phenomenon has been named «transition» in figure 2.25. Below the transition, currents increase exponentially versus electric field and show a similar trend as in positive polarity. In both cases, with electrode B and C, significant currents can be already measured at low electric field ($3\,kV/mm$), *i.e.,* in conditions relevant to HVDC GIS.

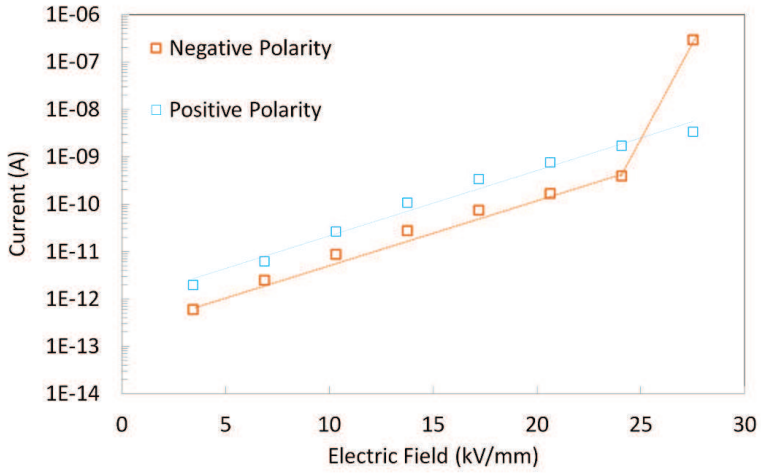

Fig. 2.26: Comparison of measured current in positive and negative polarity in SF_6, in case of electrode (C) ($0.6\,MPa$, $20\,°C$, calculated $RH = 12\%$).

A comparison between measured current in positive and negative polarity is presented in figure 2.26. Measured currents follow a similar trend in both polarities for electric field below $25\,kV/mm$. It can be noted that in same electric field range, the measured currents are slighlty higher for positive polarity than negative polarity. For electric field superior than $25\,kV/mm$, the currents in positive polarity follow the same trend, without the transition observed in negative polarity.

Influence of SF_6 pressure, in negative and positive polarities

The influence of pressure on measured currents in negative polarity with electrode (C) and with a standard conditioning procedure, is presented in figure 2.27 (a). An increase of current with pressure can be noted (approximately a decade difference between $0.6\,MPa$ and $0.8\,MPa$).

However, figure 2.27 (b) shows the poor reproducibility of consecutive measurements in identical conditions in this polarity. The threshold voltage at which the transition occurs, varies for each measurement. No clear tendency of the threshold voltage variation versus pressure is seen during consecutive measurements.

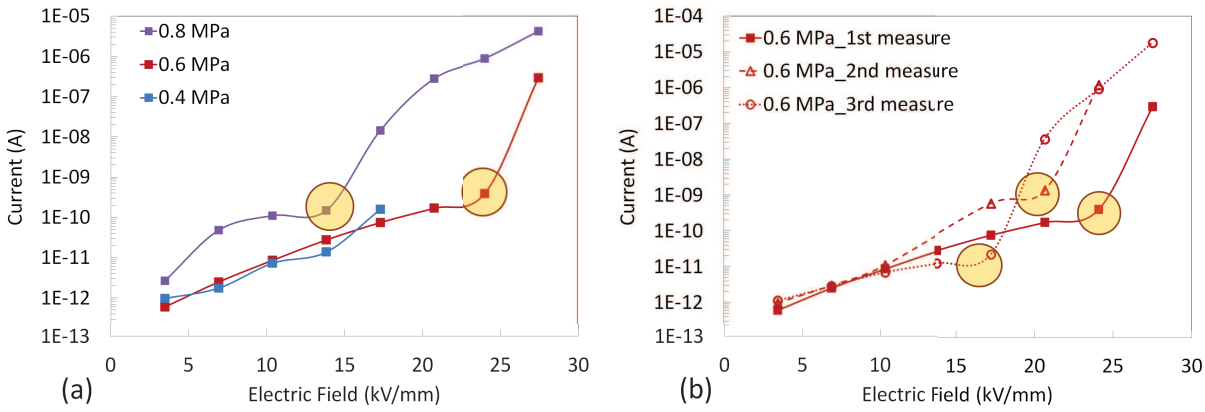

Fig. 2.27: (a) Current measurements in negative polarity depending on electric field with electrode (C) for various pressures. (b) Reproducibility of measurements with $0.6\,MPa$ of SF_6.

Similar experiments were done in positive polarity in the same conditions. In this polarity, currents show a much better reproducibility and stability in all conditions. To investigate the influence of pressure, the voltage was fixed to $50\,kV$ and maintained during the whole experiment, while the pressure was changed. Figure 2.28 (a) shows the recording of current with electrode (C) versus time when pressure is varied from $1.1\,MPa$ down to $0.3\,MPa$, and increased again by filling up to $1.1\,MPa$. Stable currents are measured. Figure 2.28 (b) presents the evolution of current depending on pressure. It can be observed that similar current are measured for both increasing and decreasing pressures. For increasing pressure the current is slightly higher than the one obtained during the pressure decrease. In this experiment, the current is rapidly stabilized (after about $500\,s$) when pressure is changed.

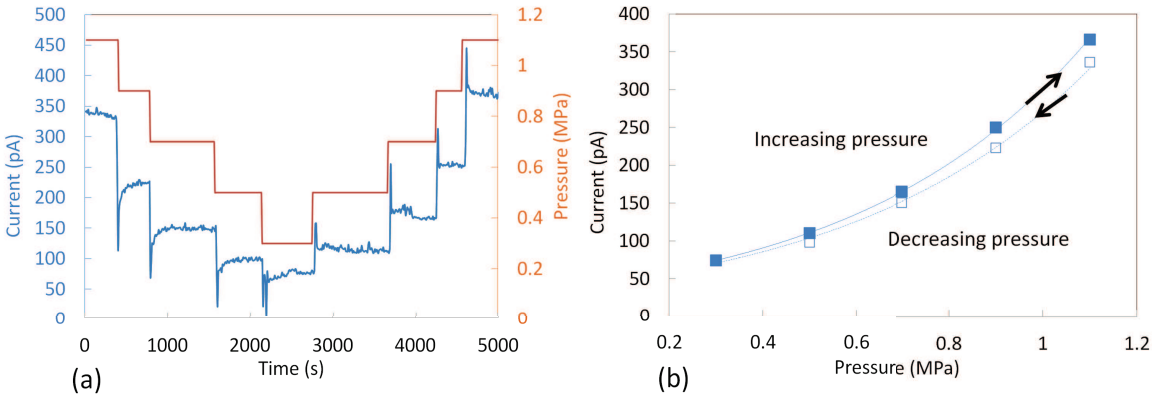

Fig. 2.28: (a),Typical recording of current versus time and pressure in SF_6 with brass electrode (C), at $V = 50\,kV$. And (b), Current measured versus pressure with brass electrode (C) in SF_6 at $V = 50\,kV$.

2.3.1.2 Comments

With the coaxial geometry, *dark currents* are observed for both positive and negative polarities. The amplitude of these currents are between $10^{-13}\,A$ and $10^{-6}\,A$ depending on the electric field and electrode surface roughness. This current increases exponentially with the electric field and does not reach a saturation value. The measured currents are too high to be explained by the ionization phenomenon. Indeed, considering only this phenomenon in a volume of $18\,cm^3$ and with a typical production rate of about 10 ion pairs/$cm^3.s$, a saturated current of $2.9.10^{-17}\,A$ should be measured, which is totally different from the results obtained. A production rate of 3.10^5 pairs $/cm^3.s$ would be necessary to obtain currents of $1\,pA$, which is an unrealistic value for the production rate.

Besides, it can be observed in figure 2.29 that $ln(I/E^2)$ does not vary linearly as a function of $1/E$ for electrodes (A), (B) and (C). This was also observed by Shibuya *et. al* in their *dark current* measurements under uniform electric field [23]. It clearly shows that the mechanism of FN emission can not be used to explain the values of the currents experimentally observed.

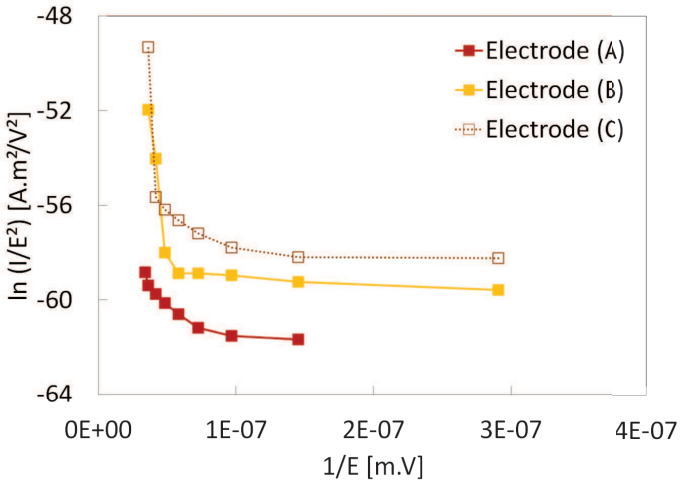

Fig. 2.29: *Fowler-Nordheim* plots of measured current with different roughnesses in negative polarity ($0.6\,MPa$ of SF_6, $20\,°C$).

Moreover, currents slightly higher are measured in positive polarity (figure 2.26). In order to better understand the origin of these currents, we assume that both inner and outer electrodes contribute to the generation of the *dark current*. Indeed, even if the electric field on the outer electrode is smaller than on the inner electrode, its surface is three times higher. It is then reasonable to assume that both electrodes can contribute to the measured current.

As observed in experiments, the total current increases following an exponential-law versus the electric field (equation 2.8).

$$I = I_0.exp^{(\alpha E)} \tag{2.8}$$

When negative polarity is applied to the inner electrode, the current is written as,

$$I^- = s.j_0^-.exp^{(\alpha E_{int})} + S.j_0^+.exp^{(\alpha E_{ext})} \tag{2.9}$$

with s and S the emission surfaces of the inner and outer electrodes, j_0^- the current density, E_{int} the electric field on the inner electrode, E_{ext} the electric field on the outer electrode. $\alpha = 0.2$ was obtained from measurements.

When positive polarity is applied to the inner electrode, the current can be written as,

$$I^+ = s.j_0^+.exp^{(\alpha E_{int})} + S.j_0^-.exp^{(\alpha E_{ext})} \tag{2.10}$$

If we assume that measured currents are only emitted from the negative electrode in both cases, the equations (2.9) and (2.10) can be simplified:

$$I^- = s.j_0^-.exp^{(\alpha E_{int})} \tag{2.11}$$

$$I^+ = S.j_0^-.exp^{(\alpha E_{ext})} \tag{2.12}$$

Two different experimental conditions have been used:

- 1^{st}: The inner and outer electrodes present the same roughness ($0.57\,\mu m$).

- 2^{nd}: The inner electrode roughness equals to $2.2\,\mu m$ while the outer electrode roughness equals to $0.57\,\mu m$.

In the 1^{st} case, a current density $j_0^- = 2.8.10^{-15}\,A/cm^2$ is obtained from equation (2.11) (negative polarity applied to the inner electrode). This value can be used to calculate the current emitted by the negative outer electrode when a positive polarity is applied to the inner electrode. The calculated current I^+_{calc} equals to $4.10^{-13}\,A$, which is ten times lower than the measured value ($I^+_{mes} = 4.3.10^{-12}\,A$).

In the 2^{nd} case, we obtain $I^+_{calc} = 4.3.10^{-13}\,A$ which is well inferior to the measured value $I^+_{mes} = 3.4.10^{-10}\,A$. Those calculations confirms that the measured current is mainly emitted from the inner electrode in both polarities and not only by the negative electrode. It also shows that the maximum contribution of the outer electrode constitute approximately 10% of the measured current when roughnesses are equals.

It has also been observed that the current increases with pressure. This strongly suggests that corona discharges (that may occur from protrusions on the high voltage electrode)

can not be considered to explain the measured current. However, this mechanism could be considered to explain the transition observed at high electric field in negative polarity.

Based on these first results, it is reasonable to assume that neither the natural ionization nor the *Fowler-Nordheim* emission can be used to explain our experimental observations. In addition, other parameters such as the electrode surface roughness and current stabilization time can provide further indications. The measured current strongly increases with the electrode surface roughness, suggesting a mechanism of charge injection from the high field electrode. A nearly exponential increase of the current versus electric field was also observed in Shibuya's experiments (figure 2.7). Our measurements carried out with a much better sensitivity (down to $10^{-13}\,A$) show that this tendency is still observed at much lower electric fields (down to $3\,kV/mm$).

In order to further identify the possible mechanisms responsible for the measured currents, we will study in the following, the influence of gas nature on the measured *dark currents*.

2.3.1.3 Experiments in air and influence of water

Influence of different types of air

Figure 2.30 presents measurements obtained in positive polarity with brass electrode (C), using the standard procedure before filling with air at $1\,MPa$. In air, the maximum electric field at $1\,MPa$ was limited to $15\,kV/mm$ to avoid breakdowns. Different types of air were used:

- Dry synthetic air (water content $< 3ppm$)

- Ambient air (20 °C \ 54% RH) compressed to $1\,MPa$

- Mixture 1 : $0.1\,MPa$ ambient air + $0.9\,MPa$ dry air

- Mixture 2 : $0.01\,MPa$ ambient air + $0.99\,MPa$ dry air

A considerable difference was first observed between synthetic air and compressed ambient air. These experiments immediately suggested that the water content could be of great importance for current measurements. With compressed ambient air, RH far exceeds 100 %, *i.e.,* water condensates in the test cell, producing a considerable increase of current (4 decades at $20\,kV$). To check this hypothesis, air mixtures with $RH < 100\%$ were investigated. Table 2.3 shows the relative and absolute humidity (calculated with the Vaisala calculator from initial gas properties) present in air at $1\,MPa$, in SF_6 at $0.8\,MPa$ (with a dew point of $-27.7\,$°C at atmospheric pressure), and in air mixtures.

The **relative humidity** corresponds to the ratio of the partial pressure of the water vapor in the air, to the saturated vapor pressure, at the considered temperature (2.13). RH

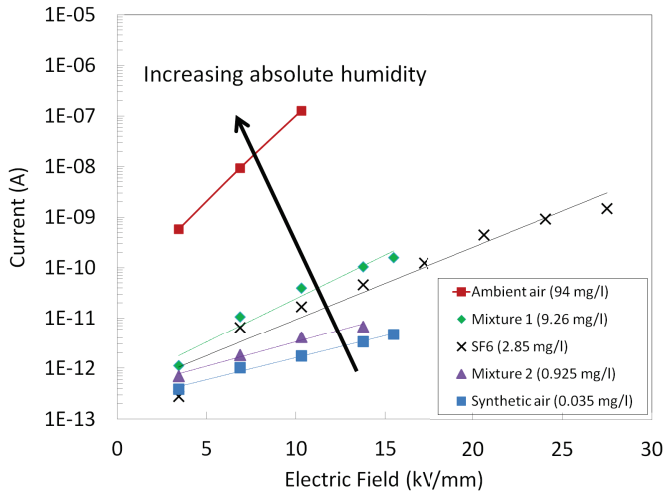

Fig. 2.30: Current measurements in positive polarity for different types of air at $1\,MPa$, with brass electrode (C), versus electric field, and comparison with results obtained in SF_6.

	RH [%]	*Absolute Humidity [mg/l]*
Dry synthetic air	< 0.2	0.035
Compressed Ambient air	540	94
Air Mixture 1	52	9.26
Air Mixture 2	5.2	0.925
SF_6 $(0.8\,MPa)$	16.5	2.85

Tab. 2.3: Calculated relative humidity and absolute water content of the gas studied at $1\,MPa$, 20 °C.

depends on the temperature and pressure of the gas.

$$Relative Humidity\,(RH) = \frac{Partial\,Vapor\,Pressure}{Saturation\,Vapor\,Pressure} \times 100\,\% \tag{2.13}$$

The **Partial vapor pressure** is a measurement of the amount of water vapor in a gas volume. In a closed enclosure, the process of evaporation will continue until there are as many molecules returning to the liquid as there are escaping. At this stage, the vapor is defined to be saturated (**Saturated Vapor Pressure**). At higher temperature, as the molecular kinetic energy is greater, more molecules can escape from the surface, resulting in a higher saturated vapor pressure

The **dew point** is also associated to the relative humidity. It corresponds to the temperature at which the water vapor in the gas condenses into liquid phase. For temperatures lower than the dew point, water will leave the gas and condense on solid surfaces. This condensed water is called «dew». In appendix A, a curve representing the water vapor

pressure versus dew point is given [36].

On figure 2.30, an influence of water on currents is still seen at low water content (down to $RH = 5.2\,\%$ in mixture 2), far from condensation conditions (Table 2.3). The comparison of the different air types shows that current increases when RH is increased. At high RH (compressed ambient air and mixture 1), a long «conditioning » sequence (several hours) was necessary before stabilization of the current. During conditioning, a slow decrease of current was observed. This effect was much reduced with dry gases, which rapidly provided stable current.

On figure 2.30, measurements obtained in SF_6 in identical conditions (same electrode) at $0.8\,MPa$ are also plotted for comparison. With a dew point of $-27.7\,°C$ at $0.1\,MPa$ (i.e., SF_6 of acceptable technical quality in GIS), the calculated relative humidity raises to $RH = 16.5\,\%$ when the gas is compressed to $0.8\,MPa$ at $20\,°C$. It is interesting to observe that recorded currents agree with those measured in humid air, between mixture 2 ($RH = 5.2\,\%$) and mixture 1 ($RH = 52\,\%$).

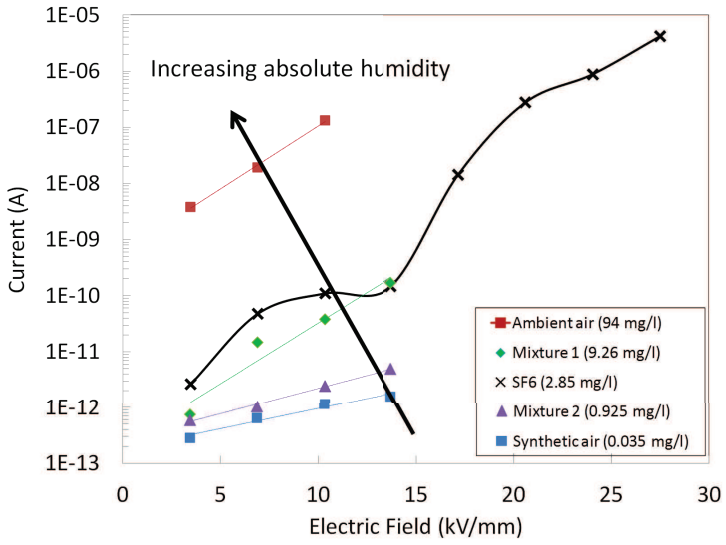

Fig. 2.31: Current measurements in negative polarity versus electric field strength with electrode (C) for various gas mixtures.

Same measurements were done in negative polarity. Figure 2.31 shows the current measured for different air mixtures and SF_6. Approximately same currents as measured for positive polarity are seen for electric field lower than $14\,kV/mm$ in air mixtures. The influence of water is also noted for negative polarity in air. In case of SF_6, currents are higher than for the 10 % air mixture while its absolute humidity is lower. This observation can be explained by the poor reproducibility of measurements in SF_6 in negative polarity. In addition, we can note that the transition observed in SF_6 is not observed for the various

air mixtures. Since this transition is seen in SF_6 for electric field higher than $15\,kV/mm$, this may explain that the latter is not seen in air (the maximum electric field in air is $E \leq 15\,kV/mm$ to avoid breakdown).

Comments: influence of relative humidity

These experiments performed in air point out the very large influence of the water concentration of the gas used. This influence is considerable when condensation is present, but it is still clearly observed at low RH (5%). This influence of water was never reported before in the few studies dealing with *dark currents* in pressurized gases. Measurements carried out with the commercial grade SF_6 available (dew point of $-27.7\,°C$ at atmospheric pressure) are compared with those obtained in air. This suggests that the gas nature may not have a large impact on measured *dark currents*. The influence of pressure (figure 2.28) can also be due to the influence of water (the higher the pressure, the higher the water content and RH). In the few papers dealing with *dark currents* in SF_6, no indication on the gas water content was given. The presence of water could have a very large influence in practical GIS, and its influence will be further studied in next sections 2.3.2 and 2.3.3.

2.3.1.4 Influence of high voltage electrode nature in positive polarity, for different pressures

Further experiments have been performed to investigate whether the material used as the HV electrode had an influence on the measured current. Figure 2.32 (a) and (b) shows the *dark current* evolution for brass and aluminum electrodes (C). Measurements were performed in SF_6 (with a dew point of $-27.7\,°C$) for different pressures.

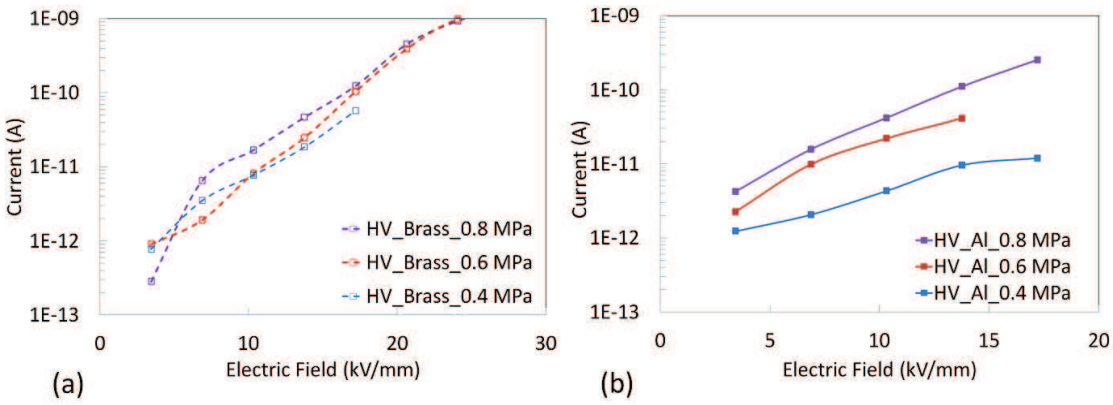

Fig. 2.32: Current measurement in positive polarity in SF_6 for both brass (a), and aluminum (b) HV electrode, depending on the pressure within the enclosure.

Prior to filling, the standard procedure was used. In these conditions, currents between $1\,pA$ and $1\,nA$ are measured in both cases for electric field between 2 to $25\,kV/mm$. It is

observed that the current measured for a HV aluminum electrode is slightly inferior than for brass electrode. Moreover, the influence observed with pressure is more pronounced in the case of aluminum.

Additional measurements were performed for both electrodes natures in three mixtures of air presented in Table 2.3. These measurements, shown in figure 2.33, evidence that when the absolute humidity increases within the enclosure, the current measured significantly increases in the case of a brass HV cathode. On the contrary, only slight variations on the current are observed in the case of a HV aluminum. This suggests that the aluminum is less sensitive to variations in the humidity. In all gases (SF_6 or air mixtures) the current measured is higher for a brass HV electrode.

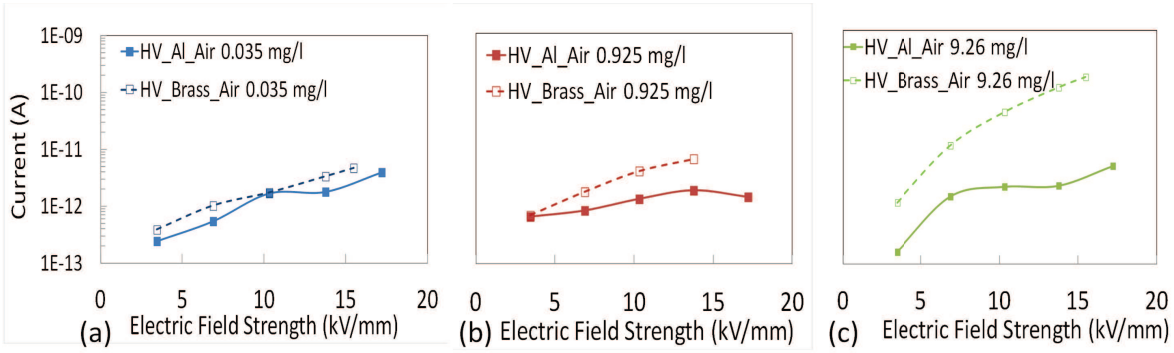

Fig. 2.33: Comparison of current measurements obtained for brass and aluminum electrodes in air mixtures (a) $0.035\,mg/l$, (b) $0.925\,mg/l$ and (c) $9.26\,mg/l$.

The presence of an oxide layer on the electrode may explain the difference in the measured currents. Actually, the aluminum superficially oxidizes, creating a thin oxide layer on the surface metal. Assuming that the measured current depends on the amount of water adsorbed on the electrode surface, as the oxide layer constitutes a barrier to the water molecules, the measured current would be lower than in the case of brass. Such mechanisms require to be further investigated through additional experiments.

In next sections, current measurements were performed using only the brass material in order to keep the same material for the anode and the cathode.

2.3.2 | Discrepancies between calculated and measured RH, and influence on the current

In the following measurements, a RH sensor was implemented in the enclosure, allowing to record its variations during the whole experiment. In many cases, discrepancies (sometimes very large) were observed between measured RH and values calculated from the initial gas properties. These experiments highlighted the large influence of the initial test cell conditioning.

2.3.2.1 Example 1: Measurements in SF_6 versus pressure

Dark currents and RH values were recorded versus pressure in SF_6 with standard cell conditioning, for positive polarity with a fixed voltage ($50\,kV$). The same experiment as in figure 2.28 is repeated. The test cell was first filled at $1.1\,MPa$, then, the pressure was reduced by steps down to $0.3\,MPa$, and increased again by filling up to $1.1\,MPa$. The black arrows in figure 2.34 (a) show the directions of pressure variations applied during the experiments. At each step, a long recording time was allowed (up to one hour), up to complete stabilization of both RH and measured current.

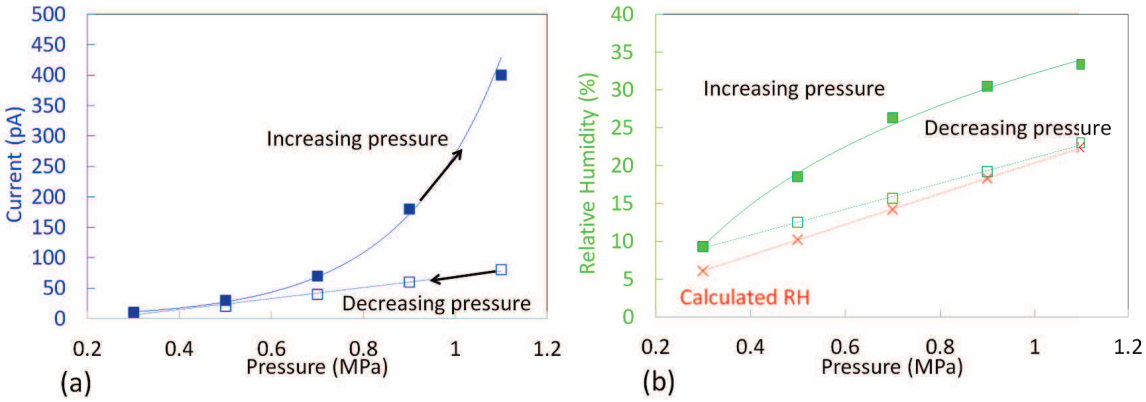

Fig. 2.34: (a) Current measurements performed with brass electrode (C) in SF_6, versus pressure ($50\,kV$, $20\,°C$). (b), RH measurements performed in SF_6, versus pressure, corresponding to (a).

Figure 2.34 (a) shows the evolution of current for decreasing and increasing pressure. It can be observed that the current increases versus pressure but following two very different trends. A slight decrease of current was first observed while decreasing pressure (from $80\,pA$ to $10\,pA$), followed by a large increase (up to $450\,pA$) when pressure was raised again to $1.1\,MPa$. This unexpected lack of reproducibility completely differs from the similar experiment presented above in figure 2.28 (b). This is also correlated to the different stabilization time observed, respectively of $500\,s$ for the preliminary experiment, and between 2000 and $3000\,s$ for this experiment. It clearly evidences that the study of the pressure alone is not sufficient to describe the *dark current* variations.

Figure 2.34 (b) shows the variations of the RH values measured while decreasing and increasing pressure. As for current evolution, two different trends are observed: higher RH values are recorded while pressure was increased again. We have added on this figure the theoretical RH values, calculated with the *Vaisala calculator* [36], from the initial gas properties (*i.e.,* dew point of $-27.7\,°C$ at atmospheric pressure, corresponding to $RH = 2.7\%$). Theoretical values roughly agree with those recorded while decreasing pressure. However, higher values of RH were observed while increasing pressure (32% instead of 22% at the end of the experiment). As we will discuss in the next sections,

the higher values of RH recorded while increasing again pressure are certainly due to the influence of water adsorbed on surfaces.

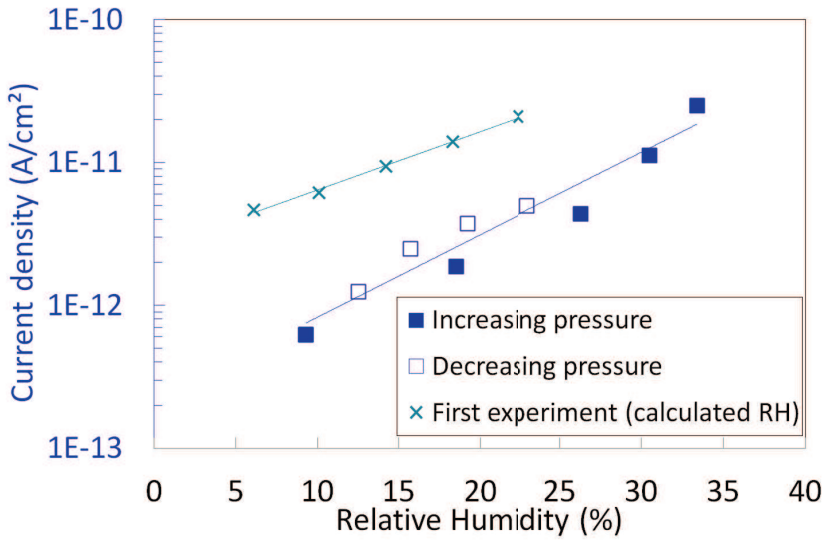

Fig. 2.35: Current measurements performed with brass electrode (C) in SF_6, versus relative humidity ($50\,kV$, $20\,°C$) with calculated and measured RH values.

The measured current as a function of RH is plotted in figure 2.35 for both measurements, increasing and decreasing pressure. These current values are compared to those obtained from the preliminary measurements (figure 2.28) in which the RH values have been calculated from the gas properties.

It can be observed that when RH measurements are performed (squares), the measured currents versus RH group together. In addition, measured RH values are lower to those calculated in case of the first experiment, showing that RH values must be measured and not only calculated from the gas properties. Besides, the current varies with RH following an exponential-law. These results clearly show that RH is an adequate parameter to describe the current measured through the gas. Furthermore, for an identical value of RH at different pressures, the same current is measured. For two different pressures (0.7 and $1\,MPa$), an identical RH value of approximately 24% and a current of around $70\,pA$ were recorded during the increase and decrease of pressure. This shows that the variations of the measured current when pressure is changed can mainly be attributed to an indirect effect (*i.e.*, variations of RH due to the pressure change), and not to the direct influence of the gas pressure. The comparison with the first measurement of figure 2.28 shows that the calculated RH was probably under-estimated compared to the actual RH in the test cell, such as in figure 2.34. Since the current varies exponentially versus RH, a small difference in RH (32% instead of 22%) induces a large difference on the current ($450\,pA$ instead of $80\,pA$).

2.3.2.2 Example 2: Measurement in air mixtures with temperature variations

Since the measured current strongly depends on the RH, and since the latter varies with the temperature (see appendix B), it is interesting to investigate the influence of the temperature on the current. A typical experiment in air with three successive steps (Table 2.4) is presented in the following. At each steps, the relative humidity has been recorded for temperatures from 10 °C up to 60 °C. We shall note that during the experiment, the device is hermetically closed. Thus, the total amount of water is fixed. It includes initial water present in the enclosure (adsorbed on electrodes and onto the bushing surfaces and its volume) as well as the initial water present within the gas.

Step	*Conditions*	*Ambiant air* $[MPa]$	*Dry air* $[MPa]$	RH_{Th}
1	Enhanced drying procedure	0	1	$< 0.2\%$
2	Evacuated to $10\,Pa$	0.1	0.9	40%
3	Evacuated to $10\,Pa$	0.3	0.7	$> 100\%$

Tab. 2.4: Summary of the experimental conditions, describing parameters applied to each experimental step, RH_{Th} corresponding to theoretical calculated value of RH.

Step 1: Dry air and thoroughly dried cell

Figure 2.36 presents the evolution of measured relative humidity depending on temperature, for a fixed pressure of $1\,MPa$, and a comparison with calculated RH.

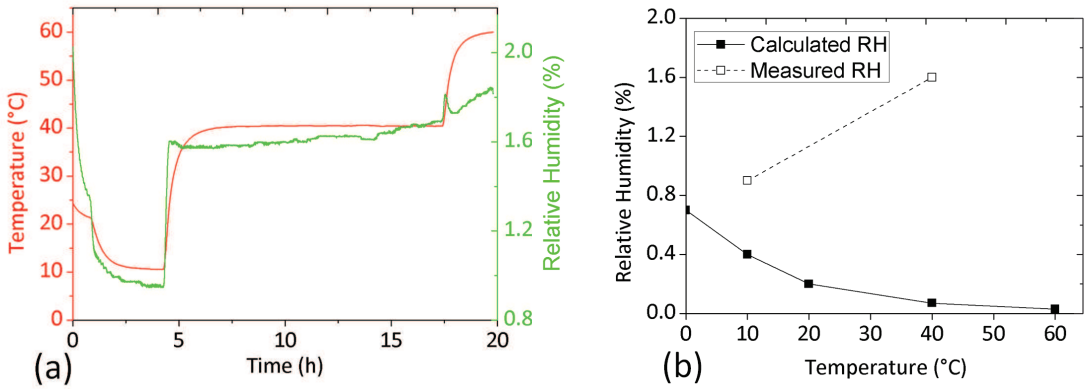

Fig. 2.36: (a) Relative Humidity and temperature time-evolution,(b) measured RH compared to theoretical RH_{Th} in step 1.

Figure 2.36 (a) shows a typical recording of relative humidity and temperature versus time in step 1. A comparison of the measured and theoretical RH based on initial gas specifications, is presented in figure 2.36 (b). It can be observed that the measured RH is

higher than theoretical values. Contrary to calculations, the measured relative humidity in the gas increases with the temperature. However, measured values are quite close to the absolute RH sensor precision (0.8%), and a large uncertainty of measurements can be expected.

It is worth noting that for such low values of relative humidities ($< 2\%$), there were no measurable currents (currents lower than the measurement noise, approximately $0.1\,pA$).

Step 2: Humid air introduced in a dried cell

In figure 2.37 (a), it is observed that in step 2 (corresponding to a higher calculated $RH = 40\%$ obtained by introducing a fraction of ambient air in the dried test cell), the relative humidity now decreases with increasing temperatures, showing a similar trend as theoretical values (figure 2.37 (b)). However, measured RH values are much lower than that calculated. At 20 °C the measured RH equals to 11% instead of 40%.

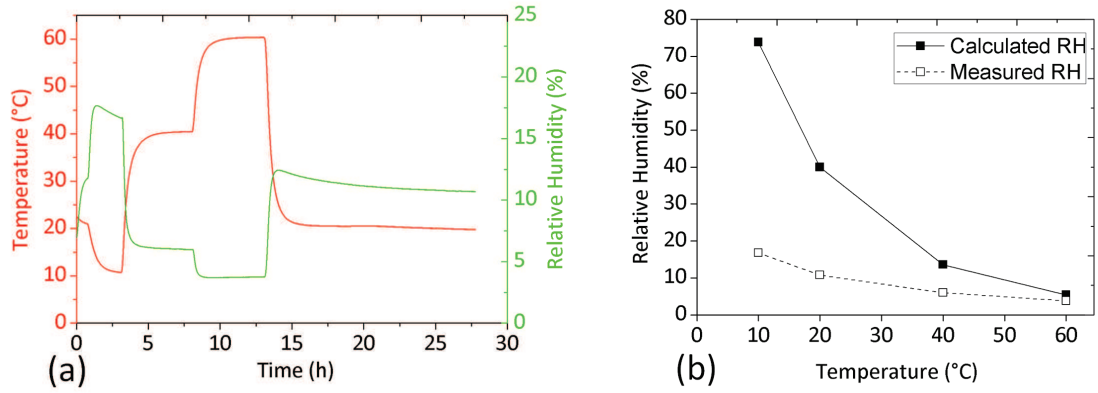

Fig. 2.37: (a) Relative humidity and temperature time-evolution, (b) measured RH compared to theoretical RH_{Th} in step 2.

Step 3: Humid air introduced in a humid cell

Further experiments in step 3 were performed with an increased water content, in order to measure *dark currents* versus temperature over a wider RH range (measured values from 10% to 60%, figure 2.38 (a) and (b)). Despite the air mixture should exceed a theoretical RH of 100% (at room temperature), the maximum measured values remained below $RH = 60\%$.

It is observed that the measured current decreases when temperature is raised. Again, the measured current is strongly related to the RH variations (as seen in figure 2.39). For each temperature step, measurements lasted approximately 5 hours in order to reach a pseudo-stabilization of the RH in time.

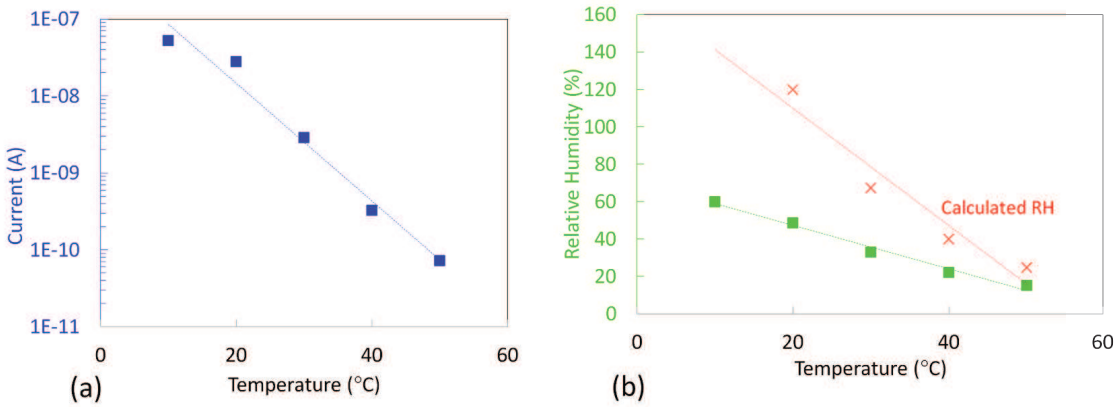

Fig. 2.38: (a) Current measurements in air versus temperature and (b) RH measurements versus temperature compared to theoretical values, in step 3, at $35\,kV$.

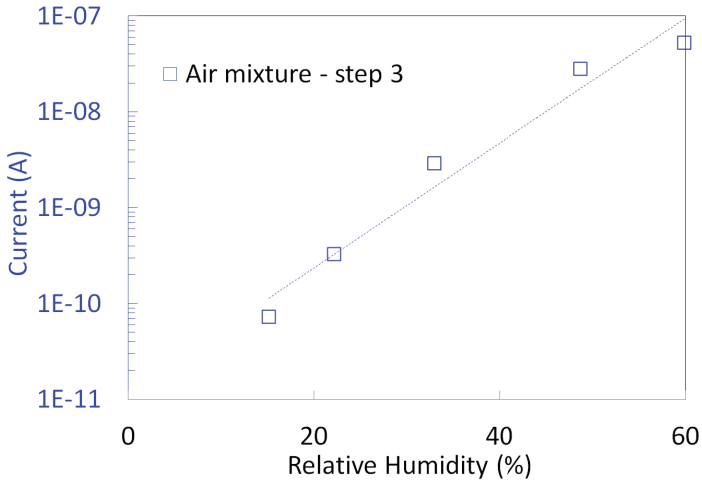

Fig. 2.39: Current measurements performed with electrode (C) in step 3, versus relative humidity, at $35\,kV$.

2.3.2.3 Discussion: The crucial influence of test cell conditioning

These three steps illustrate the fact that it is experimentally very difficult to obtain a good quantitative control of the actual water content in a closed system. Depending on the initial conditioning of the system (test cell previously dried or not), the actual measured RH can be either lower, or larger than calculated ones, and the variations of RH with temperature can be different.

With a dried test cell and a very dry gas (step 1) the measured RH was higher than the theoretical one (although the measurement had a large uncertainty). To explain this phenomenon, it is assumed that when temperature is increased, remaining water adsorbed on surfaces within the device is desorbed within the gas, increasing RH. The comparison between calculations and measurements on RH (figure 2.36 (b)) clearly shows that initially,

RH measured is higher than specification. It increases with temperature instead of decreasing. Indeed, calculations do not take into account the equilibrium of water between surfaces and gas.

In step 2 and 3, when a humid gas is introduced within the dry test cell, the measured RH decreases versus temperature as expected. However, the large difference between the measured and theoretical RH shows that some water initially contained in the gas was adsorbed on dry surfaces.

These observations show that the actual measured RH in this closed system depends on the equilibrium between water adsorbed on surfaces, and in the gas phase above the surface. Depending on the initial surface and gas conditions, water can be transferred either from surfaces to the gas or conversely. In most cases, the measured RH does not corresponds to calculations carried out by neglecting the influence of surfaces. A quantitative prediction of these effects remains very difficult since different materials are present in the test cell, with many unknown parameters.

The examples presented above were obtained with a PTFE high voltage bushing. Many other experiments carried out with an epoxy bushing showed that it was nearly impossible to get stabilized values of RH, especially at high temperature. Since epoxy is a hydrophilic material (it can absorb up to about 1% of water), the bushing could absorb or release large quantities of water in the gas, depending on conditions.

Since GIS also include large surfaces of epoxy insulators in contact with gas, similar effects can also occur. Changing the epoxy bushing to a PTFE bushing provided a better stability of RH since the latter is highly hydrophobic.

When a parameter is changed (temperature, pressure, RH), the equilibrium of water between surfaces and gas volume is modified. It is usually necessary to wait a long time (up to several hours) to reach a new steady state (controlled by the stabilization of the measured gas RH).

Those results evidence the large influence of the device conditioning and structure on the relative humidity evolution with temperature.

For all cases, the measured RH always differs from the expected one, and this explains the large scatter of experiments carried out without RH measurements. In order to perform as reproducible experiments as possible, the device conditioning must be controlled as far as possible. To minimize the effects due to equilibrium between gas and surface, the test cells were first thoroughly dried to obtain low RH. Conversely, to carry out experiments at high RH, the test cells were first humidified by filling with humid air for a long time (about one day).

2.3.2.4 Influence of temperature in SF_6

Additional experiments have been performed to investigate the influence of temperature in SF_6. Those measurements have been performed for two SF_6 water contents ($RH = 13\%$ and 38% at 20 °C and $0.6\,MPa$). Figure 2.40 shows the currents variations in case of $RH = 13\%$ at 20 °C. Two main results are highlighted. First, it can be observed that when temperature is raised, the measured RH logically decreases (from 13% at 20 °C to 6% at 60 °C). Secondly, it is observed that the current increases with temperature (it is multiplied by about 2.5 between 20 °C and 60 °C).

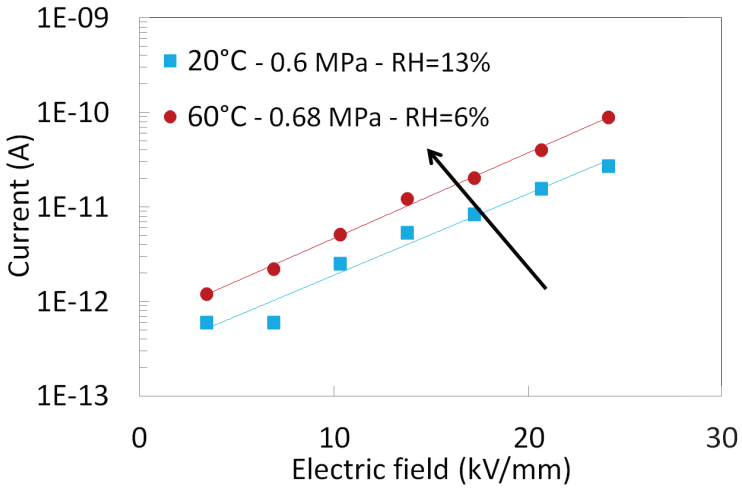

Fig. 2.40: Current variations in case of SF_6 with $RH = 13\%$ at 20 °C and $0.6\,MPa$, with increasing temperatures.

Similar experiments are presented in figure 2.41, with SF_6 containing more water (38% at 20 °C and $0.6\,MPa$). It is now observed that currents decrease when temperature is raised from 20 °C to 60 °C, with more than one decade difference. The measured RH logically decreases when temperature is raised. In this case, the current increases when RH is higher.

Such results evidence the complex influence of temperature. In case of «humid» SF_6 (38% at 20 °C and $0.6\,MPa$, *i.e.,* corresponding to a dew point of −18 °C at atmospheric pressure), the variation versus temperature is in qualitative agreement with previous measurements: the current shows a large increase (one decade), correlated to a large increase of RH (a factor of 3). In the case of a drier SF_6 (corresponding to a dew point of −30 °C at atmospheric pressure), the variation of the current is reversed and much lower. This could be explained by considering that the temperature may have two contradictory influences:

- an indirect effect: it reduces RH, and hence the current;

- a direct effect on the charge emission process: increasing temperature may enhance the charge emission process.

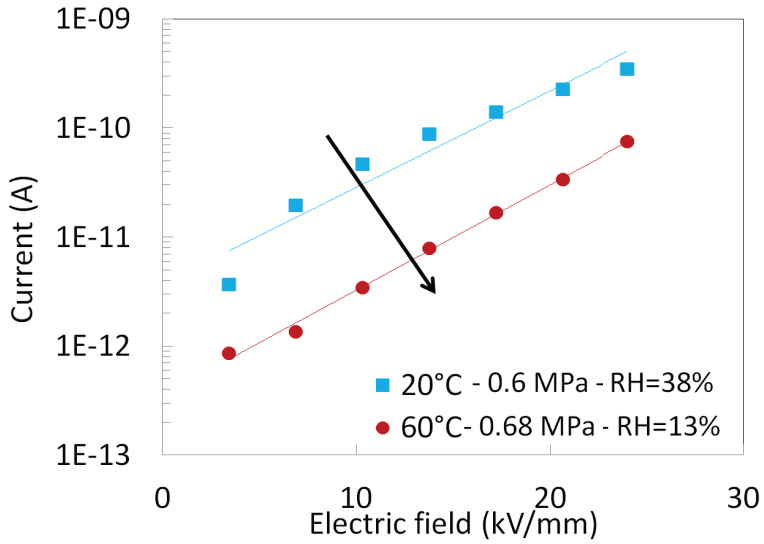

Fig. 2.41: Current variations in case of a humid test cell ($RH > 13\%$), with increasing temperatures in $0.6\,MPa$ of SF_6.

Depending on the situation, one effect may dominate: the influence on RH at high water content, and the influence on charge emission at low water content. However, the present results do not allow us to conclude on this assumption. Similar effects will be observed in uniform geometry.

2.3.2.5 Synthesis: influence of RH in SF_6 and air

Figure 2.42 shows a comparison of measured currents with two different SF_6 water contents ($RH = 13\%$ and 38% at $20\,°C$ and $0.6\,MPa$). Currents measured in case of $RH = 38\%$ are one decade higher than for $RH = 13\%$. Besides, for both RH, the current varies following an exponential law (2.8), with same slopes (α).

This shows that in both cases, the same mechanisms are responsible for the measured current, the latter being strongly enhanced for high RH.

A comparison of currents measured in air during step 3 and in SF_6 with RH variations is presented in figure 2.43. As in SF_6, the current in air increases exponentially with RH. Moreover, the slopes (β) of plots in both gases are similar. In SF_6, the variation of RH was obtained by changing the pressure at constant temperature. In air a similar experiment was not possible, since breakdown in this gas occurred at much lower voltage. Current measurements in air were possible only at high pressure (typically $1\,MPa$), in order to apply high enough electric fields without breakdown. In air, variations of RH were obtained by changing the temperature. The influence of RH on measured currents is evidenced for $RH > 10\%$. In both gases, current measurements with the small scale coaxial geometry at very low RH ($< 5\%$) with an electric field up to $15\,kV/mm$ were not possible (current below the detection limit of $0.1\,pA$).

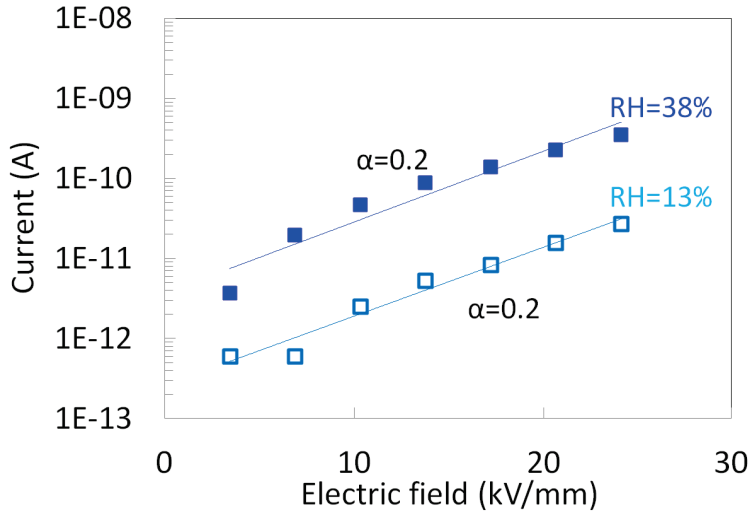

Fig. 2.42: Evolution of *dark currents* versus electric field for two different RH (13% and 38%) in SF_6 at $0.6\,MPa$ (20 °C).

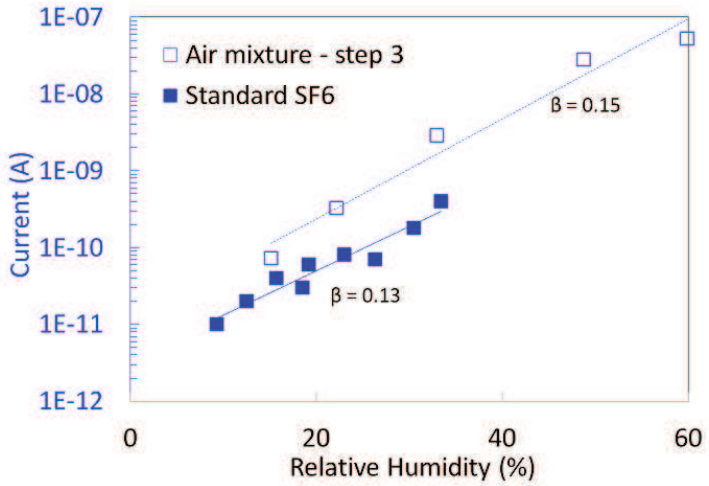

Fig. 2.43: Current measurements depending on relative humidity in air at different temperatures (step 3 at $35\,kV$) and in SF_6 at different pressures (at $50\,kV$), with α the corresponding slopes.

In our conditions (*i.e.*, $RH > 10\%$ at high pressure), the influence of pressure and temperature on the current can be mainly attributed to indirect effects (*i.e.*, variation of RH versus temperature and pressure). The experiments also show that the actual RH measured within the test cell can be rather different from calculations only based on the initial gas properties. A complex equilibrium between the water content in the gas and the water adsorbed on surfaces, has also been pointed out. The initial conditioning of the test cell (*i.e.*, initial presence of adsorbed water or not) has a large influence on the actual RH, and thus on the *dark current*. The RH measured in the gas volume is correlated to the amount

of water adsorbed on surfaces, which unfortunately cannot be directly measured. We can assume that charge injection from the high field electrode is enhanced by the presence of adsorbed water.

2.3.3 | Parallel electrodes system

In the coaxial geometry, it is difficult to change the gap distance between electrodes, as well as to adjust the electrode roughness of both cathode and anode. Those parameters are investigated in this section, in the plane to plane geometry.

2.3.3.1 Influence of gap distance and electric field in «standard» SF_6 ($RH > 15\%$ at $0.6\,MPa$)

Using aluminum electrodes with an average roughness of $3\,\mu m$ and «standard» conditioning procedure C_1, *dark currents* have been measured in «standard» SF_6 ($RH = 2.7\%$ at atmospheric pressure, 20 °C) for different voltages and gap distances (d). Two measurements series (i) and (ii) were done to check the reproducibility of measurements. In both cases, the measured RH was equal to 20% at 20 °C, $0.6\,MPa$. Figure 2.44 shows stabilized currents at $0.6\,MPa$ for gap distances from $1\,mm$ to $20\,mm$, depending on (a) voltage, and (b) electric field. *Dark currents* up to $100\,nA$ at $13\,kV/mm$ are measured for gap distances superior or equal to $2\,mm$, corresponding to current densities of about $100\,pA/cm^3$. In those measurements, a correct reproducibility is observed for both series ((i) and (ii)).

Figure 2.44 (b) shows that measurements carried out with $d \geq 2\,mm$ group together when plotted versus electric field, while currents measured for $1\,mm$ are lower for a similar electric field. It also evidences that the current varies exponentially with the electric field, following two regimes for gap distance $d > 1\,mm$. Two different slopes can be observed before and after $E = 12\,kV/mm$ (further studied in next sections). It is interesting to observe that although currents recorded at $1\,mm$ are lower, the slope of the curve is identical to that observed at larger distances. The exponential law observed for $d \geq 1\,mm$ is still valid at rather low values of electric field, down to $1\,kV/mm$, *i.e.,* in typical nominal conditions found in a GIS.

Typical current recordings are shown in figure 2.45 for (a) $2\,mm$ and (b) $5\,mm$ gap. For both measurements, the photo-multiplier (PM) signal was recorded and is plotted in green. When no light is recorded, a PM signal of $1\,nA$ is obtained, which corresponds to the photo-multiplier background noise. Two regimes are observed on the measured currents.

In the first regime I ($E < 12\,kV/mm$), low values of current and quick stabilization are obtained, while no light is recorded. At low distances (1 and $2\,mm$), currents recorded were very noisy (for instance at $V = 10 - 15\,kV/mm$ on figure 2.45). At larger distances, currents became much less noisy (for instance, $40\,kV$ in figure 2.45 (b)), and were rather stable.

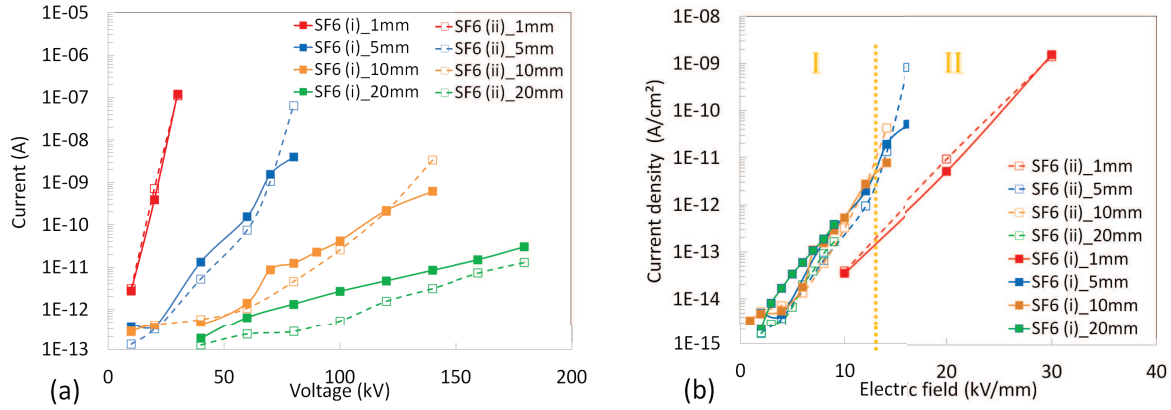

Fig. 2.44: *Dark current* measurements in standards SF_6 for gap distances from $1\,mm$ up to $20\,mm$, plotted versus (a) voltage, (b) electric field ($0.6\,MPa$, $RH = 20\%$).

In the second regime II ($E > 12\,kV/mm$), currents became instable (they decrease versus time) and a much longer stabilization time was observed (above $20\,kV$ in figure 2.45 (a) and $60\,kV$ in figure 2.45 (b)). A very faint light emission, larger than the PM noise, was observed at the highest voltage levels reached in these measurements (above $30\,kV$ in figure 2.45 (a) and $70\,kV$ in figure 2.45 (b)). Below this voltage it is not possible to ascertain that no light was emitted, since measurements are limited by the PM noise.

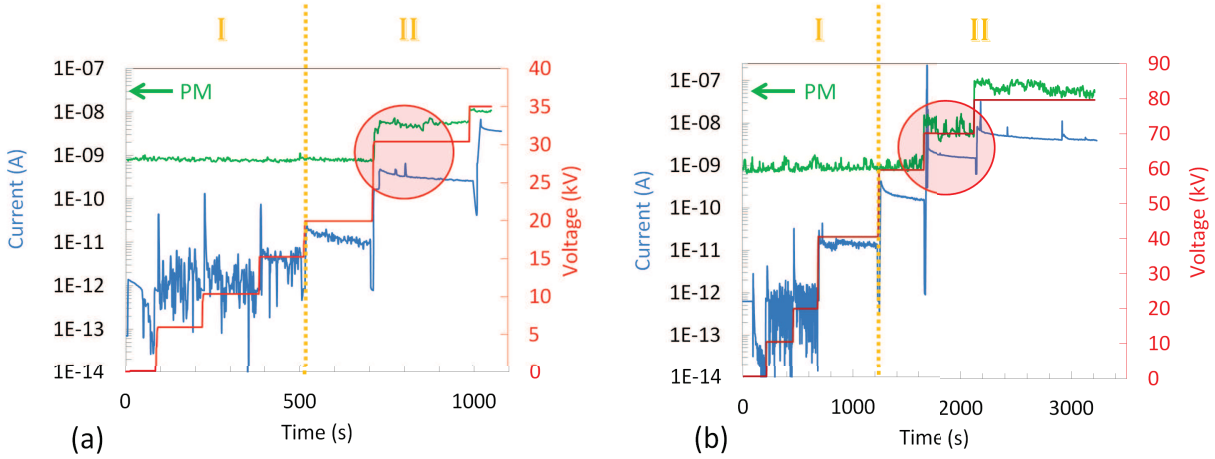

Fig. 2.45: Time-evolution of current and light emission versus voltage in standard SF_6 at $1\,MPa$ for (a) $2\,mm$ gap and (b) $5\,mm$ gap.

Another measurements series performed in similar RH conditions for higher electric field, up to $30\,kV/mm$ is shown in figure 2.46. In these conditions, three regimes of current are observed. All regimes present an exponential increase with electric field, with a large increase of current in the 2^{nd} regime observed in a narrow electric field range from $12\,kV/mm$ to $15\,kV/mm$. It is also observed that for gap distances $> 2\,mm$, measurements are grouped together while a discrepancy is observed for $d = 2\,mm$ (current shifted at higher electric

field). It is worth noting that such regimes were not recorded in case of coaxial system.

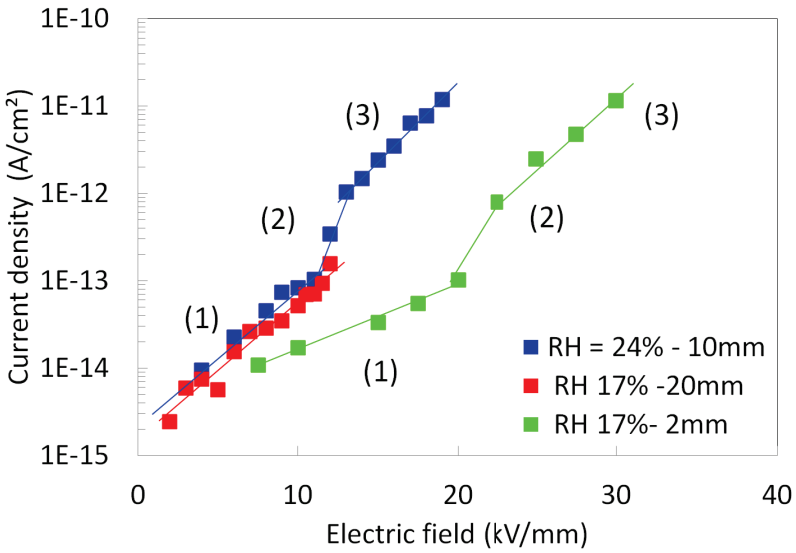

Fig. 2.46: Current density measured in SF_6 ($0.6\,MPa$, $RH \approx 20\%$, $20\,°C$) for a larger range of electric field and three gap distances.

2.3.3.2 Influence of gap distance and electric field in dry SF_6 ($RH \leq 5\%$ at $0.6\,MPa$ and $1\,MPa$)

Following conditioning C_2, the system was filled with dried SF_6 using a silica gel cartridge, allowing to reach a $RH = 0.3\%$ at atmospheric pressure and $20\,°C$. Figure 2.47 shows currents recorded for both positive and negative polarities of applied voltage up to $20\,kV/mm$ and with a measured RH of 5% at $1\,MPa$.

As previously evidenced in case of more humid SF_6 (figure 2.46), three current regimes are also observed here. Moreover, for both polarities, the same currents are obtained, revealing the good symmetry of our electrodes system. It is also worth noting that in dry SF_6, no light emissions were measurable for all regimes.

In figure 2.48, currents measured for dried SF_6 ($0.6\,MPa$) at different gap distances are shown. It can be observed again that for gap distances $d \geqslant 5\,mm$, all measurements group together, according to the three regimes already observed with three different slopes $\alpha_1 = 0.2$, $\alpha_2 = 1.3$ and $\alpha_3 = 0.4$. At $d = 2\,mm$, current are shifted for higher electric field such as in previous measurements in humid SF_6. In the following, measurements are presented for a gap distance $d = 10\,mm$ since good reproducibility is observed.

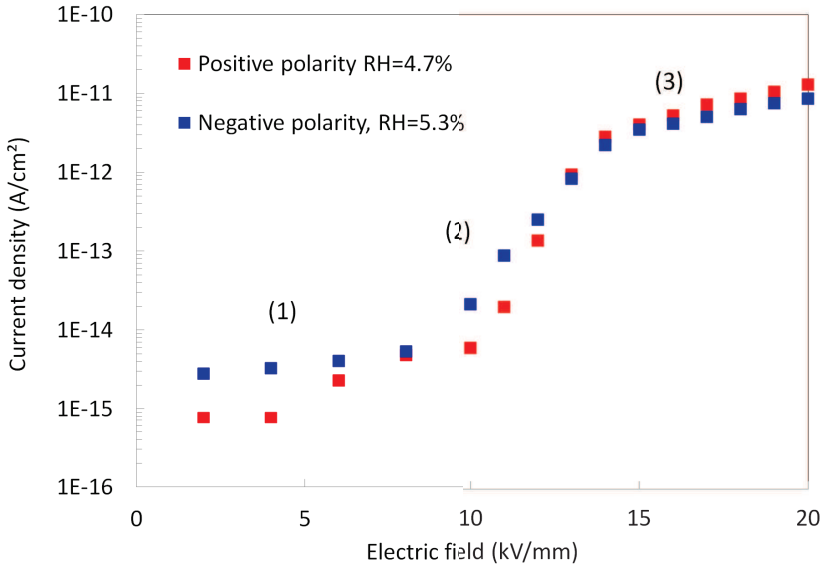

Fig. 2.47: Current density measurements for positive and negative polarities versus electric field, for a gap distance of $10\,mm$ ($1\,MPa$, $20\,^{\circ}\mathrm{C}$ and $RH \simeq 5\%$).

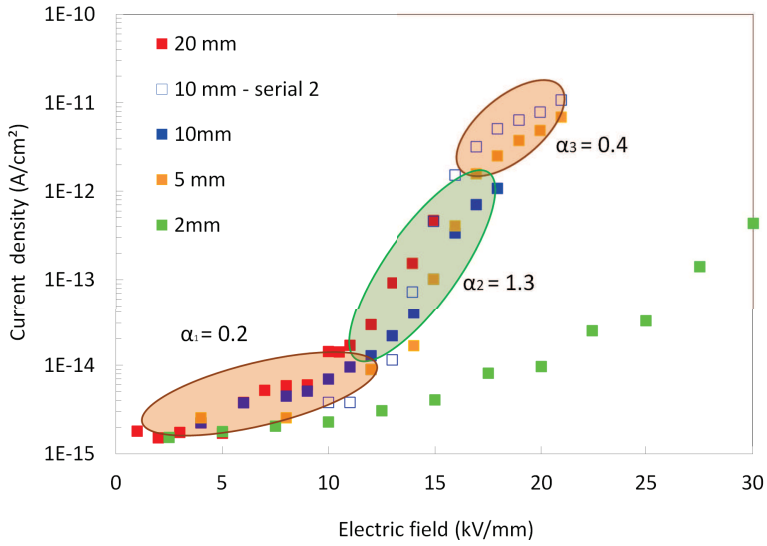

Fig. 2.48: Measured current density for different gap distances, in dried SF_6 ($0.6\,MPa$, $RH \simeq 2\%$, $20\,^{\circ}\mathrm{C}$).

2.3.3.3 Influence of pressure and Relative Humidity RH

Figure 2.49 (a) shows the evolution of measured current with decreasing (from $1.1\,MPa$ to $0.3\,MPa$) and increasing (up to $1\,MPa$) pressure, with standard SF_6 ($RH = 2.7\%$ at atmospheric pressure). As already observed in the coaxial system, the current increases versus pressure. In figure 2.49 (b), the variations of RH values recorded are presented for

increasing and decreasing pressure, and compared to the theoretical values of RH. As in the coaxial system (figure 2.34), the measured RH is higher than the calculated one. This can be explained by the influence of the adsorbed water initially present within the system (prior to filling).

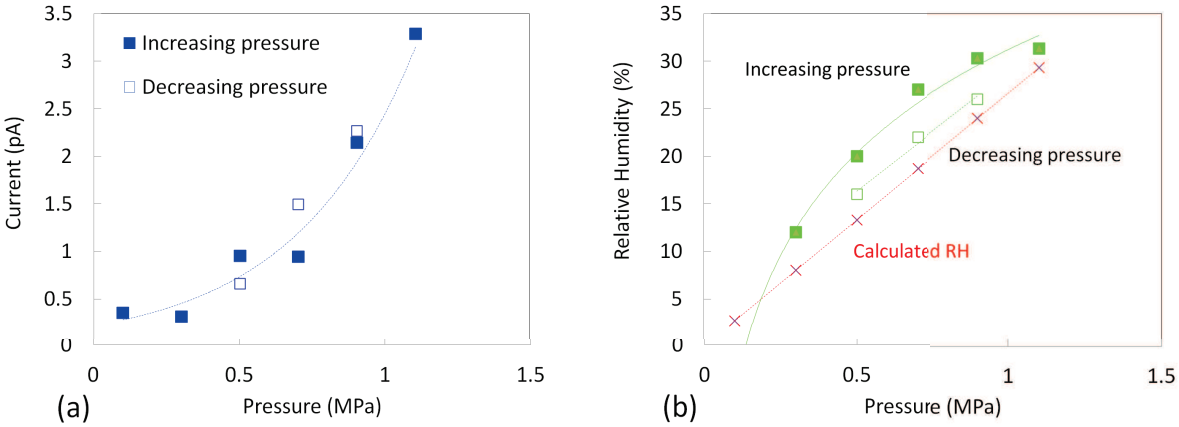

Fig. 2.49: (a) Current and (b) RH measurements performed in SF_6, with pressure variations ($60\,kV$, $20\,°C$).

The measured current density as a function of RH is plotted in figure 2.50 for both increasing and decreasing pressure. As already observed in the coaxial system, the current varies following an exponential-law with RH.

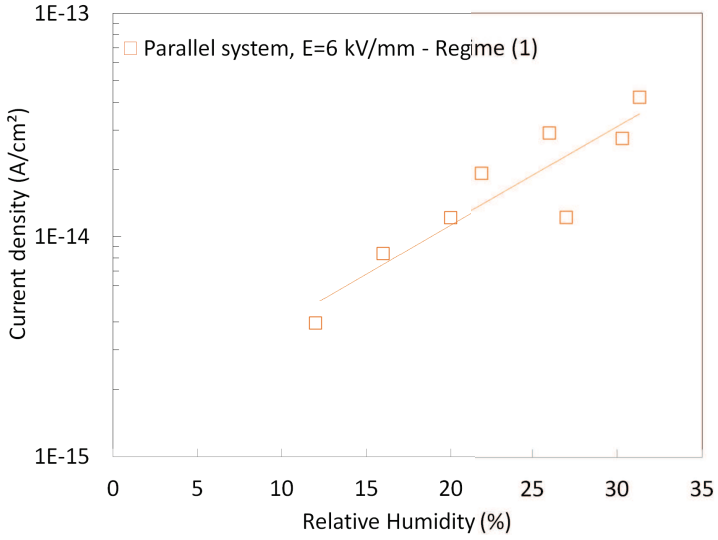

Fig. 2.50: Current density measurements performed in SF_6 at $6\,kV/mm$, $20\,°C$, versus relative humidity.

The influence of pressure on the current in dry SF_6 is observed in figure 2.51. This experiment was done first by drying the system under vacuum at $60\,°C$ for three days, and

by filling it progressively with SF_6 through the silica gel cartridge. At each pressure, it was necessary to wait a long time (about two days) to reach a stabilized RH, due to the equilibrium between the gas and surfaces. The lowest measured RH are close to the sensor resolution (0.8%) *i.e.,* a large uncertainty on values of RH exists.

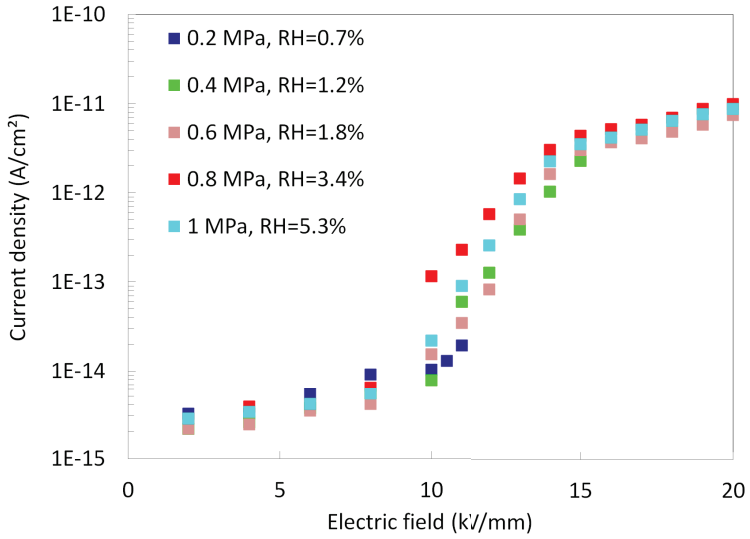

Fig. 2.51: Measured current density for different pressures, in dried SF_6, at $d = 10\,mm$ (20 °C).

For pressure from $0.2\,MPa$ up to $1\,MPa$, only a slight variation on the measured current was observed. This shows that there is no large direct influence of the pressure on the current. As in the case of humid SF_6 (figure 2.46), three current regimes are observed on figure 2.51.

Figure 2.52 shows a comparison of measured current in «dry» and «wet» SF_6 ($0.6\,MPa$). Currents measured in case of $RH = 24\%$ are one decade higher that currents obtained for $RH = 2\%$. Besides, it is shown that for both RH, similar slopes describing the two first regimes are obtained. It strongly suggests that in both cases, same mechanisms are responsible for the measured current, the latter being strongly enhanced by water in all regimes.

It is also observed that in dry SF_6, the onset electric fields of different regimes are shifted to higher values (regime (2) is observed between 12 and $14\,kV/mm$ in humid SF_6 and 13 to $17\,kV/mm$ in dry SF_6).

Based on all results obtained for different relative humidity and different pressure, the current as a function of the RH from 1% to 30% can be plotted in figure 2.53 for an arbitrary electric field value of $6\,kV/mm$, typical of the maximum electric field in a GIS.

Considering the scatter of measurements, we can postulate that an uniform trend over a large RH range (1 *to* 30%) is observed, whatever the pressure. The whole tendency was

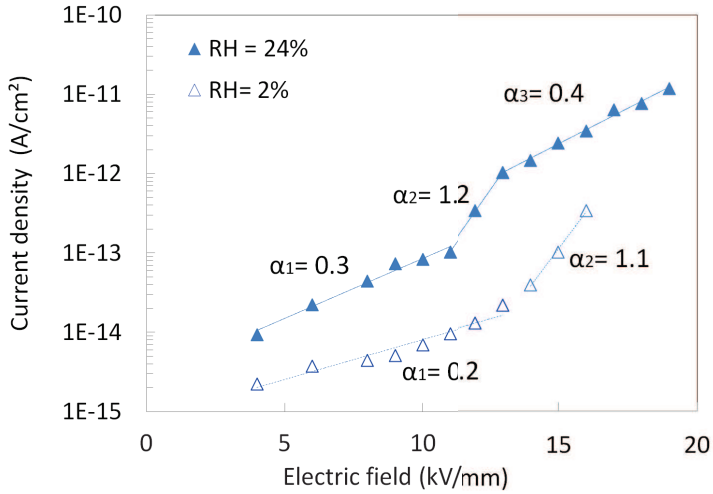

Fig. 2.52: Measured current density for two different RH, corresponding to conditioning C_1 and C_2, in SF_6 at $0.6\,MPa$.

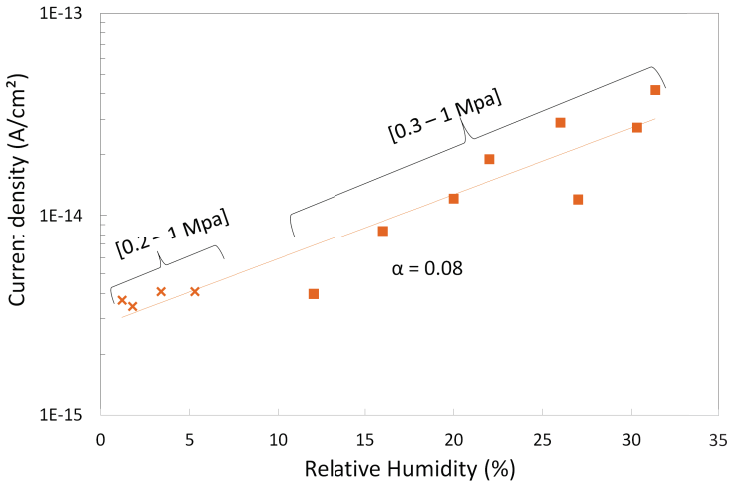

Fig. 2.53: Current measurements depending on relative humidity in SF_6 (at $6\,kV/mm$, $20\,°C$).

obtained varying the pressure from 0.2 to $1\,MPa$ in dry SF_6 (corresponding to 1.2 to 5.2% of RH) and from 0.3 to $1\,MPa$ in humid SF_6 (corresponding to 12 to 30% of RH).

2.3.3.4 Comparison with measurements obtained in the coaxial system

Figure 2.54 shows a comparison between current densities measured versus RH for coaxial and plane to plane electrode systems obtained with the same technique (*i.e.*, variation of pressure with standard SF_6). It is worth noting that those measurements were not performed in the same electric field conditions ($17\,kV/mm$ was used in the coaxial system, and $6\,kV/mm$ in the parallel system). Hence, we extrapolated the values obtained in coaxial

system from $17\,kV/mm$ to $6\,kV/mm$ using equation (2.8). In both geometries, the measured current densities versus RH vary following an exponential-law with similar slopes. This suggests that the charge injection mechanism which occurs in the coaxial system and in the 1^{st} regime of the parallel system, are similar.

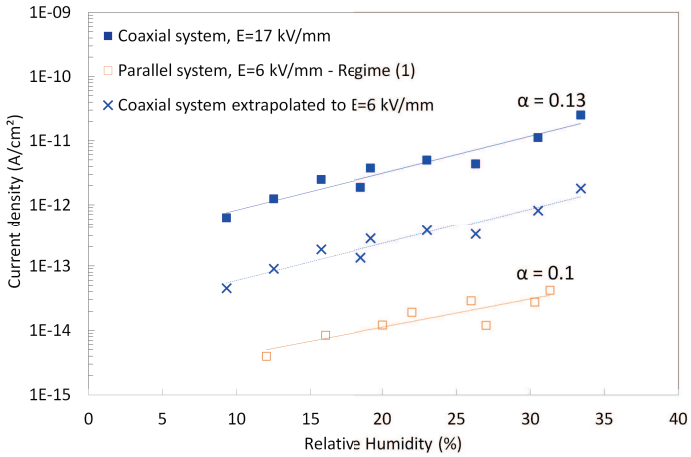

Fig. 2.54: Current density measurements performed in SF_6 for both coaxial and parallel electrode system, for different electric field, versus relative humidity, at room temperature.

It is also seen that the measured current densities in case of coaxial system are higher compared to the parallel system for the same electric field. This difference could be explained by the difference of roughnesses. In case of a coaxial system, the $2.2\,\mu m$ electrode roughness was obtained using SiC sandpaper, resulting in irregular scratches and grain inclusions. In the parallel system, the $3\,\mu m$ roughness was obtained by dry machining, resulting in a regular furrow. In addition, the electrode materials are different. Indeed, in the coaxial system brass electrodes are used while aluminum electrodes are used in the parallel system.

2.3.3.5 Comparison with measurements in synthetic dry air

A comparison of measured currents in dry air and dry SF_6 is presented in figure 2.55 for two different pressures at room temperature. As for SF_6, the two first regimes are present in air. The third regime cannot be observed in air since electric fields were too close to the breakdown voltage. In the first regime, measured currents are comparable in air and SF_6. Only a minor difference is observed in the second regime, for which currents are shifted at higher electric field in dry air. These results confirm that the nature of gas does not have a large effect on currents. As in the coaxial geometry, slightly lower currents were measured in air compared to SF_6 for similar RH (in positive polarity).

Further investigation should be performed in humid air to compare the influence of RH on measured current in both SF_6 and air. These measurements were planned during the

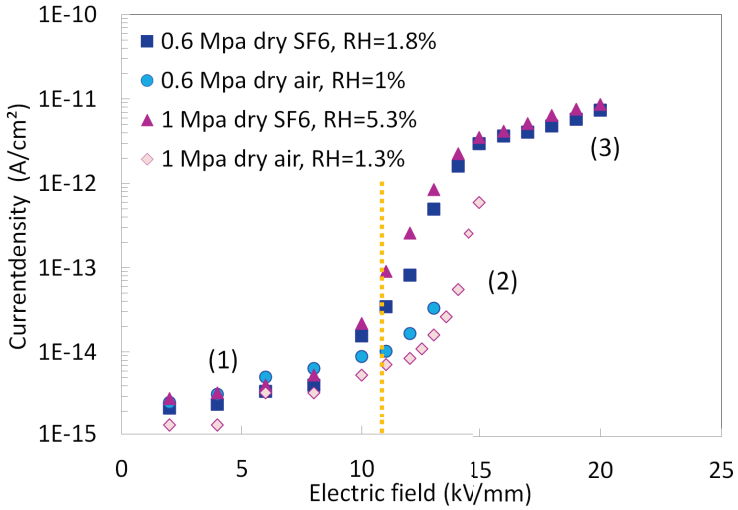

Fig. 2.55: Measured current density through dry air and SF_6 for two pressures ($0.6\,MPa$ and $1\,MPa$) at room temperature.

PhD. Unfortunately, the failure of the specific high voltage/high pressure bushing, used in the experiments did not allow us to carry out these experiments. In a similar way, it was not possible to evaluate the influence of electrode surface roughness in this system for the same reasons.

2.3.3.6 Influence of heating measurement electrode

In the parallel electrode system, only the temperature of the measurement electrode can be measured and controlled. It means that there is a temperature gradient between the high voltage and the measurement electrodes. In our system, a thermocouple allows measuring the global temperature of the gas (see figure 2.20). Whatever the electrode temperature, the global gas temperature remains almost unchanged (the gas volume between electrodes is negligible compared to the entire gas volume). As expected, the RH within the entire device does not vary significantly.

Figure 2.56 shows stabilized current measured at a fixed voltage ($+70\,kV$) in SF_6 at $1\,MPa$ ($RH = 20\%$), for a gap distance of $10\,mm$. In the system initially at room temperature, the measurement electrode (of positive polarity) was heated from 20 °C to 90 °C by 10 °C steps. During the first heating, the current strongly decreased, with two decades difference (from $500\,pA$ down to $1\,pA$) for a variation of 70 °C.

Following this experiment, the heating system was stopped in order to decrease the temperature of the electrode back to 20 °C, and the measurement was repeated (2^{nd} heating). It is observed that the stabilized current measured is now about 10 times lower than the initial current (see figure 2.56). A slight decrease of this current is still observed while the temperature is raised.

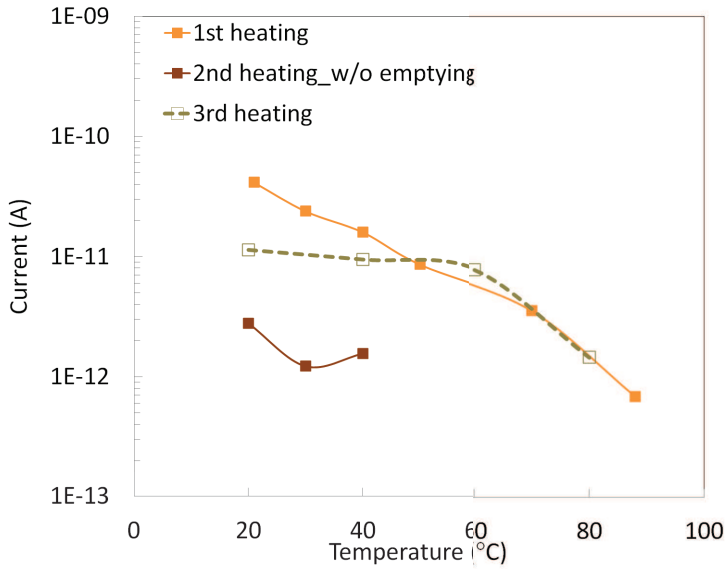

Fig. 2.56: Three series of stabilized current measurements for increasing temperature, at $+70\,kV$, $1\,MPa$ of SF_6 with $RH = 20\%$.

In order to investigate the reversibility of this experiment, the gas was evacuated, and the test cell was set under ambient air ($RH = 40\%$) at atmospheric pressure for two days. Then, after re-filling in exactly the same conditions as previous measurement ($1\,MPa$, $RH = 21\%$), the experiment is repeated (third heating). It is observed that currents measured during this third heating are similar to those measured during the first heating. This result shows the reversible character of this experiment.

These experiments illustrate that by increasing the electrode temperature, the amount of water initially adsorbed on the electrode surface decreases (desorption), resulting in a reduction of the measured current (1 decade difference). Those results evidence the major importance of water adsorbed on the electrode surface in current measurements. The equilibrium between the gas volume and surfaces will cause adsorption or desorption of water molecules. When water is adsorbed on the electrode surface, a higher current is measured. Adsorbed water enhances charge emission from the electrode surface. Once the electrode has been dried by heating, a long time is necessary to get back in equilibrium with humid ambient air. While the electrode is heated, the decrease of current can be explained by the water desorption from the electrode surface, but also by the decrease of gas RH between the electrodes. Indeed, when one electrode is heated, the gas between electrodes and thus the other electrode are also heated.

Similar experiments have also been performed with a dry SF_6 ($RH = 1.5\%$ at $0.6\,MPa$). Figure 2.57 (a) shows a typical recording of the current while increasing temperature at a constant electric field ($12\,kV/mm$). It can be observed that at each temperature increase of $20\,°C$, a strong transient current (about $100\,pA$) is immediately recorded. Following this

transient, a decrease of current is observed, and stabilized values are reached after a long time (about 1 hour). On figure 2.57 (b), the stabilized current density values are represented as a function of electric field for three temperatures. Different regimes are still observed for all temperatures. In the first regime, currents lower than $0.5\,pA$ are obtained. These values are close to the noise level and then cannot be taken into account. It is observed that the stabilized current increases with temperature in regime (2) and (3).

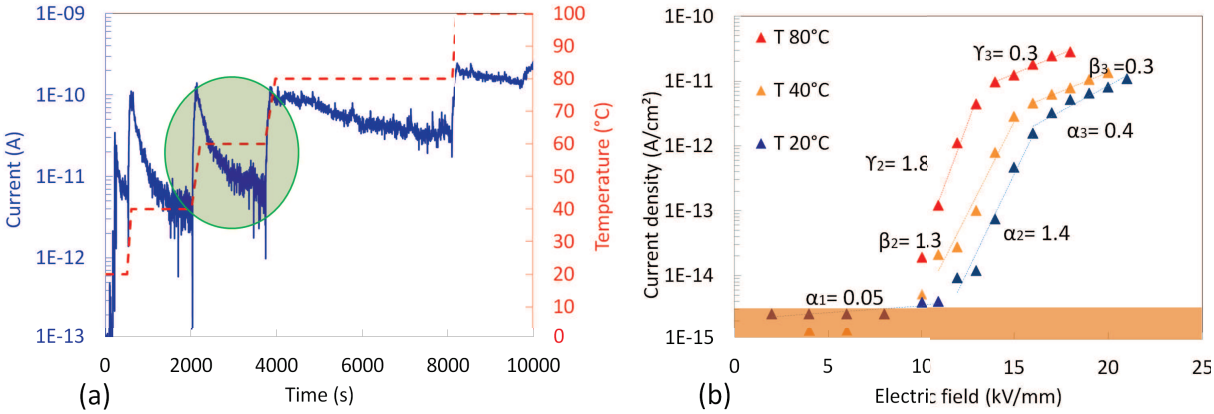

Fig. 2.57: (a) Typical recording of the current for increasing electrode temperature at $12\,kV/mm$ ($d = 10\,mm$) and (b), stabilized current density values for increasing temperatures, in dried SF_6, at $0.6\,MPa$, $RH = 1.5\%$.

Figure 2.58 shows a comparison of the current as a function of electrode temperature for both dry and humid SF_6. As the currents measured in the dry SF_6 at $6\,kV/mm$ are in the noise level, we have also plotted the values at $10\,kV/mm$. Contrary to humid SF_6, the current now slightly increases with temperature, such as in the coaxial geometry. On the one hand, we observe that the trends of both systems are opposed. On the other hand, we can note that currents measured in the dry system are much lower than that measured in case of a humid system.

We can assume that in case of $RH > 5\%$ and electric field lower than $13\,kV/mm$, the water adsorbed on the electrode surface has a predominant impact on measured current. This impact is not observed anymore for a dry system and at high temperature. In case of a dry system, the temperature of the measurement electrode plays a significant role on the charge injection mechanisms (measured currents increase with the electrode temperature).

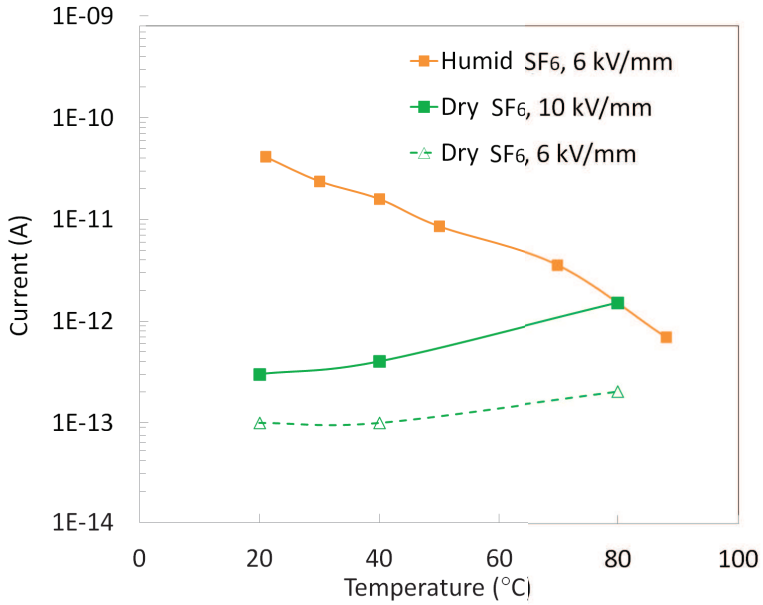

Fig. 2.58: Comparison of currents evolution as a function of electrode temperature in SF_6, between humid and dry systems at $6\,kV/mm$ and $10\,kV/mm$ ($d = 10\,mm$)

2.4 | Discussion

2.4.1 | Physical mechanisms

Experimental results presented in this chapter evidence conduction processes through gases, in both coaxial and uniform electric field geometry. Several parameters of great practical influence have been evidenced. The current increases exponentially with the average electric field (for gaps $> 2\,mm$), with relative humidity, and is strongly dependent on electrode surface roughness. We have also determined that depending on the conditioning of the device, the temperature could enhance or lower the measured current.

As previously mentioned, these currents far exceed theoretical values obtained by considering that charge production processes remain identical to those evidenced at low fields.

The natural ionization alone should induce current densities about $5.10^{18}\,A/cm^2$ in typical conditions, whereas experiments indicate considerably larger values exceeding $5.10^{11}\,A/cm^2$.

The results discussed in this section are those obtained in the uniform geometry, in case of a conditioning $C1$ (humid gas and enclosure: $RH = 24\%$), for a gap distance of $10\,mm$, $0.6\,MPa$ of SF_6 at ambient temperature ($20\,°C$).

2.4.1.1 *Fowler-Nordheim* emission

We have tentatively represented the current according to FN law in figure 2.59 in order to observe the trend of the curve, calculate the corresponding emitting surface (S) and the field reinforcement factor β. It is observed that the variations do not follow a linear representation. Three different areas are shown.

We will consider a linear fit for areas 1 and 3. The area 2 is considered as a transition. The calculated values of β and S, based on a potential barrier of $4.28\,eV$ (potential barrier of the aluminum), are given in table 2.5.

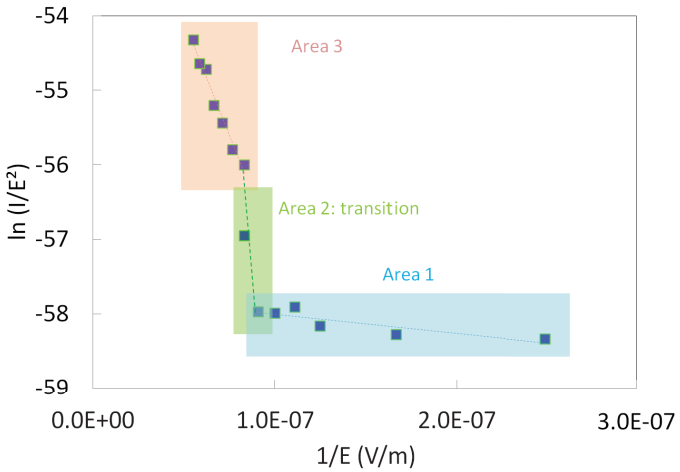

Fig. 2.59: Representation of the measured current in $ln(I/E^2) = f(1/E)$.

	Area 1	*Area 3*
β	964	19273
$S\,(m^2)$	$2.16.10^{-43}$	$6.64.10^{-49}$

Tab. 2.5: Calculated values of β and S for the two areas represented in figure 2.59.

The classical FN plot gives absurd values of surface emission and field amplification. We can thus conclude that the FN emission mechanism alone, cannot explain the measured current. Of course this conclusion is also supported by the fact that identical currents are measured in both polarities.

2.4.1.2 *Schottky* emission

In figure 2.60 the results are plotted according a representation of *Schottky* emission. It can be observed that it nearly follows a linear trend. Based on this representation and eq. (2.14), the value of the potential barrier can be calculated (eq. (2.15)).

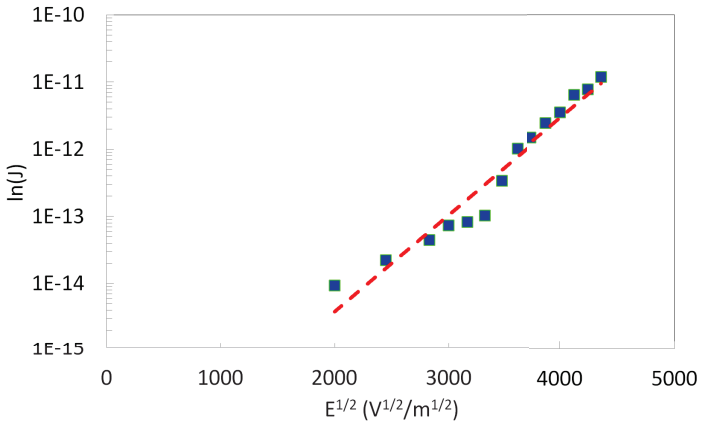

Fig. 2.60: Representation of the measured current in $ln(J) = f(E^{1/2})$.

$$J = AT^2 * exp\left(\frac{-\phi_0}{kT}\right) * exp\left(\frac{\beta_S}{kT}E^{1/2}\right) \tag{2.14}$$

$$\phi_0 = kTln\left(\frac{Slope}{AT^2}\right) = 1.3\,eV \tag{2.15}$$

This calculated value is significantly lower than the theoretical potential barrier of aluminum ($4.28\,eV$). It shows that the *Schotkky* emission model does not describe our measurements. Once again, this conclusion is supported by the fact that identical currents are measured in both polarities in divergent electric field.

2.4.1.3 Field desorption of water

As seen previously, neither the FN emission nor the *Schottky* emission allow explaining the origins of the measured current. A major parameter evidenced in our experiment is the influence of water. Hence, several mechanisms occurring on metal surface at high electric field after water adsorption are considered in the following.

Several investigations have been led in the $1970's$ concerning the work-function changes due to the chemi-sorption of water on aluminum electrodes [37–39]. These experiments, realized in vacuum, show the influence of oxygen and water adsorption on the work-function of an aluminum electrode. Huber *et al.* [37] reported that first, the water reacts to form an oxide layer on the aluminum surface. This induces only a small variation on the metal work-function ($\pm 0.05\,eV$). Then, the water adsorbs on top of this thin oxide layer as H_2O or OH, causing a large work-function decrease ($\sim 1.4\,eV$). They also pointed out that water vapor is a contaminant very difficult to eliminate even in ultra-high vacuum systems.

Indeed, as the relative humidity in our system was quite important, we can speculate that multilayers of water have been adsorbed on the surface.

However, we shall note that even if this could provide an explanation for the measured current in negative polarity, such phenomena do not explain the measured current in positive polarity.

Other investigations concerning the formation of charged «water clusters» due to field desorption of ice or moist air have been done [40–42]. Carlson [41] has demonstrated that a significant current could be measured in moist air (at high RH close to saturation) at atmospheric pressure. It has also been observed that this current significantly increases with RH and applied electric field. It has been postulated that for atmospheric electric fields superior than $100\,V/cm$, ions contributing to the measured current are produced by molecular fragmentation of water and other substances.

In the framework of field ionization microscopes, Stintz *et al.* investigated the cluster ions formation from ice [40]. They pointed out that when an ice layer is adsorbed on the metal surface in high vacuum, the application of a local very high electric field (from 20 to $100\,MV/cm$) creates ion species from water molecule following the reaction 2.16. An illustration of the creation of ion clusters is represented in figure 2.61. It has also been reported that the electric field required for the isothermal field-desorption decreases as the temperature of the specimen increases. At high desorption temperatures ($\geq 140\,K$ in their experiment), larger ion clusters (*i.e.,* containing an increasing water molecules number n) are formed and the desorption is enhanced.

$$(H_2O)_{n+1} \rightarrow (H_2O)_n.H^+ + OH^- \quad with\, n = 1, 2, ..., 10 \tag{2.16}$$

This theory of field desorption and water cluster ion formation, observed in different conditions (ice layers on very sharp points), could explain the current measured in our experiments. Field desorption was mainly observed with positive points to avoid the parasitic influence of field emission, but its existence in negative polarity was also considered by the authors. We can speculate that this phenomenon could occur in our experiments at the tip of protrusions at the electrode surface, where a large field factor β exists. The transition observed in negative polarity in coaxial geometry, as well as the steep increase in the second regime under uniform field, could be attributed to the onset of some electron field emission mechanism. However, it remains very difficult to ascertain quantitatively these hypothesis on the basis of the results obtained here.

Current and light measurements carried out with a much higher bandwidth provided no evidence of fast pulses. The presence of corona discharges in our experiments can be thus excluded.

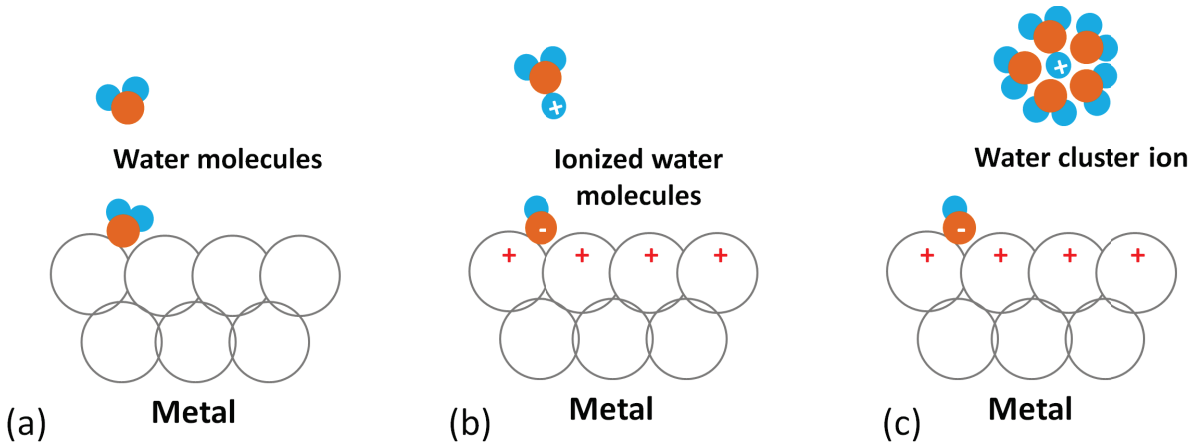

Fig. 2.61: Representation of mechanism proposed for water ion cluster formation, adapted from [43]. (a) Water molecule adsorbed on metal surface, (b) ionization of water molecule due to field desorption mechanism and (c), creation of a water cluster ion.

2.4.2 | Consequences on the industrial application

In the electric field range of a typical GIS application (up to $E_{max} = 10\,kV/mm$), it has been evidenced that a non-negligible current can be injected in the gas, in both polarities. This current is strongly influenced by several parameters that should have a great importance for the practical application: electrode surface roughness, presence of water, and temperature. These parameters provide useful indications for the optimization of GIS, with the objective to reduce phenomena associated with electrostatic charging of solid insulators.

In a fixed GIS configuration, temperature appears to be an important parameter. Indeed, it will modify the gas RH, the equilibrium between water adsorbed on surfaces and in the gas volume, and also the volume and surface resistivities of solid insulators. All these phenomena are coupled, and determine in a rather complex way the dynamics of charge accumulation and decay. For instance, let us consider a «standard» GIS situation: $0.6\,MPa$ SF_6 with a $RH = 4.8\%$ at $20\,°C$, and $6\,kV/mm$. In such system, a current density of about $5.10^{-15}\,pA/cm^2$ will be injected by the high voltage electrode in the gas.

If this GIS is submitted to low external temperatures ($\sim -8\,°C$), complex phenomena may occur. Once the equilibrium is stabilized within the GIS, a RH of approximately 34% should be measured within the system due to the temperature decrease. Thus, considering $RH = 34\%$, the current through gas should increase by about one decade. However, the actual RH within the system differs from the calculated one due to adsorption/desorption phenomena. Then, to estimate the current emitted within a GIS, a RH measurement should be performed. The decrease of temperature results in a large increase of current through gas, enhancing the charge accumulation on the solid insulator surface. However, two other opposite phenomena will occur. On the one hand, the volume resistivity of the

solid insulator significantly increases with the decrease of temperature, which will also favor the charge accumulation. On the other hand since the GIS surfaces and SF_6 are «humid», the surface resistivity of the insulator will decrease, favoring the charge relaxation. Thus, it is very difficult to estimate if charge accumulation or relaxation will be enhanced. Only a numerical simulation of the processes can provide an information on the final tendency.

In another situation, if the temperature of the high voltage electrode rapidly increases, a transition stage during which an important peak of emitted current (from 10 to 100 times the steady current), appears. During this transition, the charge accumulation phenomena may be further enhanced. Besides, as will be evidenced in chapter 4, the temperature gradient along the insulator will induce a complete re-distribution of the electric field, and an enhancement of the current through the insulator. Once again, the final influence on the charge accumulation and the field distribution remains difficult to predict without a precise numerical simulation.

2.5 | Conclusions

In this chapter, a conduction process through pressurized gas has been evidenced at high electric field in both dry and «wet » systems. It has been shown that the measured current is field-dependent and composed of three different regimes. The indirect influence of pressure allows to highlight the significant impact of RH on the measured *dark currents*. In addition, we have demonstrated that depending on the initial conditioning of the system, the influence of temperature on the measured current and on the RH equilibrium of the system, can be reversed.

To explain the mechanisms occuring within our system, we propose to consider the phenomena of chemi-sorption and field desorption at the metal electrode after water adsorption. This hypothesis fairly agrees with the higher currents measured with increasing RH. Moreover, it also agrees with the measured current in both negative and positive polarities. Further investigations should be realized to confirm this assumption.

Those results are very important for the GIS application since they point out an additional source of charge generation, which will contribute to the charge accumulation phenomenon on the solid insulator surface. Moreover, it raises the major issue of RH equilibrium between gas and surfaces. Further investigations must be performed in order to find an evolution law which could be implemented in a numerical model, in order to estimate the charge accumulation due to those conduction processes in gas.

Bibliography

[1] J. Kindersberger and C. Lederle, "Surface charge decay on insulators in air and sulfurhexafluorid - part i: simulation," *Dielectrics and Electrical Insulation, IEEE Transactions*, vol. 15, pp. 941–948, August 2008. (cited in page 30)

[2] M. Saltzer, U. Gafvert, B. Kallstrand, K. Johansson, and L. Walfridsson, "Observation of space charge dynamics in air under DC electric fields," in *Electrical Insulation and Dielectric Phenomena (CEIDP), 2011 Annual Report Conference*, pp. 141–144, Oct 2011. (cited in pages 30 and 31)

[3] A. Winter and J. Kindersberger, "Stationary resistive field distribution along epoxy resin insulators in air under DC voltage," *Dielectrics and Electrical Insulation, IEEE Transactions*, vol. 19, pp. 1732–1739, October 2012. (cited in pages 30 and 31)

[4] E. Volpov, "Electric field modeling and field formation mechanism in HVDC SF6 gas insulated systems," *Dielectrics and Electrical Insulation, IEEE Transactions*, vol. 10, pp. 204–215, April 2003. (cited in pages 10, 22, 30 and 31)

[5] N. Wiegart, L. Niemeyer, F. Pinnekamp, J. Kindersberger, R. Morrow, W. Zaengl, M. Zwicky, I. Gallimberti, and S. Boggs, "Inhomogeneous field breakdown in GIS-the prediction of breakdown probabilities and voltages. i. overview of a theory for inhomogeneous field breakdown in SF6," *Power Delivery, IEEE Transactions*, vol. 3, pp. 923–930, Jul 1988. (cited in pages 30 and 31)

[6] U. Straumann, M. Schuller, and C. Franck, "Theoretical investigation of HVDC disc spacer charging in SF6 gas insulated systems," *Dielectrics and Electrical Insulation, IEEE Transactions*, vol. 19, pp. 2196–2205, December 2012. (cited in pages 30 and 145)

[7] J. Kindersberger, N. Wiegart, and S. Boggs, "Ion production rates in SF6 and the relevance thereof to gas-insulated switchgear," in *Conference on Electrical Insulation and Dielectric Phenomena*, 1985. (cited in pages 30 and 31)

[8] J. S. E. Townsend and J. Townsend, *Electricity in gases*. Clarendon Press, 1915. (cited in pages 30 and 31)

[9] J. Kuffel, E. Kuffel, and W. S. Zaengl, *High voltage engineering fundamentals*. Newnes, 2000. (cited in page 30)

[10] F. Furuta, T. Nakanishi, S. Okumi, T. Gotou, M. Yamamoto, M. Miyamoto, M. Kuwahara, N. Yamamoto, K. Naniwa, K. Yasui, *et al.*, "Reduction of field emission dark current for high-field gradient electron gun by using a molybdenum cathode and titanium anode," *Nuclear Instruments and Methods in Physics Research Section A: Accelerators, Spectrometers, Detectors and Associated Equipment*, vol. 538, no. 1, pp. 33–44, 2005. (cited in pages 32, 33, 36, 39, 40, 41, 44 and 52)

[11] Y. Segui, "Diélectriques, courants de conduction," *Techniques de l'Ingénieur, traité Génie électrique D*, vol. 2301, p. 2000, 2000. (cited in page 34)

[12] J. Simmons, "Conduction in thin dielectric films," *Journal of Applied Physics D*, vol. 4, p. 613, 1971. (cited in page 35)

[13] N. L. Fowler, R.H, "Electron emission in intense electric fields," in *Proceedings of the Royal Society of London. Series A*, vol. 119, pp. 173–181, The Royal Society, 1928. (cited in page 35)

[14] W. T. Diamond, "New perspectives in vacuum high voltage insulation. i. the transition to field emission," *Journal of Vacuum Science Technology A: Vacuum, Surfaces, and Films*, vol. 16, pp. 707–719, Mar 1998. (cited in page 35)

[15] K. Almaksour, M. Kirkpatrick, P. Dessante, E. Odic, D. Alamarguy, P. Testé, *et al.*, "Experimental study of dark current emission: Effects of surface morphology and inter-electrode gap distance," in *Actes de la 8ème Conférence de la Société Française d'Electrostatique*, pp. 223–226, 2012. (cited in pages 36, 39, 40, 41 and 42)

[16] K. Almaksour, "Etude de l'émission cathodique sous vide en présence d'un champ électrique intense et des parametres physiques gouvernant son intensité," *Ecole doctorale des Sciences et Technologies de l'Information des Télécommunications et des Systemes*, 2013. (cited in pages 36 and 44)

[17] R. Latham, K. Bayliss, and B. Cox, "Spatially correlated breakdown events initiated by field electron emission in vacuum and high-pressure SF6," *Journal of Physics D: Applied Physics*, vol. 19, no. 2, p. 219, 1986. (cited in pages 36 and 39)

[18] C. Suzuki, T. Nakanishi, S. Okumi, T. Gotou, K. Togawa, F. Furuta, K. Wada, T. Nishitani, M. Yamamoto, J. Watanabe, *et al.*, "Fabrication of ultra-clean copper surface to minimize field emission dark currents," *Nuclear Instruments and Methods in Physics Research Section A: Accelerators, Spectrometers, Detectors and Associated Equipment*, vol. 462, no. 3, pp. 337–348, 2001. (cited in pages 36, 39, 40, 42, 43 and 52)

[19] N. Pupeter, T. Habermann, A. Kirschner, E. Mahner, G. Müller, and H. Piel, "Comparative studies on enhanced field emission from mechanically and chemically polished broad-area nb, cu, and al cathodes," *Applied surface science*, vol. 94, pp. 94–100, 1996. (cited in pages 36, 39 and 40)

[20] F. Endo, T. Kichikawa, R. Ishikawa, and J. Ozawa, "Dielectric characteristics of SF6 gas for application to HVDC systems," *Power Apparatus and Systems, IEEE Transactions*, no. 3, pp. 847–855, 1980. (cited in pages 17, 36, 37, 38, 40 and 41)

[21] J. MacAlpine and C. Shum, "Schottky emission currents in compressed sulphur hexafluoride using a point/cup electrode system," No. 4, pp. 111–1 – 111–4, IEEE, 1996. (cited in pages 36, 37 and 38)

[22] K. Nakanishi, A. Yoshioka, Y. Arahata, and Y. Shibuya, "Surface charging on epoxy spacer at DC stress in compressed SF6 gas," *Power Apparatus and Systems, IEEE Transactions*, no. 12, pp. 3919–3927, 1983. (cited in page 36)

[23] Y. Shibuya, N. Yamada, and T. Nitta, "Electrical breakdown and prebreakdown dark current in compressed sulphur hexafluoride," (cited in pages 36, 37, 45 and 58)

[24] J. Dutton and W. Morris, "The mechanism of the electrical breakdown of air in uniform fields at voltages up to 400 kv," *British Journal of Applied Physics*, vol. 18, no. 8, p. 1115, 1967. (cited in pages 36, 38 and 39)

[25] F. L. Jones and C. Morgan, "Surface films and field emission of electrons," *Proceedings of the Royal Society of London. Series A. Mathematical and Physical Sciences*, vol. 218, no. 1132, pp. 88–103, 1953. (cited in pages 38 and 39)

[26] T. Stern, B. Gossling, and R. Fowler, "Further studies in the emission of electrons from cold metals," *Proceedings of the Royal Society of London. Series A*, vol. 124, no. 795, pp. 699–723, 1929. (cited in pages 38 and 39)

[27] A. H. Cookson, "Electrical breakdown for uniform fields in compressed gases," in *Proceedings of the Institution of Electrical Engineers*, vol. 117, pp. 269–280, IET, 1970. (cited in page 38)

[28] C. Duke and M. Alferieff, "Field emission through atoms adsorbed on a metal surface," *Journal of Chemical Physics*, vol. 46, pp. 923–937, 1967. (cited in page 38)

[29] M. Jimenez, R. Noer, G. Jouve, C. Antoine, J. Jodet, and B. Bonin, "Electron field emission from selectively contaminated cathodes," *Journal of Physics D: Applied Physics*, vol. 26, no. 9, p. 1503, 1993. (cited in page 40)

[30] F. Le Pimpec, R. Ganter, and R. Betemps, "Field emission dark current of technical metallic electrodes," *Nuclear Instruments and Methods in Physics Research Section A: Accelerators, Spectrometers, Detectors and Associated Equipment*, vol. 574, no. 1, pp. 7–16, 2007. (cited in page 40)

[31] S. Okabe, "Phenomena and mechanism of electric charges on spacers in gas insulated switchgears," *Dielectrics and Electrical Insulation, IEEE Transactions*, vol. 14, no. 1, pp. 46–52, 2007. (cited in pages 10, 15, 16, 17, 18, 22, 41, 114 and 124)

[32] A. Zeitoun-Fakiris and B. Juttner, "Effect of anode gas liberation on prebreakdown currents in vacuum," *Electrical Insulation, IEEE Transactions*, vol. 23, no. 1, pp. 83–86, 1988. (cited in page 44)

[33] D. Alpert, D. Lee, E. Lyman, and H. Tomaschke, "Effect of gas pressure on electrical breakdown and field emission," *Journal of Applied Physics*, vol. 38, no. 2, pp. 880–881, 1967. (cited in pages 44 and 45)

[34] M. Hajra, C. Hunt, M. Ding, O. Auciello, J. Carlisle, and D. Gruen, "Effect of gases on the field emission properties of ultrananocrystalline diamond-coated silicon field emitter arrays," *Journal of applied physics*, vol. 94, no. 6, pp. 4079–4083, 2003. (cited in page 44)

[35] A. Simonin, H. de Esch, L. Doceul, L. Christin, F. Faisse, and F. Villecroze, "Conceptual design of a high-voltage compact bushing for application to future n-nbi systems of fusion reactors," *Fusion Engineering and Design*, vol. 88, no. 1, pp. 1–7, 2013. (cited in pages 44 and 45)

[36] "Vaisala online calculator, available on http://www.vaisala.com," (cited in pages 62 and 65)

[37] E. Huber Jr and C. Kirk Jr, "Work function changes due to the chemisorption of water and oxygen on aluminum," *Surface Science*, vol. 5, no. 4, pp. 447–465, 1966. (cited in page 87)

[38] T. Fort Jr and R. L. Wells, "Adsorption of water on clean aluminum by measurement of work function changes," *Surface Science*, vol. 32, no. 3, pp. 543–553, 1972. (cited in page 87)

[39] R. Batt and C. Mee, "A photoelectric technique for the study of adsorption: the aluminum-oxygen and aluminum—water systems," *Applied optics*, vol. 9, no. 1, pp. 79–84, 1970. (cited in page 87)

[40] A. Stintz and J. Panitz, "Cluster ion formation in isothermal ramped field-desorption of amorphous water ice from metal surfaces," *Surface science*, vol. 296, no. 1, pp. 75–86, 1993. (cited in page 88)

[41] H. R. Carlon, "Electrical properties of atmospheric moist air: A systematic, experimental study," tech. rep., DTIC Document, 1988. (cited in page 88)

[42] R. Gomer, "Field emission, field ionization, and field desorption," *Surface science*, vol. 299, pp. 129–152, 1994. (cited in page 88)

[43] V. Medvedev, C. Rothfuss, and E. Stuve, "Ionization of water in high electric fields at and near a metal electrode surface," *Electrochemical surface science*, 2001. (cited in page 89)

3 | Electrical properties of insulator materials under DC voltage

Contents

In this chapter, the objective is to characterize the current on surface and through the volume of insulators used in a GIS. We will first review the usual parameters and measurements techniques used to characterize materials. Then we will detail the experimental system used and the protocol established to perform those measurements. Finally, the results are presented and discussed.

3.1 | Definition and technological standard used for electrical characterization

To characterize the electrical properties of solid insulators, several measurements can be performed. Surface potential decay measurements can be realized in a controlled atmosphere in order to investigate the dynamics of surface charge relaxation. In addition, complementary measurements of insulator resistivities (surface and volume) can be performed to quantify conduction mechanisms. Then, the dielectric strength of the insulator can also be investigated to estimate the maximum electric field value which could be afforded.

3.1.1 | Transient current in insulators

Transient currents are illustrated in figure 3.1 and divided into two types of currents. When an electric stress is applied to an insulator, a first term composed of polarization and conduction currents can be recorded (eq. 3.1). Then, when the applied voltage is stopped, the depolarization current is measured until the current reached the zero value (eq. 3.2).

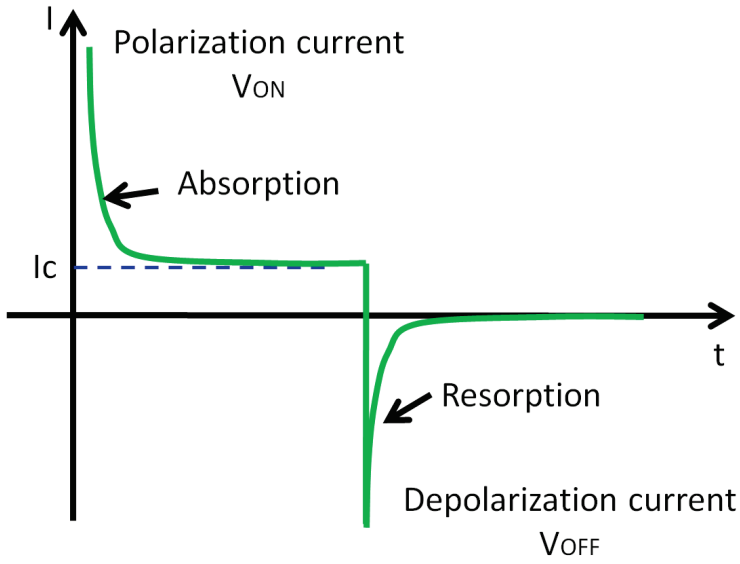

Fig. 3.1: Variations of absorption and resorption current versus time in a solid dielectric during and after electrical stress.

It is assumed that when those absorption and resorption currents are symmetric (as reported in [1]), the conduction current of the material can be calculated (eq. 3.3).

$$I(t)_{V_{ON}} = I(t)_{Polarization} + I(t)_{Conduction} \tag{3.1}$$

$$I(t)_{V_{OFF}} = -I(t)_{Polarization} \tag{3.2}$$

$$I(t)_{Conduction} = I(t)_{V_{ON}} + I(t)_{V_{OFF}} \tag{3.3}$$

In our investigation, the maximum electric field applied to the material is of $4\,kV/mm$.

The conduction current can be obtained using equation (3.3) if a V_{ON}/V_{OFF} measurement is performed, or simply by waiting the stabilization of the current under voltage. In our experiments, this second approach is used since measured absportion and resorption current are not symmetric.

3.1.2 | Volume and surface resistivities

When insulating materials follow the Ohm's law, the current density passing through the insulator can be written as a function of the electric field as follows:

$$\overrightarrow{J} = \frac{\overrightarrow{E}}{\rho} \tag{3.4}$$

Where J is the current density, ρ is the volume resistivity of the insulator, and E is the electric field strength. In this case, the current-voltage characteristic is linear with the electric field. This relation is usually limited to low electric stress (few kV/mm), when no charge injection takes place.

Other mechanisms for conduction through the insulator volume could happen such as *Poole-Frenkel* mechanisms, *hopping conduction* or also *current limited by space charges* [2]. Those mechanisms are not detailed in our work since in our study the main objective is to obtain data to build a first-order model of the electric field distribution in real insulators, with the assumption that materials are Ohmic.

The stabilized conduction current measured during the application of voltage, results in charge movement through the insulator toward the electrodes. The stabilization time may last from some minutes up to several days or weeks depending on the material considered. Measurements are often performed according to the international standard $IEC60093$ [3], which recommends to stop the current measurement as soon as two successive measurements are identical. It is noted that a short stabilization time of 1 min should be sufficient. In our case with very high resistivity materials, this recommendation is not adequate, as discussed below.

In the following (section 3.5), we will propose a well-defined protocol to measure stabilized currents since the standard $IEC60093$ is not consistent in our case.

3.1.2.1 Volume resistivity

The volume resistivity is calculated based on the «stabilized conduction current» which passes through the sample positioned between two electrodes (figure 3.2). The quotient of the applied voltage and the stabilized current measured through the insulator volume allows

determining the volume resistivity, excluding the current along the surface, and according to the electrodes dimensions. Here, the equation is written considering a circular geometry. Further electrodes geometries are described in the standard $IEC60093$ [3].

$$\rho_v\,[\Omega.cm] = \frac{V}{I_V} * \frac{S}{e} \tag{3.5}$$

With $S = \pi * \frac{(d_1+g)^2}{4}$, V the applied voltage, I_V the current through the insulator volume, and e the insulator thickness.

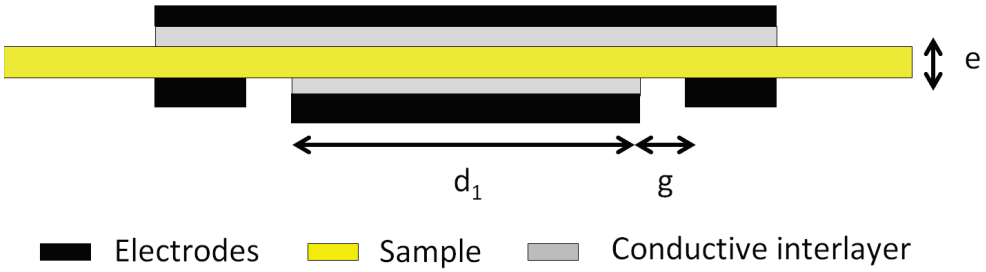

Fig. 3.2: Electrodes dimensions, d_1 the diameter of the measurement electrode and g, the gap between electrodes.

3.1.2.2 Surface resistivity

The surface resistivity is calculated based on the stabilized conduction current which passes along the sample surface, but also partly through the volume [4], in the electrodes configuration presented in figure 3.2. The quotient of the applied voltage and the stabilized current measured in a surface layer of an insulating material allows the calculation of this parameter. As for volume resistivity, the geometry considered here is circular.

$$\rho_s\,[\Omega/sq] = \frac{V}{I_s} * \frac{P}{g} \tag{3.6}$$

With $P = \pi * (d_1 + g)$, and g the distance between the guarded and measurements electrodes.

In HVDC, those properties must be very well-known, as well as their variations depending on environmental conditions (temperature, relative humidity, electric field, and so on), since the electric field distribution directly depends on those properties.

3.1.3 | Dielectric strength of insulators

The dielectric strength of an insulating material corresponds to the maximum electric field value that can be applied on it without any non reversible damages on the insulator. Such

damage, named breakdown, destroys the insulating properties of the material. Hence, after a breakdown, the initial voltage can not be applied anymore.

In case of an uniform electric field, the dielectric strength corresponds to the applied voltage divided by the distance between electrodes on which the voltage is applied ($E = V/g$).

In case of a GIS, the maximum electric field applied (some kV/mm) is far from breakdown conditions of solids (usually in the range of $100\,kV/mm$). In the geometry of a GIS, breakdown can mainly occur at the gas/solid interface (creeping distance). The electric field distribution within the solid can have a large influence on this breakdown at the surface.

3.2 | Materials

An alumina-filled epoxy resin (60% of alumina fillers) is used in GIS by Siemens to maintain the conductor and to separate compartments. This material is a mixture of organic matter and mineral charges. Our investigation is not directly performed on the real shape of spacer used for the application, but on cylindrical samples of $80\,mm$ in diameter, and with a thickness between 2 and $6\,mm$. A photograph of the sample is shown in figure 3.3, as well as a Scanning Electron Microscope (SEM) image of the surface where the alumina fillers can be observed.

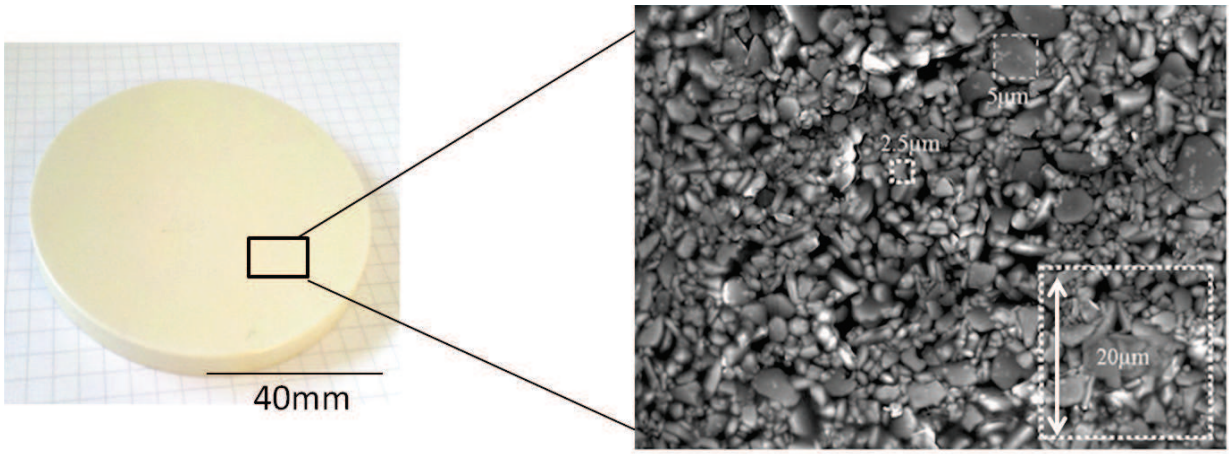

Fig. 3.3: Left: photography of the used sample used. Right: SEM image of the studied material; $X2500 - HV20k$, SEI.

Two materials of similar compositions currently in use in AC application are studied. Those materials are named *material A* and *material B* in the following. All samples are previously cleaned with ethanol to remove polar molecules, and acetone to remove the grease. Then, samples are rinsed with distilled water. In order to get quantitative data about the material water content, specific drying and impregnation procedures described below were used. This preliminary study was necessary, since epoxy composition can absorb large quantities of water (up to about 1%), which greatly influence the dieletric properties.

3.3 | Sample conditioning

3.3.1 | Determination of the drying time

The samples, as received, initially contained some water, which could be due to the transport, the storage, and also to the fabrication procedure. To remove this water, the samples are placed in a vacuum oven under temperature (65 °C or 90 °C). Measurements of mass losses with a high resolution balance (0.1 mg) are regularly performed during this drying procedure, in order to determine time after which they are fully dried. It is reached when a constant mass is recorded.

Figure 3.4 shows examples of the mass losses for both materials A and B with different thicknesses. It is observed that after 10 days, there are no more significant mass losses. In addition, it is seen that whatever the sample thickness and its initial water concentration, similar dynamics are observed, for both materials. It is worth noting that all samples delivered by Siemens initially contained water. Depending on their thickness, they contained between 0.06 to 0.16% of water in mass, which represents from 0.09 to 0.2% of the saturation at 90 °C and $RH = 60\%$ (presented below).

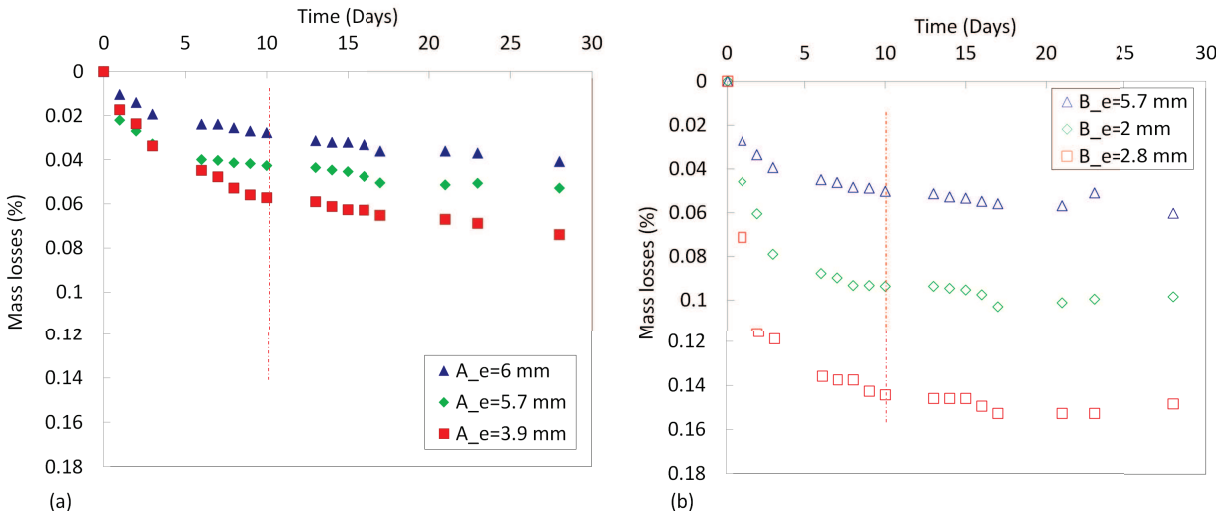

Fig. 3.4: Determination of the drying time in the vacuum oven at 65 °C for both material A (a), and B (b).

The drying procedure adopted to all samples before measurement is to dry them within a vacuum oven at 90 °C for at least 10 days. After this conditioning, the reference mass m_0 is determined.

3.3.2 | Measurements of water absorption

The diffusion kinetics of water in epoxy resins has been widely studied [5,6]. With flat disk samples the diffusion follows a one dimensional Fick's Law (represented in figure 3.5), in which the diffusion (from t_0 to t_1) is linearly controlled by the gradient of water concentration between the environment and the material, until its equilibrium (at t_∞). Shen *et al.* [7] show that according to this model, the mass uptaked M due to absorption is described by relation (1) (M_∞: mass at equilibrium, h: sample thickness, t: time and D: diffusion coefficient).

$$M(t) = M_\infty \frac{4}{h\sqrt{\pi}} \sqrt{Dt} \tag{3.7}$$

The diffusion coefficient D is then calculated based on equation (eq. 3.8). Note that the simplified Fick law (eq. 3.7) can only be applied between t_0 and t_1.

$$D = \frac{h^2 \pi}{16t} \left(\frac{M(t_1)}{M_\infty} \right)^2 \tag{3.8}$$

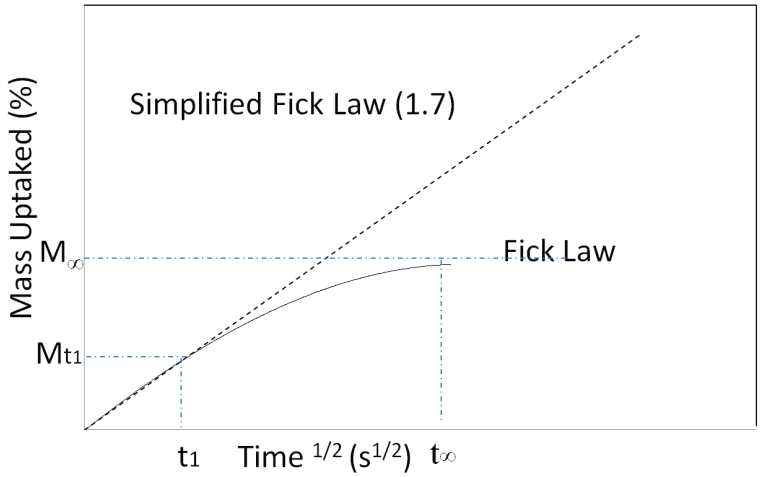

Fig. 3.5: Diffusion model.

Following the procedure presented above, samples are firstly dried in a vacuum oven at 90 °C until complete removal of water (*i.e.,* when their weight shows no more variation versus time). Periodical weighting are performed using a high precision balance (0.1 mg resolution). Then, samples are placed in a climatic chamber at 90 °C and Relative Humidity ($RH = 60\%$), until an equilibrium is reached (corresponding to 60% of saturation). During the absorption process, it is assumed that no washing-off process (*i.e.,* loss of resin or fillers) occurs.

Figure 3.6 shows the relative mass uptaked versus time: $M(t) = (m(t) - m(t_0))/m(t_0)$, for a sample of $3.28\,mm$ thickness. The shape of the curve is in agreement with a one dimension Fick's model. The water content at equilibrium is close to $Wc = 0.25\%$ (*i.e.*, $2500\,ppmw$) at 90 °C and 60% RH, (hence corresponding to $Wc = 0.41\%$ at saturation).

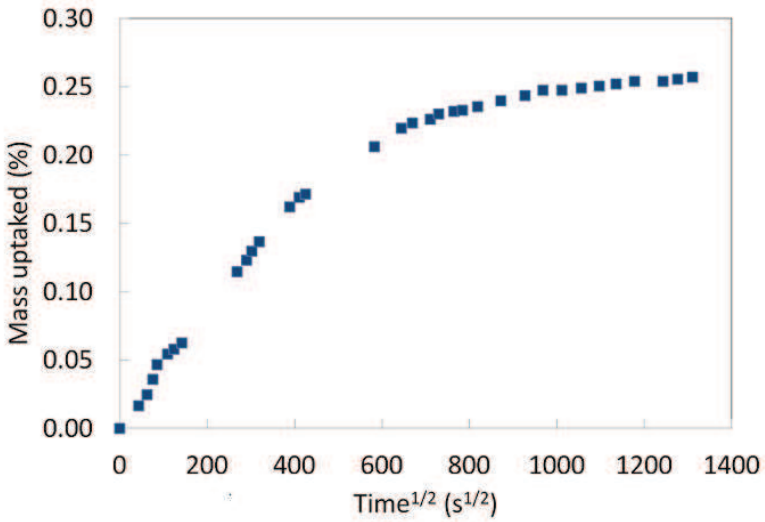

Fig. 3.6: Water absorption measurements of material A on $3.28\,mm$ sample thickness at 90 °C and 60% RH.

The diffusion coefficient D of epoxy resin at 90 °C is calculated based on the following equation [8].

$$\frac{m - m_0}{m_{sat} - m} = \frac{4}{\sqrt{\pi}} * \frac{\sqrt{Dt}}{h} \tag{3.9}$$

This expression is only verified in the linear initial part of the curve. Its slope allows determining the diffusion coefficient, based on the equation (3.9). In our case, it is equal to $6.5.10^{-12}\,m^2/s$.

To obtain reproducible measurements, we have adopted the presented drying procedure before all experiments. Concerning experiments with various water concentration, the impregnation method described here-above has been applied.

3.4 | Surface potential decay measurements

The tendency of materials to accumulate or dissipate rapidly surface charges constitutes an important parameter for HVDC GIS applications. This feature can be evaluated by Surface Potential Decay measurements (SPD). As previously reported in chapter 1, the phenomenon of surface potential decay is complex and results from the superposition of

various phenomena. Charges can dissipate following several ways: spreading over the insulator surface, conduction through its volume, and neutralization by ions present in the environment. In addition, displacement currents within the material, associated to long term polarization effects, may also contribute to the variation of the surface potential.

In our work, we use this technique to obtain a qualitative assessment of influencing parameters which worth to be studied, and to compare various materials. In this section, we will first present the experimental system, then we will discuss the results obtained according to various parameters.

3.4.1 | Experimental system

To measure the surface potential decay on insulator surfaces, the experiment is divided into two parts. The first one consists in charging the insulator using corona discharge, and the second step is the measurement of the surface potential decay during time. The experimental setup is presented in figure 3.7. A motorized device allows to rotate the support and position it under the charging system where a corona discharge occurs during $20\,s$, in order to charge the material surface with ions. The initial uniform surface charge distribution is confined into a $2\,cm$ diameter area. The experimental arrangement is presented on figure 3.7 (b). The corona discharge is created applying high voltage on a needle, which will ionize the surrounding air around it and create ions. The latter are then injected toward the sample direction. A polarized grid, placed between the needle and the sample surface, will uniformly distribute charges over the insulator surface, and also fix the value of the desired surface potential. Once the corona discharge ends, the sample is positioned back under the measurement device where the non-contact electrostatic probe records the evolution of the surface potential during time (figure 3.7 (c)). The surface potential is measured using a vibrating Kelvin probe. This electrostatic voltmeter employs a field-nulling technique that achieves DC stability and high accuracy, even if the probe-to-surface spacing changes. The probe used is a Trek model 347® with probe model 6300 (range 0 to $\pm 3\,kV$; accuracy better than 0.05% of full scale). The probe to surface separation is $2 \pm 1\,mm$.

During the whole experiment, the sample is fixed on its support to avoid any movements during the rotation. In addition, to ensure a good contact between the back-side of the sample and the grounded ring, a conductive inter-layer is placed between the sample and the ring. It had also been observed that covering the back-side of the sample using a copper tape enabled a better ground contact and a better reproducibility in measurements.

The system, placed in a climatic chamber, is remotely controlled using a software program which allows controlling the motors and other relays.

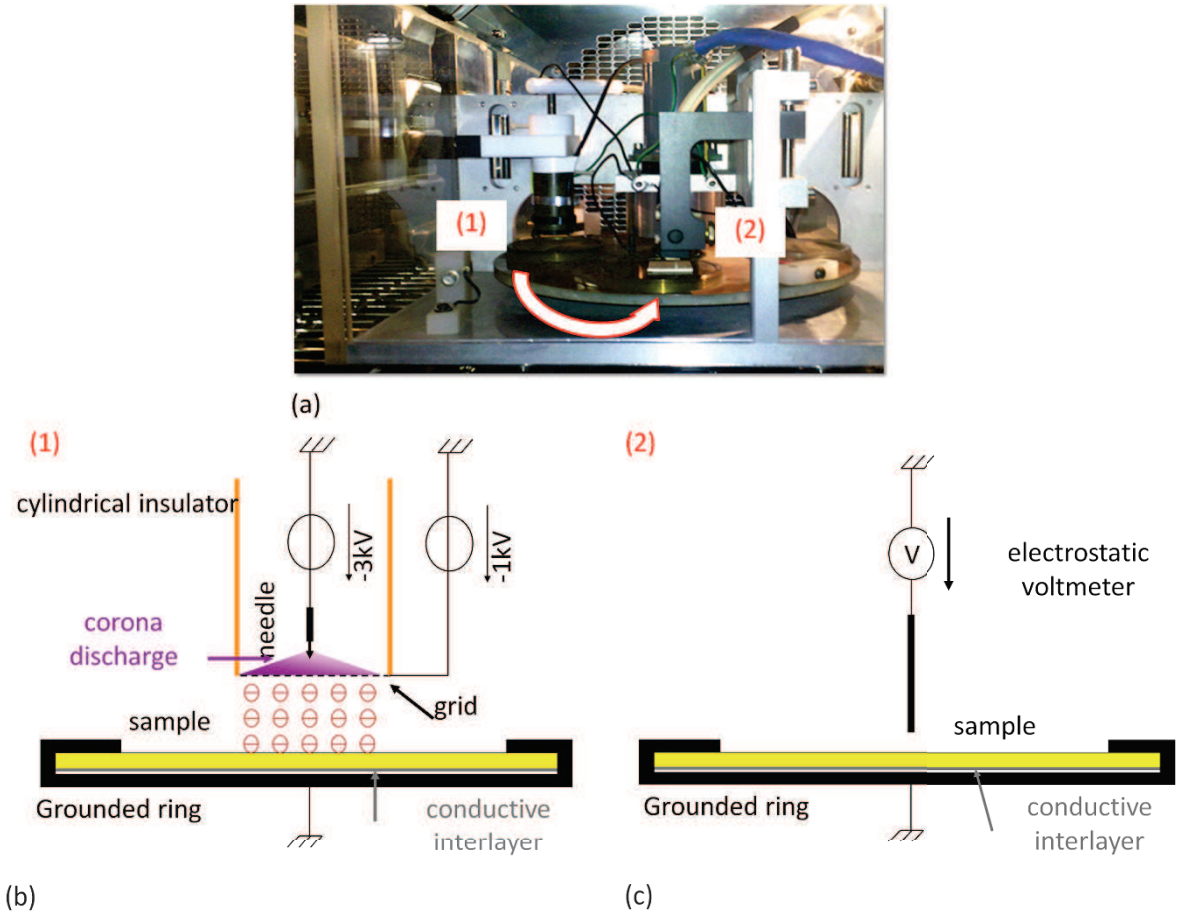

Fig. 3.7: (a) Experimental device for surface potential decay measurements at different temperatures and relative humidities, (b) charge deposition and (c) measurement principles.

3.4.2 | Experimental protocols

To perform a complete study on the SPD for various materials, the influence of temperature, relative humidity and water concentration in the sample should be investigated. For the experiments, the drying procedure presented in section 3.3 was first performed on all samples. The samples are stored under vacuum at 90 °C until they are used for an experiment. Measurements were done for different temperatures and relative humidities. A climatic chamber was used to adjust those parameters with accuracy.

Before measurements, the climatic chamber is set in equilibrium during 1 h. The sample is prepared with a conductive inter-layer on the grounded side, and placed in the climatic chamber for 15 min. After this time, the charging is performed during 20 s, and then the sample is quickly moved under the electrostatic probe, thanks to the rotating platform. The evolution of the SPD is recorded during 8 h for all samples.

Experiments were performed with either dry or $W_c = 0.41\%$ samples, following the conditioning of section 3.3. With both dry and water saturated samples, four sets of

environmental conditions, presented in table 3.1, were used according to the climatic chamber specifications.

Protocols	*Temperature*	*Relative Humidity*
P_1	40 °C	20%
P_2	40 °C	80%
P_3	65 °C	20%
P_4	65 °C	80%

Tab. 3.1: Experimental conditions used during SPD measurements.

Two main materials were first investigated: material A and material B. In a second step, materials of different compositions prepared by Siemens were studied.

3.4.3 | Results

3.4.3.1 Preliminary experiments

A preliminary experiment has been performed on material A to evaluate the reproducibility of our measurements. Three samples of 5 mm thickness, initially dried have been tested under the same conditions (40 °C, $RH = 20\%$). The potential decay on those samples is represented in figure 3.8. The initial potential on the sample surface is fixed to $-1000\,V$. The results presented are normalized to the maximum initial voltage. It can be observed that a very slow decay is recorded with a loss of $100\,V$ over $8\,h$. In addition, a maximum scatter of 1% (in black) is seen, showing a good reproducibility.

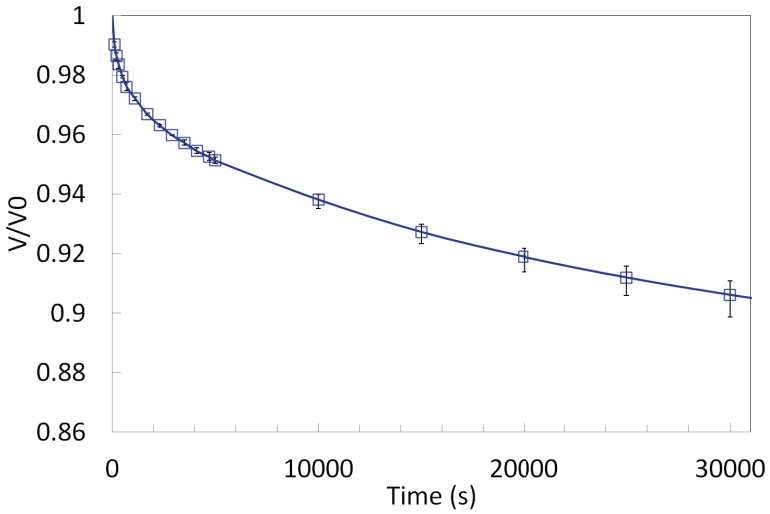

Fig. 3.8: Evaluation of the measurements reproducibility on material A for three dried samples at 40 °C, $RH = 20\%$.

3.4.3.2 SPD depending on Temperature and Relative Humidity for dry materials A and B

SPD was measured for both materials A and B at two temperatures $T = 40\,°C$ and $T = 65\,°C$ and two relative humidities 20% and 80%. Figure 3.9 presents the SPD for materials A and B at (a) 40 °C and (b) 65 °C. In those figures, several observations can be made. First, it is shown that the dynamic of the SPD is different for material A and B. At $40\,°C/RH = 20\%$, SPD of only 10% is observed for material A, whereas a SPD of 70% is recorded for material B after 8 hours. Secondly, it is observed that at 40 °C (figure 3.9 (a)) the surface potential decay is similar whatever the relative humidity (20% or 80%) for material A, while for material B the SPD is enhanced at higher relative humidity (at $RH20\%$ a SPD of 70% is recorded whereas at $RH80\%$ a SPD of 90% is observed after 8 hours).

At 65 °C (figure 3.9 (b)), the SPD is significantly enhanced for material A and B at $RH = 20\%$ and $RH = 80\%$. For material A, the temperature has a strong impact on the decay dynamics, and the RH played a non negligible role on this decay. The influence of relative humidity is very weak at 40 °C, and larger at 65 °C. For material B, with the increase of temperature, all charges had been removed after $8\,h$ since no potential was recorded.

These results show that the temperature has a predominant role in the potential decay compared to relative humidity.

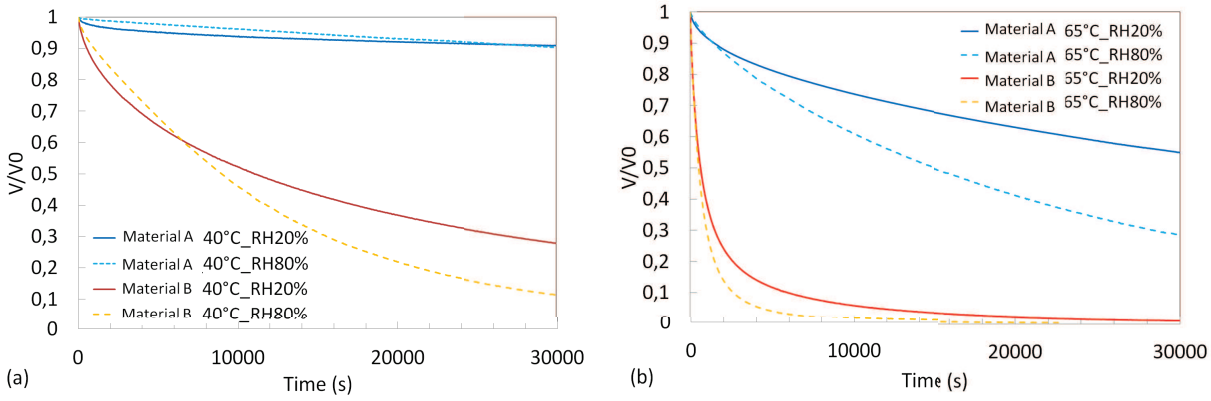

Fig. 3.9: SPD evolution on material A and B at (a) 40 °C (P_1 and P_2) and (b) 65 °C (P_3 and P_4).

3.4.3.3 SPD depending sample on water content

A comparison between dried and wet samples with fixed conditions (P_1) is made on figure 3.10. For the wet sample ($W_c = 0.4\%$), the surface potential drops by 75% after 8 hours whereas a SPD of 10% is recorded for the dried sample. The potential decay is

strongly enhanced (by a factor of 7) in the wet sample. This result strongly suggests that volume conduction has an important influence on the measured surface potential decay.

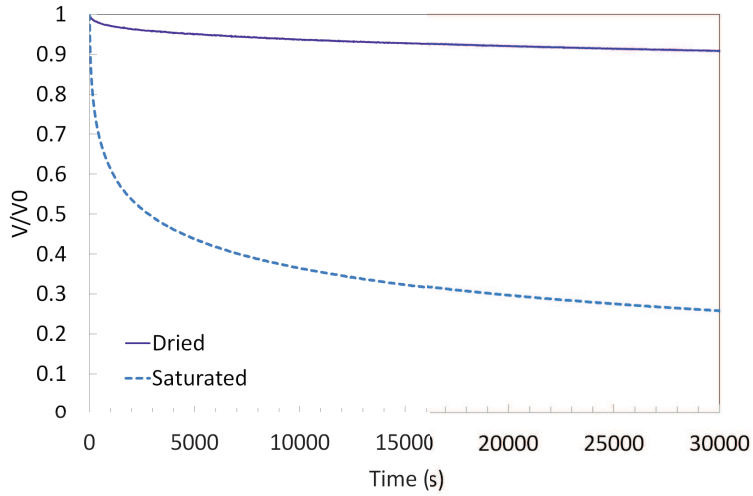

Fig. 3.10: SPD versus water contents for material A at 40 °C, $RH = 20\%$.

3.4.3.4 SPD depending on material's composition

The conductivity of standard materials A and B used in HVAC systems, were characterized by Siemens following the International Standard $IEC60093$, and were considered to present similar electrical properties (volume resistivities). However, our SPD measurements clearly evidenced a difference between those materials. Hence, the influence of the composition of materials was further investigated hereafter. Materials A and B are prepared using the same base epoxy resin and approximately similar quantities of alumina fillers. In order to determine which difference in their composition makes their SPD different, the influence of the fillers, catalyst and hardener are successively studied.

Figure 3.11 presents the SPD for various compositions of materials A and B. It can be observed that the removal of alumina fillers results in a slightly larger decay at long duration (figure 3.11 (a)). In addition, figure 3.11 (b) shows that changing the hardener and the catalyst also has a strong impact on the SPD. It can be observed that using another catalyst (K_x) during material B fabrication leads to a SPD similar to those of material A in same conditions.

These results evidence the large influence of the material chemical composition on charge decay. Additional modifications of the material composition have been performed in order to further increase the volume conduction and to obtain a material able to quickly relax charges. The investigation was focused on the influence of the nature of the resin, the concentration of catalyst used during the reaction and its position in the chemical chain. Figure 3.12 shows the SPD evolution recorded for three epoxy resins (A, B and C) and other

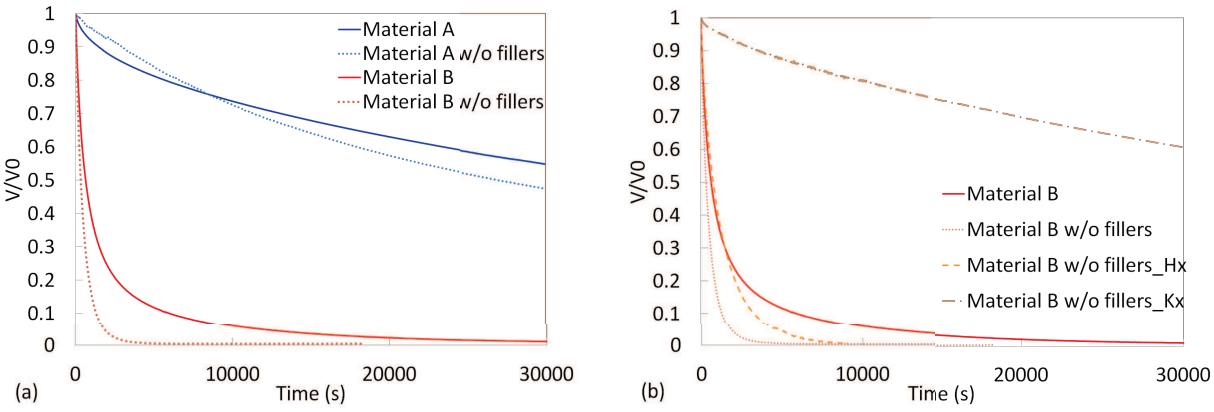

Fig. 3.11: SPD variations for (a) both materials A and B, with and without fillers, and (b) material B with various chemical compositions (H_x: other hardener, K_x other catalyst), at 65 °C, $RH = 20\%$.

variations (C2, C3 and B2 to B5) with the same base of resin, but varying the concentration and type of catalyst. The most influencing parameters seems to be the catalyst nature, position and its concentration during the reaction. The faster SPD is obtained for material B5 with a new catalyst.

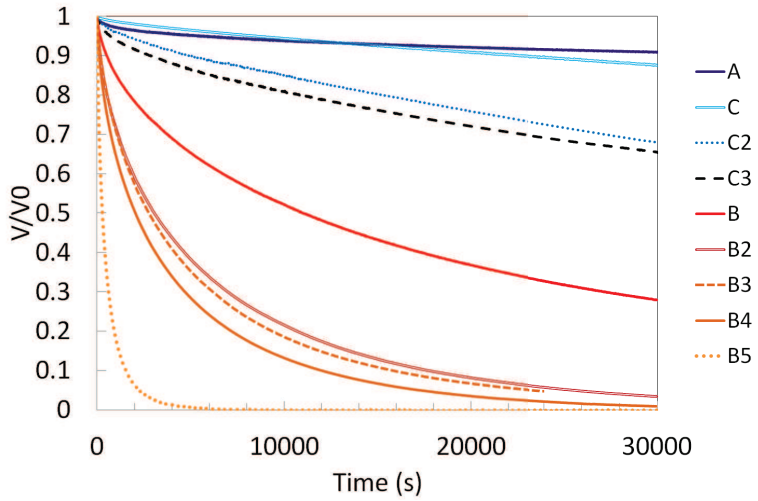

Fig. 3.12: SPD evolution for three epoxy resins and modifications on the catalyst concentration, position and nature, at P_1 (40 °C, $RH = 20\%$).

3.4.3.5 Comments

In this section, it has been evidenced that in the electric field geometry used in our device, a large difference in the surface potential decay exists between material A and B for two temperatures and relative humidities. These materials were previously considered to be equivalent, considering the results of resistivity measurements according to $IEC60093$

standard test. It has also been observed that temperature and sample water content have a great impact on charge decay. With an increasing temperature and water content, charge decay is greatly accelerated. The influence of the material composition clearly shows that the catalyst has a large influence on the decay dynamics.

This investigation of SPD allows us to point out qualitative differences between existing materials, and to evidence the large impact of several parameters: temperature, water content, and material composition.

However, it is not possible to transpose directly these results to the practical case of a $HVDC$ GIS, mainly due to the rather large difference of electric field geometry.

In the SPD measurements, the electric field is only due to the presence of surface charges, and the electric field lines are mainly normal to the surface. In a GIS insulator, a high electric field is imposed by the applied voltage, and its direction is mainly parallel to the surface. These features can induce large differences in both charge relaxation mechanisms and dynamics. In order to build a numerical model of the conduction in a realistic geometry, measurements of volume and surface resistivities must first be carried out versus several parameters: electric field, temperature, and water content.

3.5 | Volume resistivity measurements

Measurements of conduction current through the insulator volume were performed using a home-made device based on the geometry described by the standard $IEC60093$. In this section, experimental systems are presented and a protocol is proposed concerning the measurement of stabilized conduction currents. Currents are then investigated according to temperature, relative humidity, water concentration, material composition and electric field.

3.5.1 | Experimental system

The volume resistivity is calculated from conduction currents measured through the sample volume. Figure 3.13 (a) shows the experimental device used for current measurements. The sample is placed between two main electrodes plus a guard electrode. In order to carry out dielectric measurements versus various parameters (water concentration, temperature), the classical method which consists in plating the material to achieve a suitable electrical contact was not possible (the metal layer constitutes a barrier to water diffusion, and is damaged after several cycles of impregnation and dielectric measurements). Instead, soft and conformable conducting layers made of conducting silicone were placed between the electrodes and the sample (figure 3.13 (a)). These layers induce a $10\,\Omega$ resistance in series with the sample. Comparative dielectric spectroscopy measurements carried out with this system, and with a classical gold metallization showed no significant differences, which validates this system. The distance d between the guard electrode and the measurement

electrode is $d = 2\,mm$, and the diameter of the measurement electrode is $52\,mm$. Quoted values for the electric field E correspond to the average field, $E = V/d$.

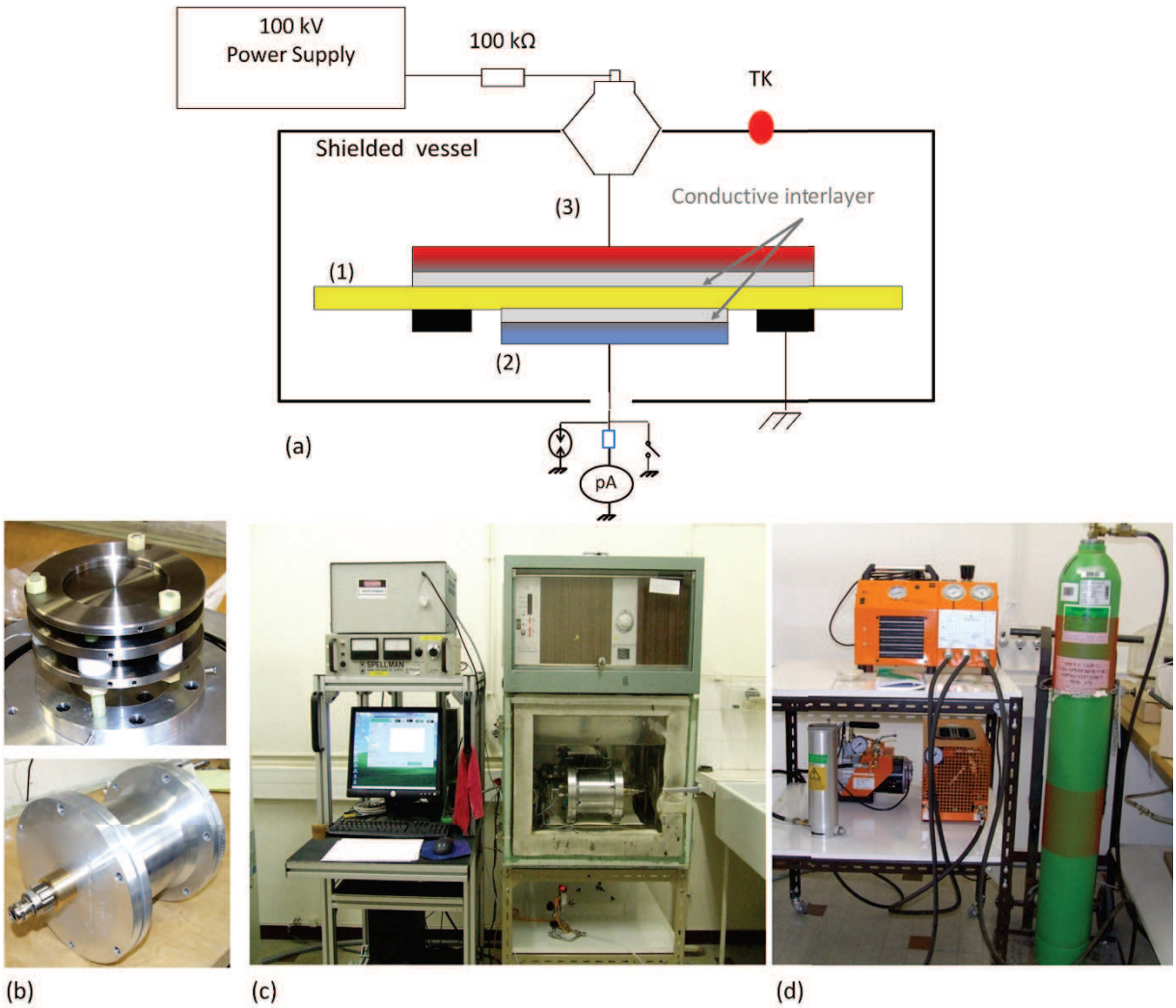

Fig. 3.13: Current measurement through the material volume. (a) Measurement principle: the insulator (1) is placed between the measurement electrode (2) and the high voltage electrode (3), TK: thermocouple. (b) Electrode arrangement and shielded enclosure, (c) illustration of the entire test setup, (d) fill-in and recovering SF_6 device.

Currents are measured with a high resolution electrometer Keithley $6517B^{®}$, using either the built-in low noise voltage source ($\pm 1\,kV$; $3\,ppm$ noise) or a $20\,kV$ Spellman power supply equipped with a high voltage filter ($0.2\,\mu F$ capacitor) to reduce the noise. The entire electrode system (figure 3.13 (b) up) is placed in a high pressure vessel (figure 3.13 (b) bottom) and connections to the electrometer are done with a low noise triaxial cable.

The noise of current measurements was reduced by using an averaging technique (quoted data represent the average of 2000 samples). The absolute error of measurements is estimated to be approximately $\pm 100\,fA$. To measure stabilized DC conduction current and avoid the influence of polarization, a long measurement time was necessary, especially with dry

samples with a very high resistivity ρ_v ($\rho_v > 10^{18}\,\Omega.cm$ @ 20 °C). The measurement lasted in this case at least 2 days, in order to reach the complete stabilization, which occurred when the polarization current becomes much lower than the conduction current.

The sealed enclosure can afford pressure up to $1.1\,MPa$. It is placed within a regulated oven (figure 3.13(c)) to accurately adjust the temperature from 20 °C to 80 °C. The latter is measured during experiments thanks to a thermocouple placed within the enclosure. The system is filled with SF_6, and unfilled using compressor and pre-compressor (figure 3.13 (d)). Such device permits to recover the SF_6 down to $20\,mbar$.

This experimental system allows determining the volume resistivity of materials according to different temperature, electric field values and water concentration. A well-defined experimental protocol, detailed hereafter, was needed to obtain reproducible and accurate measurements.

3.5.2 | Experimental protocol

In this section, we describe the measurement procedure defined to obtain reproducible measurements and to avoid the influence of charges pre-existing in the material.

3.5.2.1 Preliminary experiments

To measure the current passing through the insulator volume, a voltage of $1000\,V$ is applied on material A of $3\,mm$ thickness, using the device presented above. For this experiment, the measurement is performed in air at atmospheric pressure (40 °C, $RH = 20\%$). Figure 3.14 presents the variations of the current in time. It is observed that the current first decreases from 0 to 60 min, and tends to stabilize after. This result evidences that after 1 min (duration proposed in the IEC standard) the stabilized current is far from being reached. Even at 160 min the stabilized current is not reached yet. In this case, a longer stabilization time is needed, superior than $2-3$ hours.

The volume resistivity has been calculated for material A and B based on stabilized currents (figure 3.15). According to the standard method, volume resistivities for materials A and B are very similar (approximately $10^{16}\,\Omega.cm$ at 20 °C). On the contrary, volume resistivities calculated from stabilized currents show a difference of one decade between material A and B. For each material two measurements were performed on the same sample, showing that measurements are repeatable.

Those results highlight two main points:

$\longrightarrow$ Following IEC recommendations, no differences in volume resistivities are observed between material A and B, but stable currents were not reached.

$\longrightarrow$ Resistivities calculated from stabilized currents evidence one decade difference. This difference is in agreement with the surface potential decay measurements presented

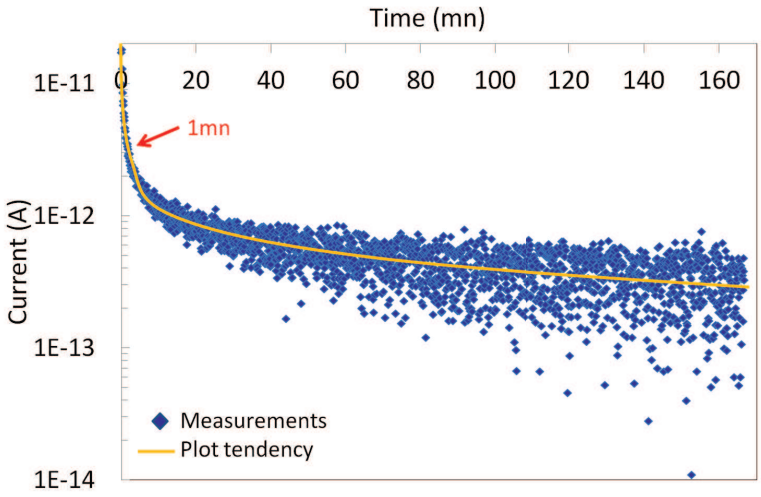

Fig. 3.14: Current measurement versus time. Voltage: $1000\,V$, at $40\,°\mathrm{C}$, $RH = 20\%$ on initially dried sample (material A).

in section 3.7, for which a faster SPD was observed for material B. In the following, we will calculate the volume resistivity only from stabilized currents. A stabilization time comprised between 3 and $4\,h$ was necessary when the device was set under constant voltage, and when temperature was changed. Altogether, this resulted in rather long experiment durations (up to several weeks) when electric field and temperature were varied.

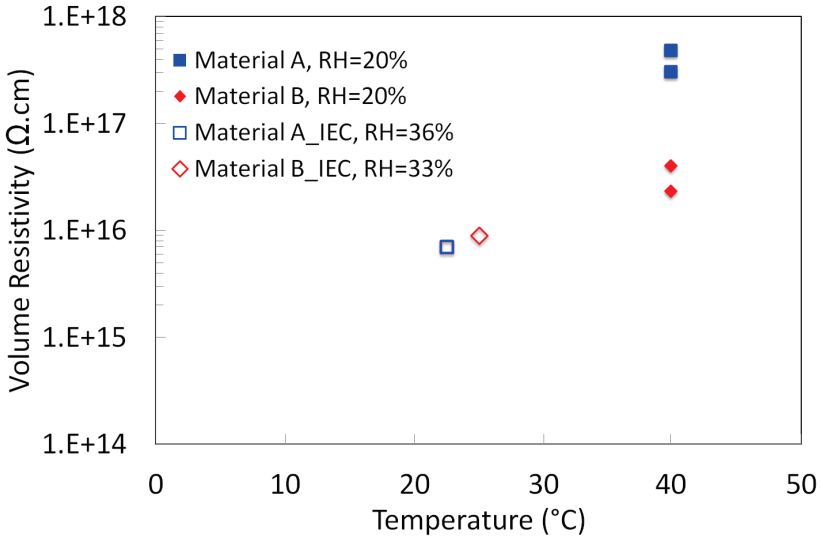

Fig. 3.15: Volume resistivity calculated following IEC standard after $1\,\mathrm{min}$ (empty symbols), and after current stabilization (between 3-4 h) on two samples (full symbols).

The electric field used to characterize our materials was comprised between 0.5 to $4\,kV/mm$ (*i.e.*, low level electric field in accordance with GIS application). The first experiments carried out showed that trapped charges initially present in the material's volume, or

remaining after voltage application may influence measurements. Figure 3.16 shows the evolution of measured current when the sample is short-circuited after a measurement series at $2\,kV$ and various temperatures (from 20 °C to 80 °C). Current peaks are observed when a temperature cycling is performed at 20 °C and 80 °C in short-circuit conditions. Moreover, it is seen that by repeating the thermal cycling, the amplitude of current peaks decreases.

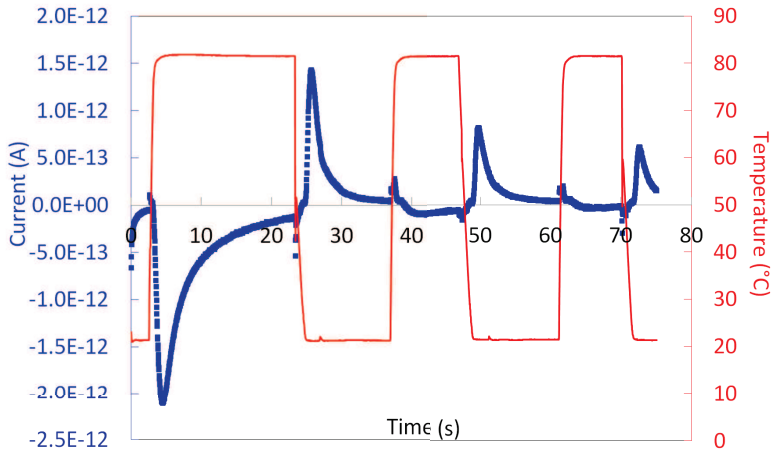

Fig. 3.16: Current measurement versus time and temperature cycling (20 °C - 80 °C) in short-circuit conditions, on material A, under SF_6.

This recording clearly shows a phenomenon of charge relaxation. To eliminate the contribution of such charges in the conduction current, it was decided to short-circuit the sample at 80 °C for one day prior to dielectric characterization.

These preliminary experiments allowed us to determine parameters which will influence the reproducibility of measurements, and improve the existing procedure. The protocol used in our work is presented in the next paragraph. The experiments were performed using material A and B.

3.5.3 | Results and discussion

The volume resistivity changes with the variations of temperature, electric field and water concentration within the material. The values of the parameters studied are listed in table 3.2. The results presented hereafter have been performed on material A of $5.3\,mm$ thickness and material B of $2\,mm$ thickness.

With material A, the behaviour of a dried sample and a sample with different water concentrations was investigated. The dried sample was characterized in SF_6 at $0.5\,MPa$. Three values of electric field were applied. For each value, the entire range of temperature was characterized. Before and after each voltage application, a depolarization step (sample short-circuited at 80 °C) was performed to eliminate residual charges. Those measurements

	Electric Field $[kV/mm]$	*Temperature* [°C]	*Water concentration* [%]
Material A	$0.5 - 1 - 2$	$20 - 40 - 60 - 80$	$0 - 0.17 - 0.2 - 0.23$
Material B	$0.5 - 1 - 2 - 5$	$20 - 40 - 60 - 80$	None

Tab. 3.2: Experimental conditions used during volume resistivity measurements.

were performed on a single sample to avoid the measurement scatter resulting from different samples.

To investigate the influence of water concentration within the material, another sample, initially dried, was used. The different water concentrations were obtained following the mass absorption protocol presented in paragraph 3.3.2. Volume resistivity measurements were done on this sample at $0.5\,kV/mm$ and 60 °C (table 3.2). When the sample reached a water concentration (W_c) of 0.2%, volume resistivity measurements were performed for the entire range of temperature.

Material B was only characterized for a dried sample at various electric field and temperatures (table 3.2). Same procedures with the depolarization step as for material A were used.

3.5.3.1 Influence of electric field and temperature on dried materials

A typical recording on material A is presented in figure 3.17 for constant electric field of $1\,kV/mm$. For each temperature step, the measurement time is fixed to $15\,h$. This time includes the time required for the temperature and current stabilization. A transition of $2\,h$ is noted when the temperature is varied, during which the current increases. Then, it tends to decrease down to its stabilized value. It is worth noting that even with those long measurements time, the current still slightly decreases after 15 hours. We consider that we are in the pseudo-permanent regime for which current variations are very low. This figure evidences the long time required to perform measurements for only one electric field value. In addition, the depolarization steps before and after measurements are not presented here. The entire measurement series including depolarization steps and measurements for each electric field values given in table 3.2, lasted approximately three weeks.

Based on these measurements, the last 20 points for each electric field and temperature were averaged and used for volume resistivity calculations. Figure 3.18 (a) shows the variations of the volume resistivity for material A versus temperature and electric field. The semi-logarithmic representation evidences a constant behaviour of volume resistivity versus electric field for values lower than $2\,kV/mm$. Moreover, a large influence of temperature is observed. A two decades difference is noted between 20 °C and 80 °C. This result is in agreement with the work reported by Okabe *et al.* [9], who evidenced that volume resistivity

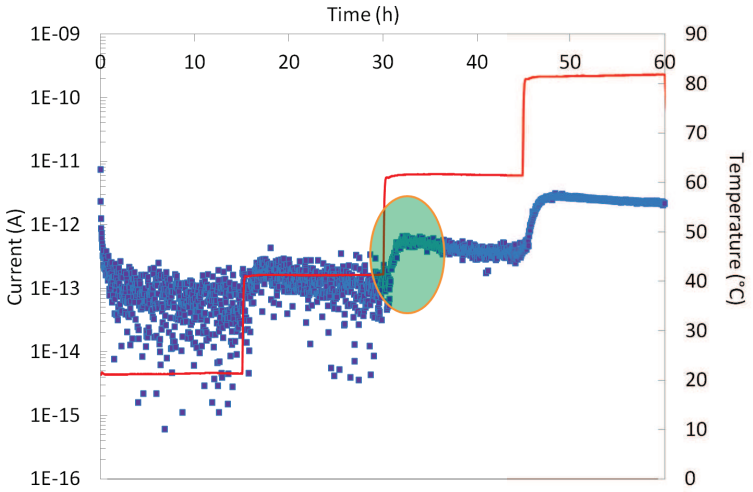

Fig. 3.17: Typical recording of current on material A under $1\,kV/mm$ in $0.5\,MPa$ of SF_6, for different temperatures.

in GIS is much more dependent on temperature than on electric field.

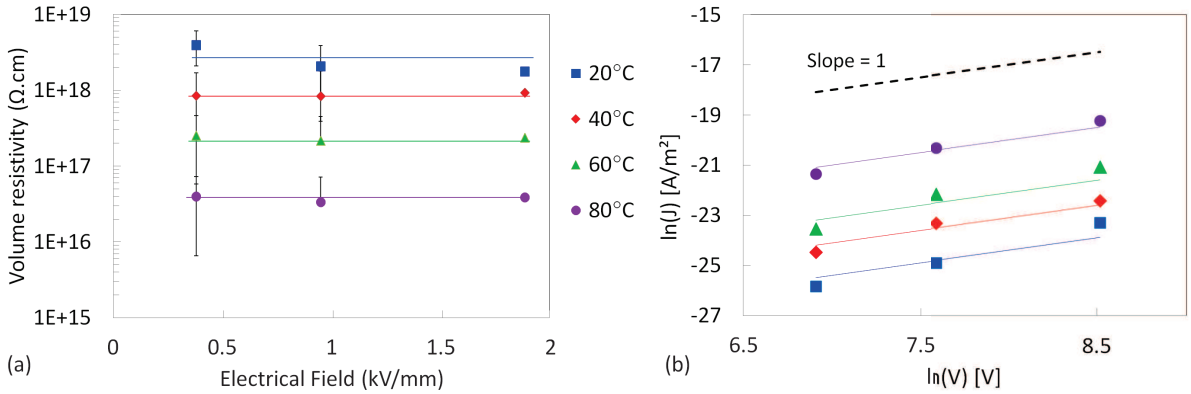

Fig. 3.18: (a) Volume resistivity variations according to electric field and temperature in SF_6 ($0.5\,MPa$), (b) $SCLC$ representation,for material A.

These measurements have been plotted according to the «Space Charge Limited Current» (SCLC) described by equation (3.10) [2], in order to evidence the conduction mechanisms encountered in our material (figure 3.18 (b)). For the range of electric field studied, a linear part with a slope = 1 is represented, which is characteristic for an ohmic conduction.

$$J = \frac{9}{8}\varepsilon_0\varepsilon_r\mu\frac{V^{l+1}}{L^{2l+1}} \tag{3.10}$$

Where J is the current density in A/m^2, V is the applied voltage, L is the insulator thickness, μ is the carrier mobility, and $\varepsilon_{0,r}$ is vacuum, relative permittivity.

Similar experiments at higher electric field have been performed on material B (fig-

ure 3.19). As in material A, the volume resistivity is fairly constant for electric field lower than $3\,kV/mm$. At higher electric field ($5\,kV/mm$), the volume resistivity tends to decrease. According to the $SCLC$ plots presented in figure 3.19 (b), the material presents an ohmic conduction for electric field lower than approximately $3\,kV/mm$ (slope = 1) while for higher field, slopes = 2 are present, which is characteristic for a space charge limited regime. However, a large uncertainty exists on this conclusion since the change of slope is only based on two points. Hence it can be assumed that for electric field superior than $\sim 3\,kV/mm$ the conduction follows a $SCLC$ mechanism for which different levels of traps can exist within the epoxy resin, but also at the interface between the fillers and the resin.

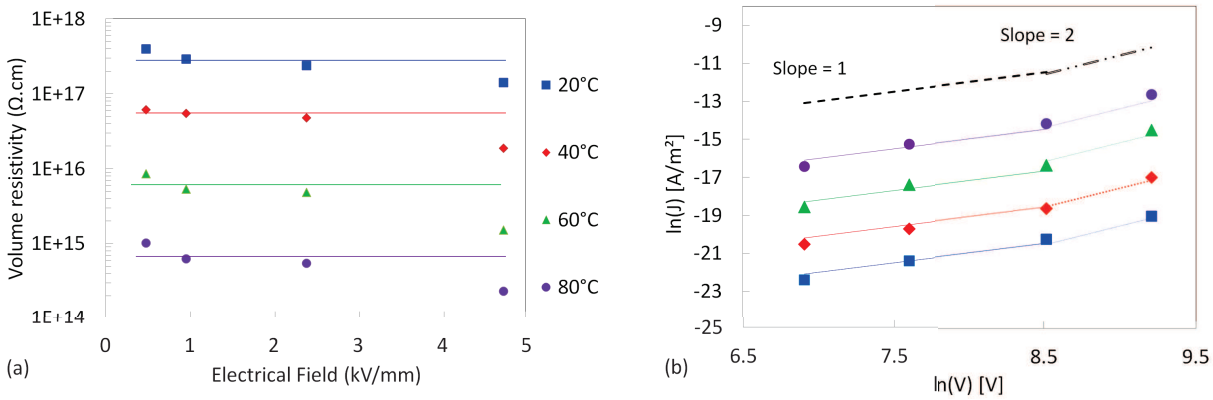

Fig. 3.19: (a) Volume resistivity variations according to electric field and temperature in SF_6 ($0.6\,MPa$), (b) $SCLC$ representation, for material B.

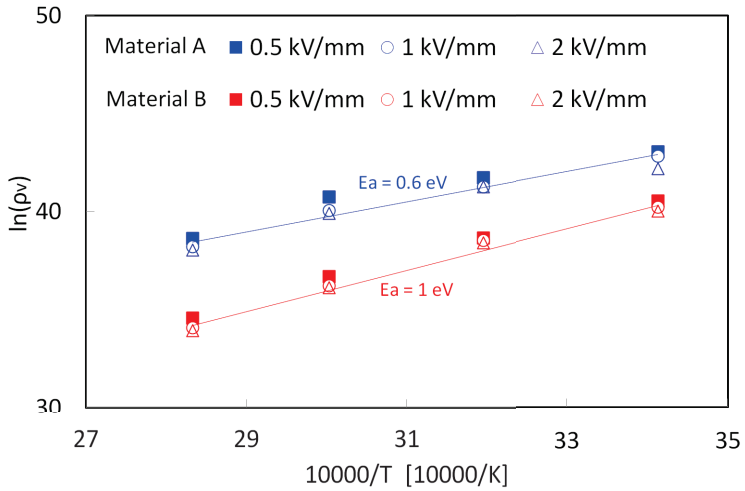

Fig. 3.20: Arrhenius plot showing the thermal evolution of volume resistivity for both material A and B.

A similar investigation on GIS epoxy materials reported by Yahyaoui et al. [10] points out similar trends. In their case, the electric field for which the conduction regime varies is

$5\,kV/mm$. For our application, the maximum electric field applied on the insulator will not exceed $3\,kV/mm$. So, an ohmic model will be used in the following simulation for simplicity.

A comparison between the thermal evolution of volume resistivities of material A and B is presented in figure 3.20. From these curves we can extract the values of activation energy for each material. For material A, we obtained an activation energy $E_a = 0.6\,eV$ and for material B, $E_a = 1\,eV$. These measurements confirm that the resistivity of material B is lower than that of material A, and is also more impacted by temperature.

3.5.3.2 Influence of water content

As presented in section 3.3, some water can be initially present within the material. The influence of water concentration on the volume resistivity was investigated on material A.

Figure 3.21 (a) shows the volume resistivity ρ_v deduced from stabilized DC conduction currents versus water content at 60 °C. A large decrease of volume resistivity (about two decades) is noted between a dried and a 0.23% moist sample. This large influence is certainly due to an enhanced ionic conduction. Ions resulting from the interaction between water and material can contribute to the bulk current [11].

Volume resistivity measurements versus temperature have also been made with $W_c = 0.2\%$ (figure 3.21 (b)). It can be observed that ρ_v strongly decreases when either temperature or the water content W_c are increased. Based on these curves, activation energies E_a have been calculated from Arrehnius plots of data. An activation energy of $0.6\,eV$ is obtained for the dry sample, while $E_a = 0.9\,eV$ for a sample with a water content of 0.2%.

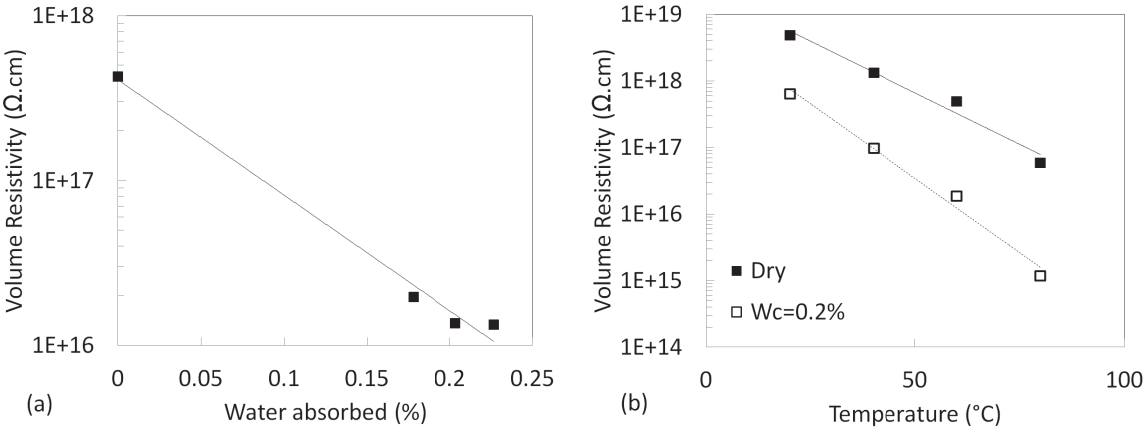

Fig. 3.21: (a) Volume resistivity measurements for various W_c at $1\,kV$ in air and atmospheric pressure, at $T = 60\,°C$. (b) Volume resistivity versus temperature at $0.2\,kV/mm$ under dry conditions and $Wc = 0.2\%$. $E_a(dry) = 0.63\,eV$, $E_a(0.2\%) = 0.91\,eV$.

3.5.3.3 Simulation model

A simulation model was developed with $COMSOL^{TM}$ in order to confirm that measured currents accurately allows us to calculate the volume resistivity.

Figure 3.22 shows the electric potential distribution in the test cell.

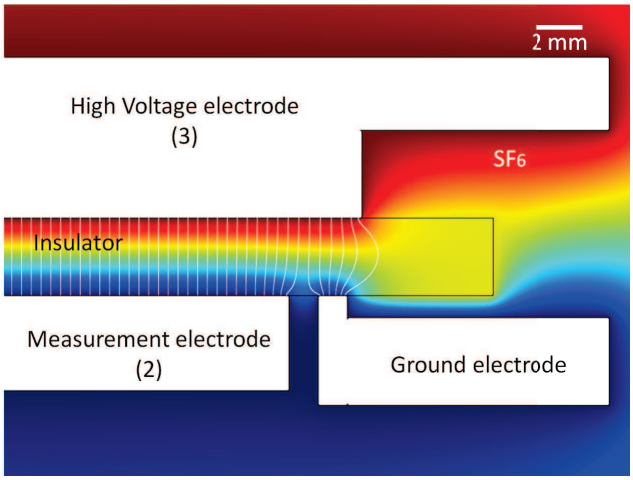

Fig. 3.22: Electric potential intensity (color) and lines of current density corresponding to our experimental setup (axisymmetric calculation of the device presented in figure 3.13, $E = 1\,kV/mm$, $\rho_v = 2.07.10^{18}\,\Omega.cm$ at 20 °C.

In our model, a very high «resistivity» of $10^{25}\,\Omega.cm$ is set to the gas. The resistivities calculated from current measurements for different temperatures in the case of a dried material A have been implemented in the simulation. The current resulting to the voltage application ($i_{simulated}$) is then calculated. The values are listed in table 3.3.

Temperature [°C]	I_{mes} $[A]$	ρ_v $[\Omega.cm]$	$I_{simulated}$ $[A]$
20	$1.02.10^{-13}$	$2.07.10^{+18}$	$1.03.10^{-13}$
40	$2.46.10^{-13}$	$8.33.10^{+17}$	$2.56.10^{-13}$
60	$9.51.10^{-13}$	$2.14.10^{+17}$	$9.98.10^{-13}$
80	$6.06.10^{-12}$	$3.34.10^{+16}$	$6.39.10^{-12}$

Tab. 3.3: Experimental values of current compared to simulated values.

It can be noted that $I_{mes} \approx I_{simulated}$, which validates the model. This indicates that the hypothesis of an uniform electric field used to calculate ρ_v was correct (*i.e.*, the influence of electric field distorsion at the edge of electrode (2) has a negligible influence).

For the simulation of real insulators, values of resistivities based on measured currents will be used, depending on the temperature. Those values are listed in table 3.4 and 3.5 for $0.5\,kV/mm$.

Temperature [°C]	Dry ρ_v [$\Omega.cm$]	$W_c = 0.2\%$ ρ_v [$\Omega.cm$]
20	$3.88.10^{+18}$	$6.42.10^{+17}$
40	$8.41.10^{+17}$	$9.81.10^{+16}$
60	$2.5.10^{+17}$	$1.88.10^{+16}$
80	4.10^{+16}	$1.18.10^{+15}$

Tab. 3.4: Experimental values of volume resistivity of material A calculated based on measured current for both dry and $W_c = 0.2\%$ sample, under $0.5\,kV/mm$.

Temperature [°C]	Dry ρ_v [$\Omega.cm$]
20	$3.9.10^{+17}$
40	$6.15.10^{+16}$
60	$8.6.10^{+15}$
80	$1.02.10^{+15}$

Tab. 3.5: Experimental values of volume resistivity of dry material B calculated based on measured current, under $0.5\,kV/mm$.

3.5.3.4 Additional investigations: influence of the material composition

Several investigations have been performed on new materials studied in section 3.7 to characterize their volume properties and verify if such materials could be suitable for HVDC applications. Indeed, a material with lower volume and surface resistivity should help charge relaxation. Hereafter, investigations are presented on material B2, B3 and B4, without alumina fillers.

Figure 3.23 shows typical recordings of currents measured through those materials at $1000\,V$ and for 20 °C and 40 °C. The pseudo-stabilization of currents is obtained after 10 hours at 20 °C. However, at 40 °C the current continuously increases with time, and does not show any pseudo-stabilization. Although those materials present a faster surface potential decay and a lower volume resistivity compared to materials A and B, they do not have a stable behavior in time under high electric field and temperature.

Figure 3.24 (a) shows the evolution of the measured current through volume of material B4 with fillers, at different temperatures. Opposed to the case of material B4 without fillers (figure 3.23), it is observed that the current at 40 °C now decreases with time, and reaches a pseudo-stabilization after approximately 40 hours. The same behaviour is noted for the other temperatures. Based on these measurements, the volume resistivity of material B4 with fillers is compared to material B at 20, 40, 60, and 80 °C in figure 3.24. Material B4 with fillers shows a lower volume resistivity compared to material B, and a similar behaviour versus temperature, with three decades difference between 20 °C and 80 °C. This result

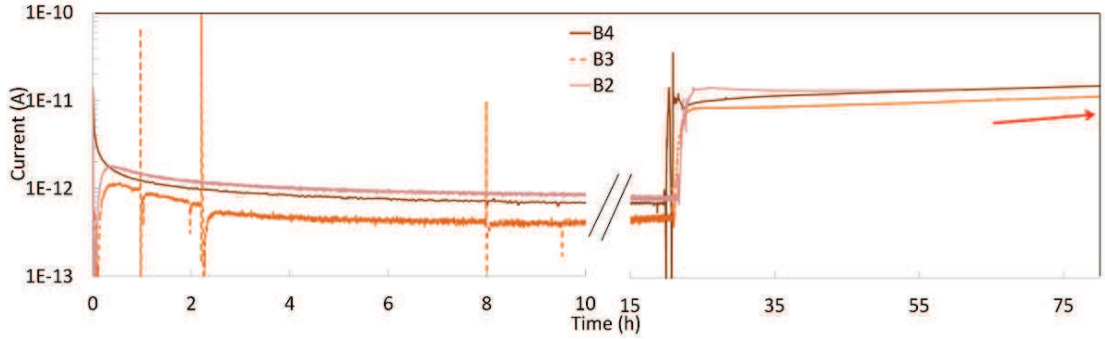

Fig. 3.23: Typical recording of current through materials B2, B3 and B4 at $1000\,V$ and for $20\,°C$ (on the left) and $40\,°C$ (on the right).

is also in agreement with the faster surface potential decay observed for material B w/o fillers$_K x$ compared to material B presented in section 3.7.

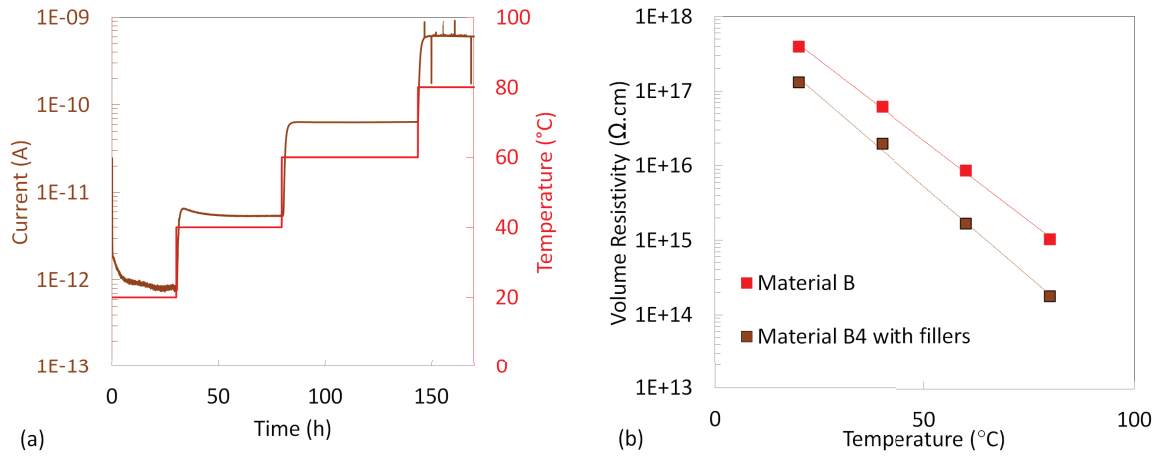

Fig. 3.24: (a) Current measurement on material B4 with fillers at $1000\,V$ and various temperatures. (b) Calculated volume resistivity of B4 with fillers compared to material B, for different temperatures.

This complementary investigation points out that a modification of the material chemical composition (catalyst or hardener) results in different volume resistivity of the material. It has been seen that without fillers in the matrice, the material presents unstable behaviour versus time for a given electric field and high temperature ($\geq 40\,°C$). By adding fillers in material B4, a stable conduction current can be reached. Such results are promising for the final industrial application. Additional experiment should be performed in order to determine a suitable value of the volume resistivity, which enables both fast charge relaxation and good insulating properties.

3.6 | Surface resistivity measurements

In this section, the experimental system and protocol are briefly presented, and the evolution of surface resistivity with temperature and relative humidity is shown. In addition, a simulation model is realized to estimate the contribution of current from the volume in our measurements.

3.6.1 | Experimental system and protocol

The surface resistivity is calculated from conduction currents measured along the insulator surface. The experimental device used for current measurements along surface is the same as the one used for current through the volume, with different connections. An illustration of the device is presented in figure 3.25. The voltage is applied on electrode (3) and current are measured on electrode (2). The same measurement procedure as described in section 3.5.1 is used.

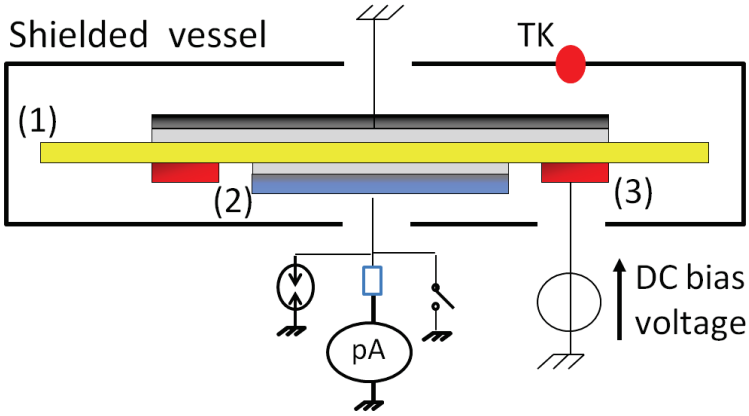

Fig. 3.25: Principle of current measurements along the surface: the insulator (1) is positioned between the measurement (2) and the grounded electrodes. The current is measured between the high voltage electrode (3) and the measurement electrode (2).

The surface resistivity was investigated on material A depending on electric field, temperature, relative humidity and also gas nature and pressure. The values of the parameters investigated are listed in table 3.6.

	Material A
Electric Field [kV/mm]	0.5 – 1 – 2.4 – 4.7
Temperature [°C]	20 – 40 – 60 – 80
Gas	standard SF_6 – Dry air – N_2
Ait at atmospheric pressure - RH [%]	20 – 30 – 40 – 50 –60 – 80

Tab. 3.6: Values of experimental parameters used for current measurement along the surface of insulating material A.

3.6.2 | Preliminary experiments: creeping discharges

The maximum electric field and pressure used for the experiments were chosen according to the creeping breakdown voltage of the material considered. Indeed, in order to avoid breakdowns during current measurements, a previous investigation on the breakdown voltage has been performed on material A and B. Figure 3.26 shows the creeping breakdown voltage (E_{BDV}) values for both materials according to pressure. For current measurements, the maximum electric field applied was $5\,kV/mm$, which is well-inferior to E_{BDV} for each pressure considered.

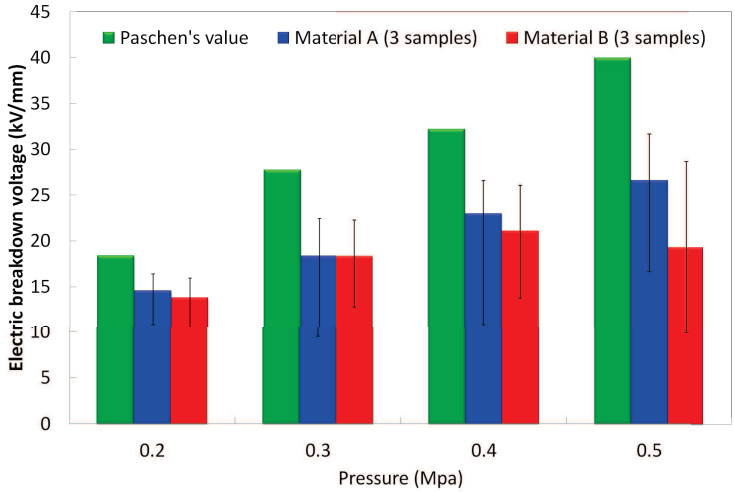

Fig. 3.26: Creeping breakdown field strength of material A and B compared to theoretical Paschen's value for different pressures.

3.6.3 | Results and discussion

3.6.3.1 Surface resistivity in dry gases

The influence of the gas pressure and nature are investigated hereafter at $V = 1\,kV$ ($E = 0.5\,kV/mm$), on dried samples, in dry gases. The water content of N_2 and synthetic

air was below 3 ppm, and the dew point of standard SF_6 was $-27\,°C$ at atmospheric pressure (*i.e.*, $RH = 2.8\%$). The test cell was first evacuated down to 10 Pa before introduction of gases. In these conditions (dry samples and dry gases), the measured surface resistivities are very high ($> 10^{18}\,\Omega/sq$), corresponding to very low currents (some $10^{-14}\,A$), at the limit of measurement capabilities. The errors on these measurements are therefore rather large. Measurements were carried out at a minimum temperature of 40 °C. At room temperature (20 °C), the measurement of surface currents with a reasonable accuracy was not possible.

Figure 3.27 shows the variations of surface resistivity for various gas nature and pressure. It is observed that the surface resistivity remains nearly unchanged when the pressure of SF_6 varies from 0.1 to 0.8 MPa.

When the gas nature is changed (N_2, SF_6, dry air) with the same sample, no significant influence is observed. In these conditions (low electric field and dry gases), the influence of the surrounding gas on the measured current is negligible.

Then, it can be considered that the calculated surface resistivities actually represent the properties of the solid alone for low electric fields.

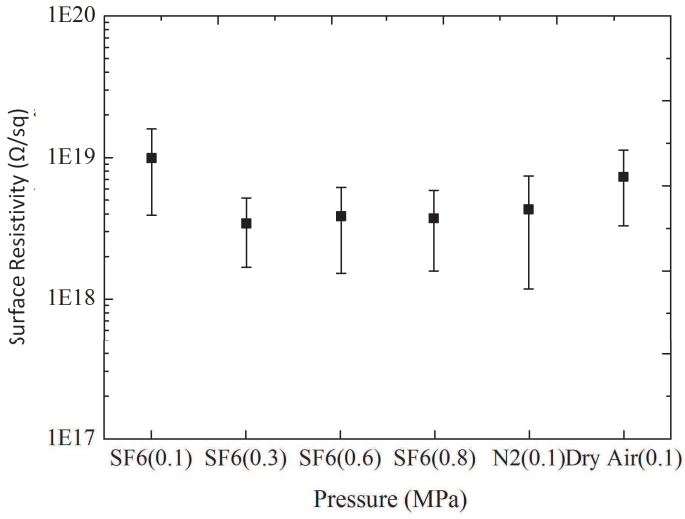

Fig. 3.27: Surface resistivity evolution with gas nature and pressure in SF_6 in dry conditions (dried sample, 40 °C, 0.5 kV/mm).

3.6.3.2 Influence of electric field and temperature

As for volume resistivity measurements, the current along the insulator surface has been recorded for various voltages and temperature. Similar measurement procedures as for volume measurements have been used (stabilization time, temperature). Figure 3.28 shows the variations of the surface resistivity for material A versus temperature and electric field. Since recordings obtained at 20 °C were very noisy, the corresponding values are not represented here, but are supposed to be $\geq 10^{19}\,\Omega.cm$. The semi-logarithmic plot points

out a non-linear behaviour of surface resistivity versus electric field, over the entire range of electric field considered. This observation is in agreement with the work of Okabe *et al.* [9] which showed a non-linear surface resistivity versus electric field in GIS materials. Our measurements also evidence the impact of temperature, with approximately one decade difference between 40 °C and 80 °C. This result also shows that surface resistivity is more influenced by electric field than by temperature within the investigated range.

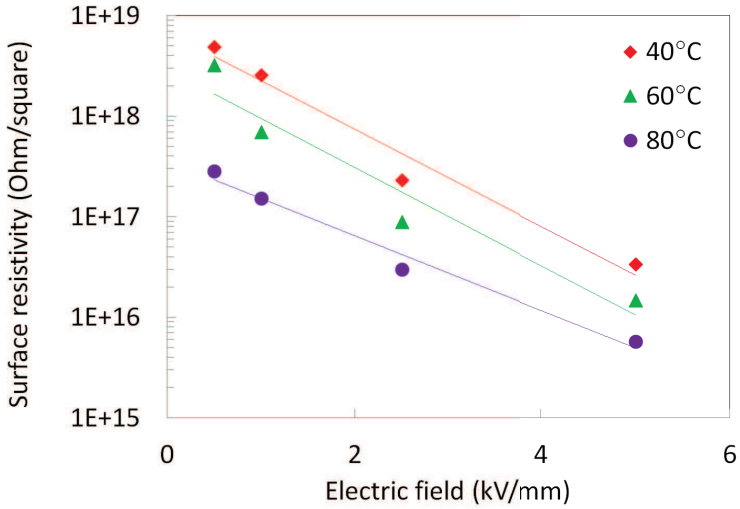

Fig. 3.28: Surface resistivity variations according to electric field and temperature in SF_6 ($0.6\,MPa$), for material A.

These measurements allows determining an empirical equation followed by the surface resistivity (ρ_s) depending on temperature and electric field, written as equation (4.1). It can be used in numerical simulations to take into account surface properties depending on local values of the electric field and temperature.

$$\rho_s = 6.10^{26} * exp[-(0.06T + 1.03E)] \tag{3.11}$$

3.6.3.3 Simulation model

The existence of an absorption current that decreases with time after voltage application, typical of the behaviour of an insulating solid, suggests that part of the measured current flows through the material volume. A numerical model of the stationary current and field distribution under DC has been done with the software COMSOL Multiphysics. In figure 3.29, static fields calculated assuming an ohmic behaviour of materials are presented. The «gas resistivity» has no physical meaning, so an arbitrary high value $\rho_g = 1.10^{25}\,\Omega.cm$ is used to account for the negligible current flowing in the gas.

With $\rho_v = 8.33.10^{17}\,\Omega.cm$ (value @ 40 °C, see table 3.4) and $V = 5\,kV$, the calculated current i_c in the measurement electrode is $3.3.10^{-14}\,A$, whereas the measured current i_m in

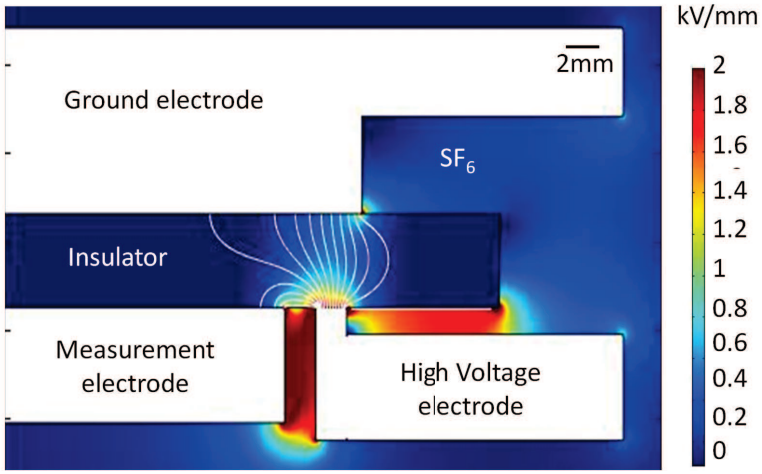

Fig. 3.29: Electric field intensity (color) and lines of current density corresponding to our experimental setup (axisymmetric calculation of the device presented in figure 3.25, $V = 5\,kV$, $\rho_v = 8.33.10^{17}\Omega.cm$, $\rho_g = 1.10^{25}\Omega.cm$, $40\,°\mathrm{C}$.

these conditions is about two decades higher ($i_m = 1.76.10^{-12}\,A$). This discrepancy clearly highlight the need to consider specific conduction properties of the surface, in order to obtain the measured current.

To take into account the specific properties of the surface, we have added to our model a thin layer on the surface, of arbitrary thickness δ, with a volume resistivity $\rho_{vL} \neq \rho_v$. An illustration of the thin layer added is presented in figure 3.30. This constitutes a simple and convenient way to implement specific surface properties in the model.

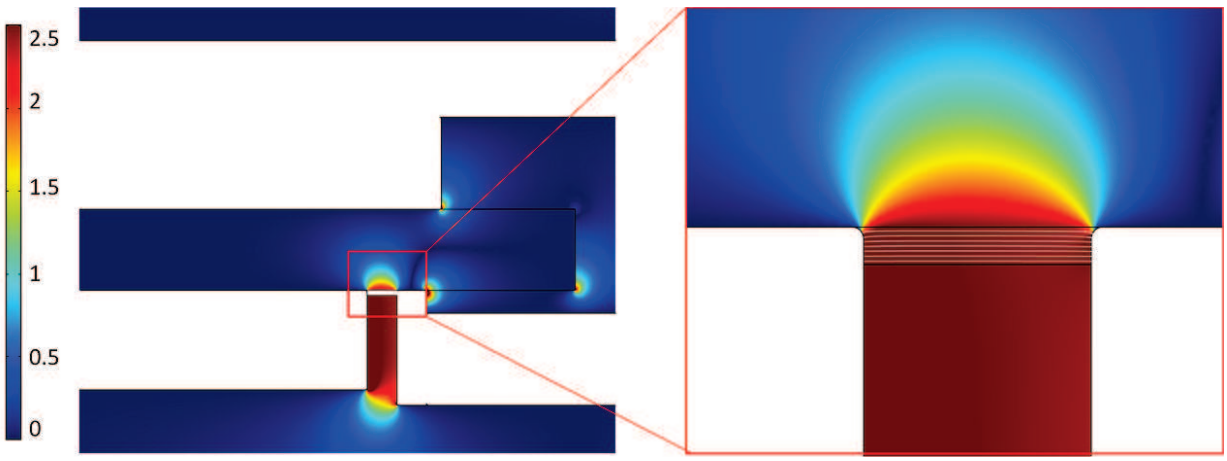

Fig. 3.30: Focus on electric field intensity (color) and lines of current density with a layer added onto the sample surface, between the high voltage and measurement electrode, to account for the electric properties of the insulator surface (axisymmetric calculation, $\rho_{vL} = 8.10^{15}\,\Omega.cm$, $\rho_v = 8.33.10^{17}\,\Omega.cm$,$\delta = 320\,\mu m$). Most of current lines flow through the surface layer.

The resistivity ρ_{vL} of this layer was then adjusted for different thicknesses in order

to obtain a good agreement between calculated and experimental currents. Figure 3.30 shows the layer resistivity providing a good agreement with measured currents versus arbitrary thicknesses δ. The values ρ_{vL} obtained are significantly lower compared to the bulk resistivity. For realistic thicknesses ($< 400\,\mu m$), adjusted values of ρ_{vL} fairly well correspond to a constant surface resistivity (eq.(3.12)), evidencing that the measured current in the set-up mainly flows along the surface.

$$\rho_s = \frac{\rho_{vL}}{\delta} \tag{3.12}$$

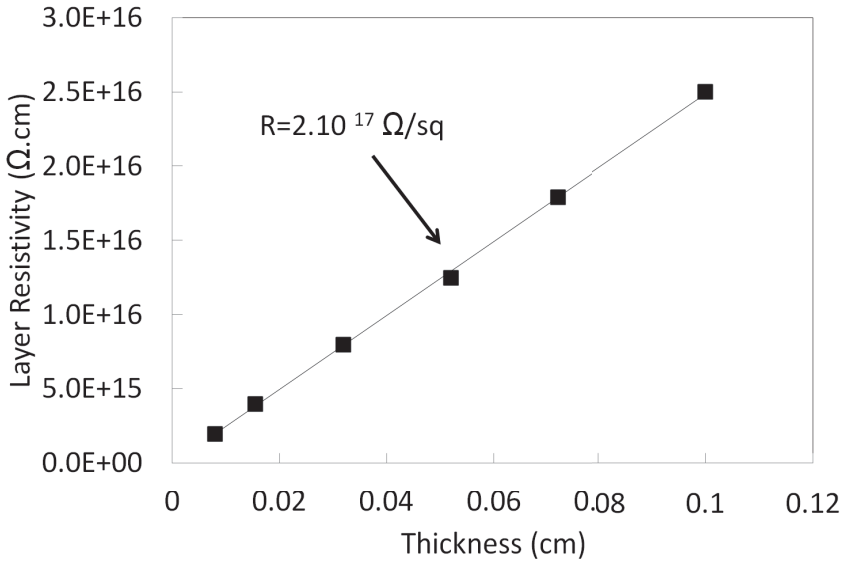

Fig. 3.31: Layer resistivity ρ_{vL} providing a good agreement between measured and calculated currents, versus arbitrary layer thickness δ. $V = 5\,kV$, $\rho_v = 8.33.10^{17}\Omega.cm$, $\rho_g = 1.10^{25}\Omega.cm$, 40 °C.

To estimate the proportion of the measured current flowing on the surface and through the material volume, the volume resistivity ρ_v was changed from its initial value ($8.33.10^{17}\Omega.cm$) to 10^2 times and 10^7 times higher values, while a layer volumic resistivity $\rho_{vL} = 8.10^{15}\,\Omega.cm$ was used with a thickness layer of $\delta = 320\,\mu m$. The calculated current with these values are summarized in table 3.7. This modification induced a very small reduction (about 2%) of the measured current. This result shows that about 98% of the measured current indeed flows along the surface between measurements electrodes. This validates the principle of measurements done with this electrode arrangement, in order to characterize surface properties.

These calculations correspond to very dry conditions. The above conclusion on the validity of measurements is reinforced when a larger difference exists between ρ_{vL} and ρ_v.

This is the case when measurements are made with a dry sample in a humid gas, leading to a drastic reduction of ρ_{vL}.

Volume resistivity [Ω.cm]	$8.33.10^{17}$	$8.33.10^{20}$	$8.33.10^{25}$
Calculated current [pA]	1.73	1.69	1.69

Tab. 3.7: Calculated current with various values of the volume resistivity, with fixed layer resistivity ($\delta = 320\,\mu m$, $40\,°C$, $5\,kV$, $\rho_L = 8.33.10^{17}\,\Omega.cm$).

Furthermore, equations (4.1) and (3.12) has been used to calculate ρ_{vL} using an arbitrary thickness of $\delta = 320\,\mu m$ and implement the surface properties within the model. This allows describing the variations of surface resistivity with temperature and electric field. Using this equation, the current along the insulator surface has been calculated. For the volume conduction, the values presented in table 3.3 are used to do an interpolation with temperature. A comparison of experimentally measured and calculated surface currents is presented in figure 3.32. Full symbols represent experimental measurements and empty symbols represent the currents calculated from the simulation. It is observed that the values of the current obtained by the simulation follows the experimental measurements, which validates our hypothesis of a thin layer between electrodes to account for surface properties, and uniform electric field between those electrodes.

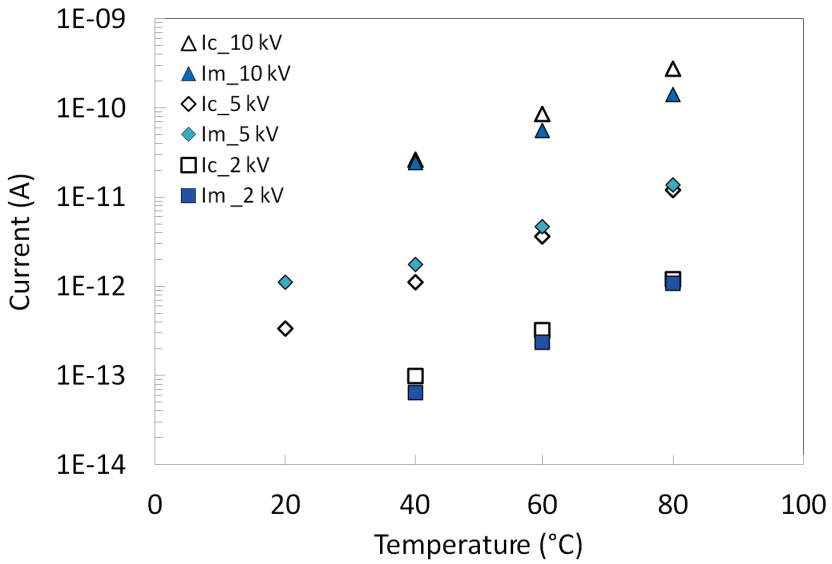

Fig. 3.32: Comparison between measured and calculated current along the insulator surface using the values of table 3.22 for the volume properties and (ρ_s/δ).

3.6.3.4 Influence of relative humidity RH of the gas

The influence of RH has been investigated on an initially dried sample in air at atmospheric pressure. The test cell containing the dry sample is placed into a climatic chamber allowing us to change the air relative humidity RH between 15% and 80%. Figure 3.33 shows a typical variation of the recorded current when RH is changed according to a cycle 15/60/15% over a long period of time (44 hours). It is observed that when RH is modified, an immediate fast variation of measured current i_m is first recorded, when RH is either increased or decreased (indicated «short term» on figure 3.33). Thereafter, a much slower variation of i_m is recorded (indicated «long term» on figure 3.33), until it becomes stable after about 20 hours.

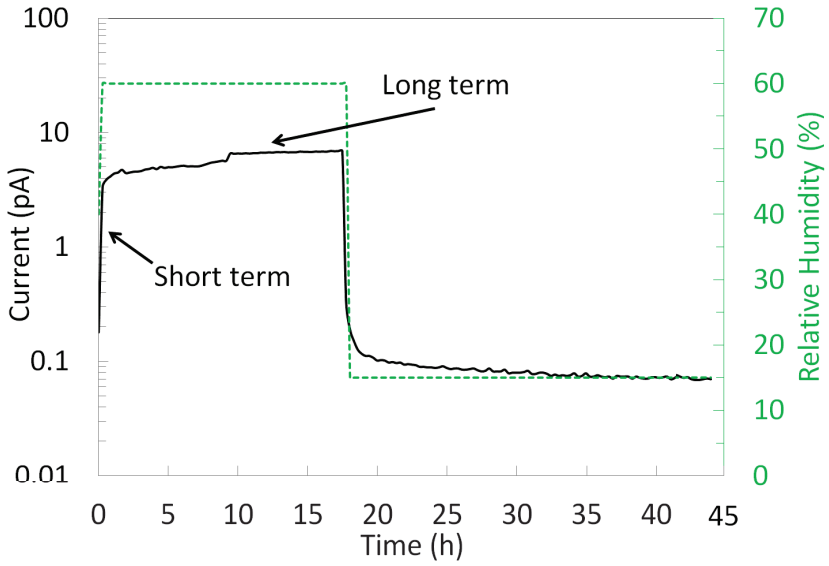

Fig. 3.33: Variations of the recorded current when the relative humidity RH is varied between 15 and 60% ($1\,kV$, 60 °C).

Figure 3.34 shows the surface resistivities calculated from measured currents, versus RH and temperature. Two different current values were used in the plot. «Short term» currents were measured 10 minutes after stabilization of RH to the preset value, and «Long term» currents correspond to stabilized values, after typically 10 to 20 hours. It was verified on several occasions that when RH is set back to the minimum value (15%) after a measurement at higher RH, the «Long term» current at $RH = 15\%$ drops back to a stable and reproducible value. No «memory» effect occurs, when a long time is allowed for stabilization.

At 40 °C, surface resistances show no significant variation with RH up to about 30%. The recorded values in this range are quite close to values previously recorded in dry gases (indicated as 0% on figure 3.34). No significant difference is observed between «Short term» and «Long term» values at this temperature. At 60 °C, surface resistances also show

a negligible variation below 30%. A larger difference is observed between «Short term» and «Long term» values recorded when RH is varied from 15% to a higher value. At both temperatures, a large drop of surface resistance is observed with $RH > 30\%$, up to about 3 decades at 80%.

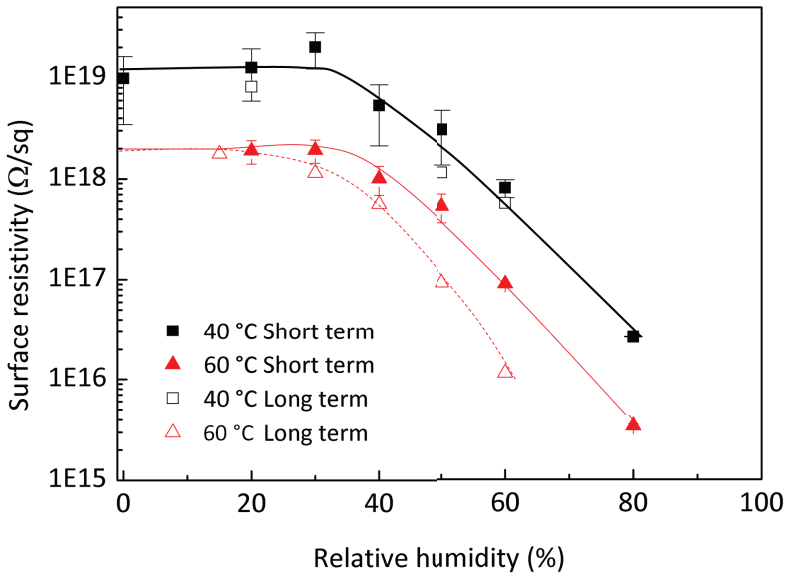

Fig. 3.34: Measurements of surface resistivity versus relative humidity RH and temperature ($1\,kV$).

These measurements show that the influence of RH can be divided in two parts. The «Short term» rapid variation certainly results from the immediate increase of the water content on the outer surface of the material. The «Long term» variation can be ascribed to the progressive diffusion of water through the first layers into the material. In turn, this impregnation induces a further decrease of the surface resistivity. This effect is logically more marked at higher temperatures and higher RH. It is also worth noting that this impregnation process is reversible.

Our measurements are in agreement with Crisci *et al.* and Lutz *et al.* [12,13] as presented in chapter 1. Indeed, similar surface resistivity trends are observed for $RH > 40\%$ with approximately a decrease of 3 decades on the surface resistivity between $RH = 40\%$ and $RH = 80\%$. These observations are totally in agreement with our experiments and point out that for $RH < 20\%$ there are only slight variations at long and short term measurements on the surface resistivity. For $RH > 20\%$, there is a large influence of the RH on the surface conduction, and thus charge relaxation on the insulator surface.

3.6.3.5 Further investigations: surface treatment

Following the results presented above, it is clear that surface resistivity can play a significant role on surface charge relaxation in a real GIS geometry. In order to reduce the charge

accumulation phenomenon, a treatment on the insulator surface could be performed to reduce its surface resistivity, without modifying the volume properties. Some investigations [14,15] have already reported that adding a semi-conductive coating on the insulator helps the charge relaxation. However, such treatment are difficult to control the layer since resistivity depends on the electric field and temperature.

Several tests were carried out with a plasma treatment, such as presented in [16]. It consists in electron cyclotron resonance (ECR) ion source which ionizes a plasma. Depending on the nature of the plasma (Argon, Methane (CH_4)), the energy of the beam and the treatment time, different surface resistivity can be obtained. Table 3.8 summarizes the various conditions used for the treatments.

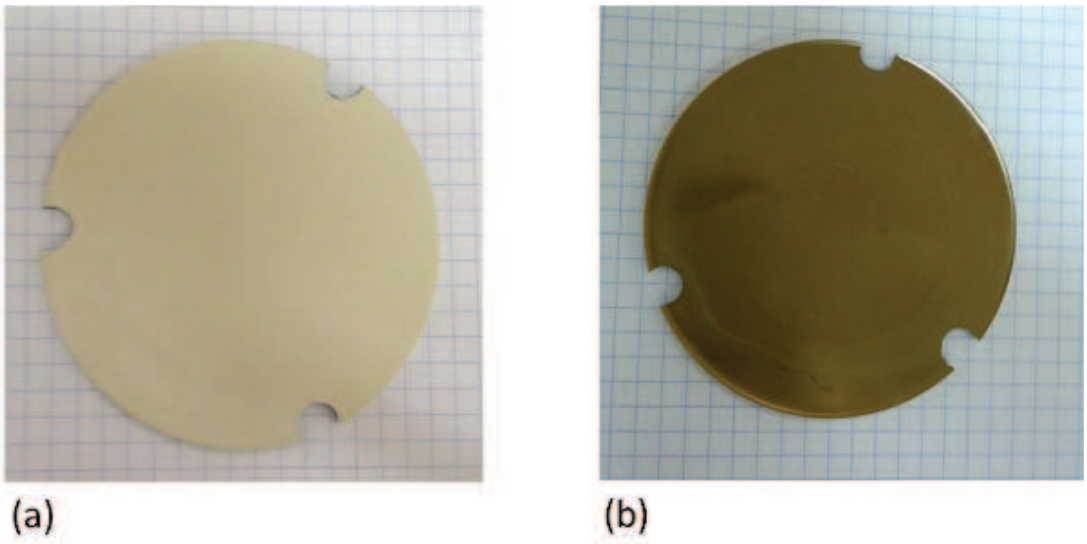

Fig. 3.35: (a) Photography of material A before (a) and after (b) treatment ($ECR3$).

Figure 3.35 shows a sample of material A before (a) and after plasma treatment (b). An EDX measurement has been made on treated samples in order to determine the surface modification caused by the ion implantation.

It was observed that after the treatment, 99% of Carbon was present on the surface. It is then assumed that the ion implantation breaks the bonds of the molecular chain and leads to Carbon bonds formation on the material surface, which explains the color modification of the insulator surface when treated with a high dose and energy.

A series of surface resistivity measurements on treated material with argon and CH_4 plasma has been performed in ambient air at 40 °C ($RH = 12\%$) and voltage up to 1000 V (0.5 kV/mm) in order to observe the influence of different treatment conditions (table 3.8). The current measurements were performed during 20 min for each voltage level in order to obtain a stable or pseudo-stable current depending on the characterized sample. Based on these data, the surface resistivity has been calculated and is presented in figure 3.36 and figure 3.37 for various conditions of implantation. Those measurements constitute a

$Implantation\ doses$ / $Energy\ of\ the\ beam$	$5\,keV$	$10\,keV$	$20\,keV$
$10^{16}\,cm^{-2}$	ECR1	ECR2/ECR9	ECR3/ECR10
$10^{15}\,cm^{-2}$	ECR4/ECR11	ECR5/ECR12	ECR6/ECR13
$10^{14}\,cm^{-2}$	ECR7/ECR14	ECR15	ECR8/ECR16

Tab. 3.8: Experimental conditions used for the ECR treatment on material A. ECR1 to ECR8 were performed with CH_4 plasma. ECR9 to ECR16 were performed with argon plasma.

preliminary study, which aims to compare the efficiency and the impact of the treatments.

It can be observed that for both CH_4 and argon plasma treated samples, no significant variations on surface resistivities are observed for doses of $10^{14}\,cm^{-2}$ and $10^{15}\,cm^{-2}$ whatever the energy of the electron beam. For both plasma, only the treatments with high implantation dose ($10^{16}\,cm^{-2}$) and high energy (10 and $20\,keV$) show a surface resistivity significantly different compared to material A.

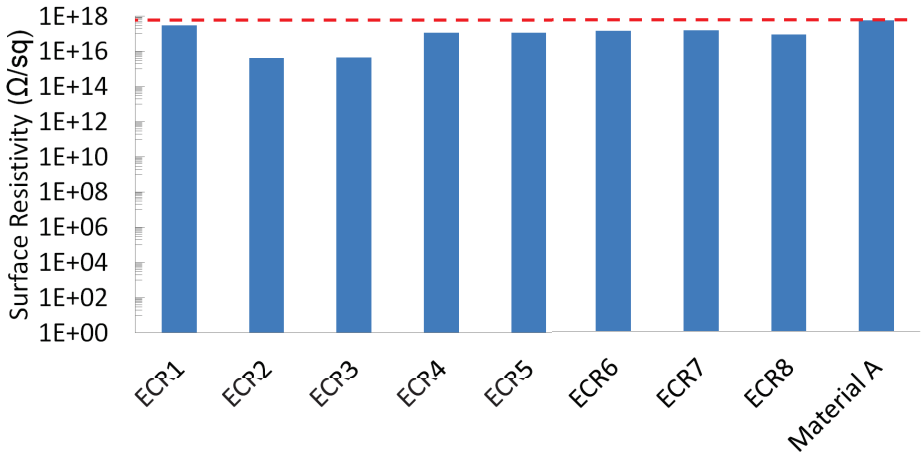

Fig. 3.36: Surface resistivity of ECR1 to ECR8, treated with CH_4 plasma, compared to material A, at $1000\,V$ and $40\,°C$.

In addition, if we compare the influence of the gas used for the plasma treatment, for similar implantation doses and beam energy (ECR2 compared to ECR9, and ECR3 compared to ECR10), it can be noted that lower surface resistivities are obtained with an argon plasma. A surface resistivity two decades lower than that of material A is measured with a CH_4 plasma (figure 3.36) while a surface resistivity five decades lower is measured with an argon plasma treatment (figure 3.37).

Those preliminary experiments evidence that the surface resistivity can be adjusted using plasma surface treatment, by modifying the chemical composition of the first layers of the material. Such treatment could be an attractive alternative to the semi-conductive

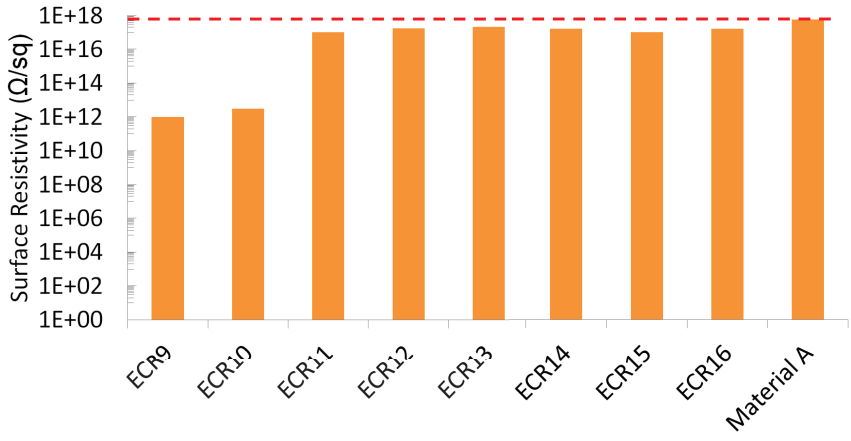

Fig. 3.37: Surface resistivity of ECR9 to ECR16, treated with argon plasma, compared to material A, at $1000\,V$ and $40\,°\mathrm{C}$.

layer added on the material surface. To validate the practical efficiency and reliability of such treatments, further experiments are required to evaluate the stability of the treatment versus time, the influence on creeping breakdown field strength, and surface resistivity measurements at higher electric field and for various relative humidities.

3.7 | Conclusions

In this chapter, the characterization of two main industrial materials (A and B) has been performed using surface potential decay and current measurement through the insulator volume and onto its surface. First, the SPD technique enables us to evidence the difference between materials A and B concerning the different decay dynamics according to various materials. Then, the characterization of material A volume and surface resistivities gives us some information concerning the evolution versus electric field and temperature. The results obtained showed that both volume and surface resistivities are strongly influenced by temperature, and that surface resistivity is non-linear with electric field. Simulation models have been built, which takes into account both volume and surface properties of the insulator. Thanks to that, a model closer to the geometry of the real application can be developed.

Furthermore, additional investigations on new materials or surface treatments have been presented to enhance the volume and surface conduction of materials, and thus favor the surface charge relaxation. A modification of the material composition can lead to a modification of its volume resistivity. Moreover, the «stabilizating» role of the fillers has been evidenced. Besides, an ion implantation treatment on the insulator surface has been investigated at various beam energies, implantation doses and for two plasma. It has

been observed that lower surface resistivity are obtained for high implantation dose and energy beam. Such investigations give an alternative to fabricate new materials with well controlled resistivities, in order to better define the electric field distribution under HVDC. Depending on the geometry considered, a compromise between adjusting the volume and surface resistivity can be determined to optimize the charge relaxation.

Bibliography

[1] D. D. Gupta and R. Brockley, "A study of'absorption currents' in low-density polyethylene," *Journal of Physics D: Applied Physics*, vol. 11, no. 6, p. 955, 1978. (cited in page 96)

[2] Y. Segui, "Diélectriques, courants de conduction," *Techniques de l'Ingénieur, traité Génie électrique D*, vol. 2301, 2000. (cited in pages 97 and 115)

[3] "Methods of test for volume resistivity and surface resistivity of solid electrical insulating materials," 1980. (cited in pages 97 and 98)

[4] C. Menguy, *Mesure des caractéristiques des matériaux isolants solides*. Ed. Techniques Ingénieur, 1997. (cited in page 98)

[5] M. J. Adamson, "Thermal expansion and swelling of cured epoxy resin used in graphite/epoxy composite materials," *Journal of Materials Science*, vol. 15, no. 7, pp. 1736–1745, 1980. (cited in page 101)

[6] C. Zou, J. C. Fothergill, and S. W. Rowe, "The effect of water absorption on the dielectric properties of epoxy nanocomposites," *Dielectrics and Electrical Insulation, IEEE Transactions on*, vol. 15, no. 1, pp. 106–117, 2008. (cited in page 101)

[7] C.-H. Shen and G. S. Springer, "Moisture absorption and desorption of composite materials," *Journal of Composite Materials*, vol. 10, no. 1, pp. 2–20, 1976. (cited in page 101)

[8] Z. Chen, *The effect of humidity and surface functionalisation on the dielectric properties of nanocomposites*. PhD thesis, University of Leicester, 2007. (cited in page 102)

[9] S. Okabe, "Phenomena and mechanism of electric charges on spacers in gas insulated switchgears," *Dielectrics and Electrical Insulation, IEEE Transactions*, vol. 14, no. 1, pp. 46–52, 2007. (cited in pages 10, 15, 16, 17, 18, 22, 41, 114 and 124)

[10] H. Yahyaoui, *Etude des mécanismes de conduction d'une résine époxy chargée d'alumine*. PhD thesis, Private communication, 2013. (cited in page 116)

[11] B. Lutz and J. Kindersberger, "Influence of absorbed water on volume resistivity of epoxy resin insulators," in *Solid Dielectrics (ICSD), 2010 10th IEEE International Conference*, pp. 1–4, IEEE, 2010. (cited in pages 20, 21 and 117)

[12] A. Crisci, B. Gosse, J. Gosse, and V. Ollier-Duréault, "Surface-potential decay due to surface conduction," *EPJ Applied physics*, vol. 4, pp. 107–1116, 1998. (cited in pages 10, 19, 20 and 129)

[13] B. Lutz and J. Kindersberger, "Influence of relative humidity on surface charge decay on epoxy resin insulators," in *Properties and Applications of Dielectric Materials, 2009. ICPADM 2009. IEEE 9th International Conference*, pp. 883–886, IEEE, 2009. (cited in pages 20 and 129)

[14] F. Messerer and W. Boeck, "High resistance surface coating of solid insulating components for HVDC metal enclosed equipment," in *High Voltage Engineering, 1999. Eleventh International Symposium on (Conf. Publ. No. 467)*, vol. 4, pp. 63–66, IET, 1999. (cited in page 130)

[15] E. Volpov, "Dielectric strength coordination and generalized spacer design rules for hvac/dc sf 6 gas insulated systems," *Dielectrics and Electrical Insulation, IEEE Transactions*, vol. 11, no. 6, pp. 949–963, 2004. (cited in pages 13, 14, 22 and 130)

[16] L. Salles, J. Reboul, D. Busardo, and B. Boudart, "Mesure des résistivités de surface et des charges d'espace par la méthode de l'onde thermique alternative dans le polycarbonate aprés implantation ionique.," 2012. (cited in page 130)

4 | Numerical calculations in a GIS geometry

Contents

In this chapter, models with an insulator geometry resembling to actual shapes existing in coaxial HVAC GIS systems (figure 4.1) are presented. Such solid insulator are designed to withstand 245 kV AC and are thus tested up to 400 kV DC. From the previous chapters 2 and 3, it has been shown that solid insulator properties (volume and surface) and gas properties, can influence the electric field distribution and the current passing onto the solid insulator surface and through its volume (figure 4.1). Table 4.1 summarizes the parameters influencing those properties.

In order to evaluate the relative influence of these phenomena, the results obtained by the characterization of the material volume and surface are implemented into the model. The calculations under HVDC are done with the FEM software COMSOL Multiphysics^{TM}, and the static fields are calculated assuming an Ohmic behaviour of materials through the volume. The non-linearity of the surface resistivity versus electric field is implemented by adding a layer on the insulator, and the resulting electric field distribution is studied.

With this model, we will first investigate the differences of AC/DC electric field distribution and resulting currents for a simplified insulator geometry, close to the industrial application. Then, in a first step, the electric field distribution and leakage currents induced by the material volume resistivity, neglecting the surface properties, are considered. The electric field repartition on both surfaces (lower and upper) are studied in case of uniform

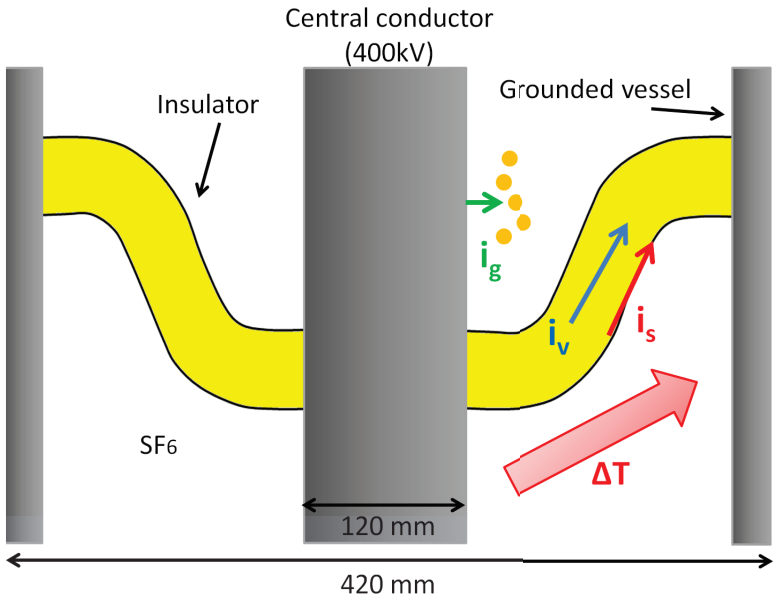

Fig. 4.1: Illustration of the simplified insulator geometry in a GIS structure, and phenomena contributing to electric field distribution and charge accumulation and relaxation.

temperature, with a temperature gradient and also with another water concentration.

In a second step, those parameters are investigated again considering the insulator surface properties with the implementation of a thin layer on the insulator surface. The latter takes into account the non-linear behaviour of the surface resistivity versus electric field. Those simulations allow to estimate the practical impact of temperature gradient and water content on the electric field distribution and on leakage currents.

Finally, in order to calculate the contribution of the current emitted from the high voltage conductor, an estimation of this current is performed based on experimental results (chapter 2).

	Volume current (i_v)	*Surface current* (i_s)	*Gas current* (i_g)
Temperature- $\boldsymbol{T}$	×	×	×
Electric field- $\boldsymbol{E}$	×	×	×
Space charges	×		
Solid water content-W_c	×	?	
Gas nature		?	
Gas water content- $\boldsymbol{RH}$		×	×

Tab. 4.1: List of parameters influencing solid and gas properties.

4.1 | 1^{st} Step: Electric field distribution induced by the material volume resistivity

In this section, the electric field distribution within the system is studied only considering the volume resistivity of the insulator.

4.1.1 | Difference between AC and DC (uniform temperature 20 °C)

In order to compare the electric field distribution in both AC and DC, a relative permittivity of 4.8 (dry materials at 20 °C) was assigned to the material, while a volume resistivity of $2.07.10^{18}\,\Omega.cm$ was used for the DC calculation. Both calculations were performed at 20 °C and $400\,kV$, and the gas was considered to be a perfect insulating gas ($\varepsilon_r = 1$ in AC, and $\rho_g = 1.10^{25}\,\Omega.cm$) to account for the negligible current flowing through the gas. Figure 4.2 shows the electric field intensity for both AC (a) and DC (b) calculations. A field reinforcement is observed in DC on the lower surface of the insulator (red arrow), which is not present in AC. It is also observed in figure 4.3 that in both configurations, the maximum electric field is localized close to the conductor (A). In addition, it is also noted that the main electric field modification under DC occurs on the lower surface of the insulator (higher electric field in DC), whereas its repartition on the upper surface is very similar in both AC and DC voltages.

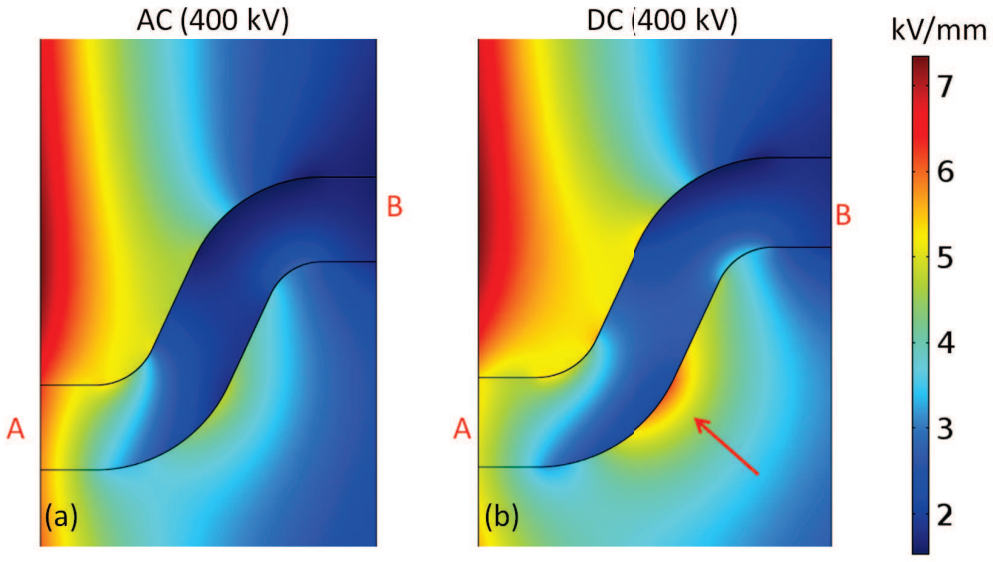

Fig. 4.2: Comparison of electric field intensity (color) in stationary state between AC (a) and DC (b) distribution (axisymmetric calculation of the device presented in figure 4.2, $V = 400\,kV$, 20 °C).

In AC the volume properties of the solid are defined by the relative permittivity of the material, which does not significantly depend on temperature variations. In DC, we have

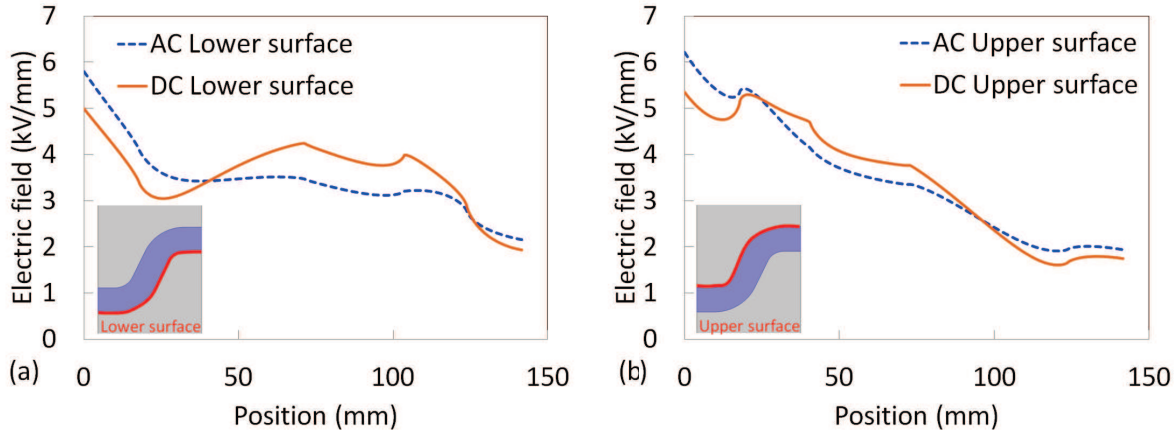

Fig. 4.3: Calculated electric field along (a) the lower and (b), the upper surface of the solid insulator at $V = 400\,kV$, 20 °C.

evidenced in chapter 3 that the volume resistivity is strongly impacted by temperature.

Thus, the influence of both uniform temperature and temperature gradient are investigated below based on results obtained in chapter 3, in case of dry and wet ($W_c = 0.2\%$) insulator, in a DC system.

4.1.2 | Influence of a temperature gradient

To investigate the influence of a temperature gradient on the electric field distribution along the insulator, calculations first include the numerical simulation of the temperature distribution, calculated by considering only the heat conduction in the solid insulator and in the gas.

To apply a temperature gradient, the temperature of the high voltage conductor is varied from 20 °C to 80 °C while the temperature of the grounded vessel remains at 20 °C. The temperature gradient induces a spatial distribution of volume resistivity ρ_v, following an interpolation obtained from data of figure 3.18 in chapter 3. Then, electric field and current through the insulator are calculated with this distribution of ρ_v. Figure 4.4 (a) shows the temperature distribution from the conductor (A) toward the grounded vessel (B) obtained. A deviation of the thermal flow is observed through the solid insulator since its upper part, near the conductor, receives a thermal flow by conduction through the gas (the thermal conductivity coefficient of the solid insulator ($k = 1.2$) is 100 times superior than that of SF_6 ($k = 0.0145$)). It is observed that the temperature distribution is different on the upper and lower surfaces. Indeed, a higher temperature is observed on the upper surface.

Thus, there exists two temperature gradients: between the conductor and the vessel, and also between the upper and lower surfaces of the solid insulator. This will result in a complex electric field repartition.

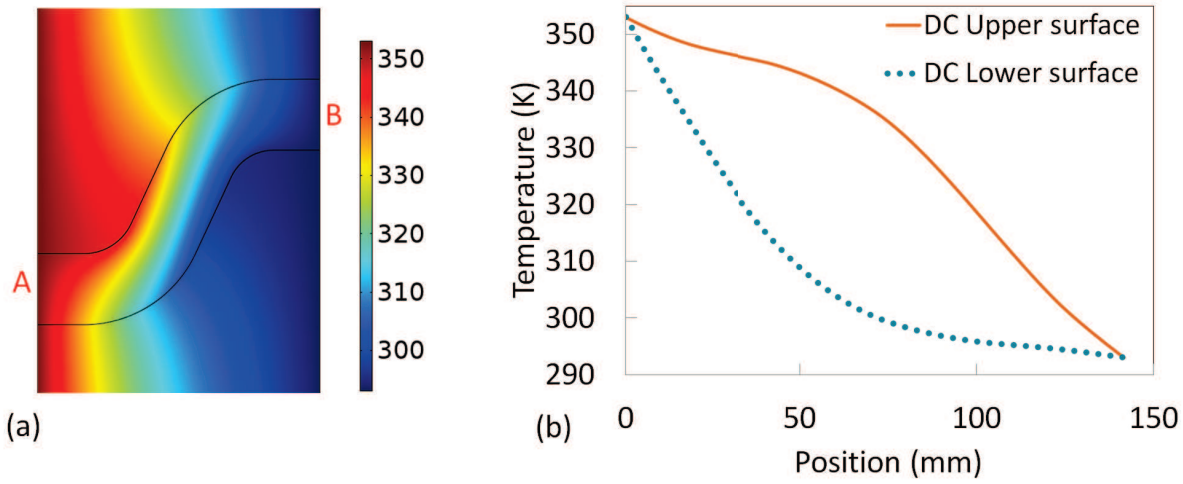

Fig. 4.4: (a) Temperature gradient within the insulator when the conductor (A) is at $80\,°\mathrm{C}$ and the grounded vessel (B) at $20\,°\mathrm{C}$. (b) Repartition of the temperature from the conductor ($x = 0\,mm$) toward the vessel ($x = 145\,mm$) on the lower and upper surface of the solid insulator.

Figure 4.5 shows the difference between the distribution of the electric field at constant temperature (a), and with a temperature gradient $\Delta T = 60\,°\mathrm{C}$ from the conductor ($80\,°\mathrm{C}$, $x = 0\,mm$) toward the enclosure ($20\,°\mathrm{C}$, $x = 145\,mm$). It is observed that in presence of a temperature gradient there is a considerable change of electric field distribution along the solid insulator.

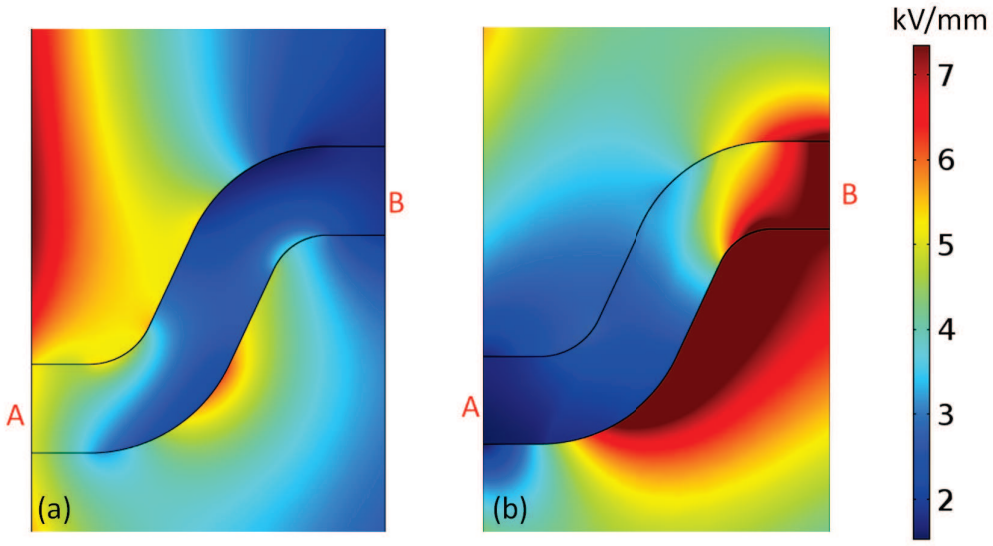

Fig. 4.5: Numerical simulation with (a) an uniform temperature $T = 20\,°\mathrm{C}$; and (b), with a temperature gradient $\Delta T = 60\,°\mathrm{C}$ ($V = 400\,kV$).

Compared to the uniform temperature case, the distribution is nearly reversed (see figure 4.6). Indeed, the electric field is reinforced on the lower surface of the insulator and

toward cold regions (grounded vessel (B)). It can be noted that the value of the maximum field is higher when there is a temperature gradient, $9\,kV/mm$ instead of $5.5\,kV/mm$. The electric field distributions along both lower and upper surfaces for different temperature gradients are shown in figure 4.6 (a) and (b) respectively. It is observed that on the lower surface, the amplitude of the electric field increases with the temperature gradient between 30 to $150\,mm$. On the upper surface, the amplitude of the electric field decreases between 0 to $110\,mm$ and significantly increases near the vessel. This difference in electric field amplitude can be easily explained by the difference in temperature distribution presented in figure 4.4 (b). Areas where the temperature increases (*i.e.*, with a lower resistivity) result in a lower electric field, while near cold regions, the electric field significantly increases.

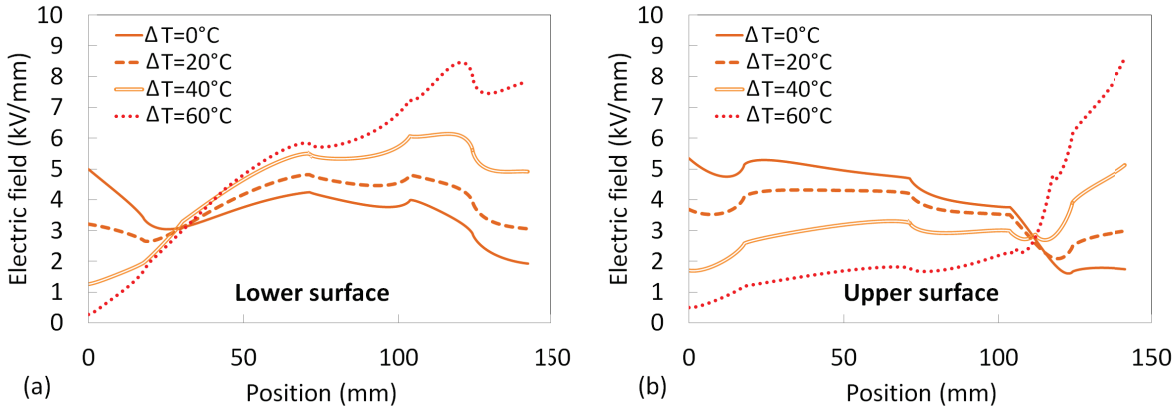

Fig. 4.6: Calculated electric field along the lower (a) and upper (b) surface of the insulator, for different temperature gradient, at $400\,kV$.

Such temperature variations also have an impact on the calculated current passing through the solid insulator. The influence of uniform temperatures and temperature gradients on the calculated current is shown in figure 4.7 (a) and (b). The current is calculated on the grounded vessel side, within the solid. It is observed that in case of an uniform temperature (a) (same temperature on the HV conductor and grounded vessel), the current significantly increases with two decades difference between 20 °C and 80 °C. When a temperature gradient is applied, an increase of the calculated current is still observed but with only one decade difference between $\Delta T = 0\,°C$ and $\Delta T = 60\,°C$.

This difference is explained by the temperature repartition. If an uniform temperature is applied along the solid insulator (identical temperature on both conductor and grounded vessel), the electric field distribution remains unchanged for both upper and lower surfaces, which is logical since the volume resistivity is uniform. Since the volume resistivity decreases with temperature, the calculated current passing through the solid insulator increases. This effect is reduced in case of a temperature gradient since the current becomes limited by high resistances (cold regions) in series with lower resistances (hot regions).

However, it is worth noting that the calculated current through the insulator in case of a temperature gradient $\Delta T = 60\,°C$ ($i_c = 1.15.10^{-11}\,A$) is superior to the calculated current obtained with an uniform temperature of $20\,°C$ ($i_c = 2.5.10^{-12}\,A$). This emphasizes that temperature gradient must be considered in order to not under-estimate the current passing through the insulator.

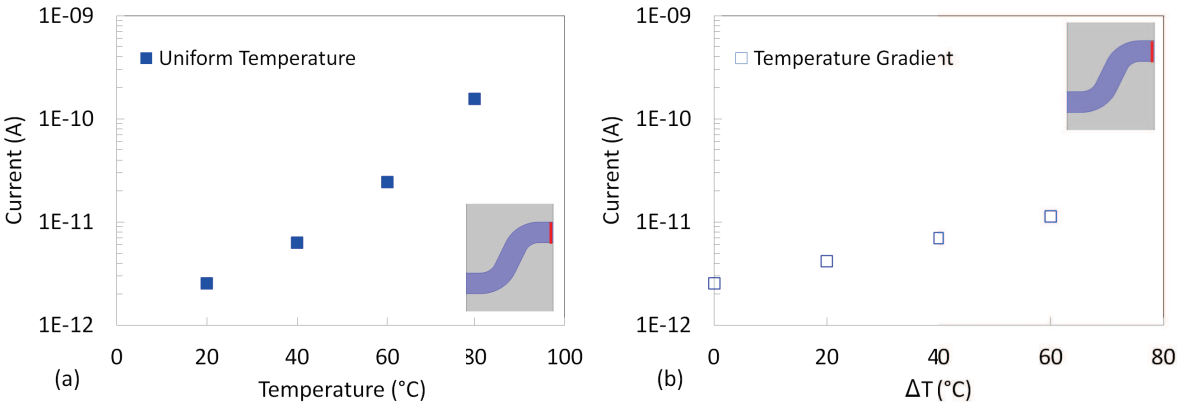

Fig. 4.7: Calculated current through the solid insulator in case of uniform temperatures (a) and temperature gradients (b), at $400\,kV$.

Those calculations first show the different repartition of electric field distribution between AC and DC. It also evidences the large influence of a temperature gradient along the insulator in HVDC on both electric field distribution and leakage currents. Since in DC, volume resistivity depends on the temperature, the resulting electric field distribution will be modified. With the same design, higher maximum electric fields are reached in DC, thus increasing the risk of breakdown. This large impact of temperature, not taken into account in most papers, must be considered for the design of insulators, in order to reduce the enhancement of electric field in cold regions. In addition, it has been shown that the temperature distribution and thus electric field repartition are different between the upper and lower surfaces of the insulator. To mitigate these phenomena, the shape of the insulator must be optimized.

4.1.3 | Impact of solid water content with a temperature gradient

In chapter 3, the influence of water content within the sample on the volume resistivity has been pointed out. It has been shown in figure 3.21 that with increasing water concentration, the volume resistivity significantly decreases. Based on those results, an interpolation of volume resistivity at high water concentration (0.2%) versus temperature has been done, following the same principle used for the previous section. Figure 4.9 shows the results of electric field calculations for a material with $W_c = 0.2\%$, carried oud with (a) an uniform temperature in the system ($T = 20\,°C$), and (b) with a temperature gradient induced by

a high temperature (80 °C) of the central conductor, and room temperature (20 °C) of the grounded vessel. The electric field distribution obtained with uniform temperature is similar to that of dry material presented above. In case of a material with a water content $W_c = 0.2\%$, the electric field is strongly reinforced toward the vessel when a temperature gradient is applied.

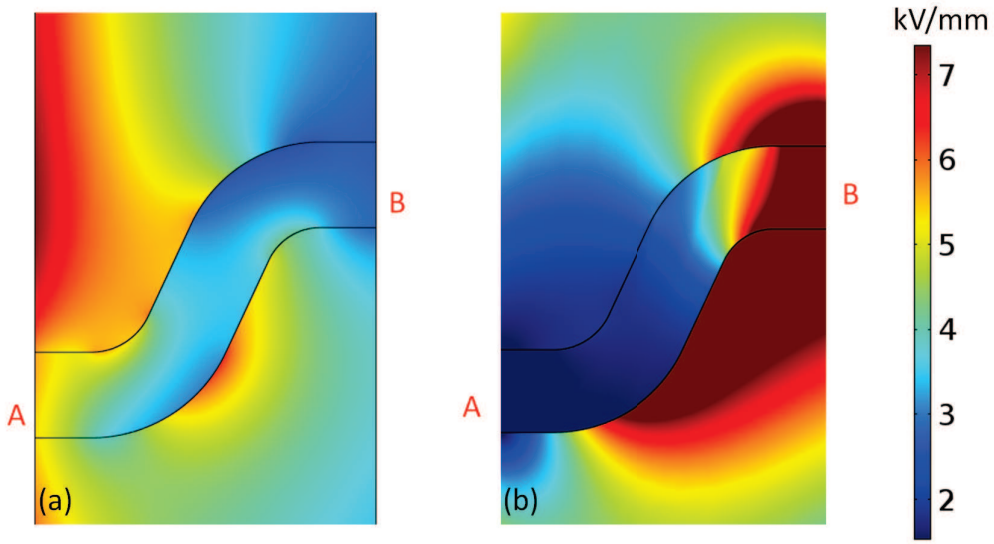

Fig. 4.8: Numerical simulation with (a) an uniform temperature $T = 20\,°C$; and (b), with a temperature gradient $\Delta T = 60\,°C$ ($V = 400\,kV$), with a water content $W_c = 0.2\%$.

A comparison of electric field distribution between a dry material and a material with $W_c = 0.2\%$ is presented in figure 4.9 in case of uniform temperature and temperature gradient, for both lower (a) and upper (b) surfaces. With an uniform temperature, an identical electric field distribution is calculated with both material, which is logical since the volume resistivity remains constant within the whole insulator.

With a temperature gradient, the electric field distribution is slightly different in cold regions between dry and $W_c = 0.2\%$, since the variations of ρ_v versus temperature are not identical. Compared to the dry insulator, the maximum electric field is nearly doubled close to the grounded vessel, and reaches high values $> 15\,kV/mm$.

Table 4.2 presents the calculated values of current through the insulator in case of a dry and $W_c = 0.2\%$ materials with and without temperature gradient. It is observed that in case of $\Delta T = 60\,°C$ calculated currents are much higher with the wet material. Those results evidence that in the presence of water within the solid insulator, the electric field reinforcement will be even worse compared to dry material, and the current will be strongly enhanced. Such conditions thus constitute «dangerous» situations, with an increased risk of electrical breakdown.

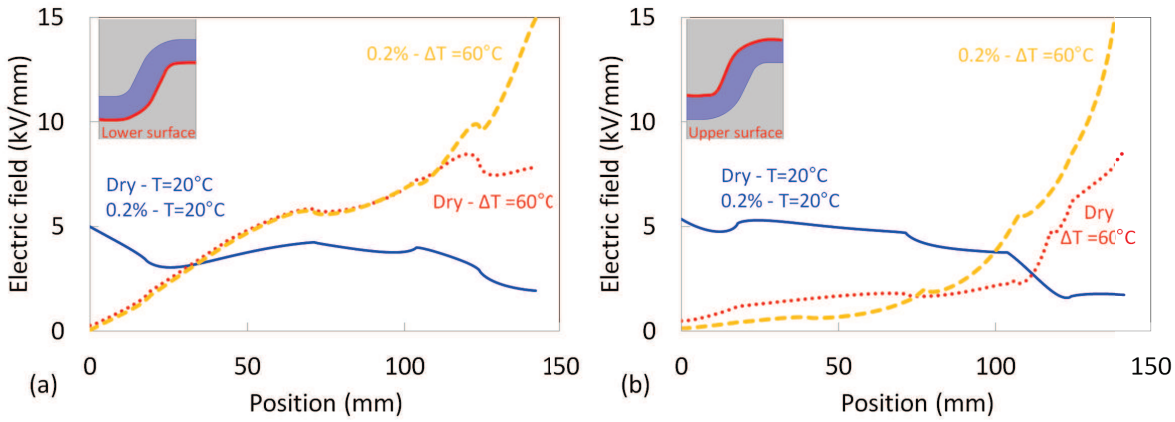

Fig. 4.9: Calculated electric field along the lower (a) and upper (b) surfaces of the insulator, with and without temperature gradient, at $400\,kV$, for both dry and wet materials.

Sample	**Dried**	**Dried**	$W_c = 0.2\%$	$W_c = 0.2\%$
Temperature	$20\,°C$	$\Delta T = 60\,°C$	$20\,°C$	$\Delta T = 60\,°C$
Calculated current (pA)	2.5	11	8.2	81

Tab. 4.2: Leakage current through the insulator calculated for dry and $W_c = 0.2\%$ insulators, with uniform temperature ($T = 20\,°C$) and with temperature gradient ($\Delta T = 60\,°C$), ($400\,kV$).

4.1.4 | Comments

The influence of temperature in a GIS geometry was studied only in a recent paper [1]. Calculations on a simplified insulator shape show that the influence of temperature will be very different in case of homogeneous distribution, or temperature gradient. In the latter case, the resistivity distribution will vary along the insulator volume, modifying the electric field distribution, which could in turn have a strong influence on the breakdown voltage of the system. From the simulations, it has been pointed out that electric field is mainly reinforced near cold regions, and that current increases with temperature. Thus, an optimization of the shape accounting for the electric field repartition in presence of a temperature gradient shall be performed in order to reduce the electric field reinforcement.

The water content considered in this study is rather large (0.2% corresponds to 50% of saturation). However, the presence of non-negligible quantities of water in real insulating material cannot be excluded since the complete drying of a such insulator with a thickness of several centimeters would require a very long time. In practice, industrial insulators are dried at $100\,°C$ in air during one day. This drying procedure can remove water from the insulator surface, but the water contained within the volume remains nearly unchanged. The electric field distribution can be further modified by water in presence of a temperature

gradient (figure 4.9), even with a small quantities of water. Besides, in presence of water concentration, the current through the insulator significantly increases. To reduce these phenomena, a thorough drying at high temperature under vacuum would be necessary.

The decrease of resistivity induced by the temperature and by the presence of water corresponds to a decrease of the material relaxation time ($\tau = \varepsilon\rho_v$). In table 4.3, the material relaxation time has been calculated for both dry and wet material at different temperatures. It is observed that dry materials present a very long relaxation time, which decreases with temperature. The relaxation time for a wet material at 20 °C is 7.5 times lower than that of a dry material.

Hence, the transient behaviour of the system (*e.g.,* during voltage application or polarity reversal) will be affected by temperature and water, and so are the electric field distribution, leakage currents and charges deposited on the insulator surface. It is worth noting that such relaxation times have been calculated for uniform temperatures, the lattice may significantly differ in case of a temperature gradient.

	20 °C	40 °C	60 °C	80 °C
Dry material	577 h	158 h	58 h	7 h
Wet material	76 h	12 h	2 h	0.1 h

Tab. 4.3: Material relaxation times calculated for dry and wet ($W_c = 0.2\%$) insulators, with uniform temperature (from 20 °C to 80 °C)).

4.2 | 2^{nd} Step: implementation of non-linear surface properties

In chapter 2, it has been evidenced that a thin layer can be added on the insulator surface to account for its specific surface properties in simulations. This model has been validated in the experimental device, showing that measured current and calculated current were equals. Hence, in the GIS geometry, a thin layer of thickness $\delta = 320\,\mu m$ was added on both insulator surfaces, as represented in figure 4.10. In this way, the insulating system consists of three finite regions (volume insulator, surface layer and SF_6). In the following simulations, the case of a dry material submitted to a temperature gradient is investigated and compared to the previous simulations where the surface properties were neglected.

In order to take into account the non-linearity of the insulator surface resistivity versus electric field, the following equation is implemented and the surface resistivity ρ_s is

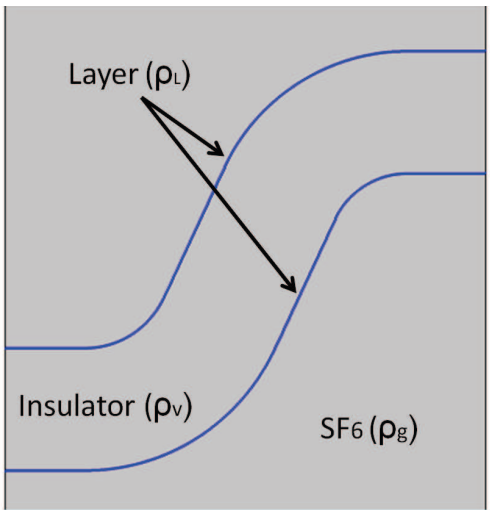

Fig. 4.10: Illustration of the geometry used for the simulation, accounting for volume and surface properties, the gas is considered as an ideal insulator.

transformed into a volume resistivity of the layer ρ_{vL} by means of:

$$\rho_s = \frac{\rho_{vL}}{\delta} = \frac{6.10^{26}}{320.10^{-6}} * exp[-(0.06T + 1.03E)] \tag{4.1}$$

Where δ is the arbitrary thickness of the surface layer. The value of $320\,\mu m$ used for the layer thickness is a compromise between the need to keep the surface mesh elements of a reasonable size, and to guarantee the accuracy of the calculated current through the insulator.

4.2.1 | Uniform Temperature

Figure 4.11 shows the electric field distribution, and lines of current density in case of uniform temperature (20 °C) neglecting surface properties (a), and with an implemented layer (b) accounting for surface properties. Similar electric field distribution are observed in both cases. However, the repartition of current density lines has changed. In (b), the major part of current density lines passes through the layer.

The electric field distributions for both simulations (with and without surface properties) are compared in figure 4.12 on the lower (a) and upper (b) surfaces of the insulator. It can be observed that the electric field variations follow the same trends, but in presence of the surface layer, the electric field is smoothened and lowered for both surfaces.

Figure 4.13 (a) shows a comparison of current density on a section of the insulator for simulations with and without surface properties. It is observed that with the layer, the current density through the volume remains the same while a very high current density passes through the surface layer. This clearly points out that by neglecting surface properties, the calculated current through the insulator is strongly under-estimated.

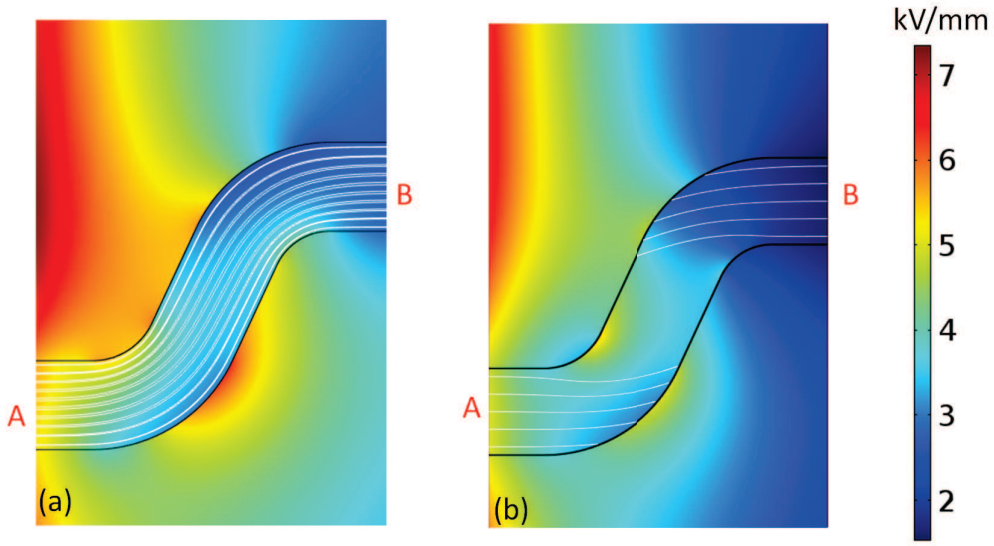

Fig. 4.11: Numerical simulation of the electric field variations (color) and lines of current density (white) without (a) and with (b) implementation of a layer to account for surface properties, at $20\,°\mathrm{C}$, $400\,kV$.

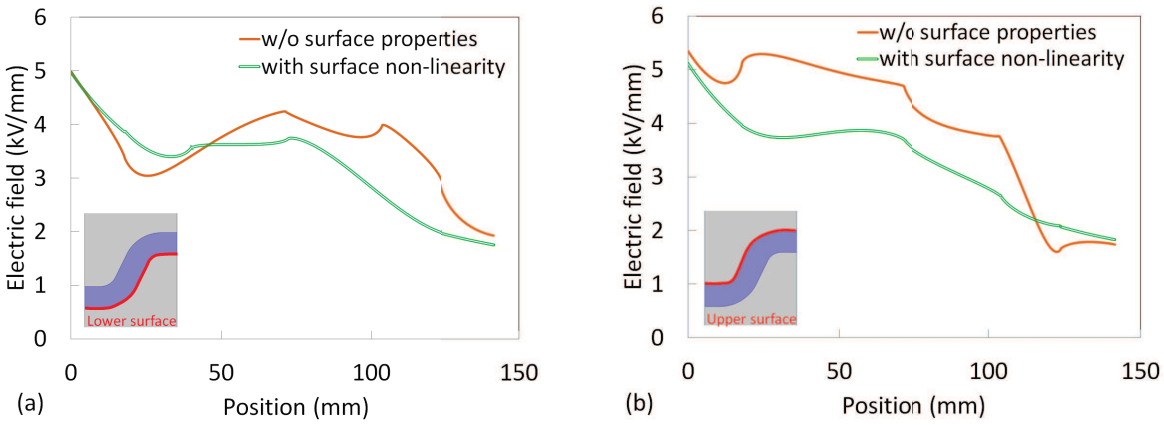

Fig. 4.12: Calculated electric field along the lower (a) and upper (b) surfaces of the insulator at $20\,°\mathrm{C}$, $400\,kV$.

Figure 4.13 (b) shows the current density for different applied voltages from $100\,kV$ to $800\,kV$. The current density increases in both volume and surface insulator with the voltage, showing one decade difference between $100\,kV$ and $800\,kV$. This increase is linear within the volume (Ohm's law), and varies within the layer according to its non-linear behaviour versus electric field. Those simulations evidence that neglecting the surface properties results in a wrong current estimation, and in an over-estimation of the electric field on insulator surfaces. The transient behaviour of the system (not studied here), would certainly show large variations due to the surface layer.

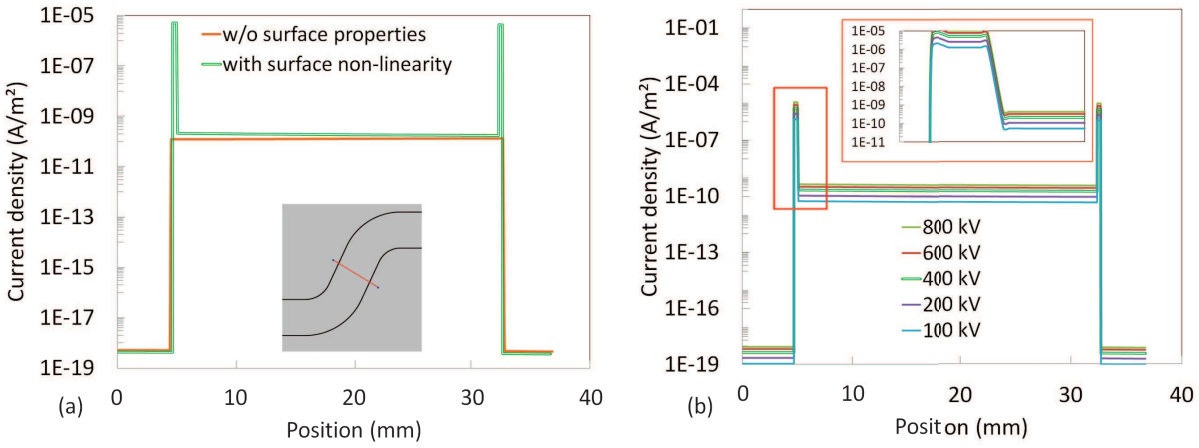

Fig. 4.13: Calculated current density along a section of the insulator at $20\,°\mathrm{C}$, showing (a) the current density through the insulator volume and its surface layer at $400\,kV$, and (b) the variations of current density for various voltages.

4.2.2 | Temperature gradient

The influence of a temperature gradient in presence of this layer has also been investigated and is presented in figure 4.14. As already observed in the 1^{st} step, the electric field is nearly reversed in case of a temperature gradient and is reinforced near cold regions (grounded enclosure).

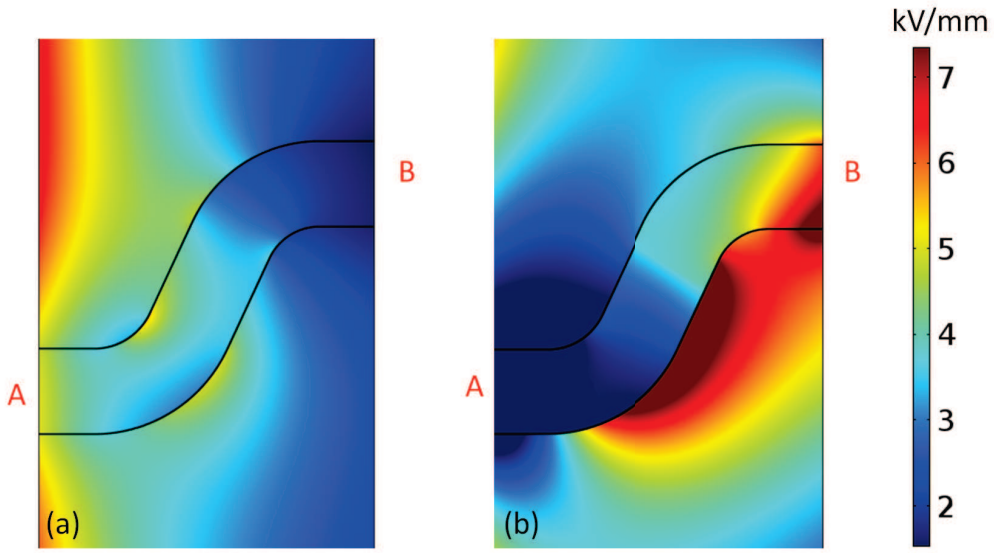

Fig. 4.14: Numerical simulation with (a) an uniform temperature $T = 20\,°\mathrm{C}$; and (b), with a temperature gradient $\Delta T = 60\,°\mathrm{C}$ at $400\,kV$.

The calculated electric field distribution is represented in figure 4.15 for both simulations (with and without surface properties). On the lower surface (a), a lower electric field is

observed with and without temperature gradient. On the upper surface, while in uniform temperature the electric field is lowered in presence of a surface layer, its distribution is modified in presence of a temperature gradient. Indeed, the electric field is not shifted to lower values, but still presents a lower maximum electric field compared to the simulation where the surface properties were neglected. This distribution shows that in addition to the influence of temperature, the electric field non-linearity impacts the electric field distribution. Instead of a strong reinforcement of the electric field near cold regions, a continuous increase of this electric field is noted with the surface layer.

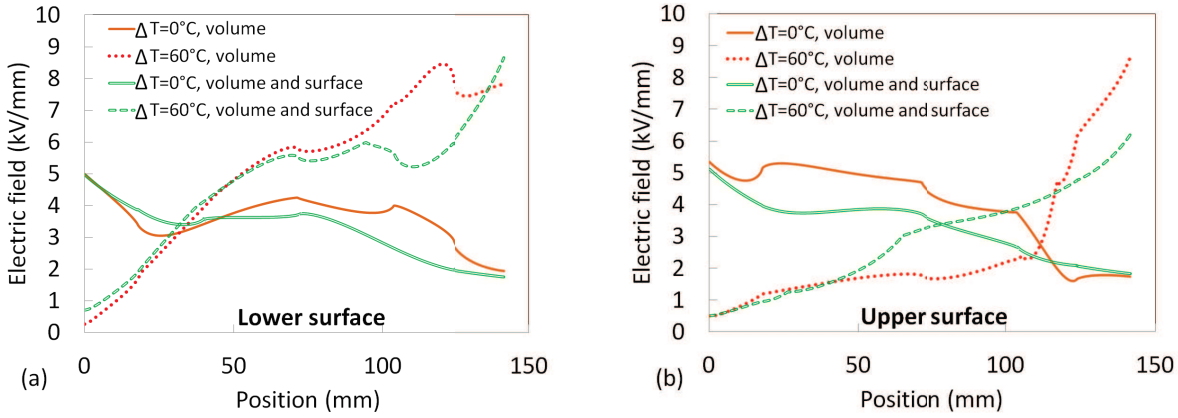

Fig. 4.15: Calculated electric field for both simulation models: neglecting or not the surface properties, in presence of a temperature gradient, at $400\,kV$ for (a) lower and (b) upper surfaces.

In addition to the electric field distribution modification, the major difference observed between both models (with and without layer) is in the calculated current through the insulator. The implementation of the surface properties within this layer results in a current of about three decades superior to that obtained without the layer at 20 °C. Calculated current are summarized in table 4.4.

	Volume	**Volume and Surface layer**
20 °C	$2.5.10^{-12}\,A$	$2.1.10^{-9}\,A$
$\Delta T = 60$ °C	$1.1.10^{-11}\,A$	$8.9.10^{-9}\,A$

Tab. 4.4: Comparison of measured current with and wth the implementation of surface properties with uniform temperature ($T = 20$ °C) and with temperature gradient ($\Delta T = 60$ °C), $400\,kV$.

Much higher currents are obtained in case of the implementation of surface properties, showing that a large part of the current passes through the layer. Accounting for surface properties significantly changes the calculated current flowing through the solid insulator.

Moreover, the case of surface properties varying with relative humidity adsorbed on the surface was not considered here. It may further enhance the current through this layer, and again modify the electric field distribution. Thus, neglecting it could result in an over-estimation of solid resistivities and in a wrong estimation of the charge accumulation/relaxation on its surface.

It is worth noting that in our case, the layer implemented corresponds to an additional epoxy resin layer, with an uniform thickness along the entire insulator surface. In practice, the local resistivity of this layer could also be due to water adsorption from the surrounding gas, or contaminations which couls also be non-uniform. For instance, a temperature gradient along the insulator surface should lead to a non uniform distribution of adsorbed water. This means that the results obtained in our simulation model could also over-estimate the current.

4.3 | Practical consequences

From the implementation of both volume and surface properties in a HVDC GIS system, it has been evidenced that temperature and the presence of water have a strong impact on electric field distribution, leakage current and also relaxation time. It clearly shown that specific surface properties must be implemented in a numerical model to account for the non-linearity of surface resistivity versus electric field and for its variation versus temperature.

Mechanisms influencing the volume and surface resistivity are quite complex. Indeed, the resistivity is decreased due to temperature and water. In industrial application, the temperature can not be controlled along the insulator and the water concentration may not be uniform within the material. Hence it will be very difficult to ensure a robust control of the electric field distribution in the geometry considered. An optimization of the insulator shape can be performed accounting for the temperature gradient in order to reduce the field reinforcement. In addition, since the relaxation time of the material depends on its resistivity and since the system equilibrium (in terms of temperature, water content, currents, etc.) is reached after many hours when temperature is changed, it is very difficult to estimate the actual transition time between AC and DC field distributions.

The simulations presented in this chapter provide a first-order estimation of the electric field distribution and currents. To complete this model, the current emitted from the conductor should be also considered. Under high voltage and depending on the electric field distribution, it has been shown in chapter 2 that a non negligible current was measured through gas. Charges are emitted from the high voltage conductor, and can accumulate on the insulator surface, resulting in a further complex modification of the electric field distribution.

4.4 | Estimation of current from the gas

Since a non-negligible current is measured through the gas, we propose to calculate an approximative value of this current based on our experimental results. Figure 4.16 shows the electric field variations (in color) and lines of current density (in white) for an applied voltage of $400\,kV$ accounting only for volume and surface properties. It is observed that in the upper part of the insulator, current lines density are localized from the conductor toward the insulator (red volume). We can imagine that emitted charges from the conductor (green area) will flow following those lines and contribute to charge accumulation. In order to estimate the contribution of those currents, calculations are performed.

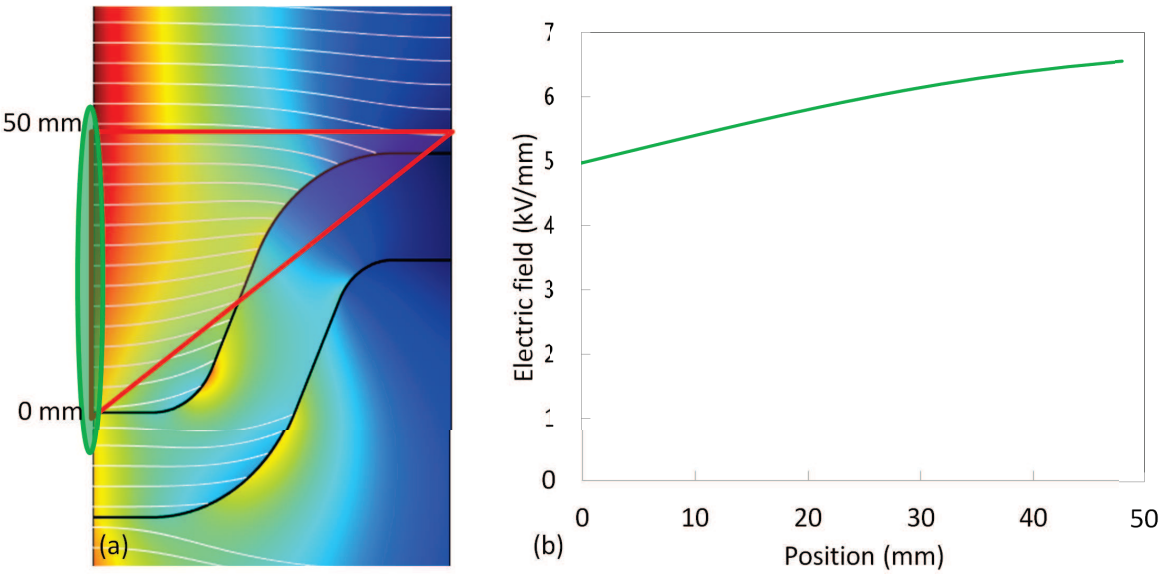

Fig. 4.16: Numerical simulation accounting for both volume and surface properties, with an uniform temperature $T = 20\,°\mathrm{C}$ at $400\,kV$.

In the simulation presented in figure 4.16, the gas was taken into account as a perfect insulator. The total current calculated through the insulator (volume and surface), equals to $2.1.10^{-9}\,A$ (at $400\,kV$, $20\,°\mathrm{C}$), is compared to the calculated current resulting from natural ionization and to the calculated current emitted from the conductor.

To calculate the current due to natural ionization which could cause charge accumulation on the solid insulator, we consider an ionization rate of 10 ion pairs/cm^3/s within the gas volume in red ($6029\,cm^3$). This results in a current $I_{NI} = 9.6.10^{-15}\,A$. The latter is negligible compared to the calculated current flowing through the insulator.

To estimate the current emitted from the conductor, as the electric field in the considered area varies from 5 to $6.5\,kV/mm$, we use an electric field value of $6\,kV/mm$. Then, using the current density obtained at such electric field in our experiments and considering a

surface emission of $170\,cm^2$, we can deduce the current flowing through the gas, given in table 4.5 for three RH.

	$RH = 2\%$	$RH = 24\%$	$RH = 34\%$
Current through gas i_g *(A)*	$6.5.10^{-13}$	$3.7.10^{-12}$	9.10^{-12}

Tab. 4.5: Calculation of current passing through gas in the geometry presented in figure 4.16 for $RH = 2\%$ and $RH = 24\%$ ($T = 20\,°C$, $400\,kV$). $RH = 34\%$ ($T = -10\,°C$, $400\,kV$).

It is observed that this current is higher than the one obtained by natural ionization. Moreover, this current is not negligible at $RH = 24\%$ and can contribute to the electric field distorsion due to charge accumulation. In addition, at lower temperatures ($< 0\,°C$) the resistivities of the insulator increases, resulting in a slightly lower calculated currents through the solid insulator. For instance, at $-10\,°C$, the current through the insulator (volume and surface) equals to $3.6.10^{-10}\,A$. In this case, $RH = 34\%$ and thus the current through the gas ($9.10^{-12}\,A$) has a higher influence on the electric field distribution since the value of the current through gas is also further increased at low temperatures, when the RH is high.

Those preliminary calculations allow estimating the current influencing the process of charge accumulation and relaxation. It is worth noting that for the electric field considered, the contribution of charge injected within gas must be taken into account, in addition, this value can be even higher in case of local field reinforcement.

Further work could permit to mathematically implement the variations of gas with electric field, accounting for natural ionization, field emission and field desorption depending on the RH within the system.

4.5 | Conclusions

In this chapter, a numerical model with an insulator geometry close to the real application has been developed to evaluate the relative influence of the current passing through the solid insulator and the one transported through gas. The influences of water concentration and temperature gradient on the electric field distribution have been shown. In presence of a temperature gradient, the electric field distribution is nearly reversed and field is reinforced near cold areas. Moreover, it also impacts the calculated current through the insulator. When temperature is increased, so is the current.

Furthermore, it has been evidenced that the implementation of surface properties by adding a layer on the insulator surface considerably modifies the electric field distribution. It is lowered and smoothened. In addition, the calculated current with the surface layer has significanlty increased. All current lines density pass through this layer, and the latter strongly depends on electric field. It clearly shows that if the surface properties are neglected, the current flowing through the insulator is under-estimated and wrong calculations are performed.

Finally, the calculations (based on experimental measurements) performed on current emitted from the conductor, point out the presence of current flowing through gas in presence of both dry and «wet» systems. Such currents must be considered since they can strongly modify the electric field distribution on the insulator surface in case of cold temperatures and humid systems.

Those calculations are of importance for the GIS application. Indeed, simulations are usually performed to predict the behaviour of solid insulator under various conditions (temperature, electric field) and thus reduce the experimental costs. In order to realize an accurate model, all injection mechanisms from the conductor must be implemented (field emission, natural ionization, field desorption). In addition, the non-linearity of surface properties must be taken into account, as well as the influence of a temperature gradient. Further work should be performed to realized a complete model accounting for those physical mechanisms.

Bibliography

[1] U. Straumann, M. Schuller, and C. M. Franck, "Theoretical investigation of HVDC disc spacer charging in SF6 gas insulated systems," *Dielectrics and Electrical Insulation, IEEE Transactions*, vol. 19, no. 6, pp. 2196–2205, 2012. (cited in pages 30 and 145)

General Conclusions and Perspectives

The control of electric field distribution and charge accumulation and relaxation on solid insulators within High Voltage Direct Current in Gas Insulated Substations, is an important challenge for the energy transport, from a fundamental and industrial point of view. The main objective of this thesis work was to investigate conduction processes and mechanisms in solids and gaseous dielectrics composing a GIS, in order to identify the main parameters which have an influence on electric field distribution and charge accumulation, and then build a numerical model allowing to estimate their impact with a realistic insulator shape.

Since the electric field distribution strongly influences the charge accumulation, we have reviewed the physical phenomena involved. This accumulation is particularly dependent on electric field orientation, and solid dielectric properties. This dependence leads to a complex equilibrium between electrical conduction through the dielectric solid (volume and surface), and charge generation and transport through the dielectric gas. It is worth noting that rather few studies were devoted to investigate the influence of other parameters of great importance: the presence of a temperature gradient, the possible influence of water present in the solid, and the non-linearity of surface conduction processes. Based on this bibliographic review, we have defined experimental investigations which allows better identifying the parameters and physical phenomena responsible of electric field distribution induced by properties of the solid, and charge accumulation due to charge creation in the gas.

We have developped two experimental setups allowing to measure very low currents under HVDC in pressuized gases, and characterize those currents. We have been able to investigate the influence of the amplitude and polarity of electric field, gap distance between electrodes, pressure, electrode surface roughness, temperature and relative humidity (RH). Many original results have been obtained, identifying the impact of different parameters.

It has been pointed out that in all cases, *dark currents* exponentially vary with the electric field, and are strongly influenced by the electrode surface roughness. Then, a large influence of pressure and temperature has been observed, resulting in the modification of the relative humidity within the system. Consequently, we have studied different equilibrium states to observe the evolution of the measured currents when pressure, temperature and RH changed. In case of a «humid» system, the measured currents increase with RH, while temperature decreases. On the contrary, in case of a «dry» system, the measured currents increase with temperature, while RH decreases.

This points out the complex influence of temperature in the system equilibrium. By varying the pressure and measuring the RH during experiments, we have highlighted that pressure only has an indirect impact on *dark currents*. Indeed, the pressure change induces a modification of the RH within the system which results in variations on measured currents.

We have also observed that influences of both temperature and RH do not modify the tendency followed by the current versus electric field. We suggest that the injection mechanisms at the origin of measured *dark currents* are similar in all our experimental conditions. Additionally, we have evidenced that these mechanisms are only enhanced or reduced by changing temperature and/or RH.

Our investigations in gases suggest that the predominant mechanism responsible of charge injection in our system is related to the theory of field ionization and desorption resulting in cluster ion formation from water molecules. These clusters, transported following electric field lines, are responsible for the measured currents.

Concerning solid dielectric characterization, we have investigated the surface and volume properties of different materials. Our approach was to develop experimental setups allowing to perform current measurements at very low noise level under pressurized gases and at high voltages. An experimental protocol was first defined in order to get reliable measurements of conduction currents. This protocol includes a drying procedure, since delivered samples contained some water, and a de-polarization procedure to remove pre-existing charges. Very long measurements have been performed in order to obtain stabilized DC currents.

Using this protocol, we have observed that both properties of the material are temperature dependent. Actually, the volume and the surface conductivities increase with temperature. Moreover, those properties are also strongly influenced by the water absorbed within the insulator and adsorbed on its surface. In both cases, the conduction increases with the water concentration. Furthermore, in the considered electric field range (from 0.5 up to $5\,kV/mm$) we have shown that volume conduction follows a nearly Ohmic behaviour while surface conductivity shows a large non-linearity with electric field variations. Those results pointed out that the surface properties of solid insulators are of major importance, and must be taken into account to build a numerical model. From these results, a data base of solid dielectric behaviour versus temperature, electric field and RH has been created.

Additional investigations on new materials and on surface treatments have been performed in order to modify the conduction properties of the solid material. We have observed that a plasma treatment on the solid surface could result in lower surface resistivities. Thus, by adjusting the implantation parameters, the surface resistivity of the solid material can be controlled. Such investigations provide guidelines to fabricate new materials optimized for HVDC. However further investigations would be necessary to confirm if these materials can be used in industrial applications.

Finally, a numerical model with a geometry close to the real application has been developed. First, volume properties were implemented, neglecting the influence of the surface properties. It has been observed that in presence of a temperature gradient between the conductor and the vessel, the electric field distribution is strongly modified, resulting in a modification of the leakage current through the insulator. In addition, the non-linear surface properties have been implemented via a thin layer on the insulator surface. It has been shown that in this case, most of current density lines pass through the layer and dramatically increase the calculated current. These investigations show that these parameters (temperature gradient, surface properties) are very important for the actual electric field distribution in a GIS geometry. Consequently, these parameters must be included in the development and optimization of practical systems. Then, estimations based on experimental measurements through gas, pointed out that the current through gas in presence of «dry» , or «humid» systems is not negligible and may also modify the electric field distribution. However, more accurate models are necessary to assess the actual influence of charges coming from the gas on the electric field distribution.

In this work, we have identified many parameters which influence the solid insulator properties and *dark currents* through gases. The results obtained show the great complexity of the problem. Under HVDC, the electric field distribution depends on many parameters (temperature, water content, electrode roughness, gas purity, etc.) which have a limited influence in HVAC.

From the scientific point of view, further experiments should be performed in gases in order to better understand the physical processus of charge injection, find a solution to control the influence of RH within gas, and reduce the charge emission from the high voltage electrode. From the industrial point of view, a more accurate numerical model, accounting for charge injection, displacement, and neutralization should be developped in order to consider all mechanisms participating to charge accumulation and relaxation. Such model should permit to predict with accuracy the behaviour of the insulator in time, versus temperature, electric field and relative humidity. Moreover, that would be also very interesting to estimate the insulator behaviour during transients of electric field and temperature.

Appendix A

The dew point is defined as the temperature at which the partial water vapor pressure of gas is equal to the vapor saturation pressure. The latter is not temperature dependent, however it highly depends on pressure. It is often measured at atmospheric pressure. An example of water vapor pressure variations as a function of the dew point is given in figure 17.

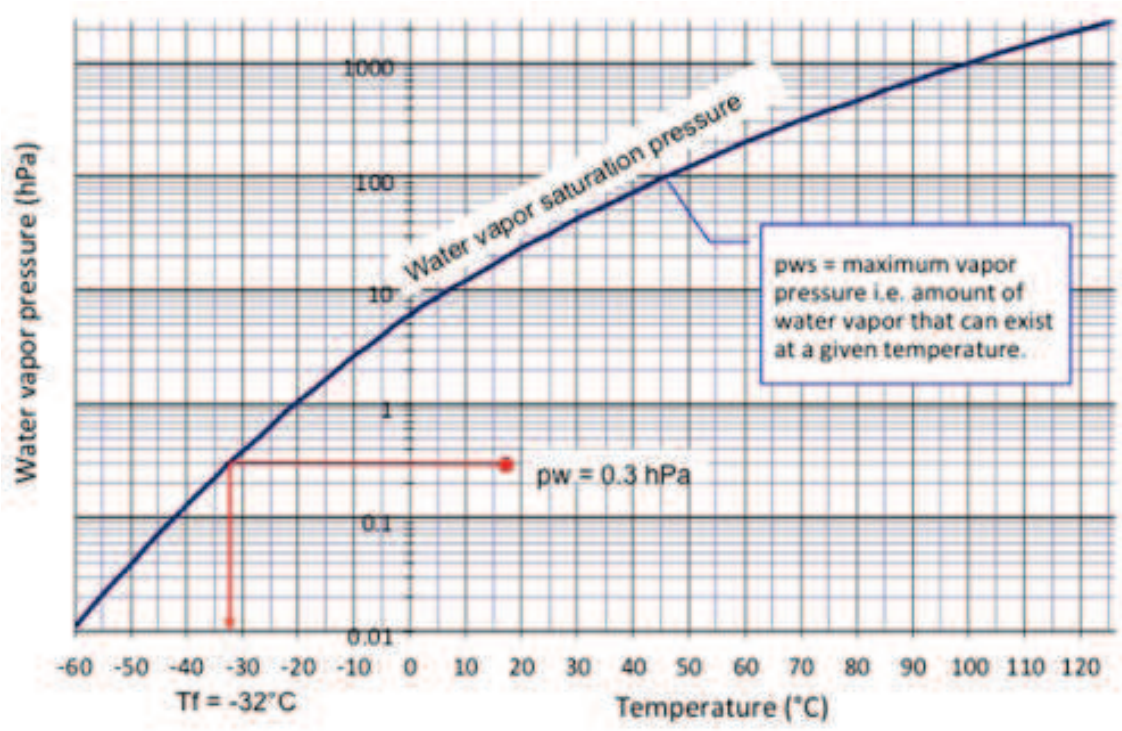

Fig. 17: Example: water vapor pressure $0.3\,hPa$ versus dew point. (available online: www.vaisala.com)

Appendix B

For a fixed pressure and absolute water content of gas, a variation of temperature results in a considerable change of relative humidity within gas. Such variations, calculated via *vaisala calculator*, are represented in figure 18 in case of air and SF_6, for a given pressure and constant water content.

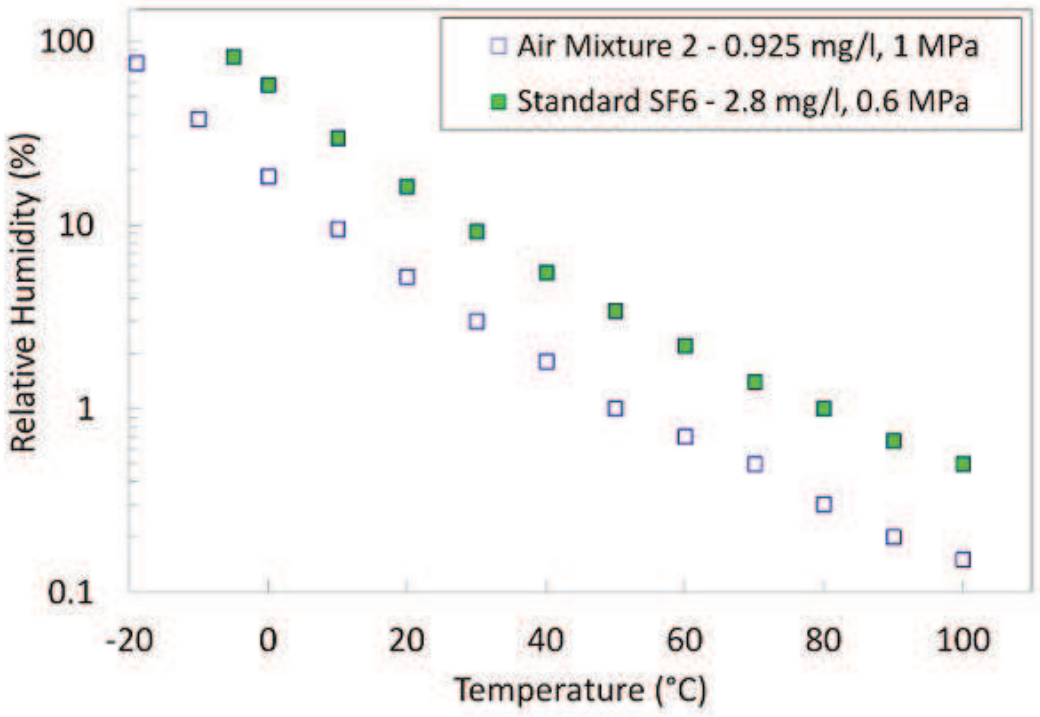

Fig. 18: Example: Variations of relative humidity versus temperature for $1\,MPa$ of air (absolute quantity of water $= 0.925\,mg/l$) and $0.6\,MPa$ of SF_6 (absolute quantity of water $= 2.8\,mg/l$), calculated via the vaisala online calculator (available online: www.vaisala.com).